UNIVERSITA' DEGLI STUDI DI PARMA

Dottorato di ricerca in Fisica

Ciclo XXIII

Coordinatore: Chiar.mo Prof. Pier Paolo Lottici

AN ORGANIC MEMRISTOR AS THE BUILDING BLOCK FOR BIO-INSPIRED ADAPTIVE NETWORKS

SUPERVISORE:

Chiar.mo Prof. Marco P. Fontana

TUTOR:

Chiar.mo Prof. Victor Erokhin

DOTTORANDO: Anteo Smerieri

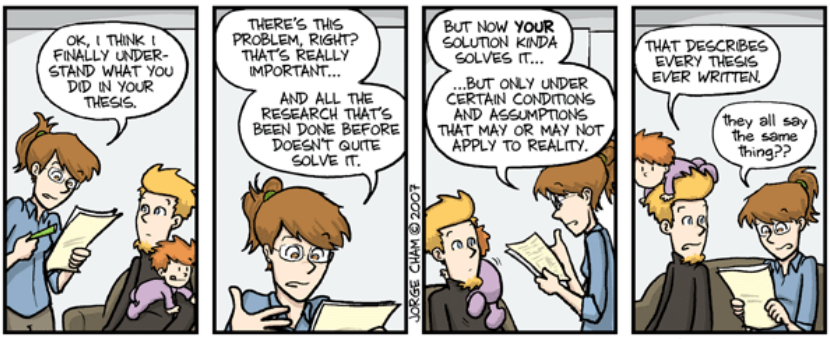

Massimo tapped at his weird screen with a gnawed fingernail. “This is just a cheap, 24-K embed. But do you see these?”

“Yes I do. What are they?”

“These are memristors.”

In heartfelt alarm, I stared around the café, but nobody in the Elena knew or cared in the least about Massimo’s stunning revelation. He could have thrown memristors onto their tables in heaps. They’d never realize that he was tossing them the keys to riches.

I could explain now, in grueling detail, exactly what memristors are, and how different they are from any standard electronic component. Suffice to understand that, in electronic engineering, memristors did not exist. Not at all. They were technically possible—we’d known that for thirty years, since the 1980s—but nobody had ever manufactured one.

A chip with memristors was like a racetrack where the jockeys rode unicorns.

I sipped the Barolo so I could find my voice again.“You brought me schematics for memristors? What happened, did your UFO crash?”

Bruce Sterling, “Black Swan”

2010 Sidewise Award Nominee Best Short-Form Alternate History

SUMMARY

1. INTRODUCTION

This thesis reports the research path I followed during my PhD course, which i followed from January 2008 to December 2010 working at the University of Parma, in the Laboratory of Molecular Nanotechnologies, under the supervision of Prof. Marco P. Fontana and Dr. Victor Erokhin. Almost all my recent research work was done within the framework of an interdisciplinary, international research project, funded by the EU. Therefore, while the focus of my research is still Matter Physics, the content of this thesis also branches out into the field of computational neuroscience, reporting the results of the research done during the year I spent in Warwick University.

1.1 Research topic

More specifically, the keystone of my research is an organic memristor, a two terminal polymeric electronic device recently developed in our research group at the university of Parma.

The device is made by a thin polyaniline (PANI) film, in its emeraldine salt (Chlorine-doped) form, connecting the two device's terminals. One of the terminals is also connected to a sliver wire buried into a lithium doped solid polyelectrolyte (polyethylene oxide, or PEO), which lies across the middle of the film. PANI's electrical conductivity is very sensitive to the doping degree of the polymer as well as to its redox state, and the film can be switched to conducting or insulating state by applying an adequate electric potential at the device's terminals. This causes a displacement of lithium ions between the polyelectrolyte and the

PANI film changing reversibly the conductivity of the film by up to four orders of magnitude, although the exact values, as for the actual threshold values at which these changes begin to happen, depend on the single device.

As of the beginning of my PhD, the device was in its early characterization stages, but it was already clear that it could be used to mimic the kind of plasticity found in synapses within neuronal circuits; some very simple circuits using our device and showing learning capabilities had already been built, and we used a simple numeric model of the device to account for its behaviour under different conditions, as for example voltage sweeps and charge accumulation in the PEO. Having a polymer based device meant also that we could work towards building a miniaturized, modified version capable of self assembly, creating a complex network that could be then trained to perform some information processing task, mimicking what happens in real neuronal circuits. However, it was also clear that we would need expertise both from chemists, in order to engineer and synthesize the components of the network, and from neuroscientists, to identify which systems could be reproduced and how; therefore, we applied for an international research project to the EU, and this was how the project BION was born.

1.2 The BION research project

Biologically Inspired Organized Networks (BION) is the name given to the research project that represented the main activity of the Laboratory of Molecular Nanotechnologies for the last three years. The main objective of the project is the realization of a new, highly innovative technology for the production of functional molecular assemblies that can perform advanced tasks of information processing, involving learning and decision making, and that can be tailored down to the nanoscale. The underlying concept is the assumption that the paradigms of learning (in particular, Hebbian-type learning rules including spike time dependent plasticity, and other forms of learning in biological cognitive systems) can also apply to complex assemblies of electrochemically controlled, conducting polymeric non linear elements. The success of this endeavour is expected to open up a totally new, bottom-up technology for the fabrication of information processing hardware capable of adaptation and decision making

BION started officially in April 2008 and it is scheduled to end in April 2011. It involves five different research groups – besides the Laboratory of Molecular Nanotechnology, which leads the project, there are the Supramolecular Sensors and Materials Group, under the Chemistry Department in Parma, the Electro-optical Responsive Polymeric Nanomaterials Group in Pisa, the Computational Biology Research Group from the Department of Computer Science of the University of Warwick and the Laboratory of Neurobiology from the Max Planck Institute in Tubingen. As of this writing, the BION project has produced more than 40 peer reviewed papers, 7 of which [1-7] were originated, totally or in part, by the research activity reported in this thesis.

1.3 Thesis Outline

As my PhD followed the evolution of the BION project, this thesis will reflect the path through different research fields that our work has followed.

Chapter 2 will introduce the concept of memristor and its properties, and outline the way it has raised in the very recent years to a very expanding and prolific research field within the scientific community, as well as some of the proposed applications. Chapter 3 will be devoted to the properties of Polyaniline (PANI) and Polyethilene Ocide (PEO) as the constituents of our device, while the device itself will be presented in Chapter 4 alongside the preliminary results that were available at the beginning of my PhD.

Chapter 5 will show some further characterization work, used for engineering the device to maximize its more useful characteristics and to deepen our understanding of the functioning of the device, as well as the work done on simple deterministic circuits that mimic closely the plasticity found in a biological specimen's neuronal circuitry (the Lymnea Stagnalis pond snail). In Chapter 6 I show a new, simplified model for our memristor that is being used to guide our research and to design training protocols and learning experiments for both deterministic circuits and circuits that are built in a stochastical way.

Chapters 7 and 8 will describe a side project that was pursued during my stay at the University of Warwick, with the aim to learn some neuroscience notions that could be useful to the project by linking more closely the two research groups of Warwick and Parma together. The project revolves around decision making in mammals, and uses an attractor based neuronal network first proposed in 2002 as a possible decision making "unit" in the visual cortex. The theory behind this model will be explained thoroughly in Chapter 7, while Chapter 8 will contain the results of some simulation work done by myself that shows how the reliability of the model and the stability of the decision states reached by the network depend on the input statistics and on the time constants of the neurons within the network, as observed already in experiments with live specimens. Finally, in Chapter 9 there will be some final considerations about the activity of the project BION in its entirety, the impact of this work within the project and the possible research outlooks as the project turns to an end.

2. MEMRISTORS AND MEMRISTIVE DEVICES

When we consider the development of the concept of “memristors” and “memristive devices”, we can identify two very different periods. The concept itself of a device called “memristor” was introduced in 1971 [8] by Leon Chua with a paper in *IEEE – Transaction on circuit theory*, without however demonstrating that it was even physically possible to build such a device. Few significant advances on the topic were made in the following 35 years, with one or two publications per year about memristive systems, until researchers at HP Labs in Palo Alto claimed, in May 2008, to have built the first memristor, a nanoscale two-electrode device based on titanium dioxide [9]. From that moment onwards, interest on the memristors surged, as figure 2.1 shows, with more than 500 between papers and patents over two years and half, two international symposia on memristors and memristive systems, two sessions dedicated to memristors at the 2010 International Symposium on Circuits and Circuits systems, and even a science fiction short story where the memristor features as a ground-breaking technology advance.

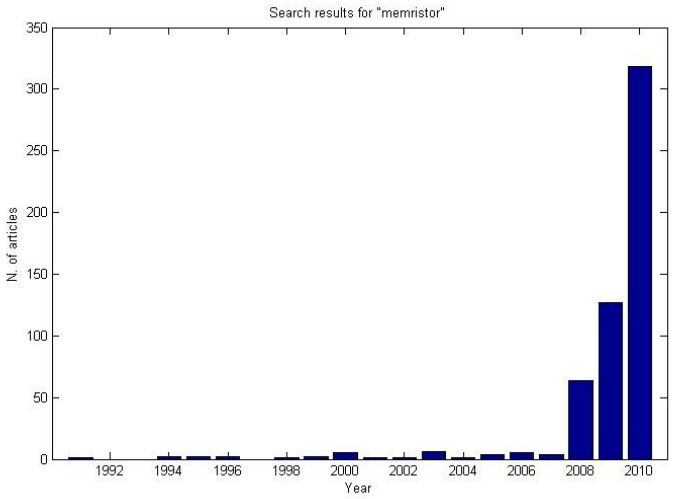

Figure 2.1: Results per year when searching for “memristor” in Google Scholar

2.1 The concept of Memristor

Chua argued the existence of the memristor in 1971 by noting that there are four fundamental circuit variables: the current i, the voltage v, the charge q, and the magnetic flux ϕ. There are six possible pairings between these variables; each pairing save one is used in the definition of either the quantities themselves ($q = \int_{-\infty}^{t} i(\tau)d\tau$ and $\phi = \int_{-\infty}^{t} v(\tau)d\tau$) or in the axiomatic definitions of resistors ($dv = Rdi$), capacitors ($dq = Cdv$) and inductors ($d\phi = Ldi$) (figure 2.2). The only pairing left out is the relationship between ϕ and q. Chua proposed that the relationship $d\phi = Mdq$ should be adopted as the axiomatic definition of a fourth basic circuit element, called *memristor* as a contraction from *memory resistor*.

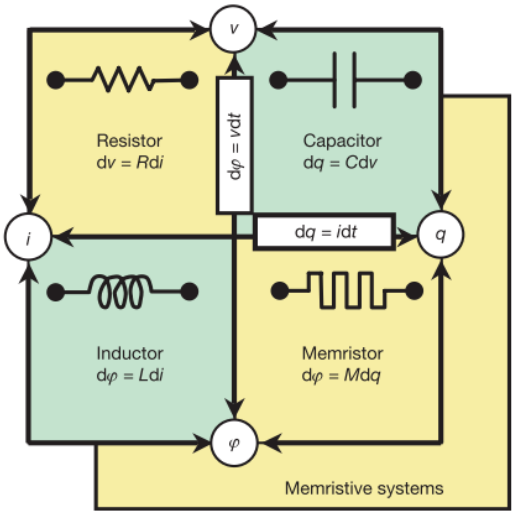

Figure 2.2: diagram showing the possible relations between *i, q, ϕ,* and *v* (from [9])

Chua showed in the paper that if the *memristance* M is constant, a memristor behaves exactly like a conventional resistor; however, if the memristance is itself a function of the charge q but not explicitly of time t, i.e. if the magnetic flux depends nonlinearly on the

charge, the relationship between the voltage at the terminals of a memristor and the charge through it is

$$v(t) = M(q)i(t) = M\left(\int_{-\infty}^{t} i(\tau)d\tau\right)i(t). \quad \text{(Eq. 2.1)}$$

In other words, while at each instant in time a memristor behaves like a resistor, the actual value of the resistance depends on the whole history of the currents that have passed through the device: the device shows a kind of "memory", hence the name "memristor". Chua furthermore showed that a memristor is a passive circuit element if and only if the memristance is always greater than or equal to zero, that no combination of other passive elements can replicate the functionality of a memristor, and gave an interpretation of the memristor in terms of quasi-static expansion of Maxwell's equations that fits with the ones already found for the resistor, capacitor and inductor [10]. In the same paper Chua showed active circuits that behaved like a single memristor and proposed some possible applications for the new device.

Some years later, the memristor first definition was expanded by Chua himself introducing the definition of *memristive system* [11], a device in which the memristance is a function of an internal state variable, of the input, and possibly an explicit function of time too. Amongst the features that distinguish a memristive system from a simple dynamical system there are the passivity, the no energy discharge property, the fact that a periodic input generates a periodic output with no phase shift (i.e. the VI characteristic curve always crosses the origin), the behaviour under an high frequency input, that approaches the one of a linear resistor. In the same paper it was also shown that a large number of systems could be modelled using a suitable memristor, amongst which the neurons' sodium channel, using the biologically accurate Hodgkin-Huxley formalism. In 1995 Chua also proposed a model of cellular neural networks [12], used for signal propagation and pattern generation, which relied also on memristors to implement the synaptic laws between the neurons.

Meanwhile, nobody actually claimed to have built a functioning memristor, although there are reports of resistive switching phenomena, especially when dealing with metallic oxides at the nanoscale, dating back to the late nineties [13,14]. Researchers from the same group that eventually claimed the memristor were already looking in that direction, by exploring the resistive switching effects in metallic oxides thin films and the possible applications of an array of many, unreliable switching elements within a structure called a crossbar [15,16]. Here the main goal of this research was to find a high density memory element, but some papers already envisioned the possibility of a new computation paradigm using what we would now call memristors [17].

2.2 The HP Labs memristor

In May 2008, with a paper in Nature, D. B. Strukov, G. S. Snider, D. R. Stewart and R. S. Williams were the first to claim to have built a memristor [9]; they proposed as well a model

that shows how memristive effects are bound to come up naturally in materials at the nanoscale where there is a strong interplay between ionic and electronic transport.

The model proposed consists in a thin semiconductor film, attached to two electrodes, in which there is a region that has a high concentration of dopants, and therefore a high conductivity, and a region in which the concentration of dopants is lower and the resistance is higher (see figure 2.3). The state variable that governs the memristive behaviour, in this case, is the position of the border between the high conductivity region and the high resistance region: as a voltage bias is applied to the film, the doping ions move in the semiconductor, expanding one region at the expense of the other, and changing the global resistance of the film

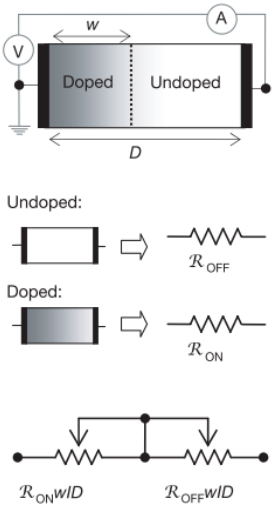

Figure 2.3 Diagram of a TiO_2-based memristor as proposed by Strukov et al.

Assuming a linear drift for the dopants, such that the drifting velocity of the border position *w(t)* is proportional to the electric field by a factor μ, we can write

$$\frac{dw(t)}{dt} = \mu \frac{R_{LO} I(t)}{D} \quad \text{(Eq. 2.2)}$$

where I is the current through the film, R_{LO} is the linear resistivity of the doped zone, and D is the total film length. If we now consider that at any time t the electrical resistance of the film is

$$R(t) = \frac{R_{LO} w(t)}{D} + R_{HI}\left(1 - \frac{w(t)}{D}\right) \quad \text{(Eq. 2.3)}$$

with R_{HI} being the linear resistivity of the undoped zone, we can integrate equation 2.2 to obtain an expression of $w(t)$ in terms of $q(t)$ and write the memristance of the system as

$$R(t) \equiv M(q) = R_{HI}\left(1 - \frac{\mu R_{LO}}{D^2} q(t)\right) \quad \text{(Eq. 2.4)}$$

under the assumption that $R_{LO} \ll R_{HI}$. Equation 2.4 shows why memristive phenomena are much more difficult to observe at the microscale than at the nanoscale, as the absolute value of the memristance component that depends on the charge depends on the square of the total film thickness.

It should be noted that the magnetic flux does not play an explicit role in the equations that define the memristance, nor in the actual physical phenomena that are involved in the ion migration; however the model satisfies the original definition of a memristor, as we can see equation 2.4 as a particular case of the function $M(q)$ that appears in equation 2.1 . Another important difference from Chua's idea of memristor is that the internal state variable is bounded, as the position of the border w can never be less than 0 or more than D. Nonlinear effects such as windowing functions can also be introduced to account for the deviations from the linear drift regime when the border between the two regions is close to one of the film's ends.

Stukov et al. demonstrate also that by varying the frequency or the amplitude of the input and by adjusting the nonlinear correction it is possible to reproduce the hysteresis found in the IV characterization curves that had already been observed in a range of different materials, from organic films to metal oxides. Furthermore, they provide their own experimental result of a TiO_2 – TiO_{2-x} device, in which the dopants are oxygen vacancies, that behaves very closely to the model proposed, and which therefore they claim as the first example of a single, passive memristive device.

2.3 Memristors after 2008

Even before 2008 researchers were trying to employ devices with resistive switching behaviour as nanoscale memory elements [15,16] to the point of patenting some of them [18-22], searching for a cheaper alternative to semiconductor-based memory elements. After the 2008 *Nature* paper, many research groups started to look more deeply in memristors and memristive systems, especially those that had researched in the same field before but without knowing the existence of the "memristor" concept.

TiO_2-based memristor represent an important share of the current research, because they're fairly easy to connect to more traditional CMOS devices; the HP group itself proposed several solutions that differ for the dimensions of the memristors and for the topology of the whole circuit [23-26]. Titanium oxide memristors are being investigated also at the Imperial College [27], where it was shown that memristive behaviour, with a contrast in resistance of two orders of magnitude, was present even in devices with a size of several microns. Some highly innovative approaches can build a titanium-based memristor on a flexible surface [28], by spin-coating a titanium solution on a polymeric substrate, in order to achieve an amorphous TiO_2 film that is cheap to produce and can be utilized in disposable "smart" sensors. A research group based in Albany is recently proposing a method to self-assemble a network of titanium based memristors [29], based on the interaction between

TiO_2 or HfO_2 nanoparticles and the phosphate endgroups of DNA oligomers, although they still have to demonstrate the memristive behaviour of the resulting circuit.

There are, however, some approaches that rely on different physical processes in order to obtain a memristive device. Amongst them, the one based on the phase transition of vanadium oxide is has already shown some possible applications [30-32]. In VO_2, there is a phase transition from insulator to metal that occurs at near-room temperatures. In these conditions, applying a voltage pulse can trigger the transition of nanoscale regions from insulating to metallic, gradually forming a conductive network that percolates through the insulating medium. One interesting property, which is not observed in memristors based on ionic drift, is that the polarity of the potential applied does not affect the resistance change, so positive and negative potentials have the same effect on the total conductivity. These memristors have been used to modify the frequency responses of some electrical circuits, and they served as a starting point to define new classes of memristive systems, called memcapacitors and memductances [33].

The concept of a conducting path forming and then breaking into an insulating medium is found also in two different approaches based on silver nanowire [34,35]. In [34], single Ag_2S nanowires were kept at a constant voltage bias, and a spontaneous switching in the nanowire resistance was observed. The sudden increases in conductivity were attributed to the formation of a conducting path made by silver atoms electromigrating, and the conductivity drops were attributed to spontaneous breakages in the wire due to the very high Joule heat caused by the current going through the filament, until the device stabilized and no more switching was observed. In [34], amorphous Si nanowires are used as connecting elements in a crossbar architecture, where the top electrode is made by silver and the bottom one is B-doped polysilicon. Applying a programming voltage step can pull a few Ag atoms into the amorphous silicon, until a conductive path is formed. The device thus obtained has only two states – one conducting, one insulating - that can be reached by applying a voltage bias above a certain threshold. However, by doing away with the crossbar architecture and co-sputtering Ag and Si above a Si layer, an analogue device can be obtained, in which the metallic Ag wires create a continuous conducting boundary in the silicon substrate that can be moved by applying a voltage potential.

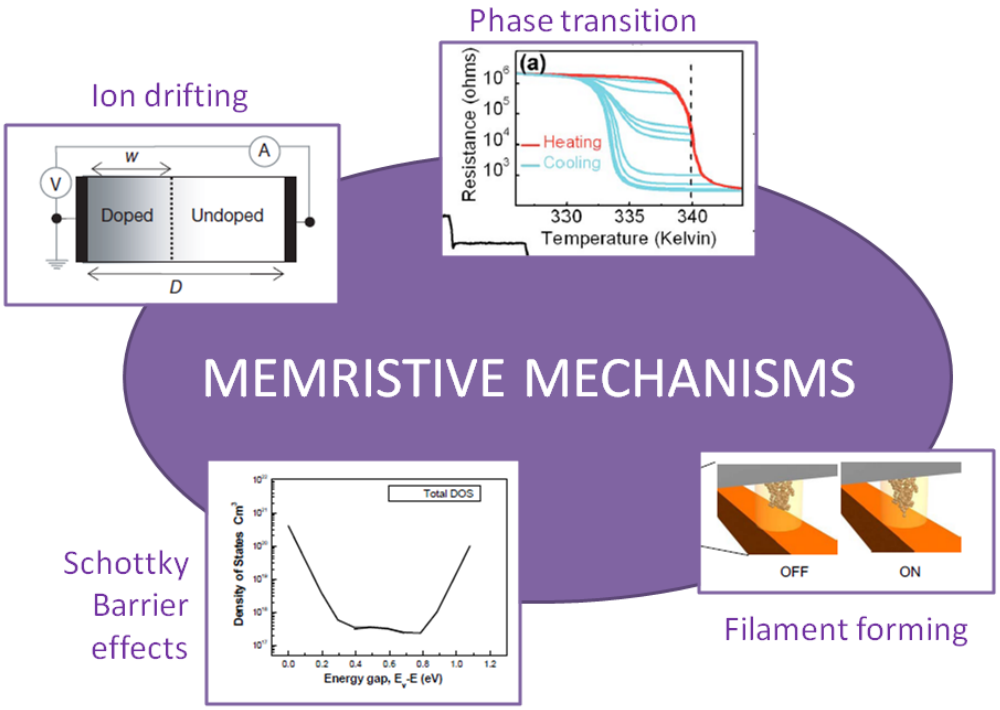

Figure 2.4: Different mechanisms that can lead to memristive behaviour of a device, taken by [9] , [31], [34] and [36]

The panorama of techniques used to achieve memristive effects is not however restricted to these three mechanism, or even to just one mechanism per device (figure 2.4). In a thin layer of Fe-doped $SrTiO_3$, for example, there are two concurrent effects that change the material conductivity [37]: the formation of conducting wires is followed by the movement of doping ions and vacancies. In [38] memristance in a $[Ru(bpy)_3]^{2+}(PF_6^-)_2$ is achieved by hole/electron injection at the electrodes, and their subsequent recombination gives rise to memory effects not only in the conductivity of the device but also in its light-emitting characteristics. Schottky barrier manipulation, finally, is the source of memristive behaviour found in Schottky Barrier FETs with poly-Si nanowire channel [36,39]. In all the examples mentioned in this section however, save from [27], the key aspect is that memristive effects only appear at the nanoscale, often involving the displacement of just a few atoms.

There is also a large interest on more theoretical aspects of memristor circuitry. The original model described in section 2.2 has been subsequently modified to include the nonlinear effects that are supposed to appear when the border between the conducting and the non conducting region approaches one of the two electrodes, by introducing some form of windowing function on the change of conductivity [40].From a mathematical point of view, general properties on the complexity of circuits containing memristors have been analyzed in [41], which also contains some definitions to categorize the different kinds of memristor and memristor-related components. Yu and Fei [42] extended the Modified Nodal Analysis approach, used to solve algebraically electronic circuits, to include a memristor element. Lahio and Lehtonen [43] showed that, in principle, two memristor are enough to compute any Boolean function, although they make no mention of the number of operations required

to do so, which could be improved by employing an ad hoc architecture or a memristor with specific characteristics.

Many papers in literature (e.g. [18,25,44-47]) propose a combination of a memristor model and experimental architecture that is intended to accomplish a specific task; the model of memristor used can either be a variation on the linear drift one, proposed for the TiO_2 model, or a totally new one that doesn't necessarily match a device already available, such as the piecewise linear (PWL) memristor [45,48]. Amongst the various models proposed, there are a few that simulate the behaviour of a memristor using SPICE [40,42,44,49-52]. SPICE is an analog electronic circuit simulator, based on modified nodal analysis, that can predict accurately the AC and DC properties of an arbitrarily complicated circuit. SPICE models of a memristor usually define it as a block of various passive and active elements, such as transistors, operational amplifiers etc. This allows experimenters to interface, with a dedicated hardware, a memristor simulation with a physical circuit [53], thus experimenting different solutions for the same problem without having to engineer every time a dedicated memristor but taking into account factors (e.g parasitic impedances, leaks) that normally are not included in a simulation.

2.4 Memristor applications

Unlike what happens with resistors, inductors or capacitors, there is a very wide range of possible characteristics that still qualifies a device as a memristor, namely, those described by all the possible functions $M(q)$ that can be inserted in equation 2.1, and an even wider range of memristive devices. For this reason, the possible applications of memristors inside a circuit are many and diverse, and research nowadays is just starting to explore all the possibilities that the new circuit element can provide; memristor models and computer simulations are an important tool to envision new applications and to direct the technological research. Phase transition-based memristors have been used to create analog circuits in which the frequency response can be modified by the input to the circuits, for example by increasing the Q factor [30] or by shifting the resonance frequency [32]. Broadly speaking, however, two classes of applications are emerging as dominant in the field, as they are somehow the more natural employ for such an element; the first is in high density, low power information storage, and the second is in adaptive circuits, with a focus on neuromorphic technology.

2.4.1 Information storage

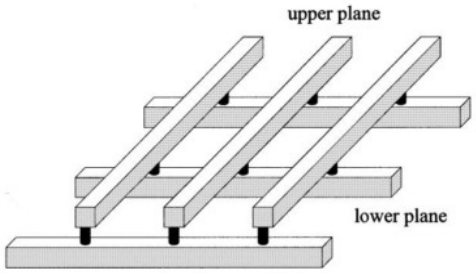

Figure 2.5: Diagram for a crossbar architecture; the white rails are metallic nanowires, the black cylinders memristive devices (from [46])

The crossbar architecture is the base for all the applications of memristors as memory units. A crossbar is a superposition of two grids of parallel electrodes, rotated by 90° with respect to each other (see figure 2.5). The active element, in this case a memristor, connects an electrode of the lower grid with one of the upper grid; a multiplexer is used to activate two electrodes at a time, reading or writing the information stored in the memristor that connects them. The advantage of such a structure is that it is very easy to build, and it's an effective use of chip area [23], as the area of a single memristor can be lower or comparable to the one taken by the two electrodes overlap without adversely affecting the memristor performance.

While large memristor based memory chips have yet to be built, Jo et al [34] claim that their 1KB device based on Silicon has a density of 2 Gbits/cm^2; the device has a pitch between electrodes of 120 nm and they also claim that decreasing it to 50 nm would only moderately affect the single memristors' performance. A 10nm pitch memristor based device could have up to 110 GB/cm^2 [54], while a 5 nm pitch device can have 460 GB/cm^2 [55]. This is to be compared with a projected memory capacity of 46 GB/cm^2 for Dynamic RAM with 16 nm pitch, expected to be reached in 2019 [56], and with the expected technical difficulties in scaling a CMOS below 10nm [49]. To achieve such densities, Strukov and Williams proposed [47] an architecture for a multiple crossbar chip, in which the crossbars are physically stacked into a 3D array, reducing the required area, even if this means having to address the single memristors with four indexes instead of the usual two.

A significant advantage of memristor-based RAMs is given by the lower power consumption; this is due to the fact that memristors are passive elements, thus not requiring alimentation to be operated, and to their non-volatility, that eliminates the need to periodically refresh the content of a single cell. A power consumption study performed using the linear drift memristor model [49] showed that the RMS power consumed by a memristor-based CAM (Content Addressable Memory) is 95% less than the power consumption measured in a standard SRAM device, while at the same time occupying 45% less chip area. Another advantage is the relative immunity to noise: while modern RAMs store very small charges and as such are prone to noise, the robustness of a memristor based memory cell to noise is given by the difference between the maximum and minimum resistance, which can be of one order of magnitude or more. On the other hand, the non-volatility of a memristor

comes at a price of reduced switching speed [57], that implies higher reading and writing times than DRAM, and a lower endurance (maximum number of operations without performance degradation).

2.4.2 Information processing

One of the most interesting features of a memristor, however, is the ability to function at the same time as an information storing and a signal processing unit. Snider, one of the authors of the 2008 HP labs paper, had already explored the possibilities of using a hysteretic resistor array for computing in two papers [15,16]. His first approach to the problem used the crossbar architecture and a convenient model for the memristor linking the two electrode planes, with a positive voltage threshold V_P that would put the memristor in a conducting state, a negative voltage threshold $V_N < -V_P$, and two "breakage" thresholds V_{B-} and V_{B+}, one positive and one negative, that would damage the memristor and leave it permanently in the insulating state if reached. With this approach, every memristor in a crossbar can be used as a *latch*, an element that can read and store the state of another element, or an *inverting latch*, provided that the right voltages are sent to both; the state can be "open", insulating, or "closed", conducting, corresponding to the binary values 0 and 1. The right combination of latches and manipulation of input voltages, in combination with a clock system, can provide universal computation: Snider demonstrated a circuit for an XOR gate, that uses 9 clock cycles to perform the operation, as well as a way to join together different logic gates and operate further on their outputs.

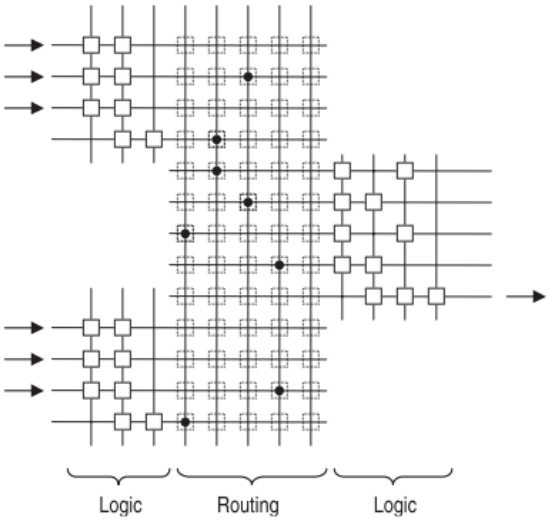

Figure 2.6: an example of memristor crossbar circuit. The two logic blocks on the left execute different logic operations on different inputs; the results are routed through the middle block to the logic block on the right, that performs further operations. From [16]

After 2008, a first memristor based architecture was proposed in HP labs [26]: two crossbars of 21x21 memristors were interconnected connected by traditional electronic components.

The first phase in the circuit operation was a test in which it was determined which nanowires were effectively operating and which were broken, as well as checking the IV characteristics of each memristor; more than 90% were reported as functioning. Subsequently, the memristors were programmed so that the circuit could receive 4 inputs in the form of voltages and perform the logic operation AB + CD; the result of this operation was encoded as an output voltage. The circuit was also able to self-program, and programming the state of a single memristor as the result of a NAND operation of two voltage inputs was shown as a demonstration of this possibility.

A memristor-based non-volatile latch circuit, to explore the possibilities of computation with intermittent power sources, was proposed in [25]. In this circuit, the memristor isn't used until the power is cut off or brought back on, when it stores the last state of the input: the performance of the circuit was shown to slowly degrade as the number of power off/power on cycles grew, but the rate of errors stayed below 1% for the first 1500 cycles, and grew continuously after that, as a consequence of failure in the memristor itself.

Field-Programmable Gate Arrays are another natural memristor application. FPGAs are arrays of logical gates, usually made by traditional semiconductor devices (complementary metal-oxide-semiconductor transistor, CMOS), in which the operations performed by the circuits are not predetermined when the chip is built but can be programmed and modified at a later time [58,59]; memristor-based FPGAs integrate memristors and CMOS elements by using the former as a reconfigurable routing element between the latter. Xia et al [24] demonstrated integration of TiO_2 memristors and CMOS transistors in a FPGA element; the memristors were laid in a modified crossbar setup and connected to a CMOS layer by tungsten vias. A first electrical analysis allowed to map defects in the chips and to program a wiring of the logical elements around the defects, by programming some memristors in the insulating state and some in the conducting states; successive wiring demonstrated that the FPGA could work as a NOT, AND, OR, NAND, NOR gate or as a D flip flop. The non-volatility of the memristors implementing those wirings meant that the FPGA configuration was kept even when completely cutting off the power, and the researchers showed that one such circuit could keep its configuration for at least five months.

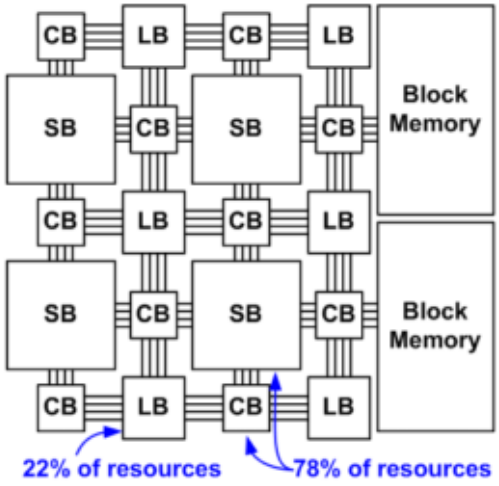

Figure 2.7: Representation of a FPGA. LB: Logic Block. CB: Connection Block. SB: Switch Block. From [60]

The circuit proposed, however, required Nano Imprint Litography to be performed on an active CMOS layer, which was not performed before in a commercial semiconductor fabrication facility before. Wang et al [60] propose a different method for integrating memristors and CMOS, doing away with the crossbar, as they argue that there are difficulties fabricating pins at different heights to connect the top and bottom wire meshes. They consider the use of 1 memristor/1 transistor units as memory elements, instead of SRAM cells, and the replacement of the usual 7-transistor switching block in the connecting blocks of FPGAs with units of two transistors and one memristors or two transistors and two memristors, to improve stability. They simulated the performances of such systems and showed that the integration of memristors and CMOS would lead to at least twice the chip density and 20% less standby power consumption.

2.4.3 Neuromorphic circuits and spiking networks

The first mention of memristors in the contest of neuromporphic circuits dates back to 1976, when Chua in a paper that described possible applications of memristive system proposed a memristor model for the Hodgkin-Huxley neuron [11]. In a 2007 paper [15], Snider argued that since memristive devices are prone to have high variability in the electrical characteristics, as well as a high defect rate [61-63], traditional Boolean logic might not be the best way to employ them. He proposed instead to use the memristors as edges in *adaptive recurrent networks* – elements that link together *nodes*, which in his examples would be traditional solid state circuits.

In a recurrent network, a node performs a nonlinear operation on the incoming signal and sends it back to the other nodes via the edges, which in turn operate on the signals crossing them, usually by applying a multiplication factor (weight). Snider assumed that the $M(q)$ function that regulated the memristances had a dependence from the voltage drop v that was proportional to proportional to $\sinh(v)$, with caps on the maximum and minimum

memristance. He then proposed a spiking network of 256 nodes and 31488 edges, where each node integrated the incoming currents and emitted a voltage pulse when the total charge was above a certain threshold. By carefully designing the spike pulse he was able to enforce a learning rule that enforced Hebbian learning [64] while at the same time avoiding edge saturation. The memristor network was used in an architecture reminiscent of Linsker's networks [65-69], as the bottom layer of a structured network that receives visual stimuli; the resulting network was used in a simulation of edge detection experiments, and its performance was demonstrated to be very robust with respect to defects and variations in the parameters that described the memristors of which the edges were made.

An interesting application of memristors is also found in CNNs, cellular neural/nonlinear/nanoscale network, which is a bio-inspired computational paradigm that performs computations through the interactions of processing cells, connected with programmable weights, that propagate to the neighbouring cells the results of local operations [70,71]. The Hodgkin-Huxley neuronal model itself was proposed by Chua [12] as a system that can be built with a one-dimensional CNN using memristive devices. Laiho and Lehtonen propose a SPICE simulation of a hybrid CMOS/memristor CNN, in which a variation of the TiO_2 memristor model is used as the connecting element between cells, following some theoretical work on Boolean logic as implemented by memristors [43]. The resulting network is ON-OFF only, in that the memristors are considered as having only two states, one conducting and one insulating; the connecting memristors were shown to be programmable individually or simultaneously. Simulations showed that the resulting network was denser than an equivalent CMOS only network, requiring only 15 CMOS transistors per cell, but at the price of a longer programming time.

Even closer to the neuroscience field are studies that link memristors with the plasticity properties of neuronal circuits. Besides the already mentioned theoretical work of Chua [11], which used a memristor in a circuit implementation of Hodgkin-Huxley neuron, there are studies that show how memristance could explain and replicate Spike Time Dependent Plasticity. STDP is an improvement of the Hebbian learning rule: with the Hebb rule, the synaptic weight that connects two neurons is adjusted by a factor that is proportional to the instantaneous firing rate of both neurons; this is often summarized with "those that fire together, wire together" [64].

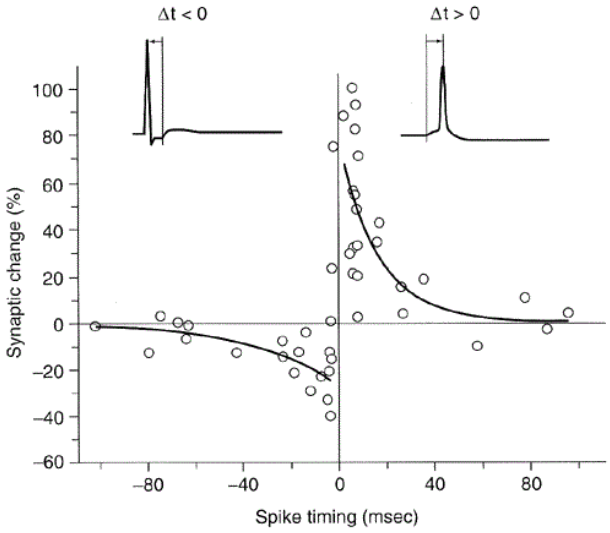

Figure 2.8: Change in synaptic strength due to the postsynaptic neuron spiking time. The presynaptic neuron spikes at *t*=0; black lines are calculated from the model, white circles are from experimental data. [Bi & Poo 1998]

STDP, in addition, also takes into account the fact that synapses are directional, and the exact timing of the spikes: for a synapse to get stronger, the postsynaptic neuron has to spike (or "fire") shortly after the presynaptic neuron has spiked, while if the postsynaptic neuron fires before the presynaptic one, the synaptic link actually gets weaker; in both cases, the change in synaptic strength gets higher as the two spike times gets closer. STDP explains cortical phenomena better than Hebb's rule [72,73] and has actually been observed in neuroscience experiments [74,75]. Recently both Afifi et al. [76] and Linares-Barranco et al. [77] proposed two different memristor models that could achieve STDP in memristor/CMOS hybrid circuits. In both cases, the spike was generated by traditional CMOS components and transmitted to the other "neurons" via a memristor crossbar; the exact spike shape, while very difficult to measure in neurophysiology experiments, is critical to achieve STDP, as it is critical the exponential dependence of the memristance change for the potential applied. The Linares-Barranco proposal has the additional merit of employing a spike shape, shown in the right panel of figure 2.9, that is very similar to the one commonly used in neuroscience and that can be generated by an Hodgkin-Huxley model [78], namely a sharp positive voltage peak followed by a more shallow, longer negative rebound. The Afifi proposal (figure 2.9, left) uses a piecewise linear spike shape in which the spike has a negative dip before going to a positive potential and then decay slowly; in both cases the idea is that the sequence of the spiking determines the polarity of the voltage across the memristor and hence the sign of the memristance change.

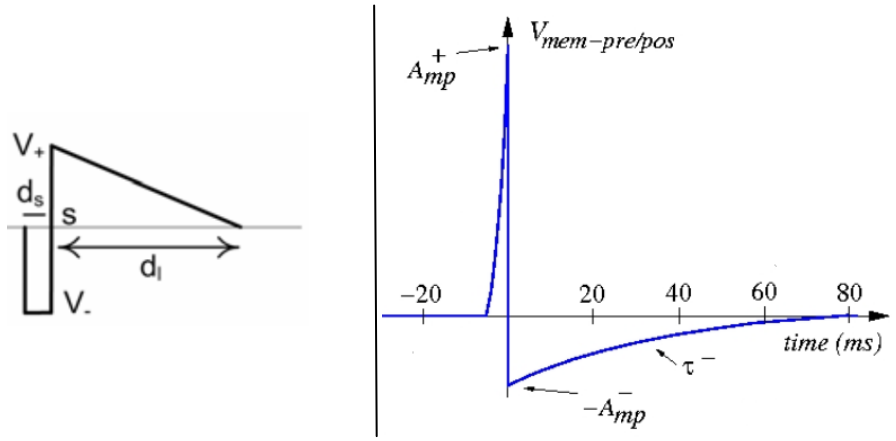

Figure 2.9: spike shape proposed by Afifi et al. (left) and Linares-Barranco et al. (right) to implement STDP in memristor/CMOS hybrid circuits

Finally, an interesting application of memristive systems is the one proposed by Pershin et al. [48], that mimics the learning behaviour showed by a unicellular organism, the *Physarum Policephalum* amoeba. Colonies of the *Physarum* have shown intelligent behaviour, by solving labyrinths and geometrical puzzles [79], and are being studied as computational engines [80]. Recently the *Physarum* has shown the ability to learn temporal intervals [81] of a periodic input, in the form of spikes in temperature and humidity of the environment, to the point of being able to anticipate the next event in regular series of inputs by adjusting its movement speed. The memory of such a time series gradually fades, but if another pulse is then sent in, the *Physarium* shows "recollection" by adjusting again the movement speed, at regular intervals that correspond to the ones of the original input series.

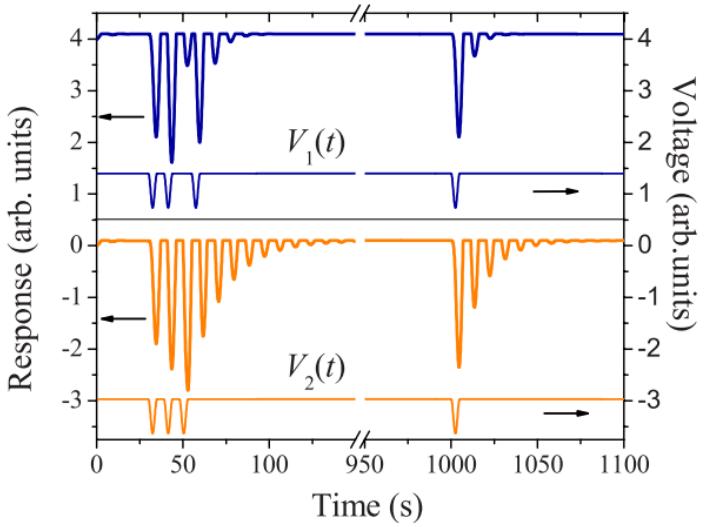

Figure 2.10: Learning in a memristor-based circuit (from [48]). Top: training with a nonperiodic input $V_1(t)$, bottom: training with a periodic input $V_2(t)$. Slow down oscillations are much stronger when training with a periodic input and recollection, as the response to a single pulse long after the training, is much stronger.

Pershin et al. proposed a piecewise linear model for a memristor that, in parallel with the capacitor in an RLC circuit, could achieve the same behaviour: when aperiodic voltage pulses were sent to the circuit, the oscillations were quickly damped, but when the pulses were applied in regular intervals, at a frequency close to the circuit's resonance, the memristor's state was changed enough that several slow down oscillations appeared even when the input was removed (see figure 2.10). Moreover, if and only if the training pulse series was periodic, a single pulse was able to create more slowdown events even a long time after the training, thanks to the non-volatility of the memristor.

3. MEMRISTOR BUILDING BLOCKS: PANI AND PEO

With the exception of the pyridine-based memristor [38], all of the memristors listed in chapter 2 are based on metals, metal oxides, or semiconductors; to this day, apart from the one presented in this thesis, polymeric memristive devices are unheard of. This is somehow to be expected, if one considers that the groups involved in research on memristors are pursuing efficient, cheap alternatives to solid-state electronic components, which are now at a very high technological standard, having been improved continuously for the latest 50 years. On the other hand, polymer electronics is a relatively new field, with a narrower spectrum of applications that are reaching the commercial level just now [82,83]; it allows however a different approach to the problem of nanodevice fabrication, offering new approaches (like the possibility of self-assembly) that are not accessible using the standard fabrication methods of solid state electronics.

In this chapter, after a brief introductory section on the history of polymer electronics and on the mechanisms of electronic conduction in polymers, we will examine the characteristics of the materials that are the main components of the polymeric memristor presented in this thesis, including some notes on their most important technological applications.

3.1 Conducting polymers

3.1.1 Brief historical notes

The last thirty years have seen a progressive and constant interest in the field of conducting polymers [84]. The first studies on polymer properties date back to the 1920s, with the

concept of macromolecules as introduced by H. Staundinger [85]; nylon was the first synthetic polymer to be produced and sold on an industrial scale, in the mid-thirties. The Ziegler-Natta method for polymer synthesis using titanium-based catalysts [86] is a milestone in the development of industrial processing of plastics.

Polymers synthesized using Ziegler-Natta cathalysts are saturated polymers, as the four valence electrons in carbon atoms are used up to make covalent bonds, and are therefore electrical insulators. In conjugated polymers, on the other hand, the π bonding leaves an unpaired electron for every carbon atom; the sp^2p_z configuration of the valence orbitals causes a partial overlap of orbitals belonging to different atoms, delocalising the electrons along the polymer chain and increasing the mobility of the charge carriers, that however depends strongly on the symmetry and the geometrical configuration of the polymer chain.

In conjugate polymers there is usually an intercalation of single and double bonds, leading to the creation of a π band and a π* band; a typical example of this configuration is the polyacetilene $(-C=CH)_n$. Every band can hold two electron for each carbon atom in the chains, therefore the π band will be filled and the π* band will be empty; this makes conjugated polymers semiconductors, with energy gap E_g given by the difference between the energy of the highest occupied state in the π band and the energy of the lowest unoccupied state in the π* band. The energy gaps depend then on the composition of the polymer repeat unit, allowing molecular engineers to design and produce semiconducting polymer with a preestabilished energy gap.

The early 1980s saw the laying out of some important theoretical work, like the discover of solitons [87] that prefigurate the possibility to have cheap, easily processed polymers with the optical properties of semiconductor and metals. Usually, metallic or semiconducting polymers are obtained by chemical [88] or electrochemical doping [89], which shifts the Fermi level to an energy where there is a high density of states, by redox reactions or acid-base chemistry; counter-ions are inserted to mantain charge neutrality, so metallic polymers are actually salts. In a polymer, every repeat unit is a potential doping site, so doping can introduce in the polymer chain an high number of charge carriers; these are then delocalized along the polymer chain, thanks to the attraction of neighbouring nuclei [88], and the delocalization can be extended in 3d space thanks to inter-chain electronic transfer. Disorder on the other hand limits severely the charge carrier mobility, and therefore the polymer conductivity; this is why achieving highly ordered polymeric structures is constantly the focus of research activity in the field[90].

3.1.2 Polymer electronics

The electronic structure of polymers has been described for the first time at the end of the Seventies, using a tight binding approach in which the electron-phonon interaction is responsible for coupling the electrons of π orbitals to the special distortions of the polymeric chain (Su-Schreffer-Heeger model, or SSH model [91,92]). This model, in which the elementary excitations are associated to the creation of a mobile charge carrier (either electron or hole, in this case referred to as “polarons”),is well suited to describe all the cases

in which the interaction between charge carriers is well screened, making the electron-phonon interaction dominant, as it is the case for conjugated polymers with electrons delocalized along the chain.

The Hamiltonian used in the SSH model includes a hopping term $t_{n,n+1}$, which describes how an electron can move from the *n*-th site to the *n+1*-th site, depending on the positions of the nuclei u_n:

$$t_{n,n+1} = t_0 + \alpha(u_{n+1} - u_n) \text{ (Eq. 3.1)}$$

The full Hamiltonian for the SSH model is

$$H_{SSH} = \sum_{n,\sigma} -t_{n,n+1}(c^{+}_{n,\sigma}c_{n+1,\sigma} + c^{+}_{n+1,\sigma}c_{n,\sigma}) + U + K \text{ (Eq. 3.2)}$$

where $c_{n,\sigma}$ and $c^{+}_{n,\sigma}$ are the construction and destruction operators of a fermion at site n,σ, *U* describes the kinetical energy of the nuclei and *K* is a term that describes with an harmonic potential the binding energy of a bond between two neighbouring atoms in a polymer chain.

Some conjugated polymers, of which polyacetilene is the most notable example [87], have two different spatial configuration that minimize the energy as written in (3.2), given by the two possible way that single bonds and double bonds have to alternate in the polymer chain (see figure 3.1); the ground state hence has a two-fold degeneracy [93,94]. However a situation may rise, for example after the insertion of a doping ion that modifies locally the geometry of the polymer, where a part of the polymer is in one of the two configurations and the rest of the polymer is in the other.

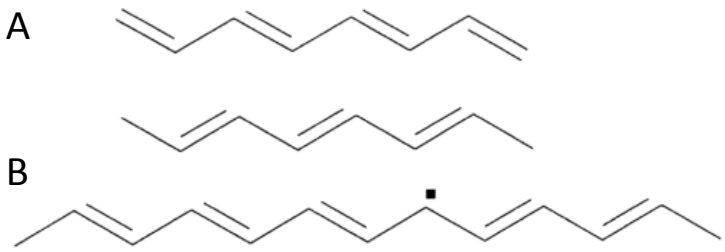

Figure 3.1: the two possible configurations (A and B) for polyethylene and a soliton at the interface of the two (bottom)

In this case, we can associate a quasiparticle, called soliton, to the deformation in the polymer's geometry at the interface between the two different states (A and B configuration in figure 3.1) [87,91,92]; this quasiparticle corresponds to an energy level created between the valence band and the conduction band, and has no net charge and nonzero spin if it is occupied by just one electron, or it has electrical charge and zero spin if the level is unoccupied or occupied by two electrons. Given the translational symmetry of the polymer along the polymer chain, the soliton can move up and down the polymer chain; where there

is another switch between the two possible states, such as in a polymer where the distribution of single and double bonds is B, then A, then B again, we may represent the situation with a soliton and an antisoliton.

In polymers where the ground state is not degenerate, the two possible configurations of single and double bonds are not isoenertgetic; a deformation of the polymer chain will create a localized soliton-antisoliton couple, called a polaron or a bipolaron [95,96]. A polaron can be tought of as the union of an electically charged soliton and one electrically neutral, where the energy levels hybridize to create bonding and antibonding states; it can have electrical charge ±*e* and has an half integer spin. A bipolaron instead is created from the union of two solitons with the same charge, or of two polarons in which the spins of the non-charged solitons are opposite to each other.

The SSH model, based on solitons, polarons and bipolarons can reliably predict experimental measurements, and its theoretical predictions have been verified via optical probing of the electrical states within the gap and by magnetic measurements of spin intensity and spin distribution [93]

3.2 Polyaniline

3.2.1 Undoped

Polyaniline (PANI) is one of the most studied polymers in the last 30 years; it is a very stable material [97-99], easily dopable, and its conductivity covers a range of ten orders of magnitude, as a function of the dopant and of the PANI's redox state[100,101]; polyaniline is the first conducting polymer that can be processed while in the metallic state. It has been used as the main material for building organic electronics analogues of traditional semiconductor-based circuit elements, like diodes [102], LEDs [103], FETs [104-108], since in the doped state its conductivity can be greater than 10 S/cm, but it can also be used to create microelectronic structures that have no semiconductor-based analogue.

Polyaniline is synthesized via polymerization of aniline, an organic compound whose formula is $C_6H_6NH_2$ [109,110]. The fabrication process is inexpensive, as the base monomer is very cheap and the polymerization reaction has a high yield.

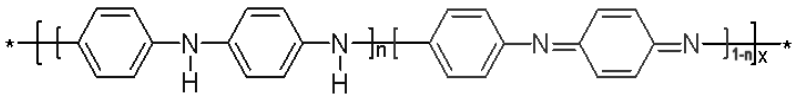

Figure 3.2: Polyaniline chain

The general formula of polyaniline is $[(\text{-B-NH-B-NH-})_n, (\text{-B-N=Q=N-})_{1-n}]_x$, where B stands for a benzene ring and Q for a quinone ring; x, the number of repeating units that make up the polymer, can vary from a few units to tens of thousands of units. At room temperature there are different stable polyaniline redox states, that specify the fraction *n* of ammine-benzene

units and the fraction 1-*n* of immine-quinone units. Although *n* can have any value between 0 and 1, four cases are usually analyzed [111,112]:

- n=1; this is the leucoemeraldine base (not to be confused with leucoemeraldine salt, which is protonated), and it's made only from benzene-ammine units. The polymer in this state is an insulator, with a pale brown colour.
- n=0.5, one benzene-ammine unit alternating with one quinone-immine unit, represents the emeraldine base. The polymer has a deep blue colour and is insulating, but can be made conducting via electrochemical doping.
- n= 0.25, nigraniline base: the majority of repeat units are of the quinone-immine type; the polimer colour is darker
- when n=0 the polymer is called perigraniline base, and is composed by quinone-immine units only; it is an insulator, and its colour is almost black

3.2.2 Doped PANI

The more noteworthy states of polyaniline are however the conducting states; they can be obtained by chemical or electrochemical oxidation of the leucoemeraldine base or by protonation of the emeraldine base [113], resulting in a bright green polymer called emeraldine salt.

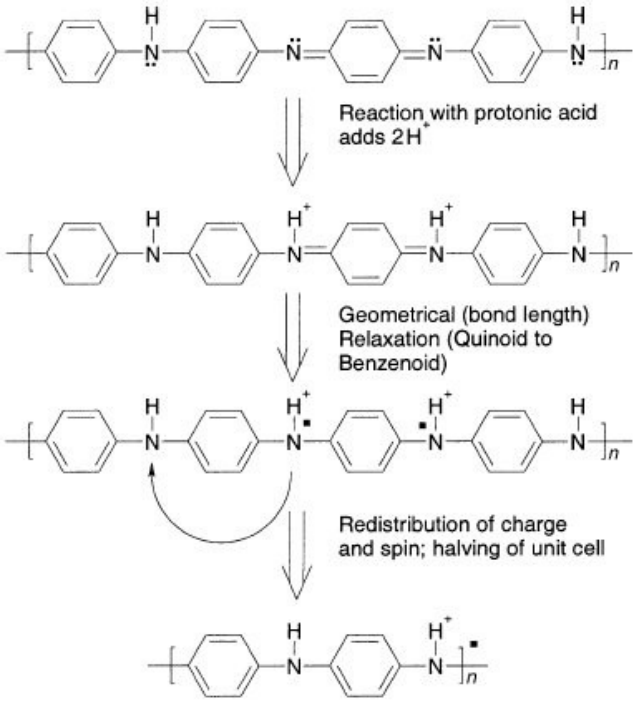

Figure 3.3: fabrication of conductive emeraldine salt by doping of the emeraldine base

Figure 3.3 shows how emeraldine base is a copolymer where there is alternation of a benzoic ring and a quinoid ring; by a reaction with a protonic acid we can add H^+ ions and counter ions like Cl^- or HSO_4^- (not depicted in the figure). The H^+ ions induce a charge and spin redistribution, leading to a configuration where there are only benzoic rings and an unpaired spin; this effectively reduces the unitary cell of the polymer and doubles the number of the repeating units along the chain without affecting the number of electrons on the polymer [111,114]. The end result of this charge redistribution is therefore a metallic half-filled band, with a positive charge for every repeat unit, balanced by the presence of counter ions; this situation can be described in terms of a polaron lattice, as for each repetition unit there is a mobile charge carrier with a total charge of *e* and with spin ½ [113,115,116].

Infrared absorption has been used recently [117] to investigate the redox reactions and doping mechanisms of polyaniline in an ion-rich environment, like an acidic solution or an electrolyte, as a function of the electrochemical potential. More specifically, it has been shown how two different doping mechanisms are involved, at different electrochemical potentials, in the passage from the leucoemeraldine salt to the emeraldine salt and in the one from emeraldine salt to perinigraniline salt.

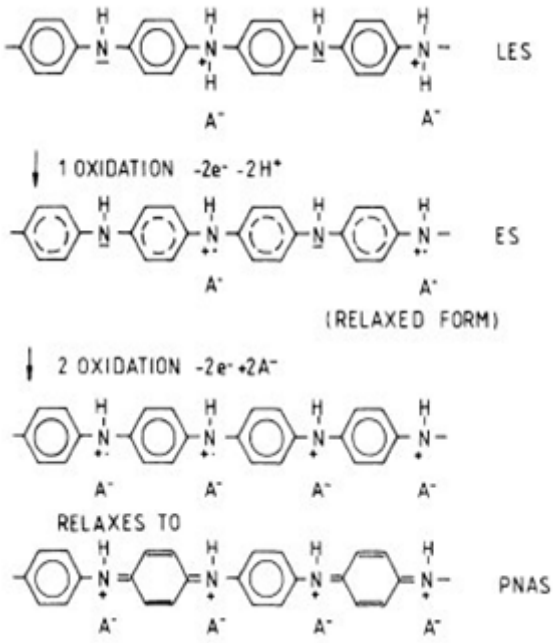

Figure 3.4: oxidation of polyaniline in an acidic solution; the electrochemical potential grows as the polymer goes from the leucoemeraldine salt (LES) configuration to the emeraldine salt (ES) and then to the perinigraniline salt (PNAS)

More into detail, starting from -0.2 V and raising the electrochemical potential, there is a first reaction in which two protons and two electrons are extracted from every repeat unit; this brings the polymer in the emeraldine salt state, which is, after relaxation, highly conductive. The reaction is accompanied by a lowering in the intensity of the 3380 cm^{-1} absorption band (which is connected with the stretching mode of the N-H bond) and by a

significant increase in the background absorption, due to the creation of polarons and the consequent increase of the number of free charge carriers.

At higher potentials there is a second oxidation process, with which in every repetition unit two electrons are subtracted and two counterions are inserted; the background absorption goes back to the leucoemeraldine levels as polarons combine in bipolarons and a new absorption band appears at 1050 cm^{-1}; polyaniline has reached the perinigraniline state, and is an insulator. The process is completely reversible, and by looking at the absorption intensities of the vibration modes of the N-counterion and N-H bonds, shown in figure 3.5, it is apparent that the two configurations are mutually exclusive.

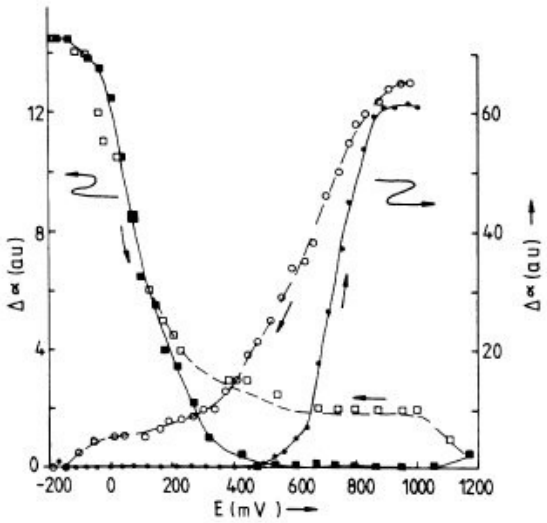

Figure 3.5: Change of absorbance for the NH-stretching mode at 3350 cm^{-1} (filled and open squares) in an organic electrolyte and for the fundamental vibration of the counter ion (filled and open circles) in an acidic electrolyte for a full cycle of the potential E.

3.2.3 Optical properties of PANI

The doping level of the polyaniline greatly influences, as we have seen, both the conductivity of the polymer and the absorption of electromagnetic waves, in a large part of the spectrum [118]; for this reason, optical investigations are very often used to monitor the doping level and/or the conductivity of PANI.

In the infrared region, for example, there are a number of absorption bands associated with the vibration of the ammine-benzene groups or the immine-quinone group. The ratio between the intensities of the peaks at 1600 cm^{-1} is very low in the leucoemeraldine, and almost one instead in the emeraldine, while the nigraniline and perinigraniline show remarkably higher absorption at 1600 cm^{-1} than at 1500 cm^{-1}. Another hint of the presence of immine-quinone groups is the weak peak at 1380 cm^{-1}, due to the stretching mode of the C-N bond in the groups Q-N-B-N-Q; this peak is present in the emeraldine state but not in the leucoemeraldine state.

In the visible and near-UV region the leucoemeraldine base shows a strong absorption band at 345 nm, due to the π-π* transition, and a weak absorption at 635 nm. The latter absorption peak is instead very pronounced in the emeraldine base, and it is associated to the presence of quinones in the polymer chain, which allow the formation of bipolarons and therefore create energy levels in the middle of the band gap

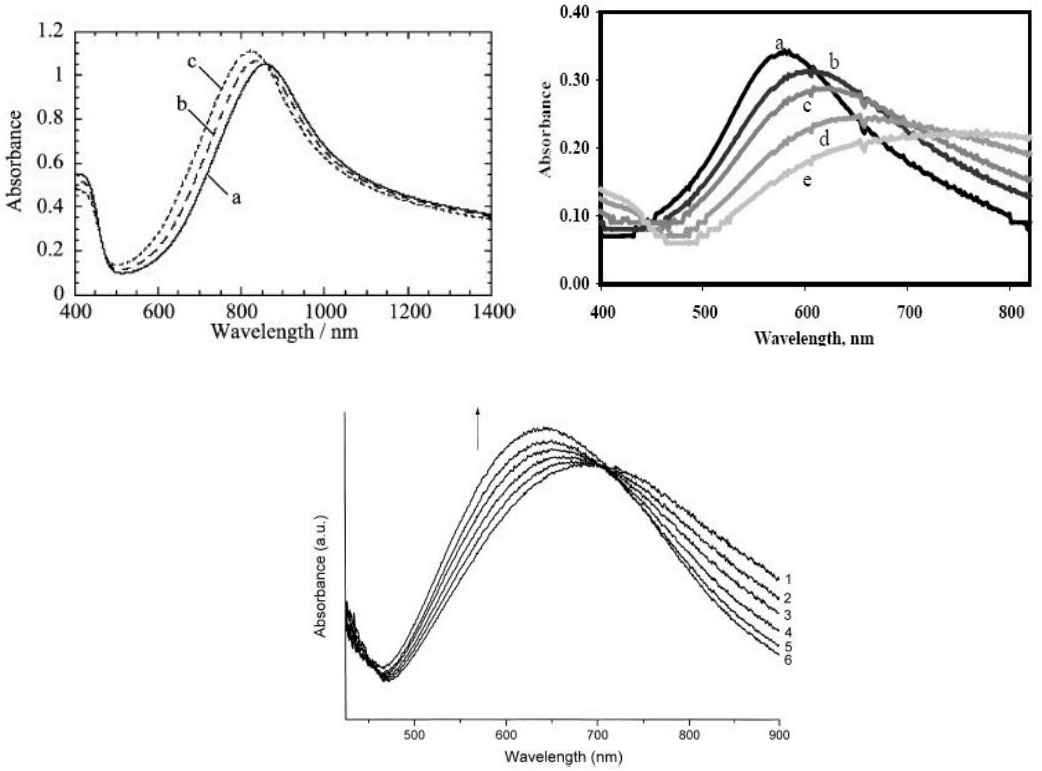

Figure 3.6 Change of absorbance of a PANI film on glass, as a function of the concentration of different gases. Top, left: in air (a), in air with 50 ppm ozone concentration (b), in air with 100 ppm ozone concentration (c)[119]. Top right: acqueous solution with sulphites from 0 (a) to 20 ppm (e) [120]. Bottom: in N_2 atmospphere with NH_3 molecules in concentrations ranging from 225 and 80000 ppm [121]

Figure 3.6 shows how the near-infrared absorption of polyaniline changes in the presence of small quantities of some gases, which oxidize or reduce the PANI; this characteristic allows to build different gas sensors in which changes in the optical properties of the polymer are monitored. Polymer-based optical sensors are cheap, easily produced, very sensitive towards some kinds of gases, and can be rendered more specific by binding to the main polymer chain functional groups like enzymes or antibodies, that are active only in the presence of a very specific molecule [122-124]. Compared to the sensors in which the electrical characteristics are measured, optical sensors offer greater immunity to electrostatic and environmental noise, faster reaction times an enhanced regenerability; among the elements that can be detected there are ozone [119], NH_3 [121,125], sulphites [120] and chlorhydric acid [126]

3.2.4 PANI Langmuir-Blodgett films

In order to take full advantage of the electrical properties of polymers in the field of molecular electronics, it is often useful to have the polymer in a phase as ordered as possible, so to maximize its conductivity. The deposition of polyaniline in a Langmuir-Blodgett film is a promising way to obtain ultra-thin films, or even monolayers [127-129]. Moreover, a polyaniline film can be processed via electron beam to obtain nanopatterns, that allow us to foresee also applications in the field of nanotechnology [130,131].

Some technical difficulties however arise [132] when trying to deposit a Langmuir-Blodgett polyaniline film, especially with conductive PANI, as the same interactions that allow inter-chain charge transfer make the polymer insoluble in most of the solvents traditionally used to prepare LB films; the deposition of an highly conducting film is a time-consuming process, especially when the film needs to cover a large area.

There are three many ways of facing these problems: trying to find a solvent in which conductive polyaniline has a high solubility, adding lateral groups to the main polymeric chain, or using a subphase that can help the film deposition. An example of the first strategy can be seen in figure 3.7, in which are shown the compression isotherms (surface pressure versus area per monomer) of polyaniline in N-methyl-pyrrolidone (NMP), a mixture of NMP and acetic acid, a mixture of camphosolphoric acid (CSA) and clorophorm, and CSA+m-cresol/clorophorm, substances that make polyaniline respectively undoped, slightly doped and fully doped with two different doping mechanisms [133]. One can appreciate from the figure how different solvents, that alter the conductibility of the film, change also the mechanical properties of the film itself.

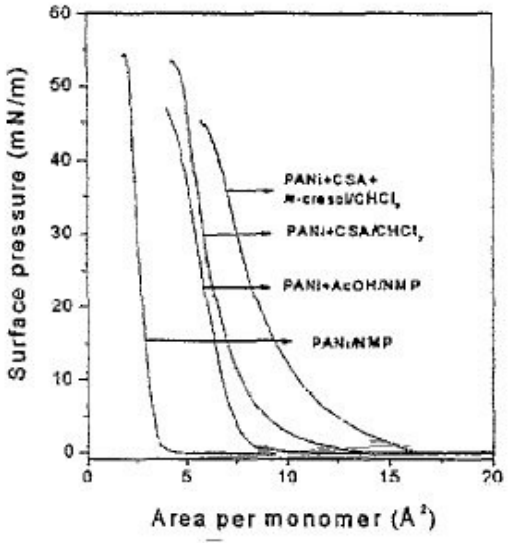

Figure 3.7: PANI isotherms using different solvents

A now well-estabilished technique is the deposition of films using the Langmuir-Schaeffler method [134], that allows a quick deposition of monolayers over a fairly large area; this technique has allowed [131] both the deposition of polyaniline monolayers and the

depositon of films that are a mixture of PANI and surfactants, where the latter could be removed afterwards to obtain a uniform film.

The best results from the point of view of the film morphology have been obtained using CP-HCA-1, a polycyanoacrilate, that however makes the film too insulating and needs to be removed with acetone. Another helpful technique is to remove the fraction of PANI that is soluble in chloroform, which increases the final conductivity of the PANI film.

3.3 POLYETHYILENE OXIDE

3.3.1 Conduction mechanism

Poly(ethylene oxide) is a polymer with formula $(-CH_2-CH_2O-)_n$ and it is one of the most studied polymeric electrolytes; it is commonly used in industrial level applications, especially as the electrolyte in lithium batteries. The first experiments that show electrical conductance in PEO, of the order of 10^4 Siemens/cm, date back to 1973 [135], but it is only from 1980 onwards that PEO begins to be considered as an electrolyte in batteries [136]. Measurements of thermoelectric potential effects have shown that, in a PEO acqueous solution where lithium salts were solved, the positive ions are the mobile charge carriers to which the PEO's conductivity is due [137].

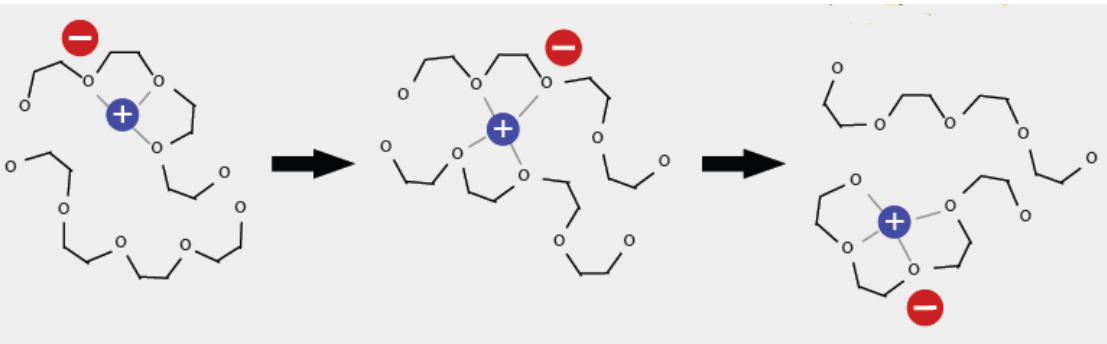

Figure 3.8: transport of positive ions from one chain to the next

Figure 3.8 shows how the positive lithium ions in such a configuration move from one polymer chain to another, under a temperature/concentration/voltage gradient: lithium ions are usually co-ordinated by four-five oxygen atoms [138], that belong to one or more polymeric chains [139].

In a polymer film in the solid phase, the movement of the lithium ions can be described with a three-dimensional hopping model with varying barrier heights [140]: the environment in which the ions move is described as porous, the ions can occupy sites with variable distances from one another, and they have to overcome energy barriers to move from one site to another (figure 3.9). In such a model a uniform distribution of negative electric charge is assumed, to provide charge neutrality; in the more detailed models the barrier heights are not of the same values, but follow a Gaussian distribution around a mean value.

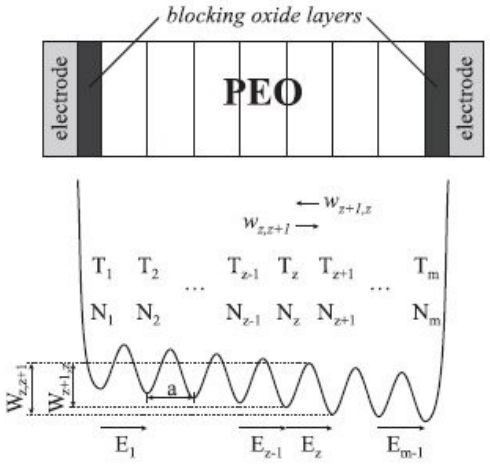

Figure 3.9: Model for the energy landscape seen by positive ions within a PEO layer. The oxide layers prevent lithium ions from touching the lateral electrodes, providing the infinite energy barriers at the sides of the diagram

This model has been used to simulated, via a dynamical Monte Carlo method, the behaviour of a PEO layer doped with $LiClO_4$, enclosed by two aluminium electrodes [141]. The simulations gave results that fitted well the experimental data [142] when looking at the dynamical properties of the system, and their dependence form parameters such as the layer thickness, the lithium ions concentration, and the voltage applied to the electrodes. It should be noted that, when the polymer is in a liquid or gel phase, the movement of the polymer chain can contribute to the ion transport, as the sites themselves that are occupied by the ions are not static anymore: they can move and lower or raise the energy barriers between themselves as they get closer or farther away.

3.3.2 PEO in the gel phase

Solvent-free solutions of salts in PEO are amongst the most studied polymeric electrolytes [143-146]. These substances have a conductivity that ranges between 10^{-8} and 10^{-4} Siemens/cm at temperatures between 40 °C and 100 °C, because of the high cristallinity of the solid PEO/salt compound and of the low solubility of the salts in amorphous PEO [147]. To achieve electrolytes that can operate at room temperature usually one tries to lower the cristallinity degree of the compound or to lower the glass transition temperature, using for examples mixtures of different polymers [148,149].

Often polymeric electrolytes are used in the gel phase, which allows for a higher conductibility even if at the expense of the mechanical properties. A gel is a phase that has the cohesion properties usually associated with the solids while having the diffusion properties of the liquids. A polymer gel is usually defined as a polymer network, in which the polymer chains are linked, containing some solvent [150]: it is important to note that it's the solvent solved in the polymer, not the other way around.

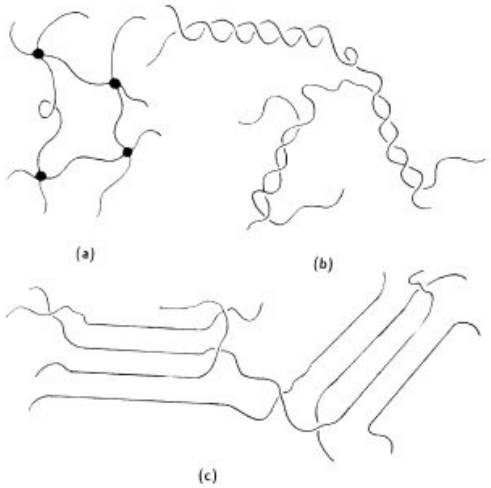

Figure 3.10: Polymer gels showing a) chemical cross-linking, b)entanglement, c) fringe micelles

A gel is obtained by a physical or chemical cross-linking process between different polymer chains; during the gelification the compound goes from a more or less viscous polymer solution to an infinitely viscous liquid; a gel in a tube doesn't flow if the tube is tilted. Figure 3.10a shows the effects of covalent cross-linking: a chemical reaction ties with covalent bonds two atoms that belong to two different polymer chains. Gels formed in this way are called irreversible and the number of junctions between polymers doesn't usually change as a function of physical parameters like temperature, mechanical stress or solvent concentration. On the other hand, the number of inter-chain bonds depends on these parameters in the physical cross-linking gels, also called "entanglement networks". There are two main ways in which polymer chains can bind, even if sometimes the ions in the solution can add further gelification mechanisms. Figure 3.10b shows chains in which the interaction is between the end zones; figure 3.10c shows a case where the interaction is between the central part of the different chains, creating configurations called "fringe micelles", in which there are some small crystalline zones weakly interacting between themselves [151].

3.2.3 Technological uses of PEO

In technological applications, the use of polymeric electrolytes shows some remarkable advantages with respect to the traditional liquid or solid electrolytes, and it has greatly impacted the development of lithium batteries for portable devices [144]. Polyelectrolytes are generally safer than liquid electrolytes, with a reduced chance of reacting with the metal electrodes; the electrolyte is actually wrapped in a thin plastic film instead of being held in a metal container, and this reduces the risk of corrosion of the metal parts and of explosion, besides attenuating the battery's vulnerability to thermal or mechanical shocks [152].

Compared to solid electrolytes, polyelectrolytes are more compact and less porous, and they can avoid the formation of metallic dendrites from the electrodes, which over time impede the efficiency of the charge/discharge cycles and can even lead to shorts in the battery itself [153]. Moreover, polyelectrolytes are better suited to deal with the changes in volume that happen at both electrodes during the charge/discharge cycles. Finally, they are more flexible and are more suitable to build batteries with a predetermined size and shape, which can be created by lamination and have a more efficient usage of their volume, as shown in figure 3.11; this is a fundamental characteristic in the field of portable electronics, where the struggle is always to minimize the bulk of the power sources [143,154].

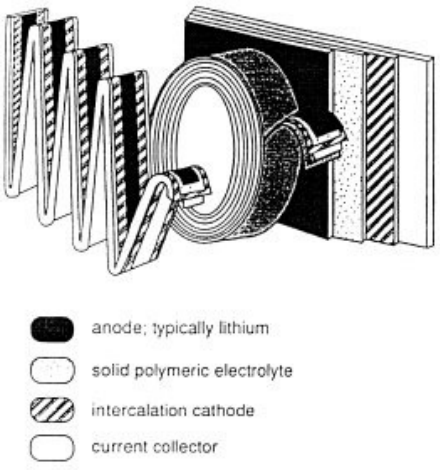

Figure 3.11: Different possible geometries for polyelectrolyte-based batteries

In the most recent technological applications PEO gels are usually treated with low molecular weight plasticizing polymers, like the PEG (polyethylenglicole)[155]; the PEGS reduces the degree of cristallinity of the polymer and increases the mobility of the molecular chains, but it has also the side effect of helping the salts to dissociate, and therefore it raises the charge mobility. The conductivity of a PEO gel at room temperature increases as its PEG content increases and its molecular weight decreases; often the PEG's hydroxyl endgroup has to be substituted to avoid the risk of reaction with the metal electrodes [156]. Another way of improving the polymer conductibility is to add ceramic nanoparticles, which are electrical insulators but they increase the free volume of the system, creating more sites for the lithium ions to occupy [157].

4. A POLYMER BASED MEMRISTOR

With this chapter we will explore the functioning of the PANI/PEO based memristive device that has been developed in the Laboratory of Molecular Nanotechnology, in Parma, in the latest years. The work cited in this section gathers all the knowledge that we had on our memristor at the time my PhD started, including some work that I personally did during and after my master thesis; the reader will notice that in the works cited the word “memristor” doesn’t appear, as it is only after May 2008 that we, as most of the world’s scientist, became aware of the existence of the term.

4.1 Device composition and functioning

The basic structure of our device has remained unchanged since the time it was first proposed [158]: it consists in a thin polyaniline film that is deposited on a glass substrate, connecting two separate metallic electrodes evaporated on the glass surface. Across the PANI film, without touching either electrode, lies a strand of PEO, doped with a lithium salt; immersed in the PEO, along the strand, there is a metallic wire that acts as a third electrode.

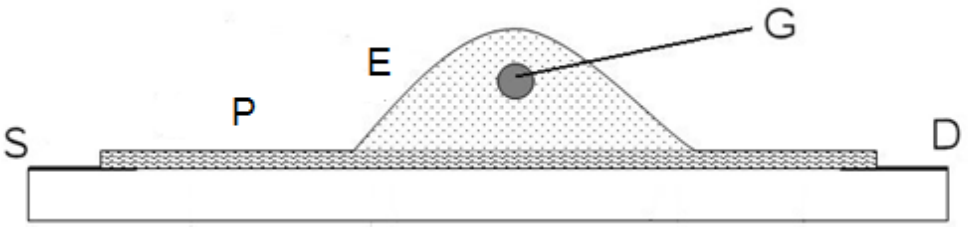

Figure 4.1 Diagram of the polymeric memristor as seen from the side. P indicates the PANI film, E the lithium-doped PEO, G the silver wire gate electrode (perpendicular to the film, seen in section), S and D the source and drain electrodes

In analogy with the nomenclature used in Field Effect Transistors (FETs), the two electrodes that are connected by the PANI film are called 'source' and 'drain' electrodes, while the wire immersed in the PEO is called the 'gate' electrode. Source and drain are usually in chrome, while the gate is a silver wire; the gate electrode material actually has some effect on the device's functioning, as we will see later. While there have been experiments with different doping agents for both the PEO and the PANI, a typical situation is to have the PANI in the conductive emeraldine salt configuration, having been doped with HCl, and to use $LiClO_4$ as the salt that is solved in the PEO. The gate electrode is usually connected to the source electrode, via an amperometer.

In the normal operation of the device, the source and the gate electrodes are kept at ground potential, and a voltage is applied at the drain electrode. In this configuration, part of the current flows from the drain to the source, through the PANI film, and some flows from the drain to the gate electrode, crossing the PEO layer; the first current is entirely electronic, while the LI^+ and ClO_4^- ions are involved in the transport in the PEO. These two currents are measured by monitoring the total current injected at the drain and by using an amperometer between the gate and the ground, in order to be able to calculate by subtraction the net amount of current that flows in the PANI film

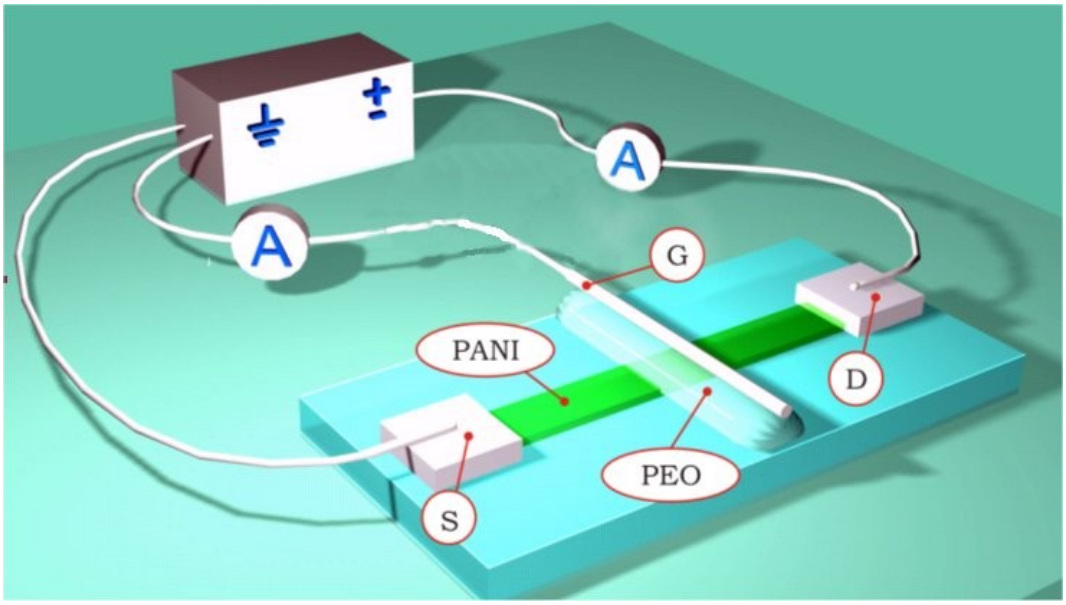

Figure 4.2 The usual experimental setup for the polymeric memristor. S, G and D indicate source, gate and drain electrodes respectively

The core of the device is the portion of the PANI film that lies under the PEO strand, called the 'active zone'. When a voltage is applied to the drain electrode, a potential difference is created between the active zone and the gate; depending on the sign and the magnitude of this potential difference, lithium ions can travel from the polyelectrolyte to the PANI film or vice versa. Lithium ions entering the PANI film actually reduce it, by subtracting the chlorine ions from the film, changing the PANI state and lowering its global conductivity, according to the redox reaction

$$PANI{:}\,Cl^- + Li^+ + e^- \leftrightarrow PANI + LiCl$$

This is the fundamental mechanism that describes the functioning of our memristor: a voltage high enough, applied to the drain potential, takes away lithium ions from the PANI, making it more conducting; a voltage below a lower threshold brings lithium ions into the PANI and lowers its conductivity; voltages in between the two values do not affect the PANI redox state. It should be noted here that it is only the electric potential gradient that drives the Li ions migration; the effect of the ion diffusion is negligible, so that the only zone in the PANI film in which the conductivity changes is the one right beneath the PEO. Also, ClO_4^- ions have a much lower mobility than Li^+ ions, and therefore are not involved in the migration to and from the polyaniline layer [137]. The exact values of the two voltage thresholds depend on the memristor components and on the fabrication process, and may change from device to device, although generally they are around + 0.4 V for the oxidation (transition from insulating to conducting) and +0.1 for reduction (transition from conducting to insulating).

Like in the TiO_2 based memristor, then, there are two different currents involved here, and the ionic one affects the conductivity of the electronic channel, by moving the border between the conducting and the insulating zones. In this case, however, the movement of the dopant agents is perpendicular to the electronic flow, and this has some repercussions

on the kinetics of the transition from an insulating to a conducting state, connected with the potential distribution within the active zone, as we shall see later in this chapter

4.2 Building a device

In order to achieve a pronounced memristive behaviour, the technique of building the device has a great importance, as some of the choices made at the building stage will have a great impact on the device's performance. Different dopants for both the PANI and PEO have an effect on the I-V curve of the device, which have been thoroughly investigated [4]; the choice of the material for the gate electrode has also proved to be crucial, as will be shown later in this chapter; the concentration of dopants in the PEO has to be high enough to have a noticeable effect on the PANI conductivity but mustn't make the electrolyte too conductive or these effects will be masked.

Finally, a critical parameter is the thickness of the PANI film, in which there is a trade-off between two desirable characteristics of the final device. As the lithium ions penetrate in the film only for a few tens of nanometers [159], having a thick film means that there will be a lower contrast between the conductivity of the memristor in its most conducting and its most insulating state. On the other hand, a thicker film will allow more current through it, which remarkably simplify the current measurements and lowers the effect of electrical noise. A film composed of around fifty PANY monolayers, with a total thickness of about 50 nm, has usually been the choice used to balance the two factors. What follows is the description of a standard building technique for the memristive device [158], which is the starting point for all the work described in this thesis.

Emeraldine base polyaniline was purchased from Sigma (M_n ca. 10 000). First the fraction soluble in chloroform is extracted from the powder. This treatment reduces the number of point-like defects in the resulting film, increasing its final conductivity. The rest of the polyaniline is dissolved in 1-methyl-2-pyrrolidone (NMP) and carefully filtered; NMP is then added to achieve the desired final concentration, that usually is 0.2 mg/ml. Glass substrates are prepared by cutting a microscope slide in rectangles of 13 by 8 mm, which are the final dimensions of the device, thoroughly cleaning them and evaporating two chrome electrodes at the two ends of each substrate.

The deposition is carried out in a KSV 5000 LB trough, using a modified [131] Langmuir–Schaefer [160] horizontal dipping technique. Pure water prepared with a Milli-Rho-Milli-Q system is used as the subphase (resistivity 18.2 MΩ cm). Monocomponent monolayers of polyaniline are compressed up to the target surface pressure of 10 mN/m, at the rate of 1 cm/min; the barriers are then stopped. The surface of the monolayer obtained is then separated into 24 independent sections by applying a plastic mask, and each section is used to deposit a monolayer of PANI by a Langumir-Schaeffer (horizontal lifting) technique on the glass substrate. The total amount of polyaniline solution spread in the subphase varies between 250 and 350 µl, depending on the mask used: the amount of PANI should be enough that when the film reaches the desired surface pressure the barriers are far enough

apart to insert the mask, which is around 10 cm in width. The substrate itself is masked too, so that at the end of the process it is not fully covered by PANI, but there is only a thin film strip (2-3 mm wide) that connects the two electrodes. The process is repeated twice, so that forty eight molecular layers are deposited.

The resulting films are doped in 1-M HCl for 2 min, and again after 40 minutes, to obtain higher and more stable values of the conductivity. The PANI film is blue when deposited but it turns rapidly to bright green when immersed in HCl, showing that the whole film at this stage of preparation is in the conductive state, and electrical measurements are performed between the electrodes with a tester, to confirm this; the film resistance at this point can vary but is in the order of the MΩ. Quality and homogeneity of the deposition are then controlled with an optical microscope; the film is considered homogeneous when visible impurities or defects are not observed.

PEO (average molecular weight 8 000 000) and LiCl were purchased from Sigma. The PEO is used in a solution of 0.1-M LiCl and 0.1-M HCl at a concentration of 30 mg/ml, yelding a polymeric doped gel. As an alternative, one can use $LiClO_4$ as a dopant, preparing a solution of PEO in 0.1M $LiClO_4$ at a concentration of 20 mg/ml. A gel strip, about 1–2mm wide, is then cast across the PANI strip, approximately in the center between the two electrodes. A thin Ag wire (approx. diameter of 50 μm) is placed over the PEO strip and then is again covered with doped PEO; a small indium patch is attached at one end of the wire to provide a stable electrical contact. At this point, due to the concentration gradient, Li+ ions flow from the PEO to the PANI layer, raising the resistance between the source and the drain electrodes by a factor of five; since placing the device again in an HCl solution would damage the water-soluble PEO layer, we usually re-dope the whole structure by exposing it to the vapours of a concentrated HCl solution, bringing the resistance between the electrodes back to approximately its starting value.

4.3 Memristive behaviour of the device

4.3.1 Memristor operation in standard conditions

As stated before, the normal operation mode for this device is to have the source electrode connected to ground, the gate electrode connected to the source through an electrometer in order to measure the amount of ionic current, and to apply a variable voltage to the drain electrode. In the most commonly used setup in our lab, this involves a Keithley 6514 multimeter to measure the current between gate and source, and a Keithley 236 source measure unit between the drain electrode and the ground. The current measured by the 236 unit is conventionally called ‘drain current’, and is the total current that is being injected in the drain electrode; the current measured by the 6514 unit is called ‘gate current’ and it is the ionic current that flows from the PANI film to the gate electrode through the PEO layer. Subtracting the gate current from the drain current yields what is called the ‘differential current’, which represents the amount of electronic current that goes through the entire PANI film, from the drain to the source

The first, basic current measurement consists in monitoring the response of the device to a constant voltage applied to the drain electrode. Figure 4.3 shows the drain current measured in time as two constant potentials, one positive and one negative, are applied to the drain electrode.

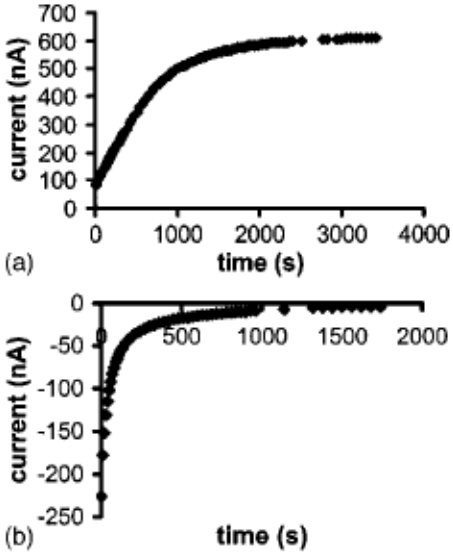

Figure 4.3: Current as a function of time when the drain potential is held at (a) 0.6 V and (b) -0.1 V

The top graph shows the temporal evolution of the drain current as a potential of +0.6V is applied to the drain electrode. It is apparent that the conductivity of the PANI film is increasing, as the current goes from less than 100 nA to more than 600 nA, without changing the drain potential. The bottom graph shows the evolution of the drain current with an applied drain potential of -0.1 V, and again the current goes from 250 nA to just a few nA. This is the first evidence that applying a positive potential to our device transfers it into a more conducting state, while applying a negative potential reverts it back to the insulating state, coherently with the hypothesis that high positive drain potentials should push lithium ions out of the PANI film and low potentials should draw them into the PANI. The two measurements reported were taken back-to-back on the same device, so the change of state induced by applying a positive potential is reversible.

A very clear difference between the two cases is the dynamics of the change of conductivity. It takes the device far more time to go from (partially) insulating to conducting than from conducting to insulating; the characteristic times of the two transitions differ by almost an order of magnitude. This difference in behaviour can be explained if we assume, like we did in the introduction of this chapter, that the two threshold voltages that trigger the change of the PANI oxidation state towards a more conductive or more insulating state are both positive.

In these conditions, when we apply a high positive voltage to a PANI film in a completely insulating state, the voltage will drop in a nearly uniform way along the length of the PANI film, since the source electrode is at ground potential anyway. This can mean that only a fraction of the PANI film under the PEO is at an electric potential high enough, with respect to the gate electrode that is also at ground, to trigger the transition to a more conducting state, while the fraction closer to the source electrode will "see" only a sub-threshold potential. As some of the PANI film turns more conductive, however, there will be a re-distribution of the electric potential, leading to more PANI going in the conducting state and further redistribution, until the configuration reaches the equilibrium; globally, therefore, the conductivity of the film will slowly increase. On the other hand, when the drain potential is negative, the whole active area is at a potential lower than the one required for the conducting-to-insulating transition, regardless of the potential distribution; this makes all the part of the PANI film that is below the PEO go from conducting to insulating, and the global transition is much faster. These considerations where later confirmed by the model that we developed for the memristor ([161], see section 4.4)

In a basic current-potential characterization, the potential at the drain is varied from 0 to 1.2 V, then from 1.2 V to -1.2 V, then back to 0, in voltage steps of 0.1 Volt; every voltage step is applied for 60 seconds. The graph in Figure 4.3 shows a typical I/V plot, obtained collecting for each potential the current value recorded at the end of the 60 second step, to account for the capacitive effect created by the presence of the electrolyte

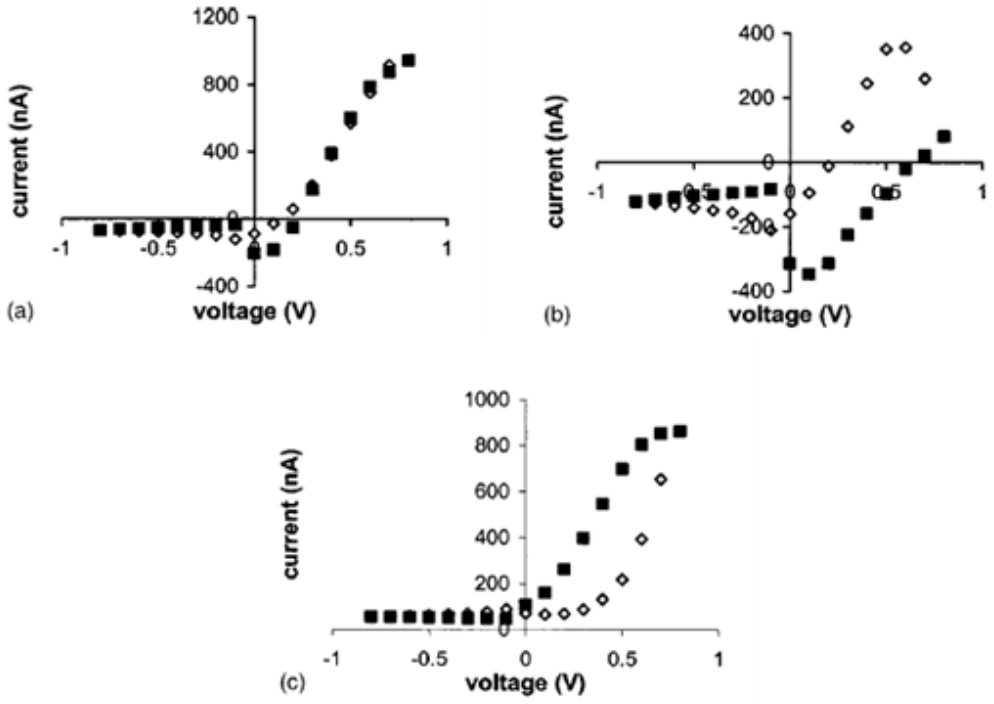

Figure 4.4: Standard I-V characteristics for a PANI/PEO memristor. a) drain current, b) gate current, c) differential current. The white rhombs represent measurements

taken when the potential is increasing, the black squares values taken when the potential is decreasing

Before every cycle, the drain potential is kept for 5 minutes at -0.5 V, to be sure that the device starts in a state that is completely or almost completely insulating. The differential current (figure 4.4c) is the one that reflects the conductivity of the PANI film: we can see from the slope of the I-V curve that the device starts the cycle as insulating, and that once the voltage reaches the 0.5V values the differential current begins to increase in a superlinear way, showing a change in the film conductivity. The conductivity increases even when the potential is descending, at least for the first couple of points taken near 1.2 V, and doesn't start to decrease until the potential reaches 0.1V; this is the reason for the hysteretic behaviour on the rightmost part of figure 4.4c. For the negative part of the voltage sweep the device stays in the insulating configuration, and the hysteresis due to the completion of the transition from conducting to insulating isn't noticeable at this scale.

The gate current plot (figure 4.4b) shows a positive current peak at 0.5 V in the region where the potential is raising, and a negative current peak at the 0.1 V part of the graph, in correspondence of the two most noticeable changes in the PANI conductivity. As the gate current is ionic and the charge carriers are the Li^+ ions [137], a positive current means that the ions are coming away from the PANI film, and a negative current that the ions are entering the PANI film. The graph bears a close resemblance to the cyclic voltammograms obtained from solid state PANI [162,163], and the peaks reveal that the redox oxidations that happen at 0.1V and 0.5V are responsible for the changes in conductivity of the PANI film.

The drain current shown in figure 4.4a is the sum of the differential and the gate current. As in the particular case shown the gate current is comparable to the differential current, the graph shows a rectifying behaviour; in more recent measurements, however, the gate current is one order of magnitude lower than the differential current, so that the drain current shows an hysteretic behaviour too, although less pronounced than the differential current.

4.3.2 Memristor operation with floating gate

While normally we would connect the gate electrode to the source electrode, thus treating the memristor as a two electrode device, it has proved useful to try and apply a voltage between the gate and the source, to further investigate the device's functioning [164]. After all, since the plan was to build a statistical network of memristors, using for example fibrillar PEO-PANI networks, it could be assumed that many memristors in the network would be in contact with a polyelectrolyte zone that was not at the same voltage as either end of the PANI active zone.

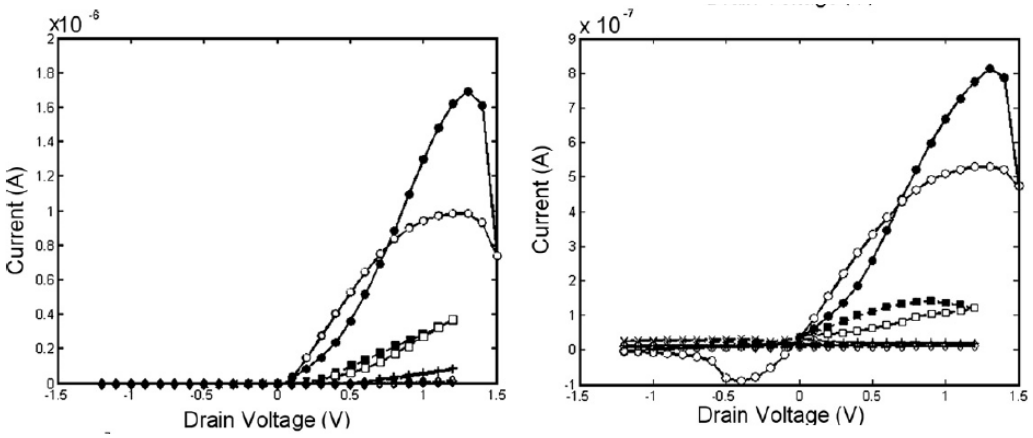

Figure 4.5: Drain (left) and differential (right) current for different gate bias voltage: V_G=0 V (circles), V_G=0.2 V (squares), V_G=0.4 V (plus signs), V_G=0.6 V (rhombs). Full or empty symbols indicate that data were collected while the drain voltage was increasing or decreasing, respectively.

Dependences of the gate and differential current upon drain voltage are shown in figure 4.5 for different gate voltages. The resistivity of the memristor significantly increases when a positive potential is applied to the gate electrode. This is due to the fact that the PANI area under the electrolyte is negatively biased with respect to the gate until high drain potentials are reached, thus keeping the PANI layer in the insulating state. In the same device, the peak value for the drain current is about 1.7 µA with the gate at ground potential, 370 nA with the gate at 0.2V, 83 nA with the gate at 0.4V, 12 nA with the gate at 0.6V. The maximum current values measured at 0.6V gate potential were reduced by about two orders of magnitude with respect to their values with the gate at ground potential. After a full cycle of measures at 0.6V gate bias, the device had lost its conductivity; the resistance between drain and source was more than 9MΩ, and we had to dope it again with HCl vapours to bring the resistance back under 2MΩ. On the other hand, negative gate potential values affect only marginally the sample resistivity; a sample with peak drain current value of 0.6µA with the gate at ground potential yielded a maximum current of 0.5µA with the gate at − 0.2V and 0.25µA with the gate at − 0.6V.

Furthermore, analyzing the gate current versus V diagrams in figure 4.6, we notice a shift in the position of the oxidation and reduction peaks. With the gate at ground potential, we are able to identify three important peaks: one when the drain potential V_D is raised at 1.4 V, a smaller one at 1.1 V when lowering V_D, and a negative peak when V_D is equal to −0.4 V. These peaks were already identified as clues of the reduction and oxidation reaction taking place in the PANI area under the electrolyte, and to a certain degree they are in agreement with those obtained on electropolymerized films in solution [165]. The first two peaks disappeared when the gate potential V_G was raised to 0.2 V and were not thoroughly investigated for fear of damaging a chrome electrode or the PANI layer itself with higher potentials. The third peak, associated with the reduction process, went to −0.2 V when V_G was at 0.2 V, +0.1 V when V_G was at 0.4 V, +0.4 V when V_G was at 0.6 V.

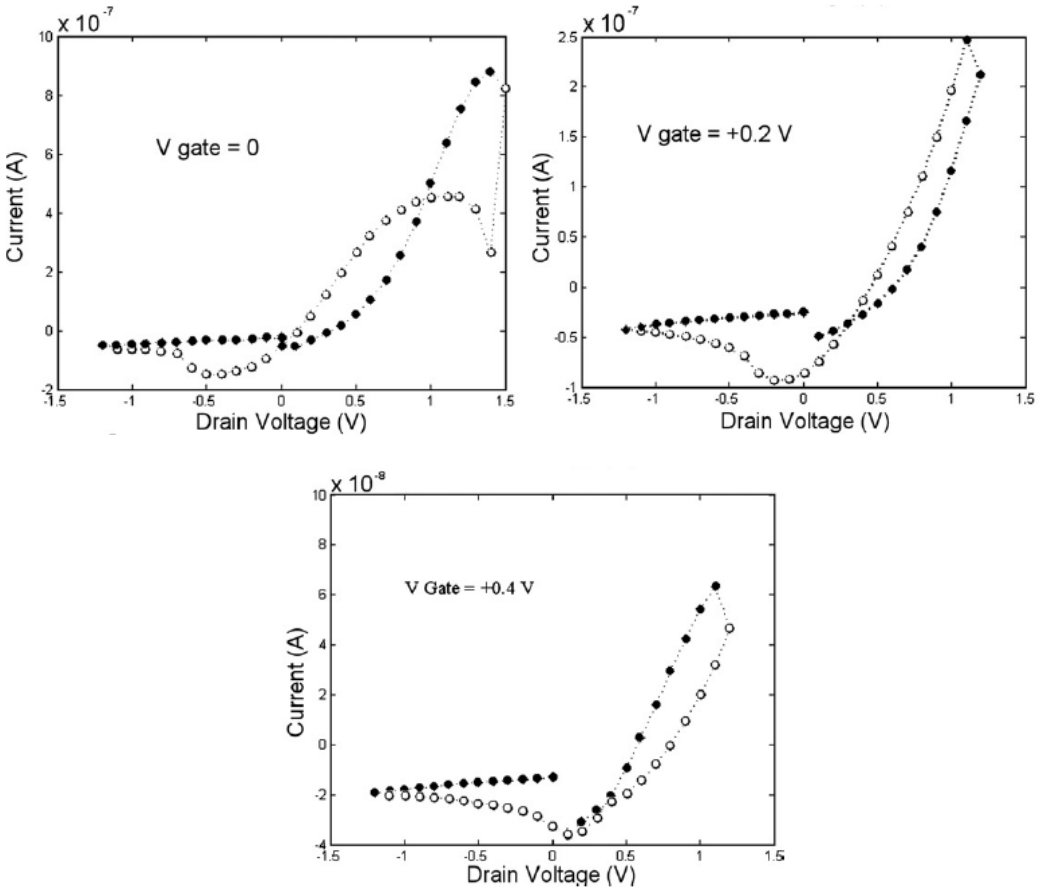

Figure 4.6 Gate currents for different gate bias voltage; full circles correspond to the data collected while the potential is increasing, empty circles to the data collected while the potential is decreasing

Such behaviour can be understood considering that the gate electrode in our element is a reference point. It means that the transformation of the active area into oxidized conducting state and into reduced insulating state takes place when the potential of the active area with respect to the gate potential reaches the value corresponding to the oxidizing or reducing potential. Thus, positive potential on the gate electrode results in the shift of the reduction potential (minimum of the I-V characteristic) in the positive direction. For negative values of V_G the reduction peak remained between −0.3 and −0.4 V. Such behaviour is not completely clear, as we expected the negative shift in the minimum position.

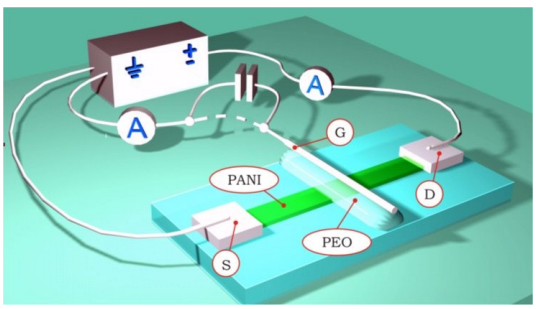

Figure 4.7: experimental setup with charge accumulation at the gate electrode

As we stated in section 4.1, the material of which the gate electrode wire is composed has an effect on the global performances of the memristors. Gold wires, for instance, have been shown to inhibit the hysteresis in the IV characteristics of the device, making it a simple nonlinear resistor with rectifying behaviour. Experiments with graphite wires have shown some oscillations to appear in the drain current: since it is well known that graphite has a capacitive effect, because it can accumulate charge between the carbon planes, the experiments were replicated using a silver gate wire and a capacitor connected between gate and source, using the setup depicted in figure 4.7.

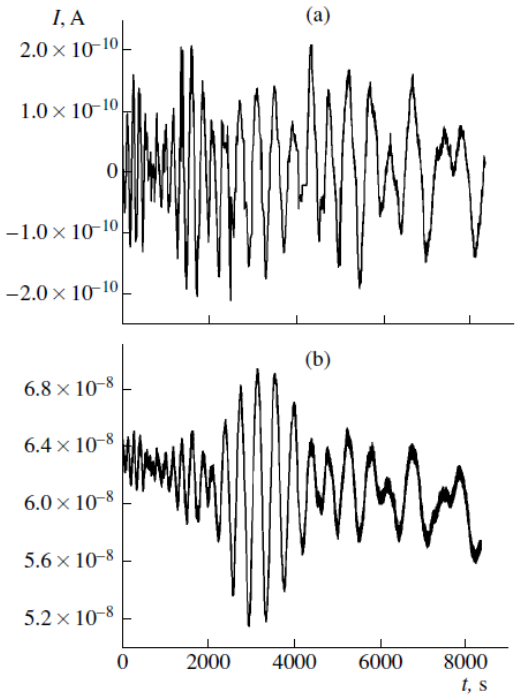

Figure 4.8: Drain current (a) and gate current (b) for a memristor with a constant drain potential of 0.1 V and a capacitor of 1 μF connected between gate and source

Figure 4.8 shows the time dependences of the drain and gate currents at a constant drain voltage for the PANI/PEO memristor when a capacitor with a capacitance of 1 μF is connected between the gate and source electrodes. It can be seen by comparison with figure 4.3 that this alters dramatically the response of the memristor to a constant voltage. Both the drain and the gate current oscillate; however, the oscillations of these currents are not synchronous, but they are shifted in phase by approximately π/2, although the period itself of the oscillations is not constant. This time is comparable to the characteristic time of the transient response of the element without a capacitor and is of the same order of magnitude as the time it takes for Li^+ ions to drift from the gate to the active region of the polyaniline [166].

In order to describe qualitatively the mechanism responsible for the appearance of the oscillations, let's assume that a positive potential is applied to the drain electrode (although a similar reasoning can be made for negative potentials) on a memristor which has a uniform

resistivity, although not necessarily the most conducting or insulating state, along the active area. The process generating the oscillations can be described in 5 steps.

1) The potential drop is uniformly distributed then over the entire length of the polyaniline film. As a result, a flux of Li^+ ions is created from the region polyaniline film near the drain electrode, where the potential is higher than the oxidation threshold, to the gate, which is at ground potential early in the process. The capacitor begins to accumulate charge and changes the gate potential, as "seen" by the active area, and globally the film conductivity increases.

2) At some instant, the potential of a part of the film beneath the electrolyte becomes lower than the increasing potential of the gate, or anyway the potential difference between this part of the active area and the gate electrode is lower than the reduction threshold for the film. This induces a return flux of Li^+ ions from the electrode to said region, lowering the charge on the capacitor, reducing the polyaniline and bringing this region towards a more insulating state.

3) As a consequence, the potential is redistributed so that more active film area is now above the oxidation threshold, and can become more conducting. This causes a new flux of Li^+ ions from the PANI to the gate, an increase in gate current and of the capacitor potential. As a result, there appears a new return flux of Li^+ ions.

5) The process will continue in a similar manner until the total resistance of the remaining reduced region becomes comparable to the resistance of the entire structure. At this instant, the flux of Li^+ ions toward the polyaniline film will be identical to that at the beginning of the process under consideration. Subsequently, the cycle should repeat.

It is to be noted that the voltage applied to the drain electrode stays constant for the whole process; in other words, in this system we apply a constant input and we obtain an oscillating response, both in the gate and drain currents. This is an analogous to what happens in chemistry in the reactions known as Belousov–Zhabotinsky reactions [167]. However, most of these reactions describe cyclic variation of the reactant's relative concentration resulting in the alternation of optical and/or viscoelastic properties of the reaction medium; to our knowledge this is the first reported case of a Belousov–Zhabotinsky behaviour for electrical components.

4.3.3 Spectroscopic investigation during the memristor functioning

To have a clearer picture of the role of the lithium and chlorine ions in the conducting mechanisms of the memristor, it is possible to follow the motion of the Li^+ ions in the PANI film during the memristor operation, via enhanced micro-Raman spectroscopy.

Raman spectroscopy data were obtained with a T64000 confocal micro-Raman spectrometer, using the lines of an argon-krypton laser for excitation. The presence of resonance effects could then be verified and studied by varying the excitation wavelength from the 456 nm argon line to the 647 nm krypton line. The confocal microscopy allows to

obtain the spectra from microscopic regions of the samples (with a minimum size of about 1μm) and to map the spectral dependence along the film conducting channel or follow the spectral behavior along the vertical direction, orthogonally to the PANI film [159].

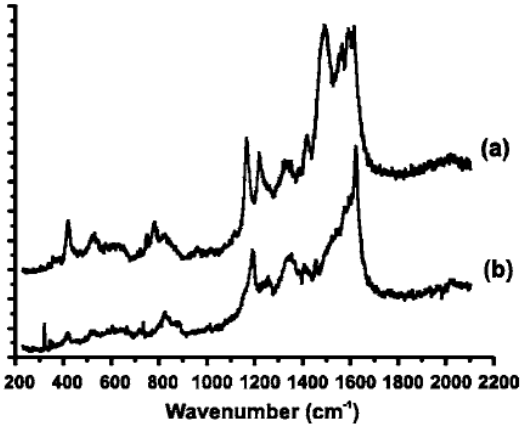

Figure 4.9: PANI Raman spectra in the nonconducting (a) and conducting (b) states; excitation at 488 nm

PANI films in their undoped (nonconducting) and doped (conducting) states, made by 48 PANI monolayers, were analyzed using a 488 nm excitation line (see figure 4.9). Although the spectra show a few changes when using different excitation lines, the most clear characteristics present in the spectra is the spectral change in the 1600 cm^{-1} region, where a strong, sharp peak appears in the conducting sample; this peak is absent in the nonconducting sample. Conversely, a strong peak at 1508 cm^{-1} in the nonconducting sample is practically absent in the conducting one; these two peaks are also related to similar peaks found in the same region using IR spectroscopy [158]. A subtler feature that however differentiates the spectra of the two states is the sharp peak at 1166 cm^{-1} which appears only in the nonconducting PANI form.

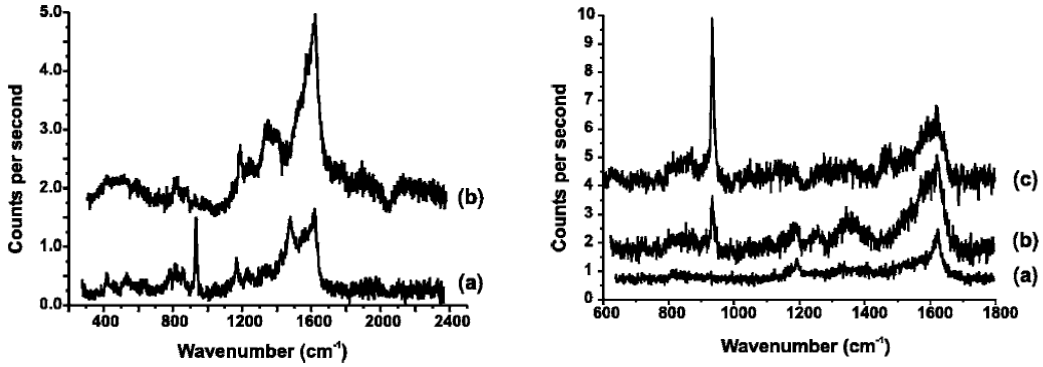

Figure 4.10. Left: PANI Raman spectra in the memristor, before the final doping with HCl, in the active zone (a) and in a region not covered by PEO (b). Right: PANI Raman spectra after doping, in a finished memristor, outside of the PEO (a), at the beginning of the active area (b), and directly under the gate electrode (c)

By analyzing the spectra taken during the building process, it is apparent that a freshly applied layer of lithium-doped PEO transfers the PANI layer from the conducting to the

insulating state (figure 4.10, left panel), and the conductive state has then to be restored with the HCl vapour doping, while the area of film not directly in contact with the polyelectrolyte remains in the conducting state. Moreover, a sharp peak at 930 cm^{-1} appears; this peak is correlated with the density of the ClO_4^- ions [168]

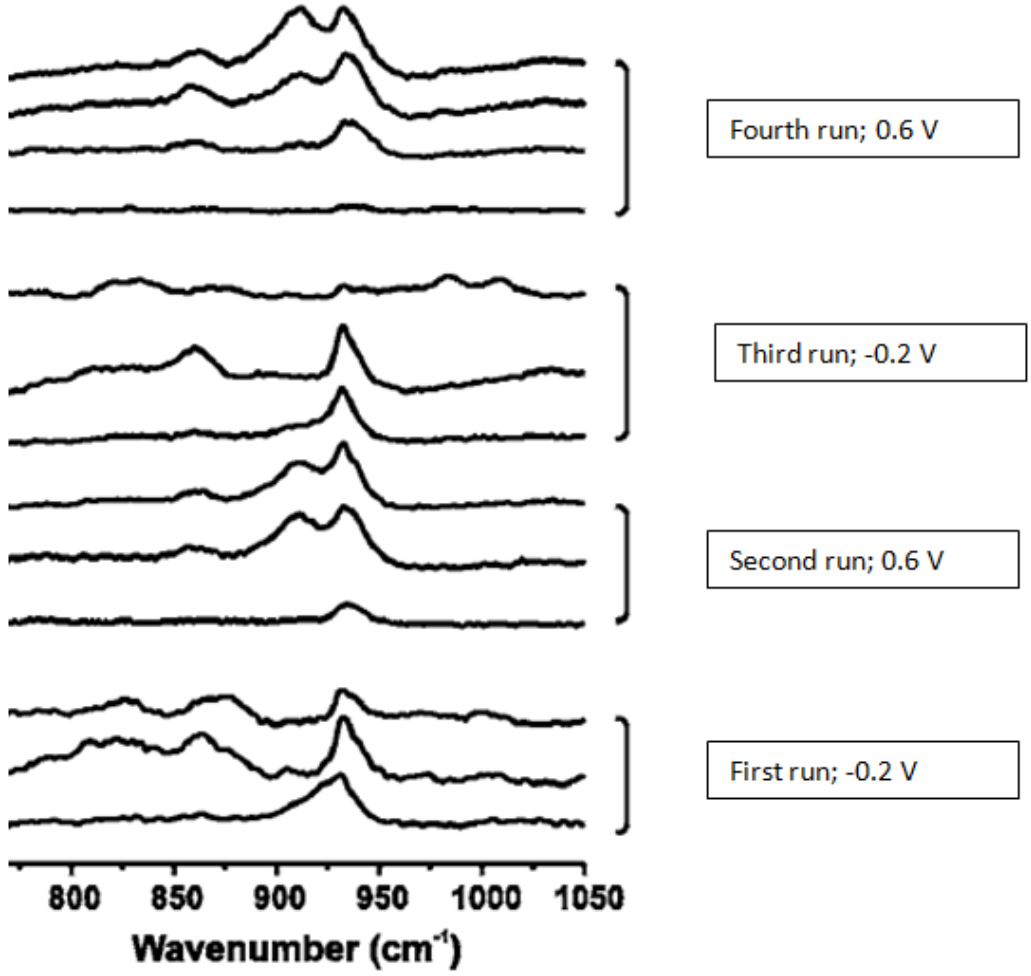

Figure 4.11: spectra taken in the active area during the operation of a single device. Lines from top to bottom are taken at minutes 0, 15, 30 (first run), 32, 35, 60 (second run), 62, 80, 120 (third run), 122, 140, 150, 180 (fourth run) from the start of the experiment

Finally, figure 4.11 shows the evolution of the same 930 cm^{-1} peak during a series of measurements where the drain potential was held negative for the first 30 minutes, then positive for 30 minutes, then negative again for one hour, then positive again for another hour. We can track the motion of the Li^+ ions by observing how the chlorine ions are taken away from the PANI by it; this is reflected following the peak evolution in the figure above, going from top to bottom, where the peak first disappears under a negative voltage, then reappears due to the positive voltage, then disappears and reappears again, following the conductivity trend, and indicating that the motion of the lithium ions is revertible and controlled by the drain voltage.

4.4 A first numeric memristor model

To achieve a better understanding of the memristor functioning, and give a quantitative explanation for the oscillation phenomena described in section 4.3, we proposed a numerical model for the memristor that could take into account the effects of the redistribution of potential over the active PANI zone and reproduce the characteristics observed in the electrical measurements [161]. Figure 4.12 gives a schematic representation of the model

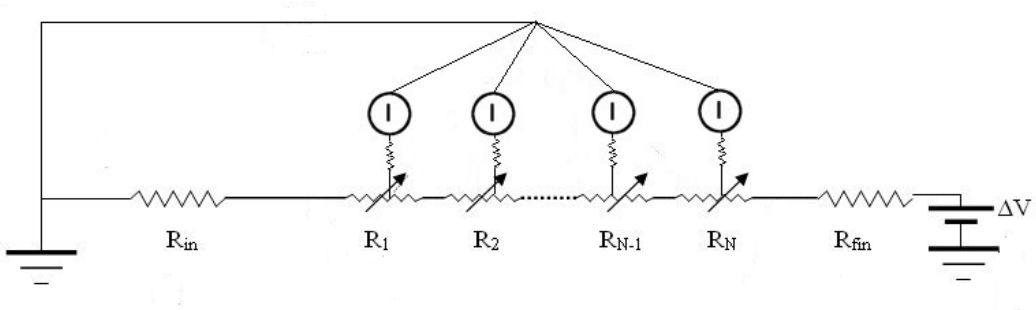

Figure 4.12: Scheme of the memristor model used. R_1,..,R_N are the resistors that simulate the PANI segments. R_{in} and R_{fin} simulate the portions of PANI not covered by polyelectrolyte; the current generators atop the gate resistances simulate the effect of Li^+ ions injection and removal due to the redox reactions in the PANI film

The model was based on several assumptions. First of all, it was suggested that all processes occur in the active zone of PANI channel under the PEO stripe, and all the variations of the PANI conductivity in the active zone are due to the redox reactions [118]; the regions of polyaniline film that are not covered by PEO are treated as simple resistors.

The PANI film in the memristor is treated as monodimensional, i.e. all points of the active zone within a line perpendicular to the PANI channel have the same electric potential; the only relevant coordinate is the distance from the drain (or source) electrode. We divided the active zone into segments and we assumed that the segments are narrow enough so that no voltage or conductivity gradients occur within each segment; all processes that take place there happen simultaneously and homogeneously. Each segment has its own resistance ("drain resistance" to distinguish from the "gate resistance" that will be considered below), the value of which can vary according to the segment potential with respect to the reference potential level; all the resistances are connected in series.

When the potential difference between the segment and the gate electrode is below the reduction potential, namely 0.1 V [165], the resistance will rise. Likewise, if the potential difference is above the oxidation potential, 0.3 V [165], the resistance will diminish. To each segment of the active zone we have associated a state variable *t* which keeps track of the history of the segment, and upon which the resistance of each segment depends, via the equation

$$R = \frac{1}{\left(\frac{1}{R_{\max}} - \left(\frac{1}{R_{max}} - \frac{1}{R_{min}}\right)e^{-\frac{t}{\tau}}\right)} \quad \text{(Eq. 4.1)}$$

which is a sigmoid that goes from R_{max} when $t = 0$ to R_{min} when t goes towards infinity (t was capped at around 1200 *s*, in order to have the flexus of the sigmoid halfway between 0 and t_{max}). The state variable t has the dimensions of time, it increases for every second that the segment is above the oxidation level and it decreases every second that the segment passes below the reduction level; in practice, it depends on how much time the segment has passed above or below either threshold, and hence indicates the oxidation state of the segment.

The time dependence of the resistance variation of the segment, given by τ, was taken from the experimental data by fitting with an exponential the drain current measured with a negative drain bias voltage ([158], see for example figure 4.3), when the material reduction simultaneously occurs for the whole active area. The assumption was that in this case all the segments were under the reduction threshold and therefore the kinetics of the total variation of the resistance mirror the kinetics of the single segment, while this doesn't happen when the drain potential is positive, as some segments may be below the oxidation potential and some above.

Each segment is also connected to the gate electrode via a "gate resistance", a resistor that connects it to the gate electrode; the resistance of each resistor depends on the segment coordinate, being minimum at the center of the active zone (the area closer to the gate electrode) and increasing when going towards the drain or source electrodes. In addition to the ohmic currents generated in the PEO by a voltage applied to the drain, the redox reactions in the film, besides changing the film conductivity, add or remove Li^+ ions to the PEO. To account for the effect of the varying number of ions, a small current is generated in the PEO whenever a segment's resistance changes.

Numerical simulations performed using the model have shown that it captures the I-V characteristics of the device, as it is shown in figure 4.13, and, more importantly, that the model reproduce the difference in the current kinetics shown in section 4.2, that depend on the polarity of the drain voltage. This is particularly meaningful as, at the level of the single segment in the model, there is no difference in kinetics between the transition from insulating to conducting and the one from conducting to insulating. The difference in kinetics at the macroscopic level, shown for example in figure 4.3, is a collective behaviour caused by the way in which the potential distribution is modulated by the changes of conductivity that gradually bring more and more of the active area above the oxidation voltage.

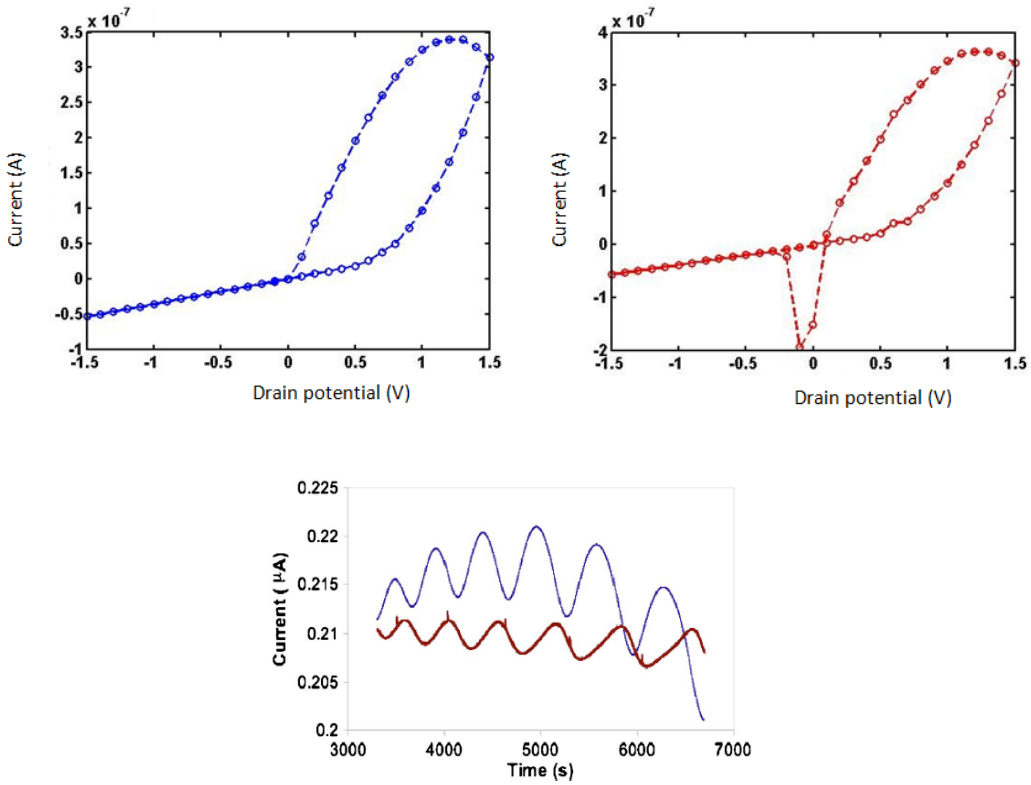

Figure 4.13: IV diagram for the drain current (top left), for the gate current (top right), and comparation of oscillations for both currents (blue=drain, red=gate, bottom) using the memristor model.

The model has even been shown to successfully reproduce the oscillating response to a constant potential when the simulation includes a capacitor between gate and source electrode, down to the phase shift between the gate and drain current oscillations, as shown by the third panel of figure 4.13.

4.5 Some simple deterministic circuits

Even before being able to identify the device described in this chapter as a "memristor", it was already clear that it was a good candidate for adaptive circuits that mimic the plasticity features of biological examples. Two circuits were proposed at this end: a two-input, two-output circuit made only by memristors, in which the memristive behaviour was used to invert a pre-estabilished input-output pairing, and a two input, one output circuit, in which the behavioural learning behaviour of the *Lymnea Stagnalis* was imitated.

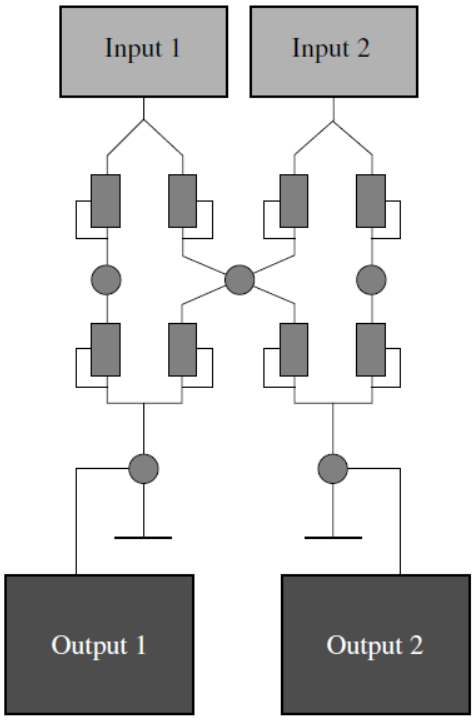

Figure 4.14: layout of the two input, two output circuit. Each rectangular element is a memristor; the lines coming out from the rectangles indicate that the gate electrodes are connected towards the circuit outputs.

The circuit shown in figure two is composed by eight memristors that connect two inputs and two outputs, although the operation of the circuit has been shown using only one output [169]. When the memristors are connected for the first time, applying an input in the form of a positive voltage to input 1 leads to a current from output 1 that is way stronger than the current from output 2. This is only to be expected, as every memristor has more or less the same initial resistance and there are two parallel paths that involve just two memristors and lead from input 1 to output 1, while there is only one such path that goes from input 1 to output 2.

However, the circuit can be trained to reverse this pairing. The training is performed by applying a negative voltage to output 2 and a positive voltage to output 1, for 5 minutes, while at the same time keeping the input 1 at ground level. Since the source terminal of each element, i.e. the one that is connected to the gate electrode and determines the polarity of the memristor, is always the one towards the circuit outputs, this means that the memristors that connect input 1 to output 2 “see” a positive voltage to the drain with respect to the gate, and start to become more conducting, while the ones that connect input 1 to output 1 “see” a negative voltage and become more insulating.

Since the layout of the voltage generators is different for the training phase and the operation phase, the effects of the training cannot be monitored in real time. However, one can apply the same input to the circuit before and after the training, and measure the output currents. For the circuit depicted in figure 4.14, applying an input potential of 0.6 V generated an output current of 120 nA if measured at the output 1 and of 32 nA if measured

at the output 2; after the training, the current measured from the input 1 was 65 nA and the current from output 2 was 124 nA. Therefore, just by applying the right combination of training potentials, the circuit internal wiring can be modified so that a signal to the input 1 of the circuit is rerouted from output 1 to output 2.

While the circuit shown is adaptive, there are no equivalents to it in the known neuronal circuits. The second circuit built, however, has a closer behaviour to a biological example: its task is to mimic the learning process at the basis of the feeding behaviour of *Lymnea stagnalis*.

This process is based on the feeding central pattern generator or CPG [170]; in it, the sensorial neurons which carry a "taste" information and detect the presence of sucrose strongly influence the CPG and send signals strong enough to initiate a feeding cycle, while neurons which carry a "touch" information don't. However the link between "touch" sensorial neurons and the CPG gets stronger when the neurons are active and a feeding pattern is started, until they become capable of starting a feeding pattern just with their own activity, i.e. after several simultaneous applications of "taste" and "touch" inputs, the feeding pattern begins to start even when only the "touch" input is applied.

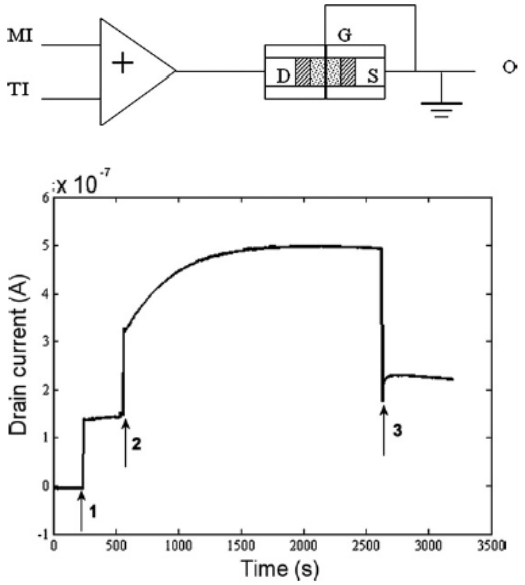

Figure 4.15: Top, scheme of the memristor-based bioinspired circuit. MI—main input, TI— teaching input, +—summator, D—drain, G—gate, S—source. Dotted area: PEO layer; shaded area: underlying PANI film. Bottom: Output current of the circuit versus time. Initially, no potential was applied. Arrows indicate application of potentials. 1. MI—high, TI—low; 2. MI—high, TI—high; 3. MI—high; TI—low.

The behaviour of the *Lymnea Stagnalis* can be thought, in a very abstract level, as the one of a system with a "main" input, a "teaching" input and one output. In a first "measurement" phase, the main input does not generate a signal in the output; in a subsequent "training" phase, the main input and the teaching input are applied simultaneously, until the system is modified in such a way that just applying a signal at the main input generates a signal in the output. For the *Lymnea Stagnalis*, the main input is the touch sensory pathway, the teaching

input the taste sensory pathway, and the output is the presence of feeding-related movements.

The circuit shown in figure 4.15 replicates this situation. In it, the two terminals labelled as 'MI' and 'TI' represent the main and the teaching inputs; the presence of one of the two inputs is simulated by applying a potential of 0.3 V to the appropriate terminal. The output signal is the current coming out of the output terminal; since the circuit response should be binary (0 or 1, presence or absence of feeding related movements), every current below a certain threshold is considered as "no signal" and every current above the same threshold is considered "presence of signal"; for the circuit proposed, the threshold was set at 0.2 μA.

An example of the operation of the circuit is shown in the bottom panel of figure 4.15. The plot represents the output value of the circuit versus the time in seconds. The measurements starts with both inputs set to low, and the memristor in the insulating state. At about 250s (arrow 1) the main input is set to high (0.3V) and the output current goes up, stabilizing to 0.14μA. This current value is rather low as the active area is not yet transferred into a conducting state. At 550s the teaching input is also set to high (arrow 2), thus starting a "training session"; the output current immediately goes to 0.32μA, and then rises steadily to 0.5μA at about 2550s coming to the saturation level corresponding to the transformation of the whole active area into the conducting state. At that time the teaching input is switched to low (arrow 3). The output current drops to 0.23μA, that is, more than 160% of the former output obtained with the same input, because the active area is now in a conducting state.

If we consider the 0.2 μA threshold for the output, we can see that the application of the main input to a system that was not trained will not generate an output signal. After the training, instead, the same main input signal results in the output current higher than the threshold value and, therefore, enough for the function execution. The training is reversible, and stable, like in the *Lymneas stagnalis*, leading the circuit presented to be one of the first realizations of a bio-inspired circuit using a memristor as the core element, in combination with traditional silicon based electronics, like the summator element.

5. STRUCTURAL STUDIES AND FURTHER MEMRISTOR APPLICATIONS

Chapter 4 of this thesis describes the state of the art of the work on our memristive device, at the moment of the beginning of my PhD work. It appeared clear that while the preliminary work showed that the PANI/PEO memristor was a promising device, further investigations on the polymeric memristors were needed, to tailor its properties to the needs that might arise in a biomimetic circuit. On the other hand, the circuit described at the end of chapter 4 only replicates the learning in *Lymnea Stagnalis* in a very abstract manner, and all the circuits created up to that point worked just in DC mode, i.e. by applying constant potentials to the device. Neuronal circuits, on the other hand, work in pulse mode, encoding the information in the frequency of potential spikes rather than in the level of a current or a voltage. In order to get closer to the biological examples, different experiments were carried on to show that it is possible to train the memristor using voltage pulses. Moreover, we built a circuit that is much closer to a part of the neuronal pathway in *Lymneas stagnalis* that is responsible for the pairing of touch stimulus and feeding movement. This chapter describes the experimental studies on the device that have been performed during my PhD.

5.1 Training memristors with pulses

While the circuit shown in section 4.5 of this thesis can mimic the conditional learning in *Lymnea Stagnalis*, it wasn't clear if the changes in memristance upon which the circuit relied could be triggered by voltage pulses instead of the application of DC potential level. To clarify the matter, a series of measurements was conducted in which the memristor was subjected to voltage "training" pulses, investigating the effect of the pulse duration and of the pulse interval [1]

The experimental setup is the same as the one used for the I-V characterizations, with the Keithley 6514 electrometer connecting gate and drain, measuring the gate current, and the Keithley 236 applying a voltage to the drain electrode and measuring the drain current.

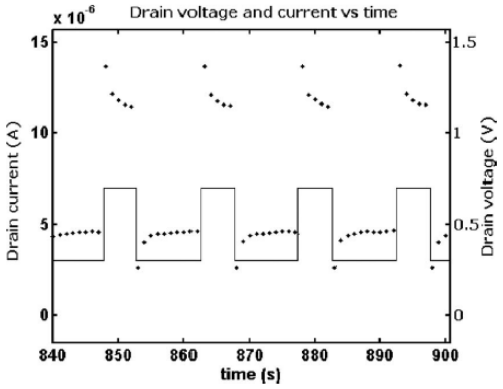

Figure 5.1: Drain current (dots) as a response to voltage pulses (continuous line)

Figure 5.1 shows the typical response of the memristor to an application of square voltage pulses. Two features present in the figure are particularly relevant: the baseline voltage and the time evolution of the current response.

As it can be noticed by the voltage axis on the right side of Figure 5.1, the square voltage pulses are not applied to a ground level baseline, but to a positive voltage baseline (0.3 V in the case shown). This is necessary because, for the majority of the devices, having the drain electrode at ground level means to be under the reduction voltage threshold, and therefore beginning a transition from conducting to insulating. This means that the effect of any positive voltage pulse that we can apply can be counteracted by having the drain at ground potential between pulses. For this reason, we chose to apply the pulses over a baseline voltage situated between the oxidation and the reduction threshold, which should give us a "neutral" starting point. It should be noted that, as there is a slight dispersion of device properties, the actual value of the two thresholds can vary from one device to another, because it depends on the potential distribution along the active zone. Before using a freshly made device in pulse mode we measured, as described in Chapter 4, its I-V characteristics, in order to find out the ideal voltage to be used as the baseline level, namely, one between the PANI reduction and oxidation potential peaks found in the gate current characteristics.

The other important feature to notice in figure 5.1 is that the drain current is not constant, but it shows an exponential relaxing after each change of drain potential. This is an effect of the RC characteristics of the device, due to the presence of the polymeric electrolyte. This behaviour is the reason why, in the V/I characterization process described in chapter 4, each voltage step was applied for 60 seconds and the value plotted on the I-V graphs was the last one for each voltage step, as we supposed that it was the one that was closer to the equilibrium value. As this effect cannot be avoided when training with pulses, we chose, in order to compare the effect of different pulse trains, to always look at the last current value of each voltage step, in order to cut off as much of the charge/discharge effects as possible.

5.1.1 Pulse effects

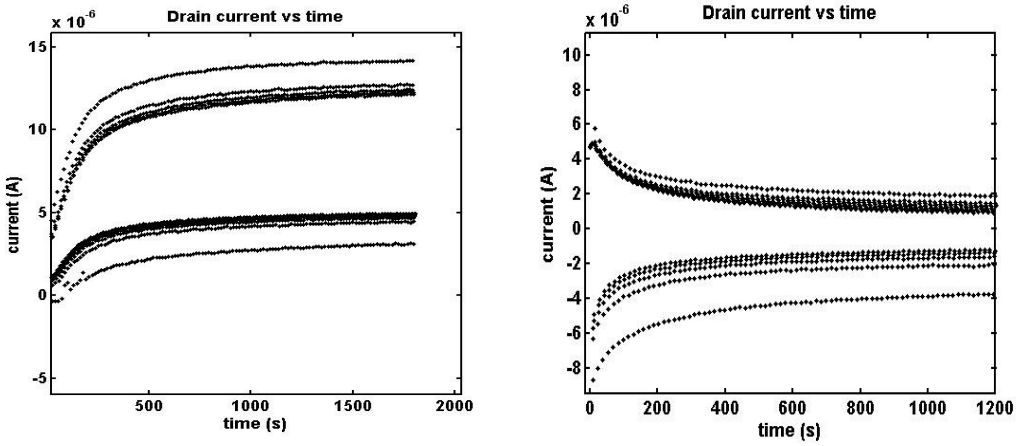

Figure 5.2: effects of positive (left) and negative (right) voltage pulses on a single device

The left panel of Figure 5.2 shows the total current that flows through our device when we apply a sequence of square voltage pulses, spaced 10 s from one another, each with an amplitude of 0.4 V and a duration of 5 s, over a baseline of 0.3 V. The capacitive effect is the reason why the plots in Figure 5.2 seem to show several lines of data: those lines are formed by the single current measurements in different points of the voltage pulses or of the inter-pulse intervals. In these cases, the lines relative to the last point of each pulse or inter-pulse interval are the bottom one of the top set and the top line of the bottom set. After 30 min from the beginning of the experiment, i.e., after 120 voltage pulses, the conductivity of our memristor was significantly increased; at the beginning of the experiment, the current associated with the 0.3 V baseline voltage was 965 nA, while at the end, it was 4.89 μA. Similarly, the current associated with the 0.7 V pulses increased from 3.04 to 12.15 μA.

We then inverted the polarity of the pulses and applied to the same baseline pulses with an amplitude of −0.6 V, thus reaching a −0.3 V potential difference between source and drain during the pulses, obtaining the current plot shown in the right panel of figure 5.2. In 20 min the response current to the baseline voltage varies from 4.93 μA to 970 μA, while the response to the peak voltage goes from −4.9 to −1.22 μA. It should be noted that as the voltage difference in this case is 0.6 V, we can expect the RC contribution to be more significant with respect to the case of positive pulses, as it shows in the left panel of figure 5.2. This last experiment shows that we have actually reversed the modifications of our device conductivity caused by the previously applied positive voltage pulses.

5.1.2 Pulse duration and pulse intervals

In order to determine the optimal conditions of the functioning of networks composed from these devices, it is important to estimate the effect of the pulse duration and interval between pulses on the characteristics of the memristor. Traditionally, in the numerical simulations of neuronal circuits, the pulse duration is not considered important [171], to the

point that the spiking of one neuron is often treated as an instantaneous event; all the information is conveyed by the spiking frequency, i.e. by the interval between spikes. With our memristor, however, these variables can be equally significant in principle, and this is the reason to investigate their role.

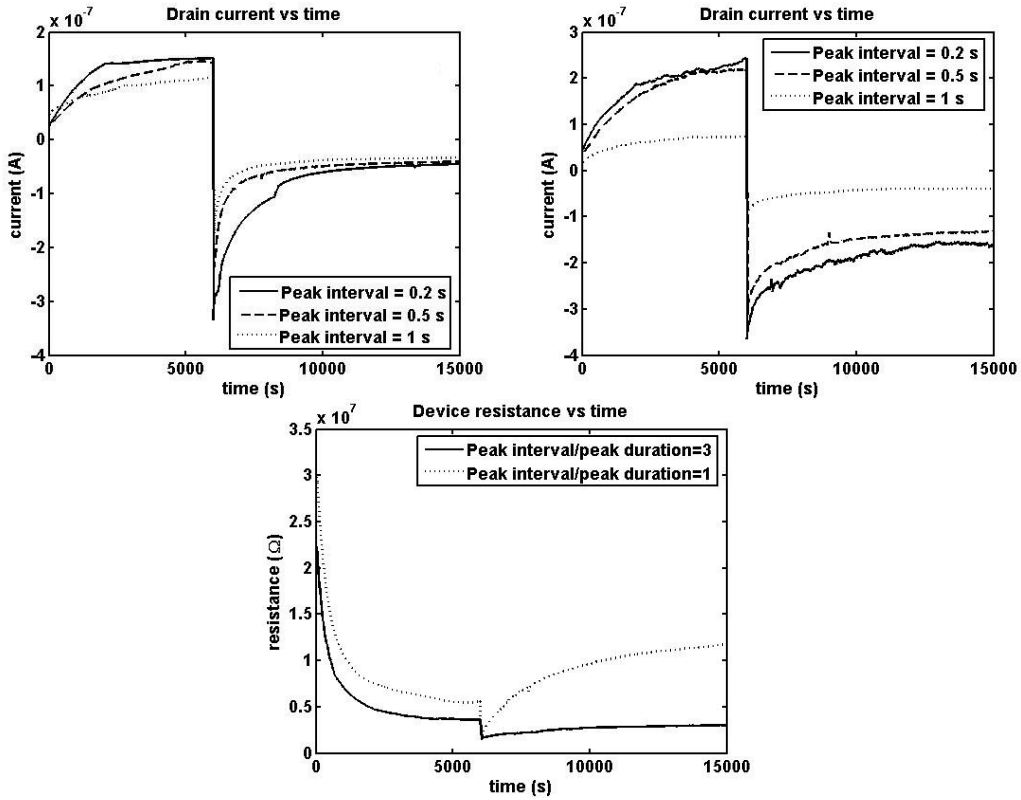

Figure 5.3 Top left: drain current when applying to a memristor three different series of voltage pulses, with the inter-pulse duration equal to the pulse duration. Top right: drain current when applying to the memristor potential pulses with the same duration, but with an inter-pulse duration that is three times the pulse duration. Bottom: comparison between the drain currents obtained with the same pulse duration (0.5 s) and different inter-pulse duration

Figure 5.3 presents the results of the experiments carried out for clarifying the relevance of the pulse duration and of the interval between two subsequent pulses; the experiments were carried out on the same device. In all the six experiments, we sent positive voltage pulses for 10 min and negative potential pulses for the following 15 min. Before each experiment, we kept the device at a negative bias for 5 min, in order to start each experiment with the device in the completely insulating state. The figures represent only the lines relative to the measurement executed at the end of the voltage pulses.

The top left panel shows the currents measured in experiments where the pulse duration was equal to the interval between successive pulses. We used pulses with durations of 0.2, 0.5, and 1 s, and the relative currents are shown in the graph with a solid line, a dashed line, and a dotted line, respectively. One can see from the figure that different pulse durations result in small differences in the device behaviour, which remains similar to the one with longer pulses shown in Figure 5.2.

The top right panel of figure 5.3 represents the currents measured in experiments where the interval between subsequent pulses was three times the pulse duration. Again, the solid line refers to the experiment with 0.2 s pulse duration, the dashed to the one with pulse duration of 0.5 s, and the dotted to the one with pulses lasting 1 s. We can see that not only the amount of current of the device depends on the pulse duration, but also that negative pulses are very ineffective, with these pulse intervals, in bringing up the device resistance. Finally, the bottom panel of figure 5.3 shows the temporal dependence of the device resistance for two experiments with the same pulse duration and different pulse intervals: shorter intervals are clearly more efficient in quickly raising the device resistance.

The data reported clearly indicates that the so-called pulse mode can trigger a change of conductivity in our device with the same efficiency as in the DC mode we have used prior to these experiments. The comparison between data reported in Figure 5.2 and 5.3 reveals that the pulse duration is not a parameter that can inhibit significantly the variations in the conductivity. This is particularly relevant when one considers that typically, the duration of the neuronal spikes is of the order of a few milliseconds [171], one order of magnitude less than the shortest pulse duration that we have tested. Testing the response of the device to pulses this short would have required extensive modifications to the experimental setup; luckily, the data shown here allows to be confident that we will very likely observe similar phenomena when we will work with potential pulses of duration comparable with that of the neuronal signals, if the correct ratio between pulse duration and interval between pulses is provided.

The fact that the frequency of the pulses has instead a great influence on the change of conductivity of the memristor is another feature that makes the device a good candidate for biomimetic circuits, as it shows that, while the pulse duration can be set at pleasure, the frequency has an important effect on the ability of the memristor to switch back to an insulating state. The data shown indicate that what matters is the ratio between the pulse duration and the inter-pulse interval, and therefore the absolute value of the frequency of a pulse train that “works” or “doesn’t work” depends on the choice of the pulse duration; assuming a pulse duration of 10 ms, this would mean that a pulse frequency of 50 Hz can change effectively the conductivity of a memristors, while lower frequencies cannot. It should be noted that for many neuronal circuits (see for example Chapters 7 and 8 of this thesis) in which there are two possible states, one “active” and one “silent”, the “active states” has an average firing frequency of around 40 Hz, while the “silent” states have frequencies of 10 Hz or less.

5.1.3 The Lymnea stagnalis circuit in pulse mode

As a stepping stone towards increasingly biomimetic circuits, we executed some experiments to replicate the *Lymnea* inspired conditional training that was already replicated with the circuit described at the end of section 4.6, adding a “blocking” training phase that reverts the positive reinforcement training operated by the association of the

"touch" and "taste" stimuli, by stimulating the taste sensory pathways with a negative stimulus [172].

This time, we represented the different stimuli in terms of potential pulses sent to the memristor: a touch stimulus was modelled with a positive potential pulse of a certain amplitude V_1, a "positive" taste stimulus with a positive pulse of higher amplitude V_2, and a "negative" taste stimulus with a negative potential pulse V_3, with respect to the ground level V_0. The response of the snail, i.e., the level of feeding activity, was represented by the output current of our device. A circuit which successfully models the learning processes found in the *Lymnea* should increase or decrease the response to the touch stimulus only as a consequence of the different training sessions executed.

In the following experiments, for both positive and negative learning of the system, we alternated between a training session and a test session. A training session consisted of five subsequent pulses of amplitude V_0+V_2 for reinforcement learning or V_0-V_3 for inhibitory learning, while a test session was made of five impulses of amplitude V_0+V_1. The interval between pulses was equal to the pulse duration; between two different sessions we usually waited for 15 s. The actual values of V_0, V_1, V_2, and V_3 were slightly varied from device to device, according to the V/ I characteristics of each single device we built. Typically, these values were $V_0 = 0.3$ V, $V_1 = 0.1$ V, $V_2 = 0.3$ V, and $V_3 = 0.6$ V.

It should be noted that, even if we did not build an actual circuit with different inputs as it happened with the DC case, it is perfectly feasible to do so; it just requires the utilization and synchronization of multiple source units. This is the reason why we chose simply to apply to the device the sum of the different inputs simulated, keeping the experimental setup unchanged.

The top left panel of figure 5.4 shows the output current when our device underwent a cycle of 15 pairs of training and testing sessions. The upper part of the graph contains the response to the training pulses, the middle part contains the response to the test pulses, and the lower part contains the responses to the base voltage. The output current generated by the application of the touch stimulus starts at 151 nA and stabilizes at about 270 nA after about ten training sessions. Subsequent iteration of the training/test sessions does not yield further increase in the output level.

In the top right panel of Figure 5.4 we show the output current when the memristor was subjected to 30 subsequent test sessions and then to 15 pairs of training/test sessions. In the left part of the graph there are two groups of data, which correspond to the currents generated by the test pulses and the base level. In the right part, we can see a third group of data, which contains the response to the training pulses. We can see that the output corresponding to the test input is 43 nA at the beginning of the experiment and 47 nA after the first 30 test sessions; it steadily increases then to reach 96 nA at the end of the experiment.

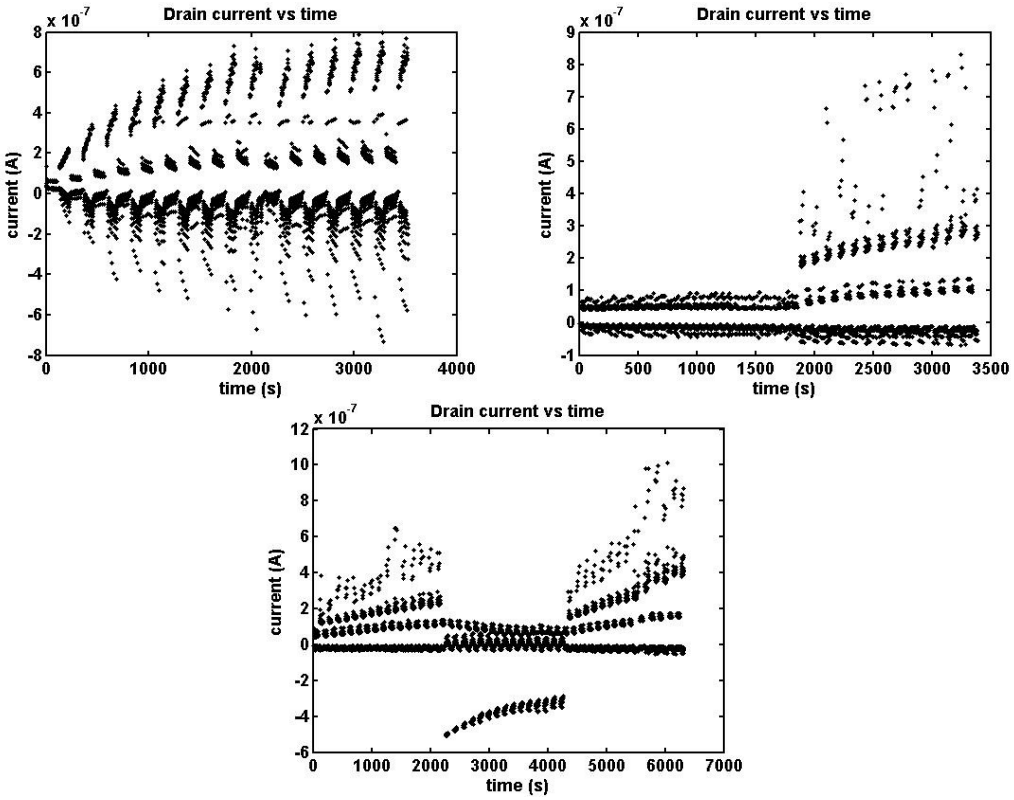

Figure 5.4: Behaviour of the memristor under different pulse sequencies, simulating training in the *Lymnea Stagnalis*. Top left: plot of the output current vs time graph during an intercalation of "taste+touch" sessions and "only touch" sessions. Top right: output current vs time for a two part experiment, with "only touch" sessions in the first part and "touch+taste" session intercalated with "only touch" sessions in the second part. Bottom: output current versus time for a three part experiment with positive training, followed by negative training, followed by a second session of positive training.

Finally, the bottom panel of figure 5.4 represents the results of the experiment in which the response to the test input is increased from 45 to 107 nA through our usual training protocol; we then proceeded with 15 pairs of inhibition session and test session, after which the output of the device was reduced to 59 nA, and then re-enforced the positive training with another set of 15 training/test session pairs, bringing the response to the test output up to 150 nA.

These experiments show that the pulse mode is even more effective than the DC mode in conditionally training a single memristor. For the DC case, the increment in current after training was of about 50% of the initial value, while in the pulse case, the output increases by a factor of 2 or more, which is comparable to the increase in signal transmission found in trained Lymnea specimen [172]. We have shown that it is only the concomitance of "touch" and "taste" input that changes the device's conductivity, as an experiment in which only the "touch" inputs are applied yields minimal changes in the memristor conductivity; moreover, we have shown that this kind of training is completely reversible and repeatable, by applying different sequences of reinforcing and inhibiting training sessions.

5.2 Different PANI and PEO dopants

The studies on the pulse mode operation of the memristor highlighted two issues with the device that required a deeper investigation; while some powerful applications of the memristor could be imagined even without solving them, it was deemed useful to try and modify the memristor architecture in order to solve at least partially these issues. Moreover, any improvement to the device's maximum conductivity or to the contrast between the conducting and the insulating states of the device is always useful, as those features would make easier the use of the memristor in adaptive circuits.

One of these problems was the memristor lifetime and the repeatability of the characterization measurements. Although a slight dispersion of the electrical properties is to be expected when building by hand each single device, even an individual device was prone to a fairly quick degradation of the electrical properties, to the point that two subsequent V-I characterizations of the same memristor seldom overlapped.

The other issue was that having both the reduction and the oxidation threshold at positive drain voltages meant that, in a complex memristor network, even when applying high positive voltages to a terminal in order to raise the conductivity of some memristor, some link could be actually below the reduction threshold. This would mean that we always run the risk of raising the resistances in some part of the network during a training phase intended to lower the resistance of the network. The problem could be solved only by finding a way to shift the reduction peak to negative drain voltages.

We decided to try and correct these issues by acting on the dopants that we used in the PANI and PEO. For the PANI film, we investigated the effect that pre-doping the PANI layer with dodecyl benzene sulfonic acid (DBSA), a strong acid with high molecular weight [2] ; for the PEO layer, our studies investgated $LiClO_4$, $LiBF_4$ and $LiCF_3SO_3$ as possible dopants for the polyelectrolyte, as well as a mixture of $LiClO_4$ and DBSA [4].

5.2.1 PANI predoped with DBSA

One possible way to improve the device characteristics is to use a heavy acid that doesn't evaporate, like the HCl is prone to do, during the device functioning. With the help of the Pisa unit of the BION project, the Electro-optical Responsive Polymeric Nanomaterials Group, we chose to build a memristor where the polyaniline was pre-doped with DBSA.

In order to do this, the polyaniline has to be synthesized directly from the aniline monomer in a DBSA-rich environment [173,174]. Briefly, in a two-necked flask equipped with a mechanical stirrer and a dropping funnel, 14.40 g of DBSA dissolved in 800 ml of water and 4g of aniline were gently added. The mixture was stirred for 3 hours at room temperature until the formation of the typical milklike solution of the anilinium salt; the solution was then cooled to 0 °C by dipping the flask in a water-ice bath. Successively, five drops of a saturated solution of cobalt sulfate were added to the anilinium salt solution and then 10 g of ammonium persulfate dissolved in 35 ml of water were slowly dropped to the solution.

After 5 hours the stirring was stopped and the solution containing a blue-dark precipitate was stored for a night at room temperature. The precipitate was collected by adding 1 l of methanol to the suspension and by filtering it with a Buchner filter. Finally the solid powder was repeatedly washed with methanol and water until neutrality. The PANI was then dried several days under vacuum pump.

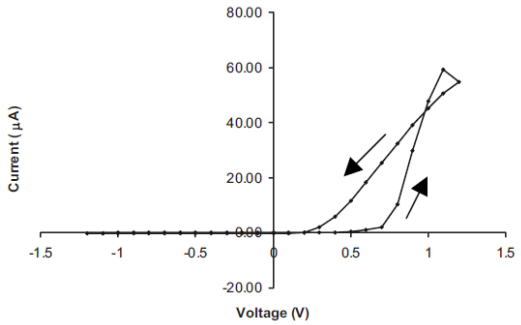

Figure 5.5 V-I characteristics of the memristor with DBSA-doped PANI.

The I-V diagram shown in figure 5.5 refers to a memristor with the usual architecture but with a DBSA-doped PANI film. The device has maintained the memristive behaviour: there is hysteresis only in the positive drain region, which shows a marked rectifying behaviour, and the transitions to a more conducting or more insulating state are very noticeable and quick, beginning at 0.5V and 0.1V respectively. The maximum current flowing in the memristor, however, is very noticeably larger than the one obtained from a memristor with an HCl-only doped PANI channel: it reaches more than 60 μA at a voltage of 1.0 V, which is much higher than our previous results (1.0–2.0 μA); furthermore, the conductivity ratio of the device in the conducting and insulating states, i.e. the contrast between the conducting and insulating states, which is probably even more important for the realization of the adaptive networks, jumped from about 100 for the previously reported results [158] to about 2000 in the present device. This improvement of more than one order of magnitude is a very encouraging result.

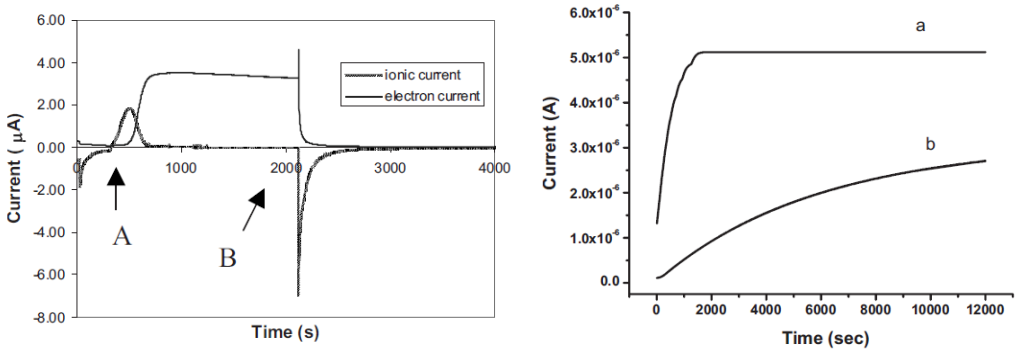

Figure 5.6: currents at constant potentials for the DBDS device (left): A and B mark respectively the moments where a constant 0.6 V and a constant -0.2 V potentials. On the right, simulations the drain current resulting from the application of a 0.6 V potential, using the model described in section 4.4, with (a) maximum conductance and ionic conductivity increased, and (b) standard parameters

The faster transition to a conductive state was confirmed by measurements of current at a fixed drain potential, shown in the left panel of figure 5.6. The figure also shows that this time, the transition from insulating to conducting, triggered by the application of a constant positive voltage at time A, is almost as fast as the transition from conducting to insulating triggered at B by applying a negative potential. The difference in the kinetics of the two transitions was attributed to the redistribution of voltage that affects the transition to the conductive state (see section 4.3); this redistribution is however affected this time by the fact that the maximum conductivity of the device is much higher than before, with respect to the minimum conductivity. We tried to reproduce this situation in the numerical model introduced in section 4.4, and found that a similar difference in kinetics could be reproduced by increasing at the same time two parameters that can reasonably be affected by a change in the PANI dopants. These are the parameter that describes the maximum conductivity of the memristor (increased by two orders of magnitude, as the experiments suggest) and the parameter that regulates the ionic conductivity of the PEO, i.e. the amount of current generated by a change in the resistance of each region of the device, which was increased by one order of magnitude; the results of these simulations are shown in the right panel of figure 5.6.

However, multicycle investigation of the device properties has revealed that the stability of the electrical properties was similar to those for the element with a standard channel, even if the PANI film was doped with DBSA: the memristor properties slowly degraded, with the maximum current dropping at every cycle and the hysteresis becoming narrower and narrower until the device remained stuck in an insulating state. As we suspected that the main cause for the degradation was the evaporation of HCl, further measurements were performed a sealed plastic chamber, (about 1.5 l volume) with dried atmosphere and residual HCl vapour (about $10^{-4}M$, corresponding to a partial pressure of about 200 Pa). The temporal behaviour of the drain current during the application of cyclic scans of the drain voltage is shown in figure 5.7

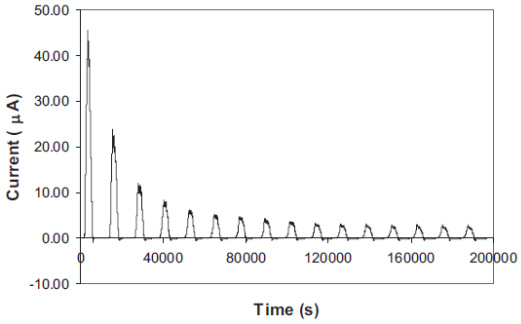

Figure 5.7: I vs T diagram during multiple scans of the drain potential, for a memristor in a sealed chamber

As the figure shows, the absolute value of the device conductivity decreases exponentially for the first 5 cycles and then becomes practically constant after the tenth cycle, remaining still very high with respect to even freshly prepared samples measured in the ambient conditions. The initial decrease in the conductivity is a normal phenomenon for the conducting polymers, which can be due to several factors, such as some contact processes

on the boundary with metal electrodes or redistribution of the dopant upon reaching equilibrium conditions. Thus, the conditions with residual acid vapour can improve the performance of the device, and slow its degradation.

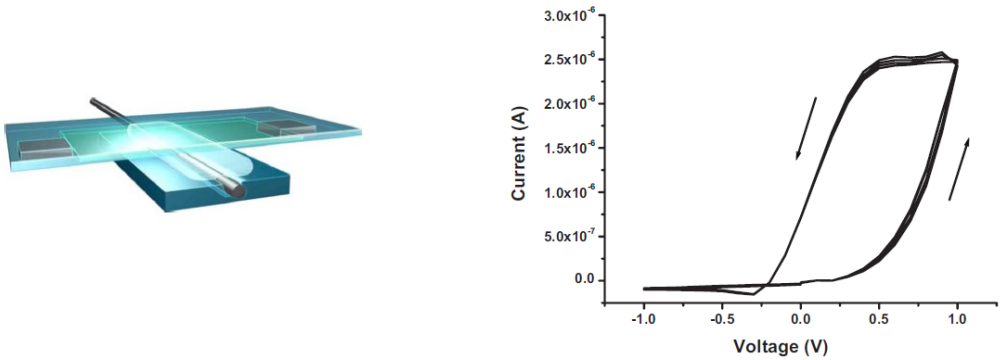

Figure 5.8: left, alternative "sandwich" architecture for the structure. The PANI film and the chrome electrodes are deposited on the top glass, while PEO and the gate electrode sit in a groove in the bottom glass. Right, multiple VI characterization cycles for a "sandwich" structure

However, a device that requires a sealed chamber or a controlled atmosphere to work properly can be unwieldy. To eliminate the need for a sealed container, a alternative "sandwich" architecture for the device, shown in the left panel of figure 5.8, was tried. A PANI channel was formed on a glass support with two electrodes, as per the usual building technique. A groove with a depth corresponding to the silver wire diameter was formed in the other solid support (glass). The reference wire was placed into this groove and covered by PEO. After drying for 30 min these two supports with formed structures were put in contact mechanically to form the device shown in figure 5.8.
The device was then subjected to several cycles of drain potential, with the same range and duration as the "standard" ones described in section 4.3; we observed the same drop in the maximum conductivity that we can observe in figure 5.7, however from the fifth cycle onwards the I-V curve of the memristor was stabilised and perfectly reproducible, as shown in the right panel of figure 5.8, which reports the I-V curves obtained in cycles 5 through 8.

5.2.2 PEO dopants

As stated before, we wanted to investigate the effects on the memristor properties of different types of PEO dopants, in order to solve the problems that arise by having both oxidation and reduction voltages in the positive drain voltage region; to this end we investigated the effects of $LiClO_4$, $LiBF_4$, $LiCF_3SO_3$, and $LiClO_4$ with and addition of DBSA.

We prepared gels of PEO by dissolving it in water until we reached a concentration of 20 mg/ml, and then added one of the three lithium salts, using the same molarity (0.1 M) for each. While we experimented with different molecular weights of the PEO, we found that low-weight PEO, with a weight of 12000 Da. or 35000 Da., doesn't form gels stable enough: in those cases the polyelectrolyte layer is too runny and tends to cover the whole memristor

surface, shorting the drain and the source terminals. For the rest of the experiments we then used high weight (8000000 Da.) PEO.

The first difference between the three PEO dopants was noticed while building the structure. Usually [158,175] we observed a drop in the PANI conductance after we applied the PEO strand on top of the PANI film; this happens with $LiClO_4$ and has happened with $LiCF_3SO_3$, and has be attributed to a spontaneous diffusion of lithium ions ion the PANI film [158], but doesn't happen when using $LIBF_4$ doped PEO.

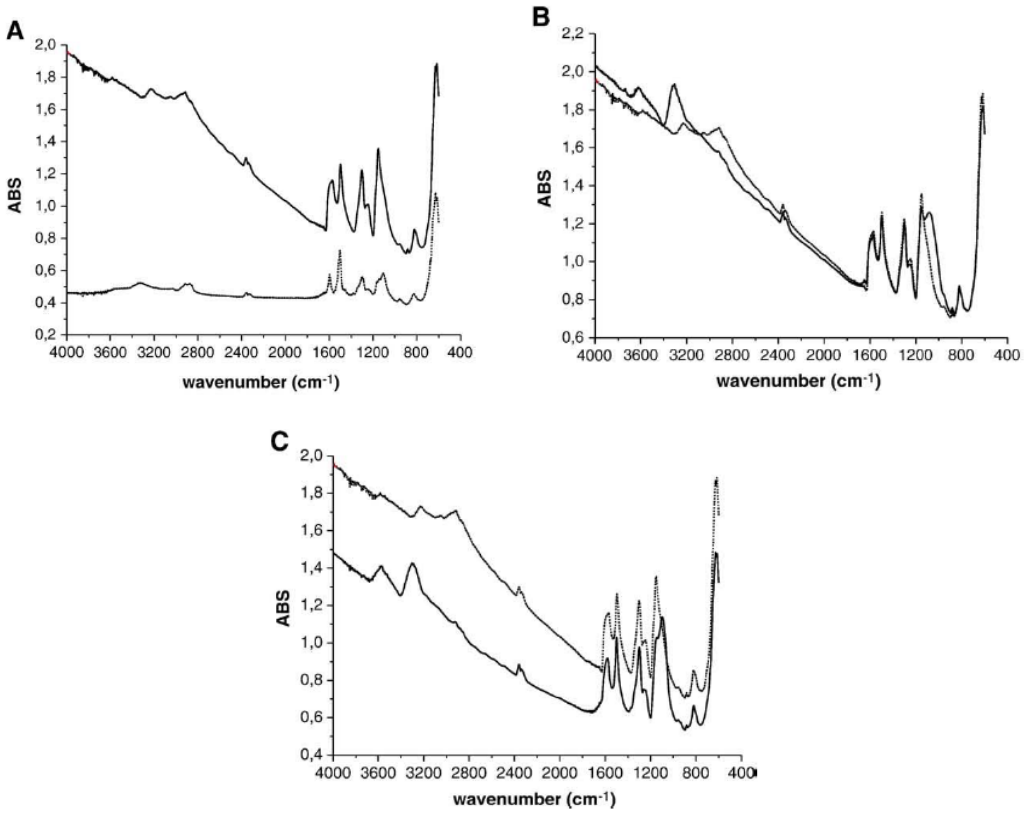

Figure 5.9 : FTIR spectra of PANI films: (A) PANI film in insulating (dashed line) and conducting (solid line) states; (B) conducting PANI film before (dashed line) and after (solid line) treatment with $LiBF_4$; (C) conducting PANI film before (dashed line) and after (solid line) treatment with $LiClO_4$.

To confirm this effect, we measured the FTIR spectra of insulating and conducting (HCl-doped) PANI; we then treated some conducting PANI films with $LiBF_4$ and $LiClO_4$ salts, recording the FTIR spectra before and after the treatment with salts; the resulting spectra are shown in Figure 5.9.

There are three main features in these spectra that can be used to judge the degree of conductivity in PANI. The first is the intensity of the Drude-like continuum, in the 2000-4000 cm^{-1} regions, which is directly related to the amount of free charge carriers in the materials; the second is the relative heights of the two peaks at 1500-1600 cm^{-1}, related to the ratio of quinoid and benzoid rings in the PANI [118]; finally there is the peak at 1150 cm^{-1}, which is

present mainly in the conducting form of PANI, while in the insulating form it is just a shoulder to a nearby peak at 1100 cm^{-1}. From figure 5.9 it is evident that applying $LiBF_4$ to the film doesn't affect much the Drude tail, leaves the region between 1500 and 1600 cm^{-1} basically unchanged and only affects the spectrum by generating a new peak at 1100 cm^{-1}, slightly lowering the one at 1150 cm^{-1}. Doping the PANI film with $LiClO_4$, on the other hand, noticeably reduces the amount of Drude absorption and lowers the peak at 1150 cm^{-1} to the point that it becomes lower than the peak at 1100 cm^{-1}, which was absent before the doping.

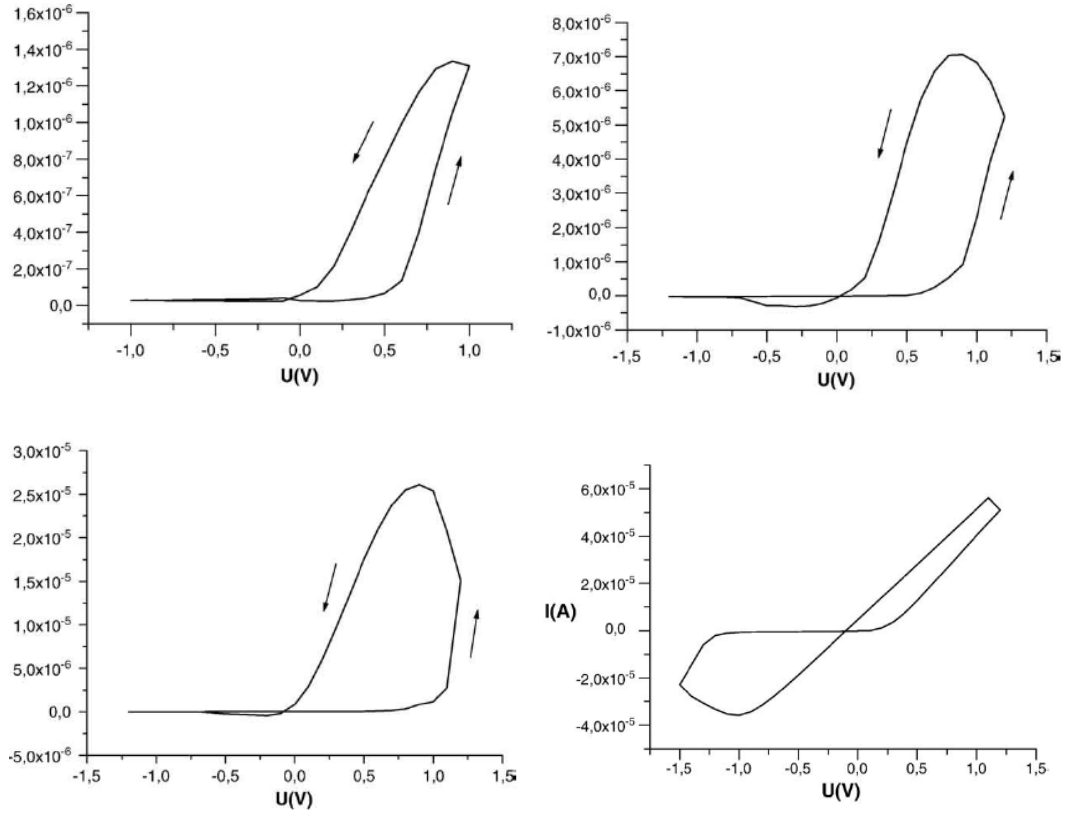

Figure 5.10: I-V characterizations for $LiClO_4$-doped (top left), $LiBF_4$-doped PEO (top right), $LiCF_3SO_3$-doped PEO (bottom left) and $LiClO_4$ and DBSA-doped PEO (bottom right).

The I-V characteristics of the memristors doped with the three salts, as well as the one for a $LiClO_4$ memristor in which DBSA was added to the PEO, are shown in figure 5.10. These curves show how the choice of the dopants for both the PANI film and the PEO layer has a great impact on the final characteristics of the memristor. The top left graph shows the "usual" behaviour of the device: both the reduction and the oxidation thresholds are at positive drain potentials, as indicated by the absence of hysteresis in the negative potential region of the graph; the drain current has a typical rectifying behaviour; the transition from conductive to insulating is quite fast, as the peak in the drain current is almost at the maximum drain potential.

In systems doped with $LiBF_4$ and $LiCF_3SO_3$ the memristor is not in its most conductive state when the drain voltage reaches the maximum value, but reaches it some minutes into the

descending part of the voltage sweep. This is the reason why the top right and bottom left panels of figure 5.10 have very wide hysteresis loops and peaks in the drain current plots at potentials lower than the maximum drain voltage. The reason for this could be a slower overall transition for the device, as it seems the case for the $LiBF_4$ memristor, or a much higher oxidation threshold, like for the $LiClF_3SO_3$ device, where the drain current rises quickly but only after having reached a drain potential of 1 V. The plot relative to $LiBF_4$ seems to indicate that the reduction peak is in the negative drain voltage region of the sweep, although if the system is slower in its transition this could be an artefact; the reduction could begin to take place at low positive voltages but, by the time it is complete or even noticeable, the drain potential can have changed and become negative.

Finally, this is certainly not the case for the $LiClO_4$ device where DBSA (0.1 M) was added to the PEO layer; the V-I characteristics of this memristor are shown in the bottom right panel of figure 5.10. DBSA was chosen because it was believed that having an acidic polyelectrolyte gel would contrast the deprotonation of PANI when the film was contacted with the PEO, thus eliminating the need for a second doping phase during the building process and possibly shifting the reduction peak in the negative drain potential region. Hydrochloric acid however cannot be used to regulate the pH of the PEO, as it destabilizes the PEO gel; moreover, as shown in section 5.2.1, HCl evaporates from the PEO and the PANI film. We had already seen that adding DBSA to the PANI actually enhances the performance of the memristor; DBSA also doesn't affect the gel stability, unlike HCl that melts the PEO layer, so it was a good candidate as a proton donor in the PEO layer

Figure 5.10 shows that, in presence of DBSA, the memristor has a fairly quick transition to a conductive state, and this is reflected in the narrow hysteresis of the V-I curve; the reduction potential is definitely in the negative region of the drain voltages, at around -1V; this is perhaps even too much, as reduction potentials closer to 0 V would be more convenient. Nevertheless, DBSA seems the right choice to modify the behaviour of the memristor so that a second doping in the building process is not needed, and no redox reaction happens when the drain terminal is at the same voltage of the source and the gate terminals.

5.3 Structural analysis of the memristor components

Although PANI is quite a well studied polymer [118,176-178], there are few structural studies focused on the mechanics of doping and dedoping. We had the opportunity to investigate the details of the doping mechanism using beamtime at the ID10B line of the ESRF synchrotron facility, in Grenoble; although these studies didn't directly lead to hints on the performance of the memristor like the ones reported in section 5.2, they have proved to be helpful to our understanding of the memristor's workings. We used a variety of different techniques - synchrotron X-ray reflectivity (XRR), grazing incidence diffraction (GID), and space-resolved grazing incidence X-ray-induced fluorescence (GIXF), both on Langmuir monolayers of PANI at the liquid-air interface and on fully assembled memristors [3].

5.3.1 Reflectivity measurements

The reflectivity studies were used to investigate the structure of the PANI monolayers, in the doped and undoped states. Samples of the 48-layer deposited film, as in the finished device, were also investigated, but no useful reflectivity curve was obtained, probably due to the high roughness of the resulting film, that has been confirmed by SEM imaging [4]" and has been estimated at about 10 nm using AFM techniques. Monolayers of PANI at the liquid air interface gave however interesting results, both when the subphase was pure water (undoped polymer) and when it was acid (0.1 M HCl, resulting in a doped film).

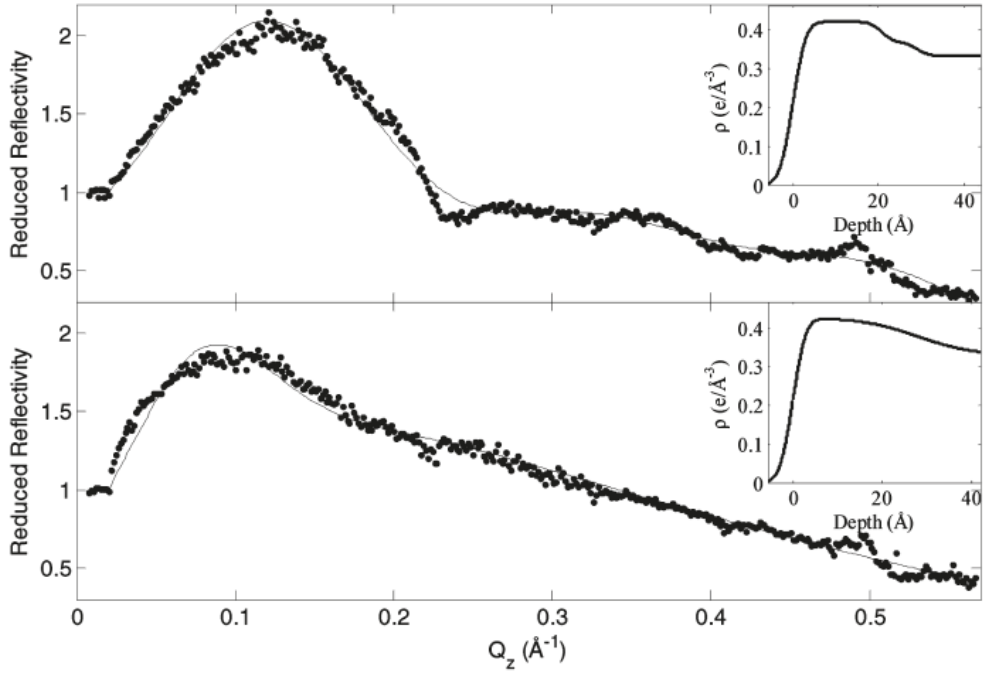

Figure 5.11: Reflectivity curves for the undoped PANI film (top) and the doped (bottom); the line represents the best fit. In the insets, the electron density profiles obtained from the fit of the reflectivity curves.

Reflectivity data, reported in figure 5.11, were analyzed with our own software, developed in the Matlab computing environment, which calculates the reflectivity curve for a given model according to the so-called "Parratt recursive approach" [179,180]. The software uses a structured model of independent layers, each with uniform electron density, to reproduce the reflectivity curve of a real multilayer, accounting for the roughness of each layer using the Nevot-Croce approximation [181].

For the undoped PANI the film structure, shown in the inset of the top part of figure 5.11, was best modelled by two slabs: one close to the air surface, accounting for the main part of the film, for a thickness of 20 A˚, with higher electron density ($\rho = 0.41$ e$^-$/Å^3), and one close to the water surface, with lower electron density ($\rho = 0.37$ e$^-$/Å^3) and thickness 8 Å. The

roughness of each interface (σ =3-3.5 Å) is comparable with that of pure water surface due to capillary waves. This fit suggests that the PANI monolayer on water is quite loose, and that some water can penetrate the lower part of the polymer film, so that the bottom slab represents PANI chain ends immersed in water, while the top slab is pure PANI: this would explain the two different electronic densities measured.

Data for the doped PANI, instead, shows that it forms a more homogenous film: the data is best fitted by a single slab with thickness of 28 Å, with slightly higher electron density ($\rho = 0.43$ e$^-$/Å^3) and a larger value of the roughness of film/water interface (σ = 5-8 Å). When integrating the electron density along the film thickness, we have 11.10 e$^-$/Å^2 for the insulating film and 12.04 e$^-$/Å^2 for the conducting one. This increase can be related to the partial inclusion of the Cl^- ions within the film; its small size could be due to the increase of roughness that could smear and make less apparent the variation of electron density.

Finally, it should be noted that the doping process doesn't affect the overall thickness of the film, which is 28 Å, in agreement with previous ellipsometry measurements [182].

5.3.2 Grazing Incidence Diffraction measurements

Further data on the film structure come from the Grazing Incidence Diffraction (GID) analysis; GID is a technique that collects the radiation scattered from a sample in three dimensions, and can provide detailed information on the ordered structures that form within a material.

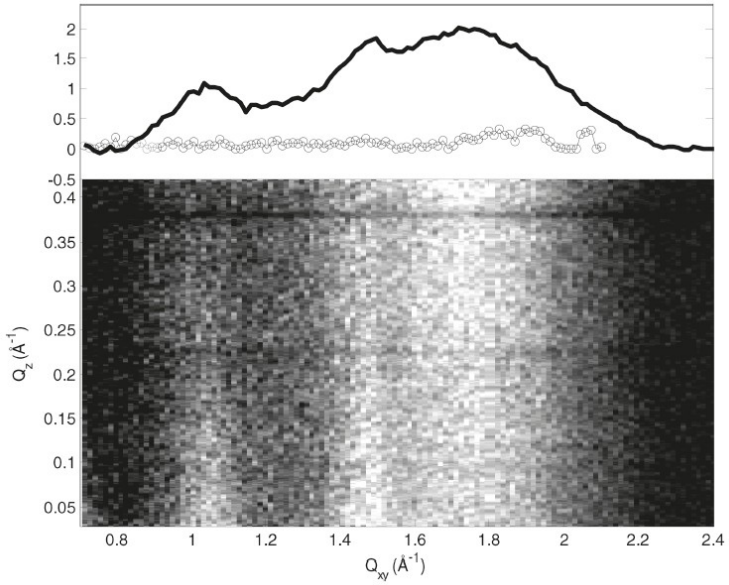

Figure 5.12: GID intensities for the insulating (circles) and conducting (line) PANI films, at 10 mN/m surface pressure (top); GID pattern for the conducting PANI film at 10 mN/m (bottom)

In our case, we tested both the doped and the undoped PANI film, at various surface pressures; at the pressure that we usually use to deposit our films (10 mN/m), there were distinctive rodlike patterns when examining the doped film (bottom panel of figure 5.12), at the in-plane position Q_{xy}=1.0 and 1.8 $Å^{-1}$, while these patterns didn't appear in the film on the water subphase. The rod patterns are a sign of a 2D order in the film at the molecular level; Debye rings, which are the signature of 3D ordered structures in the film, didn't appear until the film collapsed, at a surface pressure of 26 mN/m.

Integrating the GID intensity over Q_z yields the plot shown in the top panel of figure 5.13: in the doped film the presence of two diffraction peaks at 1.0 and 1.8 $Å^{-1}$ with a prominent shoulder at 1.45$Å^{-1}$ can be observed, while they are not present in the insulating phase on pure water; these peaks have already been reported for metallic PANI [183]. In particular, most of the intensity is concentrated in the highest Q peak which corresponds to a spacing of 3.5 Å, which matches the face-to-face interchain stacking distance between phenyl rings. This suggests a strongly planar chain conformation with reduced torsion angles between the phenyl ring and the plane of the backbone, resulting in elongation of the effective conjugation length. However, from the relatively large width of the peak we can also evaluate the lateral coherence length being only of the order of a few (3-4) repeat units.

5.3.3 Grazing Incidence X-Ray Fluorescence measurements

The movement of the single ions in and out of the PANI film can be followed more closely by using Grazing Incidence X-ray Fluorescence, or GIXF. GIXF is a direct, element specific, surface sensitive, and nondestructive technique in which the fluorescence from the ions (chemical sensitivity) is recorded as a function of the grazing angle of incidence (depth sensitivity) to test for the presence of ions in the structure of the molecular layer and therefore directly measure the ionic depth distribution. The film of PANI was prepared on three different subphases, i.e. pure water, HCl 0.1M and KCl 0.1M, to distinguish between the effects of the mere presence of Cl^- ions in the subphase and the effect of the different pH of the subphase. We were able to monitor directly the fluorescence intensities of K and Cl ions; moreover, we used the fluorescence intensity of Ar atoms, present naturally in the atmosphere, to normalize our data and account for different geometric effects, such as the variation of the beam footprint when changing the incidence angle. The curves for the films with HCl and KCl subphases are reported in figure 5.13

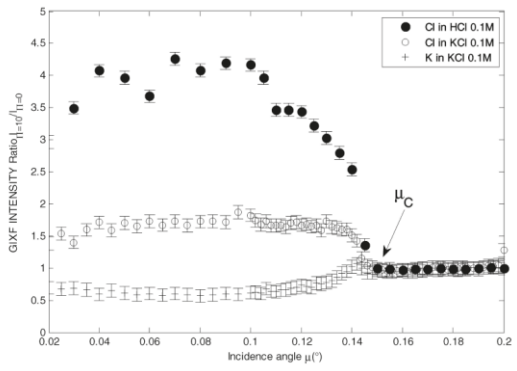

Figure 5.13 Fluorescence intensities as a function of the beam incidence angle

In GIXF the angle of incidence of the beam determines the depth at which the sample is probed. Below the critical angle μ_C, the penetration depth ξ depends on k_z, the normal component of the incident wave vector in the solution, through the equation $\xi = 1/2\mathrm{Im}(k_z)$ [184]. Above the critical angle, the penetration depth diverges rapidly to micrometers; the intensities measured above the critical angle can therefore give information on the bulk properties of the sample, and be used as a mean of comparison.

For the film on liquid subphases, the bulk intensities are given by the molarity of the subphase; looking at the data taken below the critical angle, in figure 5.13, we can see that the potassium ions are repelled by the film (the fluorescence intensity is lower than the one in bulk), while the chlorine ions are attracted to it; the Cl^- intake is however much higher in the case where the subphase is pure HCl and the resulting film is doped. This indicates that the doping process is not merely H^+ attachment to the film but also intercalation of the H^+Cl^- complex within the PANI molecular layer structure. In other words, doping proceeds via the incorporation of Cl anions within the layer. Moreover, from the comparison with the KCl subphase data we find that Cl anions are weakly attracted by the PANI monolayer, and at the same time the K^+ cations are repelled in the same fashion. This is in agreement with the known cationic nature of the PANI monolayer in these conditions.

GIXF was also applied to 48-layers PANI films deposited on glass slides, with a design slightly modified from the standard memristor in order to have a larger area available for the beam inspection. We scanned the length of the film with a lateral resolution of 0.5 mm; at each point in the scan we measured the fluorescence intensities below and above the critical angle, to measure the concentration of each ion on the surface of the film and in the film bulk.

At first we monitored a PANI film, previously doped with KCl and in the insulating state, through chemical doping and dedoping phases. We scanned the pristine film to obtain a baseline reading of the chlorine level in the insulating state, with a resistance greater than 200 MΩ; we then doped the film with HCl vapours until the resistance dropped to 16 kΩ, and repeated the scan, obtaining an increase of 25% of the fluorescence intensity, confirming the intake of Cl^- ions in the film already shown by the measurements on the film at the liquid/water interface. Finally, we exposed the film to NH_3 vapours, which are known to convert the metallic PANI to the insulating form: the resistance of the memristor went back to over 200 MΩ, and the Cl^- level dropped to 15% of the value measured in the pristine state.

We also followed the evolution in real time of the chlorine ions density when applying an electrical potential to a PANI film. To this end we used a 2 cm glass slide covered with 168 layers of HCl-doped PANI; at one end of the slide we attached an electrical contact with eutectic paste, while at the other end we deposited a strand of PEO and immersed in it a silver wire. While we normally use LiCl or $LiClO_4$ as PEO dopants, we couldn't detect the lithium fluorescence peak due to the beam energy that we used; we chose CsCl instead, although caesium atoms have much lower mobility than lithium. We applied the electric field between the PEO-immersed electrode and the one directly contacted on the film; while

this setup doesn't exactly mirror the original memristor architecture, it however should result in ion migrations in the PANI film.

We performed three runs of measurements: the first with no voltage between the electrodes, the second applying a -1V bias to the eutectic paste electrode, and the third applying a -2V bias to the same electrode while keeping the other electrode grounded. We found that when the bias reached -2V, a significant migration of Cl^- ions occurred away from the negative electrode within the surface of PANI film, as probed with an incidence angle below the critical angle (penetration depth: about 5 nm). At the same time the bulk of the PANI film was not interested by the Cl migration, as detected by the data collected above critical angle. Notably, no Cs migration could be detected, possibly because of its much larger ionic radius, as its fluorescence signal is constant thorough the various scans.

We concluded that the fact that preferential ion migration occurs in the topmost part of the film is presumably related to the presence of a "pseudo liquid" layer at the polymer/air interface, which exhibits enhanced molecular mobility, with respect to the bulk of the polymer at the same temperature, as detected by a number of techniques, including second harmonic generation (SHG) and ellipsometry [185,186].

5.4 Mimicking homosynaptic and eterosynaptic learning

Available results in experimental neuroscience show the possibility to distinguish between two types of synaptic plasticity, homosynaptic or Hebbian-type [64] and heterosynaptic or modulatory [187,188]in the *Lymnea stagnalis*. It was suggested that homosynaptic, activity-dependent plasticity is mainly responsible for learning and short-term memory, while heterosynaptic, input-specific plasticity is involved in the maintenance of learning and long-term memory [189]

We built two memristor based circuits that mirror both types of plasticity, in what is to our knowledge the first circuit that uses a single element to mimic a synapse in a neuronal circuit analogue; at the moment of writing of this thesis, the work is submitted but yet unpublished. We should note here that although a recently published paper [190] reports interesting results on a synapse-like behavior obtained in an organic-nanoparticulate field effect transistor, the described system demands preprogramming and rather high operation voltages. These features do not allow direct comparison with biological synapses and make difficult even in perspective the realization of the very complex material circuits which can mimic the learning and information handling properties of biosystems. We also note that although the imitation of synaptic STDP through a single memristor has been proposed from a theoretical point of view [76,77], as described in section 2.4.3 of this thesis, no real measures on circuits showing STDP have been reported.

The learning mechanism that we chose to imitate in this case is very similar to the one described in section 4.5 and 5.1 of this thesis. It consists in the association of a neutral chemical cue (conditioned stimulus, CS; amyl-acetate) with the initiation of a series of rhythmic movements of the feeding muscles via which the animal captures and ingests food.

Without training, these feeding movements are normally elicited in the presence of food particles (unconditioned stimulus, US), but not in the presence of the CS only. Training is achieved through single-trial, food-reward classical conditioning, a learning protocol consisting of a single, simultaneous application of amyl-acetate and food stimuli to the sensory apparatus of the animal, after which application of the CS only can trigger movements of the feeding muscles [191]. In other words, the animal has learned to respond to a previously neutral stimulus (CS).

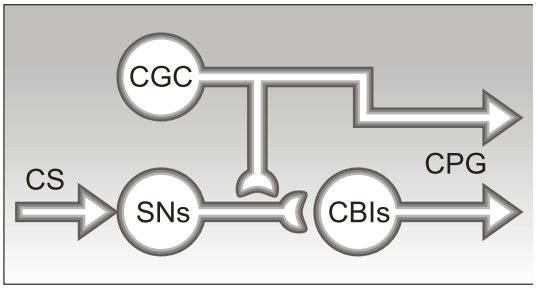

Figure 5.14: Diagram of the showing the interactions of the CGCs with sensory (SNs) and command interneurons (cerebro-buccal interneurons; CBIs), which mediate the increased response of the system to the conditioned stimulus (CS) after conditioning

The feeding neural network of *Lymnaea* can be divided in functionally distinct groups of neurons: the sensory neurons, the modulatory interneurons, the Central Pattern Generator (CPG) interneurons and the motor neurons [192]. An important component in this circuit is the Cerebral Giant Cells (CGCs), a pair of serotonergic interneurons with extensive synaptic connections on sensory, CPG and motor neurons. These cells have important modulatory effects on their postsynaptic targets [193]; recent experimental studies have shown that CGCs play an important role in the establishment of long-term memory formed during associative learning [191]. Specifically, after single-trial, food-reward classical conditioning, the membrane potential of the CGCs appears persistently and significantly depolarized (i.e. its resting potential is closer to 0V than before the training) and this depolarization is sufficient to explain the increased feeding response of the animal in the presence of the CS. According to the current model [170], the membrane depolarization of the CGCs facilitates the synaptic connections from sensory neurons (SNs) on a group of afferent command interneurons (CBIs), leading to a stronger stimulation of the feeding CPG in the presence of the conditioned stimulus and an enhanced feeding response.

The two circuits created were then the implementation of two different mechanisms. One, the “homosynaptic” circuits, had the two inputs, both the CS and the US, feeding in the same “synapse”, a memristor. The inputs were an oscillating voltage for the CS and a DC voltage pulse for the US, that were fed into the drain terminal of the memristor; the output voltage, taken from the source electrode across a test resistor, would simulate the neuronal circuit output. This circuit is very similar to the one shown at the end section 4.5; the purpose of building this circuit was to have a reliable comparison with the “heterosynaptic” circuit, besides validating the results already obtained. In the “heterosynaptic” circuit a further memristor is inserted between the US input and the one already present; its purpose was to mimic the CGC plasticity. Both circuits are shown in figure 5.15

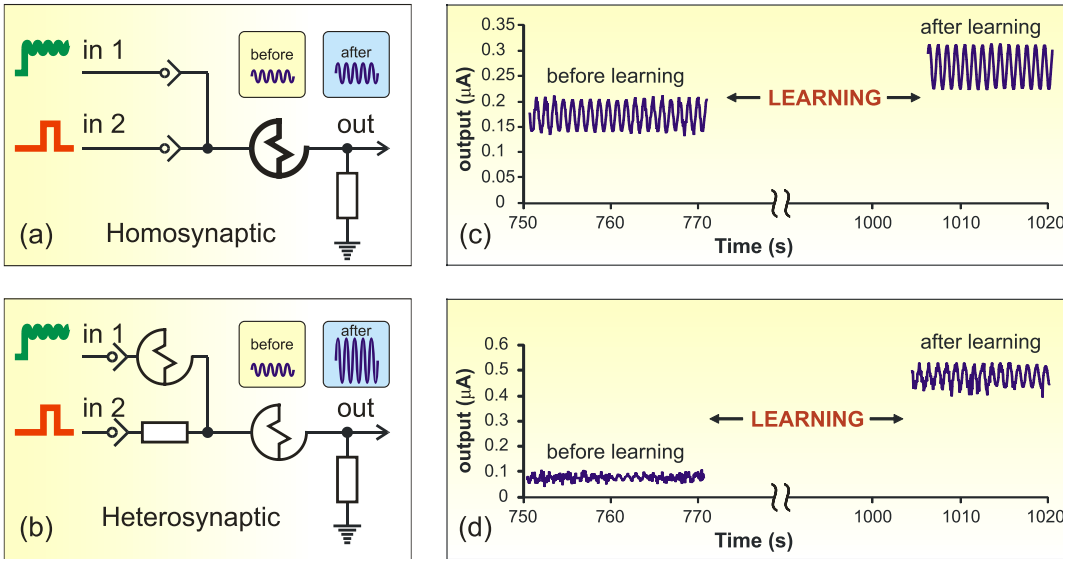

Figure 5.15: (a) and (b), schemes for the homosynaptic and the heterosynaptic circuits; (c) and (d), response to the CS of the same circuits before and after the training.

For the “homosynaptic” circuit depicted in Figure 5.15(a), the values of the input signals, dc (CS analog) and periodic (US analog), are such that their temporally separate application is not sufficient to switch the memristor to its conducting state. The simultaneous application of both signals provides a sufficient potential for switching the memristor. Output current data measured in this circuit before and after “conditioning” as a result of the action of the periodic input signal (US analog) only are shown in Fig. 5.15 (c). Such “conditioning” results in about 50% increase of both the amplitude and DC offset of the output current values, as a result of the change of the memristor resistance.

The functioning of the “heterosynaptic” circuit in Figure 5.15(b) is a bit more complicated. The periodic signal applied to input 1 would has an amplitude that would be high enough to switch one synapse analogue to the conducting state. However, as this amplitude is divided between two memristors, it is not sufficient to make either of them conducting. During training, the dc potential on input 2 is sufficient to switch the second memristor (the one close to the output) to the conducting state. After this, the dc component of the periodic potential of input 1 falls mainly across the first memristor and its value is sufficient for its transition to the conducting state. Experimental results of the output signal before and after training as a result of the action of the periodic input signal (US analogue) only are shown in Fig. 5.15(d). Both the amplitude and offset values of the output signal were increased by approximately a factor of 5 compared to initial values.

This behaviour is in good agreement with the modulatory role of heterosynaptic connections in biological neural circuits and their presumed involvement in the establishment of long-term memory [189]. The strength of the synaptic connection between two neurons can be

regulated by modulatory input from a third neuron. Moreover, this modulatory input can trigger a cascade of intracellular molecular events, which lead to relatively long-term modifications of synaptic function. Importantly, heterosynaptic interactions provide an elegant explanation for the neural basis of associative learning. Specifically, while activation of the homosynaptic pathway (e.g. SNs→CBIs; Fig. 5.14) by the CS does not lead to a significant response, simultaneous activation of the modulatory pathway (CGCs→SNs; Fig. 5.14) persistently facilitates the synapse (SNs→CBIs; Fig. 5.14) and allows for an increased response of the circuit to the CS only. Similarly, in the artificial circuit we present here, activation of the homosynaptic pathway by the CS analogue only leads to a relatively weak response (Fig. 5.15(a)). However, activation of both the homosynaptic and heterosynaptic pathways by the CS and US analogues respectively, conditions the circuit so that a stronger response is triggered by the CS analogue only. In this response particularly important is the strong increase in the DC offset signal, which mimics the depolarization observed in the biological neural circuits.

6. A MEMRISTOR MODEL

The model described in section 4.4 of this thesis was able to describe successfully some non trivial properties of our memristor, like the different characteristic times between the transition from the conducting state and the insulating state, starting from some simple assumption, the most important of which is that both processes follow the same kinetics on a local scale. However, in order to implement those assumptions in the model, one needs to simulate what happens in each local portion of the memristor, leading to more than 200 equations that have to be solved at each timestep to give the behaviour of a single memristor [161].

It is clear that such a model is inadequate to simulate a circuit including more than one memristor, and that we need to find a computationally inexpensive model if we want to simulate complex memristor circuits with stochastic architecture, which are the final goal of the BION project. On the other hand, the need for a model that could guide the process of building and training such networks became more and more pronounced during the evolution of BION related research; even if it was not foreseen in the original project schedule, we devoted some months to create and perfection a model that could simulate a circuit containing many memristors.

In this chapter we will describe how the model works, and how it was tested on the 8-memristor circuit presented in section 4.5. We will then proceed to analyze the case of a simple 3-input, 3-output circuit composed by 27 memristor, and how we have found an adaptive training protocol that is able to create an exclusive input-output pairing starting from a large amount of different initial conditions. Finally, we will look at simulations of stochastical circuits; some of those simulations can mimic some very recent experimental result, and overall they suggest that a stochastic network composed by our memristor can behave like a nonplanar circuit and it is able of unsupervised learning.

6.1 Memristor model description

The electrical model of the device, reported in figure 6.1, consists of one capacitor C_g and two variable resistors R_s and R_d linked together with a "star connection". The two variable resistors R_d and R_s are respectively linked to the drain and source terminals while the capacitor C_g is connected to the gate electrode.

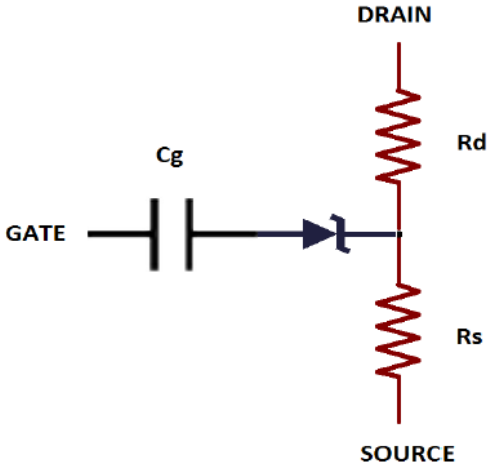

Figure 6.1: electric scheme of the model

The resistances of the two resistors, representing the two portions of PANI film between the gate and the source and between the gate and the drain, are variable, since the polymer changes its conductivity as a function of its redox state, which in turn depends on number of ions migrating from the PEO gel inside the film. We recall here that a Li^+ ion entering the PANI film reduces the conductive form of PANI (emeraldine salt) to the insulating one increasing the device resistance. The variable resistors depend therefore on the average oxidation state, that we define as

$$q = \frac{Q}{Q_M} \quad \text{(Eq. 6.1)}$$

where Q is the total charge migrated outside the film and Q_M is maximum ionic charge that can be stored on the PANI layer. The parameter q can be seen as well as the ratio between the number of oxidized sites and the total number of sites available; this is the "internal state parameter" that governs the resistance of our memristor. As a first approximation, we suppose a linear dependence of the resistances as a function of the oxidation state:

$$R_D = R_M - q\Delta \quad \text{(Eq. 6.2)}$$

where R_M is the highest value of resistance in a totally reduced film (q=0), while Δ is the resistance variation obtained by a complete oxidization (q=1).

We have also introduced in the model a Zener diode in order to take into account the redox potentials which must be overcome to move the ions from or to the film. In particular, for most of the simulations described in this chapter, we put the diode Zener (reverse) voltage equal to the oxidation potential $V_{OX} = 0.4$ and the forward voltage equal to the reduction

potential $V_{RED} = 0.2$. These numbers should not change anyway the memristor behaviour from a qualitative point of view. Finally the gate capacitor C_g represents the electrical capacitance of the active zone of our device, namely the interface between PEO gel and PANI layer.

Given such premises, the electrical behaviour of the device for a small amount of time dt can be simulated by a simple loop consisting in two steps:

1) calculate of the variation of redox state q (or the current flowing through the gate capacitor C_g) given the applied voltage and the current state of the device, i.e. the value of q
2) update both the resistances by inserting the new value of q in equation 6.1.

To calculate the influence of the voltage applied on the memristor, let's suppose, as it is very often the case, that the gate electrode is at the same potential as the source electrode. In such configuration we can calculate the current flowing in the device by considering its Thevenin equivalent circuit reported in figure 6.2

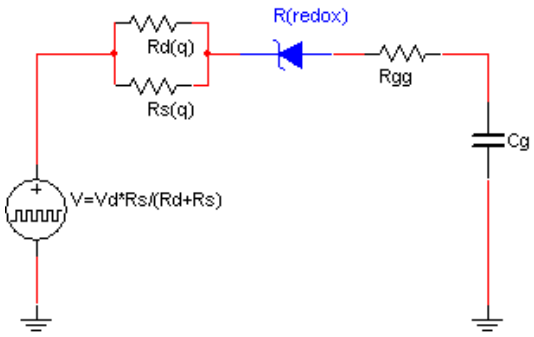

Figure 6.2: Thevenin equivalent of the circuit shown in figure 6.1

In this circuit the variation of charge on C_g, which is the gate (ionic) current, can be calculated by the equation

$$\dot{Q} = \left(\frac{V_x - \frac{Q}{C}}{R}\right)\frac{N(q)}{N_{TOT}}(V) \quad \text{(Eq. 6.3)}$$

where the first factor is the current calculated by the Ohm law, the voltage difference between the applied potential V_x and the capacitor potential Q/C_g, divided by R, the parallel resistance of R_d and R_s. This current is then multiplied by two probability factors: $N(q)/N_{TOT}$ and $P(V)$. The factor $P(V)$ accounts for the fact that the voltage difference must overcome the redox potentials in order to move the ions to and from the PANI, while $N(q)$ represents the number of available sites for the redox reaction on the active area of device. If we are considering a reduction reaction, the fraction $N(q)/N_{TOT}$ of available sites, i.e. of sites that can be reduced, will be equal to q, while the sites available for an oxidation are 1-q; this is because q indicates "how full" is the active area, being the ratio between the charge already accumulated and the maximum charge storable.

The equation 6.3 in the oxidation case becomes therefore

$$\dot{Q} = \left(1 - \frac{Q}{Q_M}\right) \frac{V_x - \frac{Q}{C_g}}{R_M - q\Delta} P(V, V_{OX}) \text{ (Eq. 6.4)}$$

while a similar equation applies for reduction,

$$\dot{Q} = \frac{Q}{Q_M} \frac{V_x - \frac{Q}{C_g}}{R_M - q\Delta} P(V, V_{RED}) \text{ (Eq. 6.5)}$$

These equations can be made dimensionless dividing both members for Q_{max} and factoring Δ and C_g, becoming respectively for oxidation and reduction

$$\dot{q} = \frac{1}{C_g \Delta}(1 - q) \frac{v - q}{g - q} P(V, V_{OX}) \text{ (Eq. 6.6)}$$

$$\dot{q} = \frac{1}{C_g \Delta} q \frac{v - q}{g - q} P(V, V_{RED}) \text{ (Eq. 6.7)}$$

where $g = R_M/\Delta$ is the inverse of the relative resistance variation and *v*, defined as $v = \frac{V}{\frac{Q_M}{C_g}}$, is the applied voltage divided by the maximum capacitor voltage (the voltage generated at the PANI-PEO interface by the accumulation of the maximum charge Q_M). The difference between the two dimensionless parameters *q* and *v* determines if and which reactions are happening in the memristor: the device is in equilibrium if $q = v$, oxidations will take place if $v > q$, and reductions will take place if $v < q$.

We point out here that a reduction process can take place in our device even when a voltage above the reduction threshold is applied, if the capacitor C_g has been previously charged; another remarkable aspect of the obtained equations that is also evident in the experimental data is that they becomes the charge/discharge equations of a capacitor under certain circumstances. Such conditions are

- $g \approx 1$ (or equivalently $q \approx 1$), the charge stored on the active area is almost at maximum
- $q \approx 0$ the gate capacitor is discharged, the device is in its most insulating state
- $P(V) \approx 1$ a voltage difference well above the oxidation threshold or below the reduction threshold is applied.

6.2 Memristor circuit simulations

All the simulations in this chapter were executed in the MATLAB computing environment, using scripts and functions written for the purpose. We chose to use the Modified Nodal

Analysis (MNA) method to solve circuits composed by memristors and resistors. The MNA technique is a method that can solve any resistor circuit, independently of the topology, even in the presence of floating current or voltage sources. We will give a brief description of the method here and refer the reader to [194] and [195] for further reading.

MNA solves the circuit by calculating the voltage at each circuit node using Kirchhoff's first rule, which says that the algebrical sum of the currents into or out of a node must be equal to the total current injected by current generators, if they are present, in that node. This equation can be written for the *i*-th node in the circuit as

$$\sum_j I_{ij} = \sum_j \frac{V_i - V_j}{R_{ij}} = \sum_j \frac{1}{R_{ij}} V_i - \sum_j \frac{V_j}{R_{ij}} = I_i^G \quad \text{(Eq. 6.8)}$$

Where the sum is over all the nodes *j* connected to the node *i* with a resistance R_{ij} and $I^G{}_i$ is the sum of the currents injected into the node by all the current generators connected to that node ($I^G{}_i = 0$ if no current generator is connected to the node). There is one such equation for every node, so we can put them together in a system

$$\boldsymbol{AV} = \boldsymbol{I}, \boldsymbol{V} = \boldsymbol{IA}^{-1} \quad \text{(Eq. 6.9)}$$

where the known term column vector $\boldsymbol{I}$ contains all the currents generated by current generators in the circuit, the unknown vector $\boldsymbol{V}$ contains the voltage at all nodes, and the matrix element A_{ij} is defined as

$$A_{ij} = \begin{cases} \sum_k \frac{1}{R_{ik}} & if\ i = j \\ -\frac{1}{R_{ij}} & if\ i \neq j \end{cases} \quad \text{(Eq. 6.10)}$$

In other words, on the main diagonal of $\boldsymbol{A}$, at row *i*, there is the sum of the conductances of all the elements connected to the node *i*, while any off-diagonal element of $\boldsymbol{A}$ in position *ij* is simply the conductance of the element connecting *i* with *j*, with a minus sign in front.

Modified Nodal Analysis can also take care of floating voltage generators. Those bring a new equation in the system, of the type $V_i - V_j = V_{gen}$, but also new unknowns $\mathrm{I_k}$, the currents flowing through them. The new equations are handled by rewriting the system into a larger one,

$$\boldsymbol{GE} = \boldsymbol{K}, \boldsymbol{E} = \boldsymbol{KG}^{-1} \quad \text{(Eq. 6.11)}$$

$\boldsymbol{E}$ is the new unknown vectors, which contains all the voltages in each node followed by all the currents in each voltage generators. The new known term vector $\boldsymbol{K}$ contains all the currents injected in each node, followed by all the potential differences created by each generator. The new $\mathbf{G}$ matrix is composed by four submatrices,

$$G = \begin{pmatrix} A & B^T \\ B & C \end{pmatrix} \quad \text{(Eq. 6.12)}$$

where $\mathbf{A}$ is the matrix defined in equation 6.10. $\mathbf{B}$ has as many columns as $\mathbf{A}$ and as many rows as the number of voltage generators; the entries of $\mathbf{B}$ are all zeros, save for the entries

B_{kp}, where the positive terminals of the generators are connected, that are equal to 1, and the entries B_{kn}, where the negative terminals are connected, that are equal to -1. B^T is the transpose of B, and C is a matrix whit all entries equal to zero. The system described in equation 6.11 recovers with the last lines of the matrix G all the equations added by the voltage generators and includes in the equations 6.8 the currents through the generators, using the matrix B^T. It should be noted that solving a circuit using MNA requires inverting a matrix of size n + k – g, where n is the number of nodes in the circuit, k is the number of voltage generators, and g is the number of nodes connected to the ground potential, which do not generate equations to be included in the matrix A, as we already know their voltage.

Equation 6.1 gives a biunivocal relationship between the state variable q of a memristor and its resistance, and the change of q is determined by the potential difference between the drain and the source electrode; moreover, as we stated in chapter 2, a circuit of memristors behaves instant by instant like a circuit of resistors, as no charge is stored in the memristors themselves. Therefore, our simulations of a circuit proceed with the following algorithm:

a) collect all the memristors' resistances at step *t* of the simulation
b) build the $\boldsymbol{G}$ matrix of equation 6.11
c) calculate the potential values at each node at step *t* by inverting $\boldsymbol{G}$
d) create a vector with the potential differences at the terminals of each memristor and one with the q values of each memristor
e) update the q values using the Euler rule $q_{t+1} = q_t + \dot{q}\Delta t$, where Δt is the simulation step length used
f) calculate the new memristors' resistances and start back from point a)

Basically, this means that at each simulation step we consider our circuit as a resistor only circuit, which means that our time step must be short compared to the characteristic times of the memristor evolution. As those are of the order of hundreds of seconds, we found that a time step of one second is usually short enough, and that further shortening it does not change the simulation results. Also, MATLAB is well suited for calculating in one step the evolution of all the memristors in the circuit, as the passages d), e) and f) can be written in terms of single operations between vectors

We should also point out that, as the potential distribution is calculated at each time step, we are not limited to constant voltage and current generators, but we can simulate generators whose output is an arbitrary function of time as well; finally, it should be noted that we discard, during the simulations, the gate currents, instead of adding them to the source currents, partly because the model we use does not handle them correctly; in the real device, however, these currents are two orders of magnitude smaller than the source-drain currents, so that the effect of the gate-source currents on the current distribution in the circuit can be considered negligible [2]

The benchmark for the model and the circuit simulation technique was the 8-element circuit described in chapter 4.5 and pictured in figure 6.3: it is an 8-memristor circuit with two inputs and two outputs that was trained to modify its spontaneous input/output pairing [5]

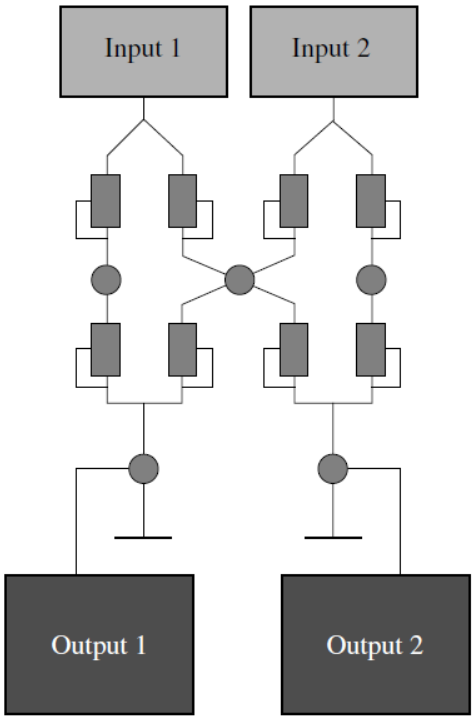

Figure 6.3: layout of the circuit simulated. The grey rectangles are memristors, the grey circles are circuit nodes

We will recall here that at the beginning of the experiment it was observed that the application of a positive DC voltage to the input number 1 of this network yielded a current through output 1 that was much higher than the one flowing from output 2 (120 nA and 32 nA respectively). The circuit was then subjected to the training procedure, in which a positive voltage was applied between input 1 and output 2, and simultaneously a negative voltage was applied between input 1 and output 1. As the result of the training, the application of the same input at input 1 of the network resulted in increase of the current value at output 2 to 124 nA, that is, almost the same as the previously obtained from output 1, which in the meanwhile had dropped to 65 nA, about half of the original value [169].

This behaviour was simulated with the model, providing the additional advantage that, unlike in the experiment, we could visualize the changes in the output currents in every moment during the training phase, and not just measure a pair of values before and after the training. The simulations were performed with a time step of 1 s. The currents from the two different outputs during the training period are shown in Figure 6.4. Reported current values were calculated applying a test potential (+0.5 V), that is different from training potentials (+1.2 V and −0.7 V, respectively for Input 1 and Input 2).

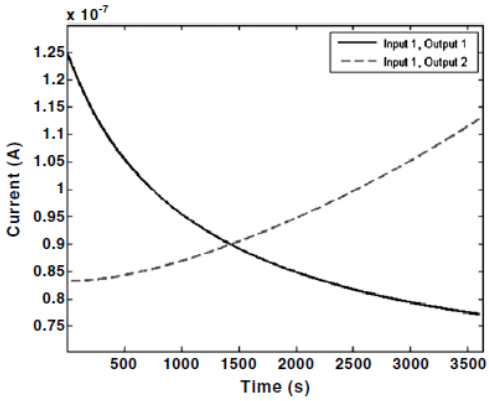

Figure 6.4: simulation of the output currents during the training phase of the circuit. Lines represent the current obtained from output 1 (continuous line) or output 2 (dashed line) when applying a test input potential to input 1

The figure shows clearly that the simulated training changes the spontaneous pairing of input 1 and output 1 in the network; when applying a test potential of 0.5 V to input 1, the current from output 1 changes from the 125 nA measured before the training to 77 nA after the training, while the current from output 2 changes from 83 to 112 nA. While the model didn't capture perfectly the time needed for the training completion (it takes 1 hour of training for the outputs to "switch", instead of the 5 minutes reported in [169]), this is just a matter of rescaling the time step or more generally to fine-tune the parameters (like Q_M, C_G and so on) that describe the single memristor: we are interested in capturing the qualitative behaviour of a whole circuit of memristors, which we achieved with the simulation reported above and we confirmed with a simulation reported in section 6.4.4

6.3 Adaptive training for nonplanar memristor networks

All the circuits presented until now are very simple, with a predefined architecture, and they contain a few memristors at most. However the goal of the BION project has always been to build complex statistical networks, in which the circuit layout was not predefined but was created using some stochastic process, and then train it to perform some task.

During the last year, the studies performed within the BION project allowed us to present three alternatives that can allow us to build such a network: either using gold nanoparticles functionalized with cavitands, PANI-PEO block copolymers, or a fibrillar support to be decorated with a PANI-Gold nanoparticles mixture (see section 9.1 for more details). All these networks would have a higher complexity and a larger number of elements than anything that we're currently able to build deterministically; these features would greatly help when facing the task of mimicking neuronal systems, and would allow us to reproduce more closely the behaviour of simple neuronal circuits.

We note here that it has also been shown [15] that several layers of very simple information processing units lead to information processing capabilities and even feature recognition for the whole network of elements: studies on complex networks are therefore of the maximum

importance if we want to fully explore the capabilities of a memristor network. As a first step towards the study of complex memristor circuits, we decided to run computer simulations of model memristor networks, to help us in the research of training protocols for more complex structures. The data shown in this section is unpublished yet, but we plan on publishing it shortly.

6.3.1 The network

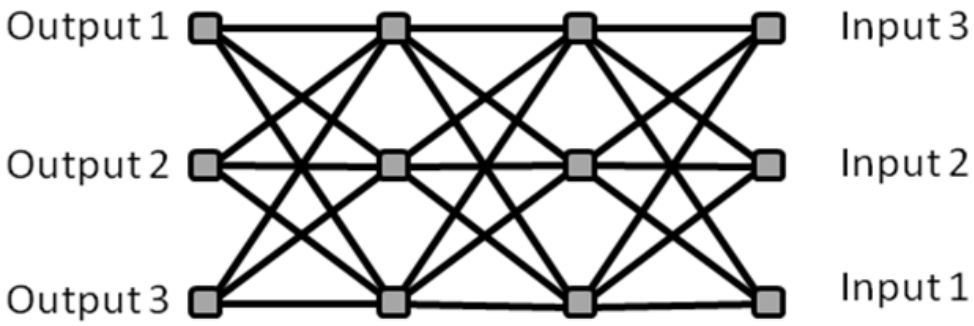

Figure 6.5: network model. The black lines are memristors, connected through the gray squares. For each memristor the "source" terminal is the one closest to the output layer

The network chosen for our simulation is depicted in figure 6.2. It is made of an input node layer, two hidden node layers and an output node layer. Each layer is made of three nodes; each node is connected to all nodes in the layer before and in the layer after. In total there are 27 links and six terminals, three of which are labelled as inputs and three as outputs. Every link in our network is a memristor; the orientation of each memristor is such that the source terminal is the one towards the output layer and the drain terminal is towards the input layer. Each terminal of the network can be connected to a voltage generator, a current generator, to ground via a test resistance, or left floating. The reason for choosing this particular geometry is that this is one of the simplest configurations that allow us to have a "middle" layer of links, i.e. links that are not connected to an input or an output node, and at the same time have a non planar network. We think of this network as an approximation of a more complex, self-assembled stochastic network, in which we're sure to find links that are not connected to circuit terminals, as well as a strong degree of non-planarity.

The purpose of this study was to establish training strategies that can modify the properties of a randomly generated network in a way that modifies its response to externally introduced inputs towards a desired goal response, as a result of the application of electrical inputs to the whole network, with constraints similar to what we would find in an experiment on a real polymer network. Although the network chosen for the simulations has a rather simple architecture, we believe that this study is a necessary first step in order to understand in detail what happens in different regions of the circuit during the training, and to devise more complex training protocols that can be used on different networks. While the network examined in this paper has a rather simple and arbitrary topology, we expect to be

able to extend soon this method of search of training protocols to networks more similar to a self assembled polymeric network, described in terms of average connectivity, average length and resistance of the memristive links, and so on. Once the description of the networks is complete, we expect to be able to quickly adapt the method proposed in the following sections to a real case and to provide training protocols that can be implemented in a real lab experiment.

The goal that we have chosen for the network training is “input-output pairing”: the network has a certain number of inputs and outputs, and the task of the training is to modify the internal resistances of the network in such a way that a signal presented on one of the inputs causes a strong signal at only one output, previously chosen, that should be both stronger than the signals obtained from the other outputs with the same input and the signals obtained by the same output when using different inputs.

6.3.2 Training strategies

To create a path that pairs a input with an output in the network, we have to change the conductivity of some memristor by applying the correct voltage at their terminals. When a single memristor is not in a totally conductive or insulating state, the equations used to model it basically tell us that for a voltage drop higher than V_{OX} (0.4 V in the simulations) the device starts to become more and more conducting, while for voltage drops lower than V_{RED} (0.2 V) the device becomes more insulating. It is trivial to make every link in the network more conductive or more insulating, since it is just a matter of applying a voltage high enough between all the input and output terminals; but to create a selective path, that is to create a pairing between only one input and only one output, some links usually need to become more conductive and some others to become more insulating.

If we had access to every node in the network, configuring it to have a conductive path would be very simple: it would just be a matter to make the path links conductive and the other links insulating, one by one. We’re interest however in simulating a physical system that is buildable in our laboratory, and in finding training strategies that are implementable in a real network; so we must limit ourselves to what we could do in a laboratory. This means that we can only apply potentials at or inject currents through the terminals of the network, and we cannot operate directly on the hidden nodes. Our training strategy should act on the whole network at once, creating a potential distribution that suits our needs just by applying inputs to the terminals of the network.

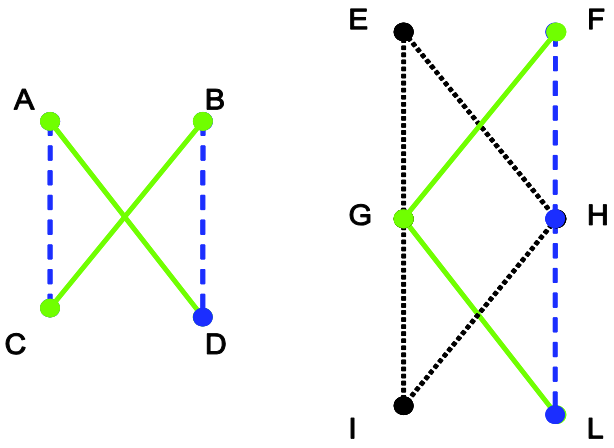

Figure 6.6: Some examples of training patterns that cannot be enforced in a single training step. On the left: a pattern bound to occur when trying to train two different paths at once. On the right: Training a path to become more conductive and a competing path to become more insulating. In both panels, green continuous lines are memristors that should become more conductive, blue dashed lines are memristors that should become more insulating, black dotted lines are memristor which behaviour we do not specify.

Acting on the whole network at once, however, means that there are limitations on what is achievable by a training strategy. For example, in the situation depicted in the left panel of Figure 2, even if we could control the potential at every node, it would be impossible to create a potential distribution such that the links AD and BC become more conductive and at the same time the links AC and BD become more insulating, or vice versa. This effectively tells us that there is no way to create two separate paths, linking two different input-output pairs, at the same time, since, given the topology of the network, we would incur in a situation like the left panel of Figure 2 in many regions of the network. Likewise, the right panel of Figure 2 shows a situation that is bound to happen when we create a single path that crosses more than one layer of links. In this case, it is impossible to make the path FGL more conductive while at the same time making the competing path FHL more insulating.

Having considered these limits, we created three different training strategies, which are going to be examined and compared in this chapter. These strategies consist in the specification that at every step of the training some link must become more conductive, some more insulating, and some can behave in either way. In all the three strategies, given an input node and an output node, the links that will form the path between the chosen nodes are selected; at every step of the training, these links should become more conductive. The difference in the three strategies is in the choice of links that should become more insulating. In the first strategy those are the links that go from a node of the selected path to a node that does not belong to it on the next layer; we call this strategy “outbound links”. In the second strategy, called “inbound links”, the links that should become more insulating are the ones that start from a node not belonging to the path and end in the next layer in a node that does belong to the path chosen. The thirds strategy, called “alternate”, is a combination of the previous two, alternating one step of “inbound links” with one of “outbound links”

6.3.3 Applying the strategies

The method used to implement these training strategies in terms of electrical inputs to the network is based on the consideration that in a resistor network, if multiple currents are injected into different nodes, the resulting potential distribution is the sum of the ones that would result from injecting the currents one by one in the respective nodes; that is, the potentials generated are linear in the currents injected.

When we specify in a training strategy that some of the links should become more conductive and some more insulating, we are actually setting some condition on the voltage at the nodes connected by the links. For example, if a link is to become more conductive, the voltage difference across its terminals needs to be always higher than V_{ox}. To apply a training strategy means essentially to look for a potential distribution that satisfies all the conditions created by the strategy. On the other hand, any potential distribution that we can generate in the circuit acting on the six terminals at our disposal is the linear combination of the distribution we get by injecting a unity current into each of the terminals. Moreover, since what regulates the change of state of the memristors is the voltage difference between connected nodes, we can ground one of the terminals to use as a reference electrode, without losing the possibility to create any distribution that could be useful for our training.

Our procedure to implement a training strategy onto a particular network is divided in two parts: the initial choice of the path to train and the training itself. First, given the input and output node, we create a list of all the possible paths in between, looking only to paths composed by three links, one per layer. For each path we find out the conditions on the potential distribution to train the network using that path, according to the current training strategy. Then, leaving Output 1 grounded, we calculate the potential distribution of the network when we inject a unity current in each of the other terminals, labelled 1 through 5. In this way we find a collection of five potential distribution $\mathbf{V_1},\ldots,\mathbf{V_5}$; we then look for a linear combination of the five potential distributions that satisfies the conditions imposed by the choice of training strategy and path. If no such combination exists, we try the next path in the list, which has different conditions attached, until no more paths are available. If there is a combination $a\mathbf{V_1} + b\mathbf{V_2} + c\mathbf{V_3} + d\mathbf{V_4} + e\mathbf{V_5}$ that satisfies all the conditions, we can start the training.

We multiply the five coefficients $a,\ldots,e$ by the unity current to get the five training currents. Then we apply the five currents to the network and use the resulting potential distribution to evolve the memristors in the network for the time dt, assuming that the potential at the terminals of each memristor doesn't change during this time. Since after the evolution the resistance distribution of the network has changed, for the next training step we have to recalculate the five distributions $\mathbf{V_1},\ldots,\mathbf{V_5}$ and a new set of coefficients $a,\ldots,e$ that satisfies all the conditions; from the new coefficients we calculate the new set of currents and evolve the network for the second step. The process goes on until the network has reached a configuration in which no combination of input can satisfy the conditions on the potentials,

or the input currents exceed a predetermined value (±10 mA, a value that would damage the memristors in a real network), or the number of steps taken exceeds a predetermined limit.

It should be noted here that this method is not only confined to simulated networks, but it can also be applied in lab experiments; all we need to apply this method is the ability to measure the electric potential at every node of our network, or, failing that, to measure the resistance of every memristor in the network and then compute the potential distribution. The latter option seems more feasible as we have demonstrated [196] that the conductivity of a PANI film, and hence of a memristor, can be measured optically, without the need of placing many electrodes along the network and without sending the test unit currents through each input at every step, which could change the oxidation state of the network. This method of implementing a training strategy is also independent from the task that our strategy should accomplish and from the strategy chosen.

6.3.4 Measuring the training

To measure the effectiveness of the training, four indicators were introduced. The first two, which we call "gain" and "offset", measure how a current injected in the input selected for the pairing distributes itself in the various outputs. We define I_{AB} the current flowing through output B when all three outputs are grounded and a test potential of 1 V is applied to input A. If the task is to pair, for example, Input 3 with Output 2, we define the gain G and the offset O as

$$G \equiv min\left(\frac{I_{32}}{I_{31}}, \frac{I_{32}}{I_{33}}\right), \; O \equiv min(I_{32} - I_{31}, I_{32} - I_{33}) \text{ (Eq. 6.13)}$$

Gain is greater than one, or offset greater than zero, when more current flows through the selected output than through any other outputs when applying a potential to the selected input. The two quantities are indicators of how strongly and selectively the chosen input is connected to the chosen output.

The other two indicators used are called "reverse gain" and "reverse offset". Using the same example task as above, we define the reverse gain R and the reverse offset S as

$$R \equiv min\left(\frac{I_{32}}{I_{12}}, \frac{I_{32}}{I_{22}}\right), \; S \equiv min(I_{32} - I_{12}, I_{32} - I_{22}) \text{ (Eq. 6.14)}$$

These quantities are related to how much current flows from the chosen output when we apply a test potential to inputs other than the one chosen, i.e. how well the chosen output is isolated from the other inputs. It is evident that gain and offset are related, as well as reverse gain and reverse offset: they are two different quantities that convey the same information about the network training, so using only one of each couple should be enough in quantifying the effectiveness of the training. On average, for a randomly generated network *G* and *R* are slightly less than one, and *O* and *S* slightly less than zero, which seems natural considering the symmetry of the circuit and the slight bias towards lower values induced by picking the minimum value in the equations 6.13 and 6.14. In the rest of this

chapter we use gain and reverse gain, as they are perhaps the most natural choice, not depending on the magnitude of the potential applied to the inputs. However, offset and reverse offset can be more useful if, for instance, we have some circuit elements that have to compare the two quantities; in that case the absolute difference between the currents may be more important than their ratio.

6.3.5 Training results

We applied each strategy to 1000 randomly generated networks. Since the topology of each network is fixed, the random component lies in the initial oxidation state (and hence the initial resistance) of every memristor in the network. Half of the networks were initialized using every possible initial resistance value for the memristors, hence using the range 50kΩ - 1 MΩ; in the other half of the network the initial memristor resistance values were restricted to the range 500kΩ - 1 MΩ. The second range was chosen because, due to our building processes, freshly assembled memristors are more likely to be near their maximum resistance value. Each network was trained until either 1000 training steps were reached or it wasn't possible to train a network anymore. For each network, we recorded the performance indicators of the network before and after the training, as well as the total training duration.

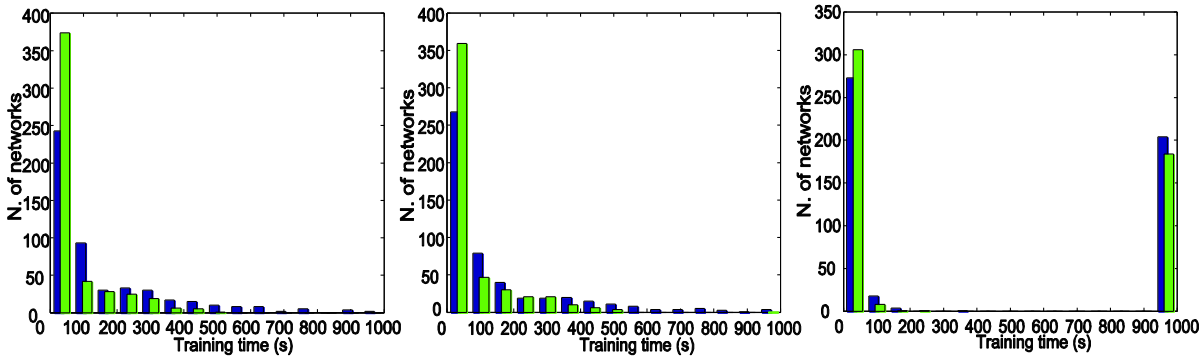

Figure 6.7: Training times distribution for the three strategies, over 500 trials. From the left: "outbound links" strategy, "inbound links" strategy, "alternate" strategy. Blue columns show the distributions for the trials in which the networks were initialized using the full resistance range (50kΩ - 1 MΩ), green columns the trials where the networks were initialized using the 500kΩ - 1 MΩ range.

Figure 6.7 shows the distribution of training steps executed using the three strategies. It is clear that while the training duration distribution is similar in the cases of "outbound links" and "inbound links" strategies (left and centre panels), we have a different situation using the "alternate" strategy. In the latter case, shown in the right panel, almost half of the networks have been trained for the maximum training duration, and the rest have been trained for less than 150 steps (indeed, in the majority of these cases the training steps were less than 20). For the "outbound/inbound links" strategies, instead, the training time distributions follow a fast decaying distribution, with only a minority of the cases having

undergone more than 100 training steps, and none having reached the maximum training step limit; the cases in which the network started with a limited resistance range underwent on average less training steps than the ones where the initial conditions were totally random.

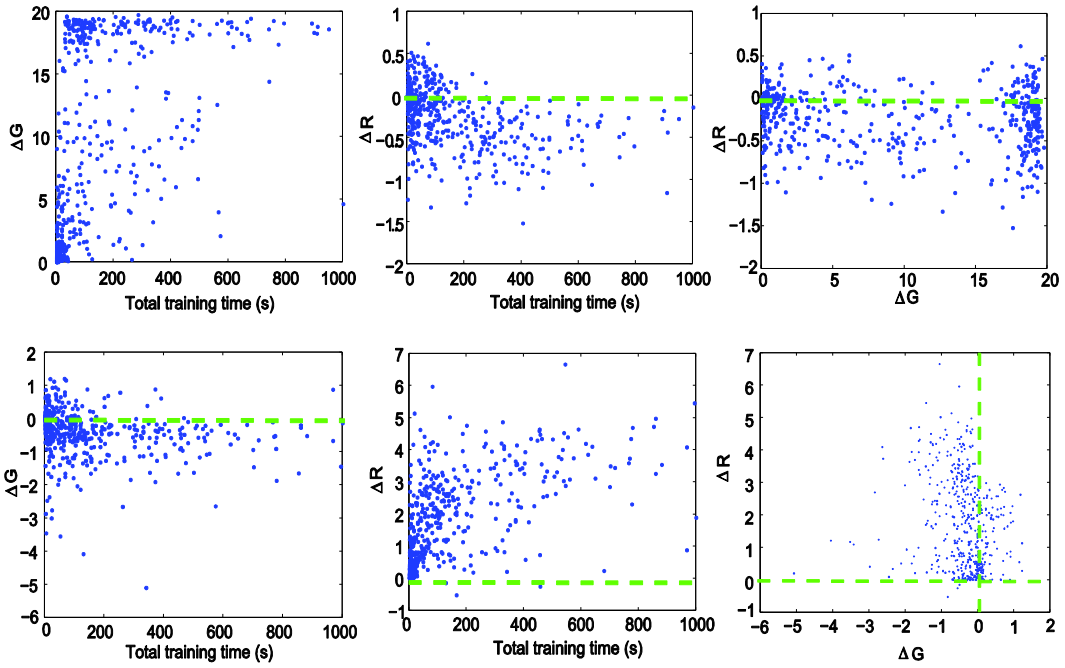

Figure 6.8: Change in the gain *G* and reverse gain *R* parameters after training. Each point represents a single network evolution, for a total of 500 networks. Dashed lines mark the axes for ease of inspection. Top row: networks trained using an "outbound links" strategy, bottom row: networks trained using the "inbound links" strategy. Left hand plots: differences in gain Δ*G* vs total training times. Middle plots: differences in reverse gain Δ*R* vs total training times. Right hand plots: differences in reverse gain Δ*R* vs differences in gain Δ*G*.

Figure 6.8 collects the results of the training for the three strategies. We chose to measure the training effectiveness using the direct gain G and the reverse gain R; the same graphs can be plotted with little difference using the offset O and the reverse offset S. For both G and R the data plotted represents the difference between the value before and after the training, in order to evaluate the effect of the training procedure.

Panels a), b) and c) show the effect of the "outbound links" strategy, plotting respectively the difference in gain before and after the training (ΔG) as a function of the total training time, the difference in reverse gain (ΔR) as a function of the total training time and the difference in reverse gain versus the difference in gain, for each network. Panels d), e) and f) show the same data for the "inbound links" strategy. In every graph we plot a point for each of the 500 network trained, for the case where the full range of resistances was used to initialize the networks.

It is very noticeable that the "outbound links" and "inbound links" have a somewhat symmetrical effect on the networks. The first strategy tends to improve the gain G at the expense of the reverse gain R; the longest the training can go on, the higher the difference

in G tends to be, although the maximum difference in G, which is around 20, can be reached even in a few training steps. Conversely, in most of the cases, and in every case in which the training lasts more than 300 steps, the reverse gain R actually diminishes. Looking at panel c) we can see that while G has always improved there are very few cases in which the training has improved also R. The cluster of cases around (0,0) in the same graphs is related to the abundance of networks that have been trained for very few steps, while the one around $\Delta G=20$ is due to the fact that ΔG cannot be more than 20 with this topology and the limits on the single memristors that we're using.

Panels d), e) and f) show the same plots for the "outbound links" strategy: here, symmetrically, in almost all the cases R is improved, although never reaching its maximum value of 20; in most of the cases, G is instead decreasing, with a ΔG value usually comprised between 0 and -1.5. Again, in panel f) there is a cluster around the (0,0) point, due to networks that have been trained only for a few steps, while from panels d) and e) we can see that longer training lead to increased ΔRs and negative ΔGs

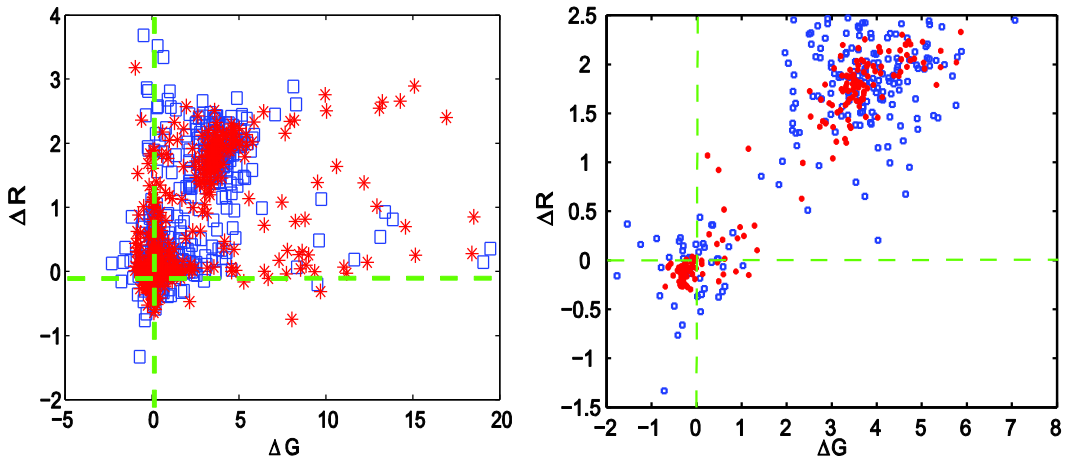

Figure 6.9: ΔR vs ΔG plots for 1000 networks trained using the "alternate links" strategy. Left panel: all the networks. Right panel: only networks that did not stop the training before the training time limits are plotted. Squares represent networks initialized using the full resistance range (50kΩ - 1 MΩ), asterisks networks initialized using the 500kΩ - 1 MΩ range.

The "alternate" strategy shows instead different characteristics, as suggested also by the different distribution of training times. We can see from figure 6.9, left, that there are two clusters for the network evolution in the ΔR vs ΔG plane. One is around the origin, while the other is roughly centered around the point (4,2). The great majority of cases lies in the first quadrant of the ΔR vs ΔG plane, meaning that usually this training strategy improves both the gain and the reverse gain. Moreover, if we only consider the networks that have reached the training step limit, we still see the same two clusters (figure 6.9, right); the points corresponding to prematurely ended trainings are those along the axis of the plane or far from the clusters. We can see in this second picture that the networks that were initialized using the full range for the initial memristors values are more spread out than those starting in the 500kΩ-1MΩ range.

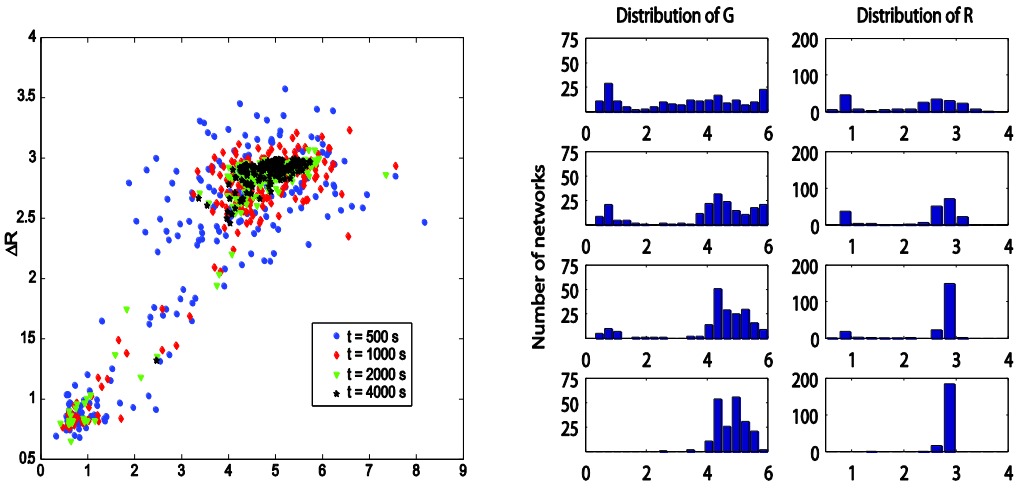

Figure 6.10: Left, evolution in the Δ*R* vs Δ*G* plane of a population of 1000 randomly generated networks, during an "alternate links" strategy training. Right, distributions of *R* and *G* in the same population at various times during training. Histograms in the left column represent the distributions of *G* at 500, 1000, 2000 and 4000 training steps, from the top to the bottom; histograms in the right column represent the distributions of *R* at the same times.

Figure 6.10 shows the evolution of 1000 networks trained with a time limit of 5000 steps, using the "alternate" strategy and the full range for the initial resistance values. To enable a comparison between different networks, and to better evaluate the final result of the training, here the points on the plane show the actual values for G and R, not the differences from their values before the training. Again, the networks either stopped evolving very soon (before 200 steps) or reached the upper step limit; only the second category is plotted in Figure 6.10. 500 steps into the evolution, many networks have already reached the vicinity of the final attractor, which in this graph is in the vicinity of the point (5,3) given that all the networks start with G and R values close to (1,1). As the training goes on, the spreading of the clusters diminishes, and the number of networks around the (1,1) initial state decreases, until at 4000 training steps every network is clustered around (5,3).

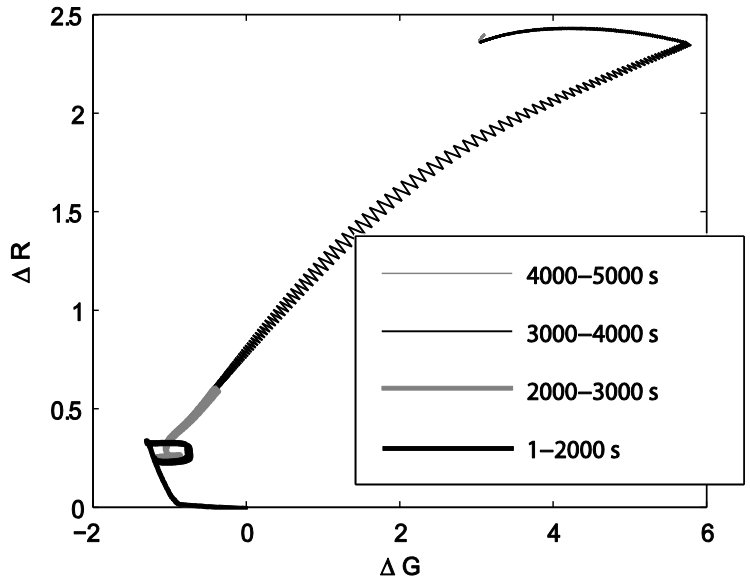

Figure 6.11: Trajectory of a single randomly generated network in the Δ*R* vs Δ*G* plane under "alternate links" training strategy. The trajectory starts at (0,0): the first 2000 training steps are shown with a bold black line, steps from 2001 to 3000 with a bold gray line, steps from 3000 to 4000 with a thin black line, steps from 4000 to 5000 with a thin gray line.

Finally, in Figure 6.11 we plot the evolution of a single network in the ΔR vs ΔG plane during the training. The network spends the first 3000 steps around the first attractor, in a region where ΔR is less than 0.5 and ΔG is negative; the next 1000 training steps bring it closer to the region dominated by the attractor, and the final 1000 steps have very little effect on the position of the network in the ΔR vs ΔG plane. Between steps 3000 and 4000 the effect of the intercalation of the two strategies is clearly visible; the trajectory of the network is actually a zigzag line in which the different strategies employed at each step send the network in very different directions, nearly opposite and nearly orthogonal to the trajectory, so that after two steps the actual displacement of the network in the plane is much smaller than the one occurred in a single step. This suggests that, for this kind of network and under this training strategy, there are two main dynamics: at the beginning the network stays in a configuration very similar to the initial one, that is continuously and slowly modified with little effect on the performance parameters, until at some point a relatively quick transition brings it into the final state, where both gain and reverse gain are significantly increased with respect to the starting value.

It appears evident from the results described that the "outbound links" strategy and the "inbound links" strategy have symmetrical effects on the network. Both improve one of the two parameters that quantify the training, at the expense of the other, and the training usually goes along for few steps, before stopping; both are slightly more effective when the network is initialized using 50kΩ - 1 MΩ as the range for the initial memristor resistances. They probably can be used when a randomly generated network has one of the two parameters (gain or reverse gain) already quite high and we only need to raise the other.

The “alternate links” strategy has actually a very different behaviour. First and foremost, it appears that this strategy divides the randomly generated networks in two classes; networks belonging to one of these classes end their training shortly, within 200 steps, while networks in the other class can be trained for at least twenty times as much. It appears that the two classes are roughly equally populated, for both possible choices of initial starting conditions. For both classes of networks the training usually implies an improvement of both the parameters that measure the training; however for the second class of networks the final values of G and R are very similar, whatever the initial conditions.

Future studies should be directed to clarify what makes a network belong to one of the two categories, and to explain the nature of the attractor state and of the peculiar dynamics observed. It should be noted that these networks solve the same task (pairing input 3 of the network with output 2) using the same general strategy, however they use different paths within the network to solve the problem, choosing between 9 possible alternatives. Due to this issue, to the number of links in the network and to the fact that changing a single element in the network has repercussions on the currents in all the links of the network, a direct comparison between network configurations is very difficult. It would be interesting to find a generalized description of the networks that, regardless of the path chosen for the training, makes it apparent whether a network belongs to one of the two categories and when is the transition between the initial state and the final, stable state of the training.

6.4 Simulations on networks with random architectures

The network presented in section 6.3 has highlighted some issues with the process of estabilishing a training protocol. From the very first experimentations it appeared clear that, if we want to train the network “realistically” and not by operating on the single links, the protocols have to be adaptive, that is, information about the network state is needed in order to send the right training inputs. Also, not even the case of the “alternate links” strategy, which is the best that we have found, can train correctly all the networks, even if the network topology is predetermined.

All these issues will only be exasperated by the case of the randomly built networks. It appeared necessary to perform, then, some simulations on adaptive networks that could clarify which tasks can be performed by an adaptive network of memristors, and what is the best way to approach them.

6.4.1 Unsupervised learning by a memristor network

A series of simulations was devoted to find out if the network can perform some kind of unsupervised learning, i.e. if it can react spontaneously to features of the input signal, by modifying its output or some other measurable quantity of the network.

To this end, we wrote a program capable of generating a random memristor network. While ideally this program aims to replicate a self assembled memristor network, at the moment of writing it we had practically no information on the possible structure of such a network. The program therefore is meant to be used as a general tool, both as a way to study what a generic memristor network can and cannot do, and as a way to model more closely a self assembled network once the parameters describing it are found.

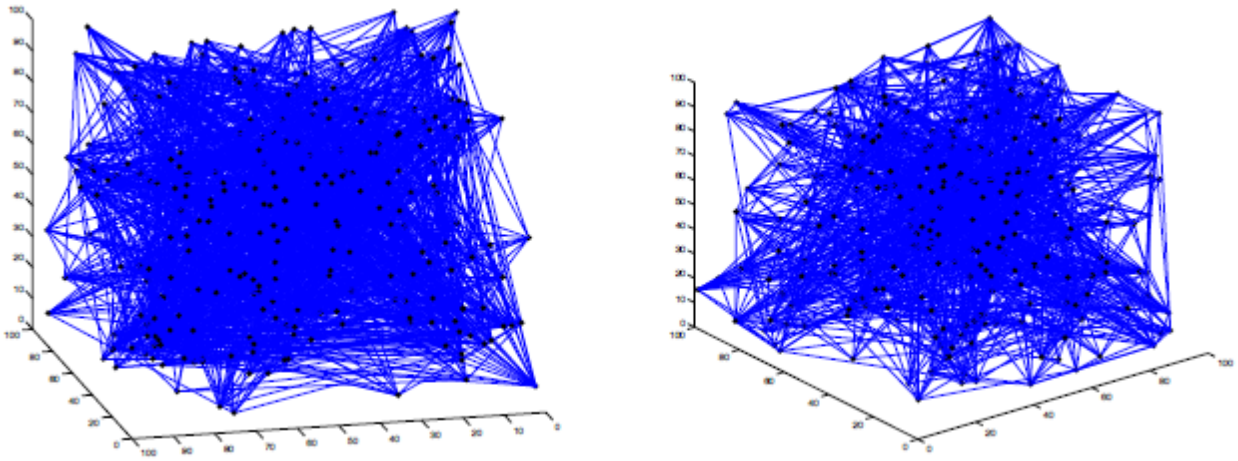

Figure 6.12: visualization of a randomly generated network, with random connection length distributions (left) and with a logarithmic distribution of connection lengths (right)

The network is generated by randomly distributing a certain number of nodes in a cubic space; all the simulations reported in this section use 250 nodes. Connections between nodes are then randomly assigned by extracting the nodes to be connected, until a predetermined number of connections is reached (in this case, 1500). At this step an optional dependence from their distance of the two nodes of the likelihood that they are connected can be inserted, by accepting or rejecting the connection extracted with a probability that depends on the node distance, therefore imposing a certain distribution of the connection lengths. Each connection is then converted into a memristor or a resistor, again with a certain probability – in our simulations the probability of a connection being resistive instead of memristive is 0.2. We implemented this passage because it's very likely that in a self-assembled network, that relies on many PANI-PEO junctions creating a distribution of memristors, there are bound to be filaments of conducting PANI that don't contact enough PEO to noticeably change their conductivity. For both memristors and resistor the initial resistance value was drawn from the range of possible resistance values of our PANI-PEO device, i.e. 50 kΩ – 1 MΩ; the evolution of each memristor under an external voltage occurred then according to the model presented in this chapter. At the last step of the procedure that builds the network, two nodes are randomly chosen as inputs and other two as outputs. The output nodes are set to the ground potential, while the input nodes receive constantly varying input potentials.

In a typical unsupervised learning experiment one feeds to an adaptive network a large batch of data that belong to two or more “classes”, without labelling them in any way or without performing on the network any other action that is correlated with the class to which each input belongs. The network then self-organizes in such a way that its response to inputs of different classes is different in some aspect. For the network, the input was a sequence of random electrical potentials applied at the input nodes, of absolute value bounded between two thresholds. We used two input classes for all the experiments: inputs belonging to class A had the voltages applied to both input nodes positive with respect to the ground level, while inputs belonging to class B were one positive and one negative. The thresholds for the absolute values of the voltages applied were calculated for each network built, so that any voltage within the thresholds could, alone and not accounting for the polarities of the memristor, raise the conductivities in 10-20% of the network elements at the beginning of each simulation.

To check for unsupervised learning, we applied to each network that we created inputs of class A for 100 seconds, then we reset the network and applied 100 seconds of inputs of the class B; in each case we changed the voltage applied to the inputs every 20 seconds. Application of 100 seconds of inputs of the type A or B was called an ‘epoch’; one ‘session’ was the application of 50 epochs of both input classes to the same network, always resetting the network between one epoch and the next to its initial state. The conceptual scheme of our simulations is shown in figure 6.13

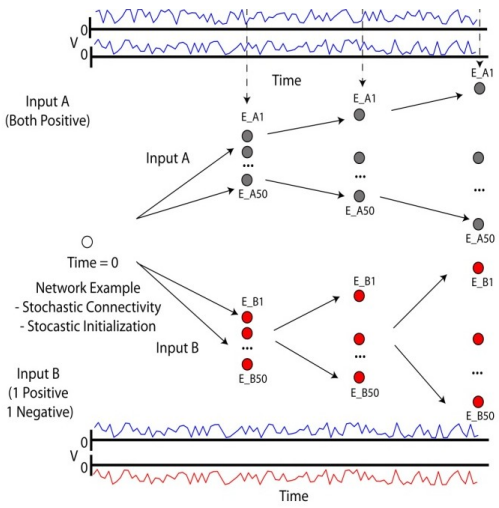

Figure 6.13: scheme of the simulation procedure to detect unsupervised learning

As the exact input voltages change randomly from epoch to epoch, we expect the network evolution to be different from one epoch to another. The more adaptive the network is, and the more its evolution will be different from one epoch to another; moreover, if the network is to distinguish between inputs of class A and inputs of class B, the network evolution in those two cases should be noticeably different.

To measure how different are two networks at a given time we used the Pearson correlation coefficient (the covariance between two vectors divided by the product of the standard deviations of their values) between the network states. For example, the similarity between

two given epochs *i* and *j* at the time *t* of the training of a network, stimulated with independent random patterns of the type A, was defined by the function $corr(EAi(t), EAj(t))$. The vectors $E_{Ak}(t)$ contain the resistance values of all the memristors and resistors in the network at time *t* of epoch *k*, as these values identify univocally the state of the network. The overall similarity (indicated here as S) as a function of time, using the input pattern A, was given by the average correlation across all possible paired comparisons between all the simulated epochs or experiments:

$$S_A(t) = \frac{1}{N}\sum_{i,j} corr(E_{Ai}, E_{Aj}) \quad \text{(Eq. 6.15)}$$

where N is the number of possible *i,j* choices. In an analogous manner we can define the similarities between the evolutions due to the presentation of inputs of type A to the network and evolutions due to inputs of type B with the parameter

$$S_{AB}(t) = \frac{1}{M}\sum_{i,j} corr(E_{Ai}, E_{Bj}) \quad \text{(Eq. 6.16)}$$

Finally, both parameters S_A and S_{AB} only refer to a single network; to have an idea of the unsupervised learning capabilities of a generic memristor network, we must average S_A and S_{AB} over different networks, randomly generated.

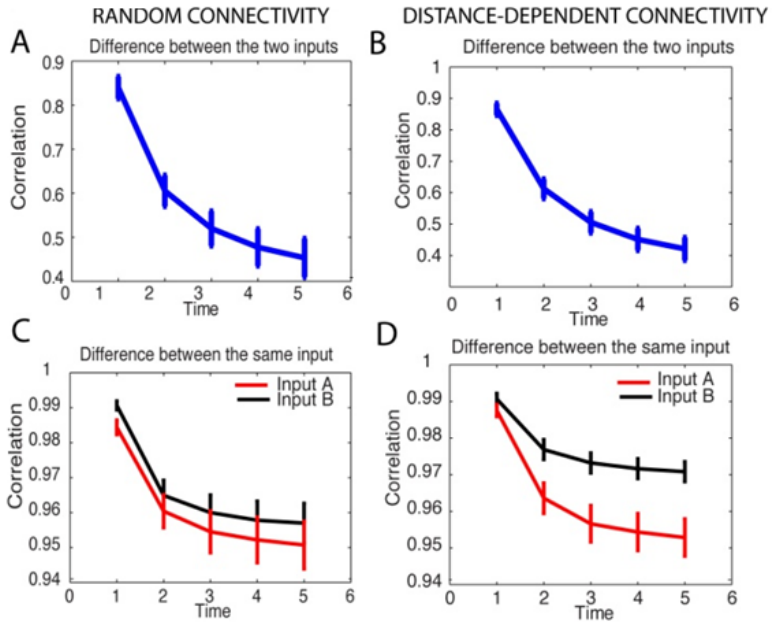

Figure 6.14: Correlation as a function of training time in two classes of networks – with random connectivity and distance-dependent connectivity. The blue lines show the average correlation coefficient between evolutions caused by different input classes (S_{AB}), the black and red lines correlation between evolutions caused by the same input class (S_A and S_B respectively)

Results of the simulations on networks with random connectivity, as well as on networks with distance-dependent connectivity, are shown respectively on the left and right side of figure 6.14. Each plot shows the average correlation value (S) of the 20 different networks as a function of time. Plots on the upper part of the figure show the average correlation between epochs with the same type of input. Black and red curves represent the results

according to the stimulation pattern used (input A: black and input B: red). The plots on the bottom show the correlation between epochs in which different inputs patterns where used (input A vs input B).

As it is shown by the curves in all plots, the monotonic and decreasing correlation values as a function of time indicate that the network epochs tend to diverge the longer we stimulate. This behavior was stable regardless of the type of input used and of the architectures simulated, and leads us to believe that the network can perform unsupervised learning at least between those two classes of inputs, as its evolution is very different in the two cases.

We also found a difference between random and distance-dependent connected networks on how fast their epochs decorrelate depending on the input used. Networks with a distance-dependent connectivity decorrelated faster when the input was positive in one node and negative in the other, compared to the case in which both inputs were positive. As observed in Figure 6.14, this is not the case for the randomly connected networks.

6.4.2 Localization of information processing elements in memristor networks

Data shown in figure 6.14 can be interpreted as an indication that, while the evolution of the memristor network caused by an input of type A Is radically different than an input of type B, different inputs of the same type have very similar effects on the network evolution. The formulas 6.15 and 6.16, however, include vectors that contain the resistances for each and every element in the network; there may be parts of the network that are more sensitive to features in the input sequences and some parts that instead evolve in the same way every time, if they evolve at all. For example, depending on the network generated and on the position of the input/output nodes, in some branches of the network there could even be no flow of current, leading to a difference in potential of around 0 between the terminals of each memristor in those branches: the net result of this situation is that all the memristor slowly become insulating, whatever the input of the network. It might be interesting, then, to look only at specific parts in the network

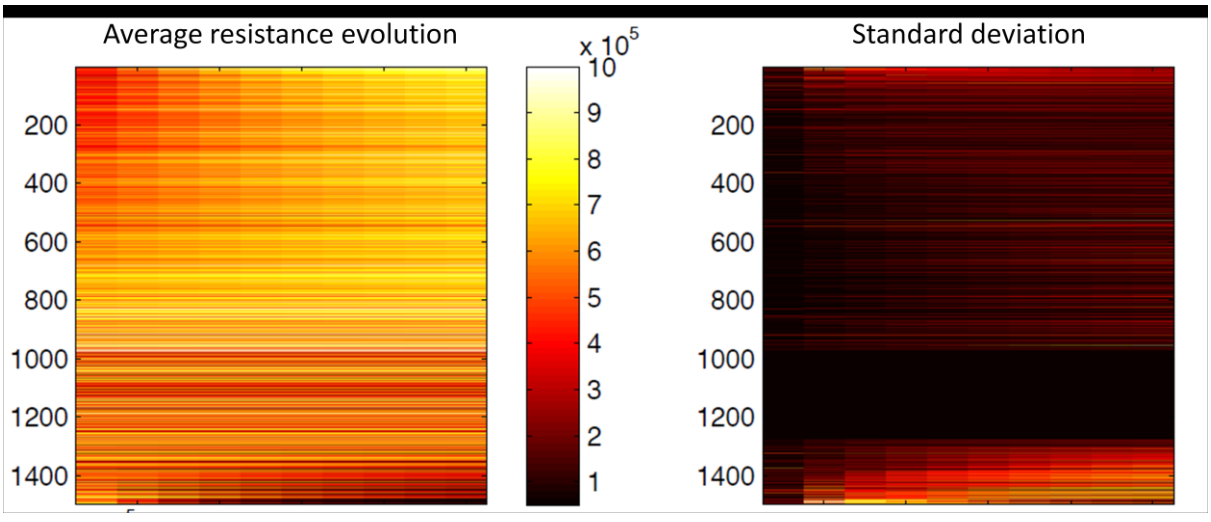

Figure 6.15: Average resistance evolution for one network, over 100 epochs of "type A" input

Figure 6.15 shows the evolution, within one epoch, of each network element, averaged over 50 epochs in which the network was presented with inputs of type A (both voltages positive). The left panel shows the evolution of the resistance of each link in the network. Each line represents one element, and the lines are ordered according to the average change of resistance, so that at the top of the graph there are the network elements that on average have much higher resistance at the end of the epochs than at the beginning, and at the bottom there are the elements that on average become more conductive during one epoch. The right panel shows the variance for the same evolution, leaving unaltered the order of the lines from the one used in the left panel.

The black band in the right panel of figure 6.15 corresponds to the 20% of resistor in the network (their resistance never changes, so the variance is always zero). We can then use this band as a reference to identify the resistors in the left panel, and this tells us that the lines above the band are the memristor that become on average more insulating and the lines below are the memristor that become more conducting.

There are two general properties of a memristor network that can be deducted from figure 6.15: one is that the memristors that become more and more insulating are much more in number that the ones that become more and more conducting. The other is that the variance in the evolution is much higher in the memristors that become more conducting than in the ones than become more insulating. In other words, while each memristor becomes more insulating more or less in the same manner, every memristor that on average becomes more conducting does so in very different ways from one epoch to the other. The conclusion that we can draw from these data is that not only a memristor network is capable of unsupervised learning, but also that the information about the input is "stored" in the memristors that become more conductive, which represent the most adaptive part of the networks.

6.4.3 Reproducing memristor network experimental results

In parallel with the simulations, research on the material science side has provided us with some methods to build a 3D memristor network. The alternatives proposed were the use of a porous structure as scaffolding for a polymer network, the use of gold nanoparticles functionalized with cavitands that can capture the endgroup of a PANI polymer, resulting in an entropy driven phase-segregated network, and the use of a PANI-PEO block copolymer. This last alternative is the most promising, as there are some preliminary experiments, as yet unpublished, that hint that a network obtained from this block copolymer shows memristive behaviour.

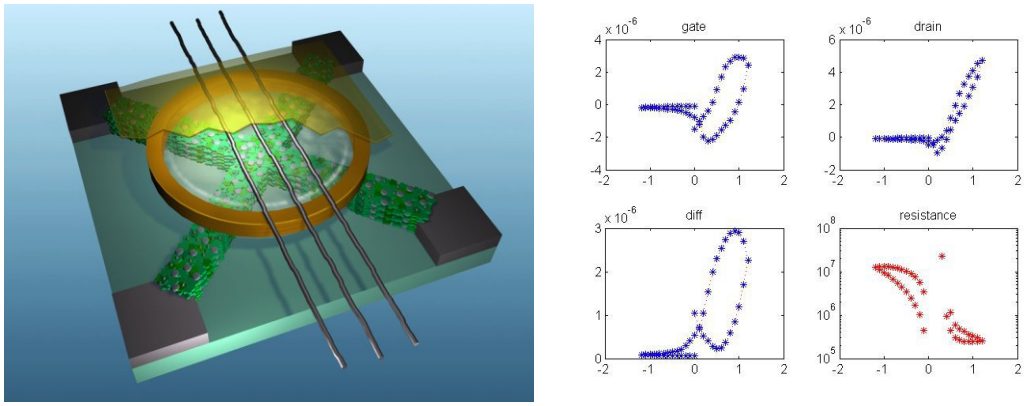

Figure 6.16: drawing of the 3D network in the experimental setup and VI characteristics for two opposite electrodes in the setup.

As shown in figure 6.16, two strips of PANI-PEO copolymer were deposited so that they contacted four electrodes at the four corners of a square glass support. The whole structure is then covered with Li-doped PEO, contained with a plastic ring, in which several silver wires are immersed. The reason for this solution is to give the same reference potential to all the memristors that are present in the network, in order to keep the experiment simple and understandable; the V-I characteristics were measured using the standard protocol described in section 4.3.1 and are reported on the right hand side of figure 6.16.

We tried to reproduce these results using our network simulations, as this would validate further the results obtained with the simulations. In order to do so, however, we had to introduce three modifications in the network description. One is that the randomly generated network does not occupy any more a cubic volume, as was the case for the networks depicted in figure 6.12 and used for the unsupervised learning simulations; instead, the volume used had one size that was 1/10 of the other two, thus making the volume used a square box, as the polymer strips depicted in figure 6.16 are a few millimetres wide but only a few micrometers thick.

The second important modification was that, in the networks used for the unsupervised learning simulations, each memristor had his gate electrode, connected to one of its two terminals, and the voltage to use in equations 6.6 and 6.7 was calculated by taking the difference between the voltage at the two terminals of the memristor, with the right polarity; as the gate electrode is now common for all the memristors and the silver wires were kept at ground potential in the experiments, the voltage used in Eq. 6.6 and Eq. 6.7 to calculate the resistance variations of each memristor was the average between the voltages at its two nodes.

Finally, in the unsupervised learning simulations the two input nodes and the two output nodes were chosen at random within the network. As the new simulations aim to reproduce the configuration of the system shown in figure 6.16, by modelling the part of the system where the two copolymer strips cross, for each network generated the closest nodes to the centre of two of the square box side walls were chosen as the input nodes, and the closest to the middle of the two opposite side walls were chosen as the output nodes.

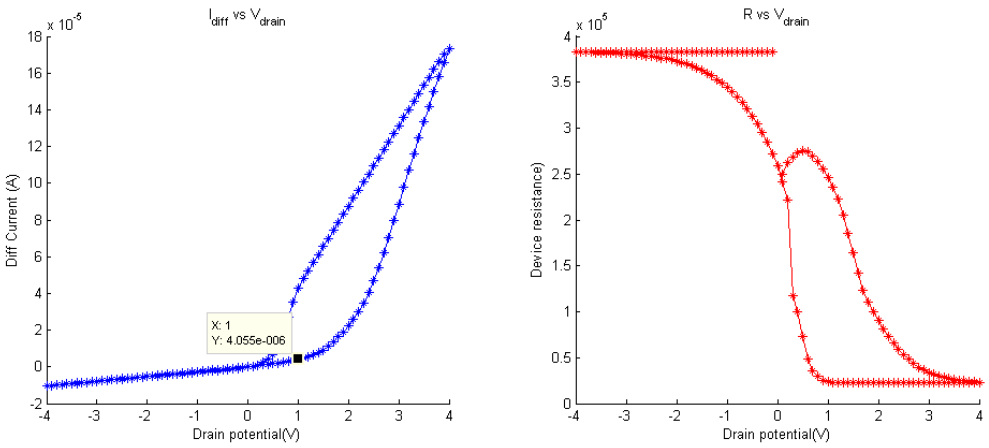

Figure 6.17: I-V characteristics for a square network of memristors, as resulting from the simulations. Left: current from one electrode to the one opposite, as a function of the potential applied to the input node. Right: equivalent resistence of the circuit

The I-V characteristics of the simulated memristor network show the same hysteretic behaviour as the experimental ones, confirming that the model used for the simulations captures the essential aspects of the structure used in the experiments. The experimental protocol used for the simulation replicates the one used in the experiment, with the difference that the voltage is ramped up to 4V and down to -4 V, instead of being between 1.2 V and –1.2 V. Also, as the model discards the gate currents, as described in section 6.1, we cannot observe the drain and gate currents, but we have direct access to the differential current, i.e. the current that flows through the polymer film without entering the PEO layer, and the equivalent resistance, so the data shown in figure 6.17 should be compared with the two bottom panels on the right hand of figure 6.16. It should also be noted that these preliminary results are an attempt to capture the qualitative behaviour of the network, without attempting to actually fit the data of the simulations; it wouldn't make sense to try and get as close an agreement as possible with the experimental data, both because the qualitative behaviour is constant in the various experiments but the numerical data change widely between one experiment and another, and because many parameters that describe the network structure in our model are still educated guesses that have not yet been confirmed by data coming from a structural analysis of the networks actually built.

Finally, an interesting issue still open for the self-assembled block copolymer memristor network, which should have a 3D physical structure, is if the resulting circuit has a 3D functionality, or it is merely a planar circuit. The first case of course would mean that the circuit has many more possible applications, while having only a planar circuit can be limiting. There is also the possibility that a circuit showing planar properties can be trained, with the proper inputs, to a circuit that shows non-planar properties.

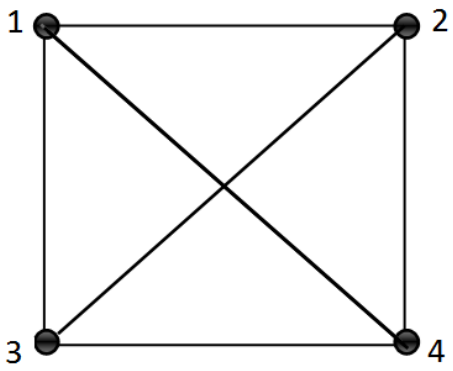

Figure 6.18 simplified layout for an equivalent circuit of the experimental one showed in figure 6.16

For a four terminal "cross" circuit like the one shown in figure 6.16, represented in a simplified form in figure 6.18, a sure sign of non-planarity would be if the conductivity between both couples of opposite terminals were greater than the conductivity between adjacent terminals; in other words, if we number the terminals 1,2,3,4 going clockwise for any terminal in the circuit, and we denote with I_{AB} the current that flows in the circuit between the terminal A and the terminal B, a circuit that satisfies the conditions

$$\begin{cases} I_{13} > I_{23} \\ I_{13} > I_{14} \\ I_{24} > I_{23} \\ I_{24} > I_{14} \end{cases} \quad \text{(Eq. 6.17)}$$

is surely non-planar. The proof of this is that if it was planar, the path linking terminal 1 with terminal 3 would need to cross the path between terminals 2 and 4 (see figure 6.18). Now if the total resistance was the same for the two paths, this would lead to the creation of equally conductive paths between 2 and 3 or between 1 and 4; if one of the paths from 1 to 3 or from 2 to 4 was instead more conductive than the other, crossing the paths would make the conductivity of the two newly created path from 2 to 3 or from 1 to 4 at a conductivity level somewhere between the one from 1 to 3 and the one from 2 to 4; in other words the conditions in eq. 6.15 are only satisfied if the path from 1 to 3 does not cross the one from 2 to 4, and this is not possible if the circuit is planar.

Any further direct path between, for example, terminals 1 and 4, not represented in figure 6.18, would only be used if their overall resistance would be lower than the one considered, leading to even higher values of I_{14}, This means that while the conditions dictated in equation 6.15 are not necessary to have a circuit with 3D paths that do not cross themselves, they surely are sufficient

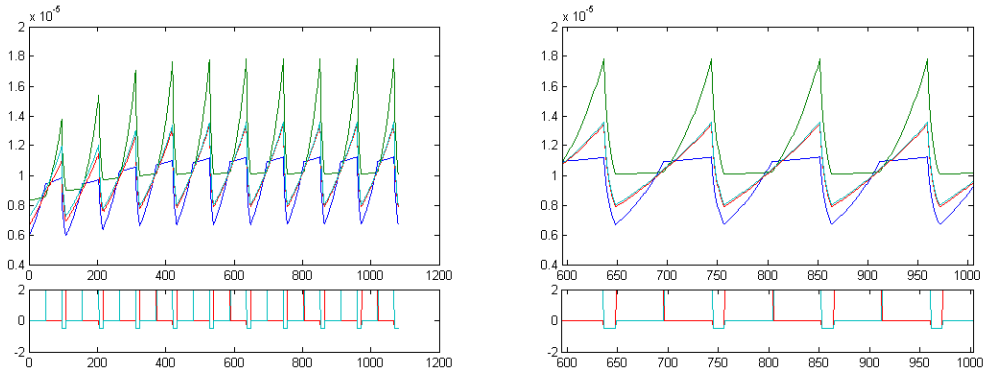

Figure 6.19: response of a simulated 4 terminal random memristor circuit to a series of voltages applied to the terminals. Left panel: view of the whole simulation. Right panel: detail of the middle part of the simulation. In the upper graph, the blue and the green line represent I_{13} and I_{24} respectively, the red and the cyan line represent I_{14} and I_{23}; in the bottom graphs, the red line represents the potential applied to terminals 1 and 3, the cyan line the potential applied to terminals 2 and 4.

In figure 6.19 we can see the effect in a simulated 4 terminal circuit of a series of training voltages that are applied at two terminals at once: the gate electrode in this experiment is always at ground level, while the terminals 1 and 3 are always at the same potential, as are the terminals 2 and 4; those potentials can be positive or negative. The currents $I_{13,}$ $I_{24,}$ I_{14} and I_{23} are measured at every instant during the training, by applying a sample potential to the first of the two terminals, keeping the other terminal at ground level and measuring the resulting current, without modifying any resistance in the circuit, like we did for the first simulation reported in section 6.2.

We can see from the figure that although at the beginning of the simulation I_{13} has the least magnitude, as the training goes on there are times, highlighted in the right panel of figure 6.19, where both the I_{13} and the I_{24} lines are above the other two lines, thus satisfying the conditions dictated by equation 6.17 and proving that the circuit simulated has indeed a non-planar functionality. Although we haven't found a protocol that can show this kind of behaviour in every circuit that we simulate or built, the correspondence between the I-V characteristics of the simulated circuit and the ones measured experimentally allows us to believe that the nonplanar characteristics can be found also in the real world, non-simulated circuits.

7. STUDIES IN COMPUTATIONAL NEUROSCIENCE

As the BION project started and the first results were reported, it became clear that there was quite a gap between how the physicists and the chemists involved in the project faced their research, and reported their results, and how the neuroscientists involved in the project approached the same problem. It became clear that the project would benefit from having a person with a background in one subject but also knowledge of the other field, to try and put together research directions that, while still facing the same problem, could look at it from different angles. To this end, I spent a year at the University of Warwick, in the Department of Computer Science, working with Professor Jianfeng Feng's group of Computational Biology.

This chapter and the next contain the results that came from that period; in fact we thought that the best way to study computational neuroscience was to tackle an open problem from the field and do research on it, rather than just studying the available literature. The studies reported here are centred on a decision-making module, localised in the visual cortex, and governed by a winner-takes-all dynamic; although it is not a topic that can be put in direct connection with BION, and therefore the research done about it can only be thought of as a side project within my PhD, these studies did give me the background needed to fully understand and contribute to the neuronal-mimicking circuit described in section 5.4 and the unsupervised learning and supervised learning simulations described in sections 6.3 and 6.4.

In this chapter the reader will find the theoretical description of the basic tools used during the studies – the computational models for single neurons and neuronal networks – as well as the theoretical part of a study on a pshycophysical law, a study which has been reinforced

by the simulations run with the models described here. The next chapter will contain the results of those simulations, as well as some simulations that include variations on the model structure that give interesting and biologically meaningful results.

7.1 Computational models for single neurons

The problem of how to model the behaviour of a single neuron has been around even before the use of computers in science; as calculation power became more and more affordable, and computational neuroscience became a subject in its own right, many models for the single neurons (as well as for the synapses connecting them) were proposed [172].

While computer neuron models strive for maximum accuracy and try to capture every meaningful aspect of the behaviour of the neurons as observed experimentally, they normally have to find a balance between how close they reproduce the features of the observed neurons, and how computationally intensive are the calculations needed to use the model; this is especially true when considering, as is the case of the work shown in this thesis, complex neuronal circuits with hundreds of interacting neurons.

It is also clear that, in nature, there is no such thing as a "standard neuron": neurons are different from one species to another and even within the same species, from one location to another in the brain. A good computational model therefore is one that, while capturing the essential aspects of the system that it is trying to reproduce, is still flexible enough to be applied to more than a single case, and can mimic different features, found in different specimen, relying on the same base mechanics.

While presenting all the possible models for the single neurons is beyond the scope of this thesis, this section will present two neuronal models, on which I worked during my studies, that are somehow at the two extremes of the possible model choices for single compartment neurons: the Hodgkin-Huxley model, which is very detailed, flexible and computationally expensive, and the Leaky Integrate and Fire model, which is the simplest neuron model possible that still is biologically meaningful [197]

7.1.1 The Hodgkin-Huxley model

The Hodgkin-Huxley model has been proposed in 1952, and it is one of the first models to capture the quantitative behaviour of a spiking neuron; it was originally developed to reproduce the membrane currents measured in the squid giant axon, but it can be used to mimic a large quantity of excitable cells [198]. It consists in a set of differential equations that describe the evolution of the membrane potential of a neuron, using a set of currents, mediated by different ions, that penetrate the membrane through one or more 'gates'

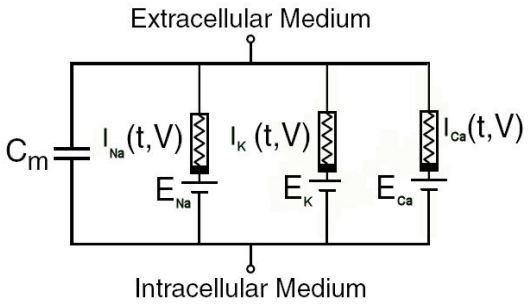

Figure 7.1: schematic representation of the Hodgkin-Huxley model

As shown in figure 7.1, in the Hodgkin-Huxley model the cellular membrane can be thought of as a capacitive layer with a number of current generators, whose effect on the membrane potential itself is mediated by variable resistors. As a side note, these variable resistors have then actually been replaced by memristors in one of Chua's works [11], where he proposed a memristor based circuit to reproduce the Hodgkin-Huxley model.

Overall, the equation that governs the voltage potential can be written as

$$C_m \frac{dV}{dt} = -\sum_n I_n \quad \text{(Eq. 7.1)}$$

$$I_n = g_n m_n^{p_n} h_n (V - V_n^{rev}) \quad \text{(Eq. 7.2)}$$

Each current $\mathrm{I_n}$ represents a current mediated by a different ion, to which is associated a different reversal potential V_n^{rev}. The effect of each single current on the membrane potential is basically to drive the membrane potential towards its reversal potential. The variables $\mathrm{m_n}$ and $\mathrm{h_n}$ are called, respectively, the activation and inactivation variables: they are limited between 0 and 1 and they model the opening and closing of the membrane channels that allow ions into and out of the neuron membrane. The exponent $\mathrm{p_n}$ of the activation variable $\mathrm{m_n}$ is always an integer, and it simulates the presence of different "gates" in the ionic channels, that must be open at the same time to allow the passage of ions. The parameter $\mathrm{g_n}$ is the maximal conductance for each current, i.e. the conductance of the cell membrane when the activation and inactivation variables are all equal to 1.

Both the activation and the inactivation variables are functions of the membrane potential and of time; an usual way to describe this dependance is to define a steady state m_∞ (but the same reasoning can be done for the inactivation variables h_n) which is only a function of the voltage, and a relaxation time τ_m, also a function of the membrane potential, with which the $m(\mathrm{t})$ value decays to m_∞, via the equations:

$$\frac{dm}{dt} = \frac{m_\infty(V) - m}{\tau_m(V)} \quad \text{(Eq. 7.3)}$$

$$\frac{dh}{dt} = \frac{h_\infty(V) - h}{\tau_h(V)} \quad \text{(Eq. 7.4)}$$

The functions $m_\infty(V)$ and $h_\infty(V)$ are usually sigmoidal functions of the membrane voltage, one of which is 0 for $\mathrm{V} \to -\infty$ and 1 for $\mathrm{V} \to +\infty$, and the other is 1 for $\mathrm{V} \to -\infty$ and 0 for $\mathrm{V} \to +\infty$, so that there is a rather small range of V values where their product is different from 0,

while the τ_m and τ_h functions are either constants or the sum of a constant term and a Gaussian term. This means that when fitting neuronal data with the Hodgkin-Huxley model, there are from 7 to 11 parameters available for each current used in the model: one maximal conductance, two parameters for $m_\infty(V)$ and two for $h_\infty(V)$, from one to three for both τ_m and τ_h (the exponents p_n are usually set using anatomical information and are not fitted).

There is, however, an alternative way to describe the opening and the closing of the ionic membrane channel. We can think of m (or h) as the fraction of activation (inactivation) gates open at any given time. The variation of m and h can be written as

$$\frac{dm}{dt} = \alpha_m(V)(1-m) - \beta_m(V)m \text{ (Eq. 7.5)}$$

$$\frac{dh}{dt} = \alpha_h(V)(1-h) - \beta_h(V)h \text{ (Eq. 7.6)}$$

where α_m is the probability of opening a closed activation channel at voltage V and β_m is the probability of closing an open activation channel at the same voltage. Comparing equation (7.5) with equations (7.3) and (7.4) yields

$$m_\infty(V) = \frac{\alpha_m(V)}{\alpha_m(V) + \beta_m(V)} \text{ (Eq. 7.7)}$$

$$\tau_m(V) = \frac{1}{\alpha_m(V) + \beta_m(V)} \text{ (Eq. 7.8)}$$

and a similar consideration can be made for h_∞ and τ_h. The steady state function m_∞ is a sigmoid, provided α and β are monotonic functions of V, one increasing and one decreasing. Considering the opening and the closing of channels as Boltzmann processes yields a functional form for α and β of the type

$$\alpha = a_0 e^{\delta\frac{V}{S}} \text{ (Eq. 7.9)}$$

$$\beta = b_0 e^{\frac{(1-\delta)V}{S}} \text{ (Eq. 7.10)}$$

with a_0 and b_0 positive, δ bounded between 0 and 1, S positive if the gates of the channel considered tends to open on hyperpolarization, negative otherwise. This formulation then substitutes, for the activation and inactivation variables of a single current in the Hodgkin-Huxley model, the three (or five) parameters needed to describe the steady state function m_∞ as a sigmoid and the relaxation time τ_m as a constant (or constant + Gaussian) with the four parameters a_0, b_0, δ and S. The advantage is in having to fit four parameters that actually relate to some physical quantities and processes in the neuron cell membrane, instead of using arbitrary function forms.

As an example, we show here data taken from a *Lymnea Stagnalis* spiking neuron in current clamp mode, that is, in a configuration where a constant current is injected into the neuron, that we fitted with a six current Hodgkin Huxley model, using the formulation where the

evolution of every activation or inactivation variable is described with the four parameters a_0, b_0, δ and S.

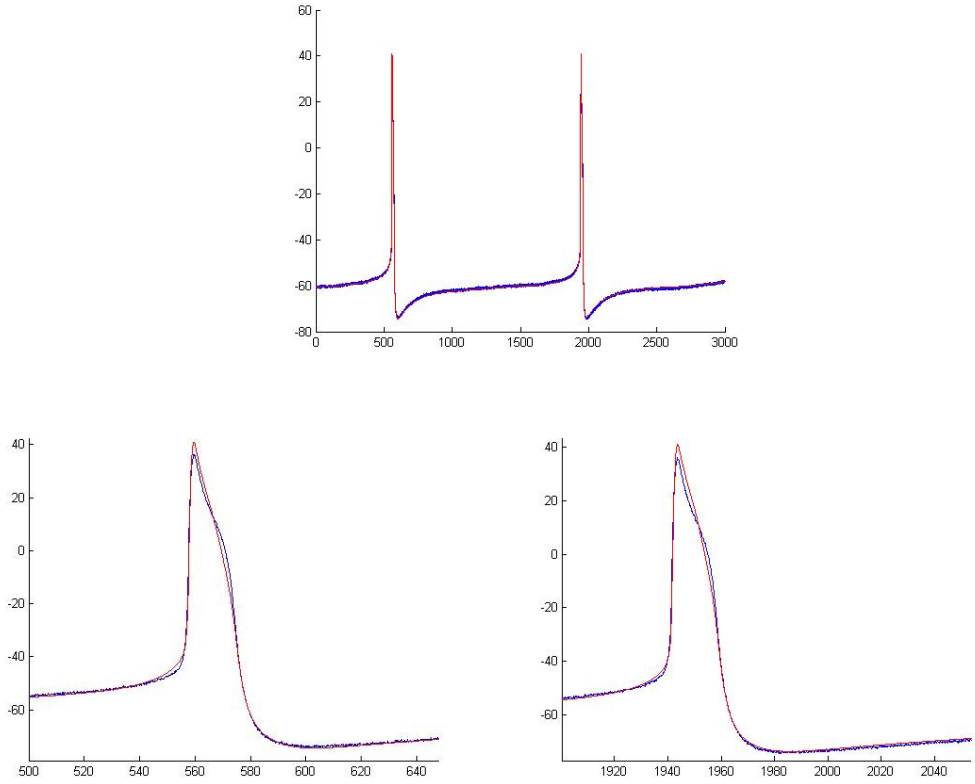

Figure 7.2: Biological trace of a spiking neuron (blue) fitted with an Hodgkin-Huxley model (red). Above: total trace, below: zoom on the two spikes

From figure 7.2 we can see the typical behaviour of a spiking neuron; the membrane potential is in the region of -60 mV, then spikes suddenly, rebounds to a lower potential, at almost -80 mV, and then ramps up constantly until the next spike; the spike width is of around 30 ms, to be compared with an inter-spike interval of 1.5 s. The red line in the figure is the fit of the data using the six current model: two potassium-mediated currents, called respectively "transient" and "persistent" (I_A and I_D), two sodium-mediated currents, again "transient" and "persistent" (I_{NaT} and I_{NaP}), and two calcium-mediate, the High Voltage Activated current (I_{HVA}) and the Low Voltage Activated current (I_{LVA}). The sodium and calcium currents are depolarizing, meaning that they drive the membrane potential towards a positive potential, while the potassium currents are hyperpolarizing, driving towards a more negative potential; their separate effect on the spiking activity can be appreciated from figure 7.3

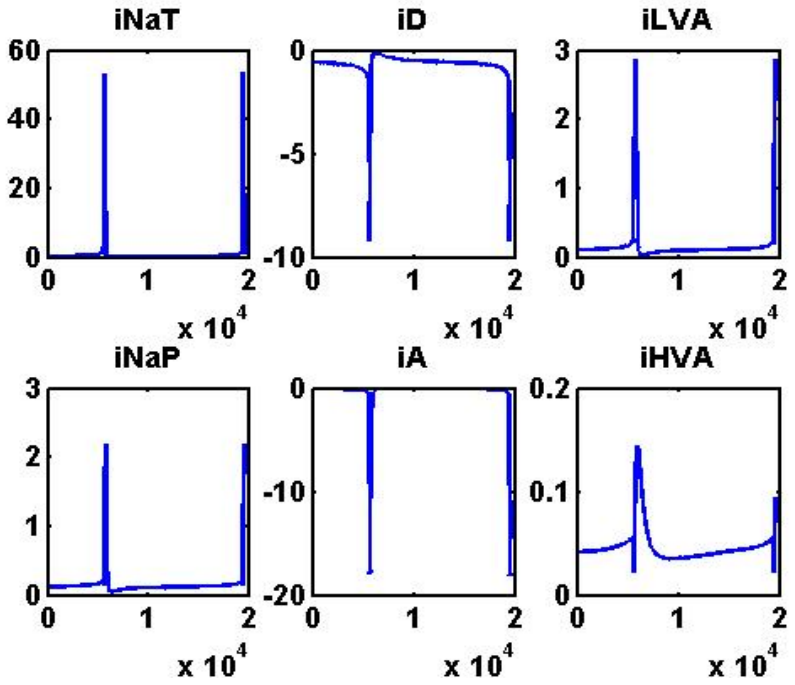

Figure 7.3: single current values as calculated from the Hodgkin-Huxley fit of the data shown in figure 7.2

As we can see, the Hodgkin-Huxley model can fit the data shown quite accurately, even during the spiking phase; this is due to the high biological fidelity of the model. However, as it requires the evolution of several sets of partial differential equation, which is computationally intensive, and as the various parameters have strong and non-intuitive effects on the whole system, this model is not well suited to simulate systems in which there is more than one neuron; for these systems, one needs a simpler model, where the temporal evolution is less computationally expensive.

7.1.2 Leaky Integrate and Fire model

Although the Hodgkin-Huxley model is capable of reproducing quite well the spike shapes, and although there are researchers that try to establish a connection between the spike shape and the information conveyed with the spike [199], usually neuroscientists consider the spiking of a neuron as a single event, and they gauge a neuron activity by looking at the spiking frequency and at the pattern of spikes that a single neuron or a group of neurons generates when exposed to certain inputs.

For this kind of investigation, the Leaky Integrate and Fire (LIF) model is the simplest possible model to use [200]. In the LIF model, the neuron is modelled with a capacitor that accumulates the charge incoming from other neurons, and slowly dissipating (leaking) some of it if it finds itself above some resting potential. The equation for the membrane voltage of a leaky integrate and fire neuron is

$$C_m \frac{dV(t)}{dt} = -g_L(V(t) - V_L) - I_{syn}(t)$$ (Eq. 7.11)

where I_{syn} is the synaptic input that the neuron receives from other neurons in the circuit. In absence of synaptic input, the membrane potential $V(t)$ slowly relaxes to V_L, with a time constant given by C_m, the membrane capacity, and g_L, the leakage conductivity; V_L is usually set to -70 mV. If there is enough synaptic input, the membrane potential starts to grow, until it reaches a firing threshold V_{th}, usually set at -50 mV. At this moment, the neuron is said to "have fired", its voltage is reset to a lower potential V_{re}, usually -55 mV, and kept there for a refractory period, of 1 or 2 ms, before being allowed to integrate the synaptic inputs again; two typical membrane potential vs time plots are shown in figure 7.4.

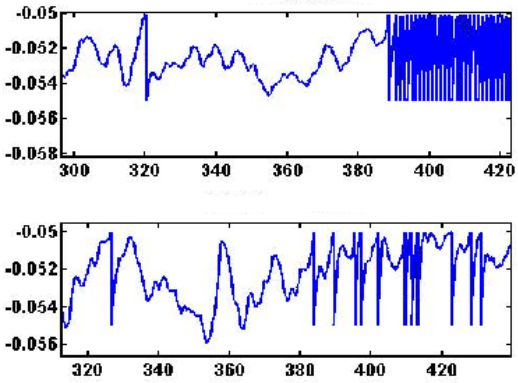

Figure 7.4: typical membrane potential traces for two different LIF neurons

When an LIF neuron "fires", it generates synaptic currents in the other neurons connected to it, mediated by synaptic weights. The shape, intensity and duration of the synaptic currents generated can be described by several equations, according to the kind of interaction between neurons that one wants to simulate. There can be excitatory connections, in which the membrane potential of other neurons is pushed towards the firing threshold, or inhibitory connections, that push the membrane potentials towards the resting membrane potential. It is usual to talk about "excitatory neurons" and "inhibitory neurons", to indicate neurons connected to the other neurons in the circuit with excitatory connections or inhibitory connections; although anatomically these two neurons are different, they are still described by the same equation 7.11, and the difference at the model level is only in the choice of parameters that describe them and in the input synaptic currents that they generate in other neurons with their spiking.

In general, the interaction between neurons is simulated with the generation and the subsequent decay of a current spike in the $I_{syn}(t)$ part of one neuron, triggered by the firing events occurring in the other neurons. One usually assumes that there are one or more neurotransmitters that mediate the excitatory or inhibitory interactions: the type of neurotransmitter dictates the shape of the input current spike and its characteristic time. For example, one can have a "fast" excitatory neurotransmitter, like AMPA (α-amino-3-hydroxyl-5-methyl-4-isoxazole-propionate), which generates inputs described by

$$I_{syn,AMPA}(t) = g_{AMPA}(V(t) - V_E)\sum_{j=1}^{N} w_j s_j^{AMPA}(t)$$ (Eq. 7.12)

$$\frac{ds_j^{AMPA}}{dt} = -\frac{s_j^{AMPA}}{\tau_{AMPA}} + \sum_k \delta(t - t_k^j)$$ (Eq. 7.13)

The variable s_j can be seen as an internal describes the amount of excitatory activity generated by the j-th neuron; every time a neuron fires its value of s is increased by one, as the sum over the firing events t_k^j indicates. The current entering in a single neuron is then given by the sum of the excitatory activity in all the N neurons, mediated by a synaptic weight w_j, a pure number that describes how strongly two neurons are connected, multiplied by a conductance g_L and by the difference between the neuron's membrane potential and the reversal potential for excitatory connection V_E, which in this case is equal to 0 mV.

There can also be "slower" excitatory neurotransmitters, like the N-Methyl-D-aspartic acid (NMDA); in this case the evolution of the state variable s_j^{NMDA} depends on another internal state variable, x_j

$$\frac{ds_j^{NMDA}(t)}{dt} = -\frac{s_j^{NMDA}}{\tau_{NMDA,rise}} + \alpha\, x_j(t)(1 - s_j^{NMDA}(t))$$ (Eq. 7.14)

$$\frac{dx_j(t)}{dt} = -\frac{x_j(t)}{\tau_{NMDA,rise}} + \sum_k \delta(t - t_k^j)$$ (Eq. 7.15)

$$I_{syn,NMDA}(t) = g_{NMDA}(V(t) - V_E)\sum_{j=1}^{N} w_j s_j^{NMDA}(t)$$ (Eq. 7.16)

x_j^{NMDA} is again increased by 1 everytime a neuron fires; the equations 7.14 and 7.15 give rise to a current input spike that has a non-negligible rise time, unlike the AMPA mediate currents, as it can be seen in figure 7.5.

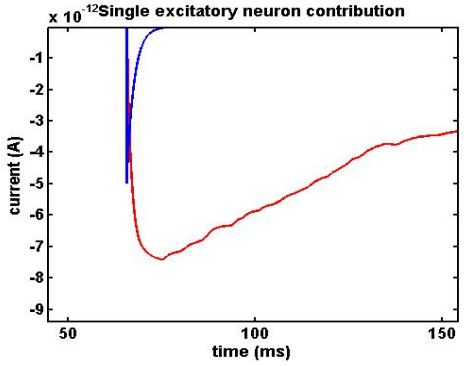

Figure 7.5: AMPA-mediated (blue) and NMDA-mediated (red) excitatory currents generated by the spiking event of a single neuron.

The excitatory inputs generated by this kind of connections are negative, and this raises the membrane potential because of the minus sign in front of the I_{syn} term in equation 7.11.The voltage dependence of the synaptic currents, described by equation 7.16, explains the "wobbly" appearance of the NMDA synaptic current in figure 7.5: the membrane potential of the receiving neuron is changing as the NMDA pulse decays, and this changes the total current generated by the neuron activity.

Models	biophysically meaningful	tonic spiking	phasic spiking	tonic bursting	phasic bursting	mixed mode	spike frequency adaptation	class 1 excitable	class 2 excitable	spike latency	subthreshold oscillations	resonator	integrator	rebound spike	rebound burst	threshold variability	bistability	DAP	accommodation	inhibition-induced spiking	inhibition-induced bursting	chaos	# of FLOPS
integrate-and-fire	-	+	-	-	-	-	-	+	-	-	-	-	+	-	-	-	-	-	-	-	-	-	5
integrate-and-fire with adapt.	-	+	-	-	-	-	+	+	-	-	-	-	+	-	-	-	-	+	-	-	-	-	10
integrate-and-fire-or-burst	-	+	+		+	-	+	+	-	-	-	-	+	+	+	-	+	+	-	-	-		13
resonate-and-fire	-	+	+	-	-	-	-	+	+	-	+	+	+	+	-	-	+	+	+	-	-	+	10
quadratic integrate-and-fire	-	+	-	-	-	-	-	+	-	+	-	-	+	-	-	+	+	-	-	-	-	-	7
Izhikevich (2003)	-	+	+	+	+	+	+	+	+	+	+	+	+	+	+	+	+	+	+	+	+	+	13
FitzHugh-Nagumo	-	+	+	-		-	-	+	-	+	+	+	-	+	-	+	+	-	+	+	-	-	72
Hindmarsh-Rose	-	+	+	+			+	+	+	+	+	+	+	+	+	+	+	+	+	+		+	120
Morris-Lecar	+	+	+	-		-	-	+	+	+	+	+	+	+		+	+	-	+	+	-	-	600
Wilson	-	+	+	+			+	+	+	+	+	+	+	+	+	+		+	+				180
Hodgkin-Huxley	+	+	+	+			+	+	+	+	+	+	+	+	+	+	+	+	+	+		+	1200

Table 7.1: Properties of different neuron computational models, taken from [171]. The # of FLOPS columns refers to the number of operations needed to describe the evolution of the neuron modelled for 1s

The table 7.1, taken from [171], shows how the LIF model and the Hodgkin-Huxley model are at the opposite ends in a spectrum of models that go from the very simple and somehow inaccurate to the very accurate and computationally prohibitive; while the Hodgkin-Huxley model can reproduce a wide range of behaviours, it takes 240 times as much mathematical operations to evolve the model for just 1 ms. Both models however share the characteristic of being widely accepted standards, and this plays a great role for the survival and the usage of the LIF neuron; although more complex and flexible models that do not require much more computational power have been developed, the LIF is a standard that allows to compare the results obtained with many others in literature.

7.2 An attractor based neuronal network

A notable example of a network that has employed successfully the LIF model to reproduce some decision making dynamics, inspired by the observations recorded in experiments with biological specimen, is the attractor based network described in this section. The network has been proposed in the late nineties by Amit and Brunel [201], then has been studied extensively by Wang [202,203] analysing its short term memory properties and the possibility of decision reversal, and has been adopted by Deco and Rolls as a basic unit that can explain some aspects of decision making mechanisms, including the effect of attention,

distractors, and on the dependence of the decision times on the "difficulty" of the experiment [204-208].

7.2.1 The task to be modelled

The network has been used as a tool to study data from the Ventral Prefrontal Cortex (VPC) in trained macaques, during a vibrotactile stimulus discrimination task [209]. The activity in this region of the brain seems correlated with both the input intensities and the final choice made by the subject of the experiment

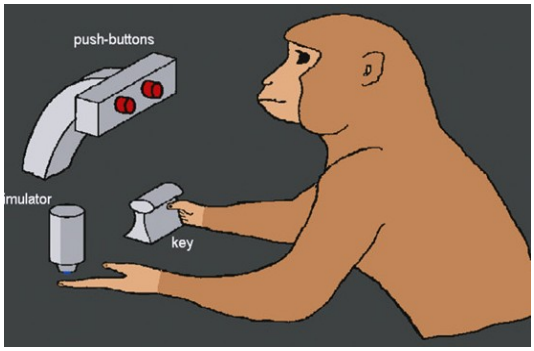

Figure 7.6: schematic representation of the experiment.

The experiment involved the discrimination between two vibrotactile inputs, sent to the monkey's index finger tip; the first input, a vibration of a stimulator with a frequency f_1 in the range 5-50 Hz (flutter range), lasted for 500 ms, and after a pause of 3 s, a second input f_2 in the same frequency range was sent to the stimulator. The monkey had to press the button corresponding to which of the stimuli it believed that had the higher frequency of vibration. This not only involves comparing the two inputs, but also storing the first one in the short term memory and then recalling it in order to compare it with the second input received.

Many neurons and neuronal circuits are involved in this task, in a sort of hierarchical chain that goes from the sensory neurons to the motory neurons. Information about the frequencies f_1 and f_2 is encoded first in the firing rate of neurons in the primary somatosensory area, called S1, without storing the information[210]; in neurons from the second somatosensory area, S2, the information is mirrored and stored for a few hundreds of milliseconds; in this area there is also the first sign of information elaboration, since towards the end of the f_2 input the neuron activity is correlated to the result of the comparison between f_1 and f_2 [211]. Neurons in the prefrontal cortex (PFC) store the information about the frequency f_1 until the second frequency arrives [212], while some comparison of the two inputs happens also in the medial premotor cortex (MPC) [213].

The network presented in this section is used as a model for the activity of some neurons in the VPC [209] , that are active only during the comparison of the inputs: some of these neurons are active when $f_1>f_2$, some when $f_1<f_2$. Overall, the activity of these neuron groups is both correlated to the sign of f_1-f_2 and to the behavioural response of the monkey;

it is believed that the competition between the two groups of neuron in the VPC is the key element in the decision making process.

7.2.2 Neuron model and network architecture

The model chosen to represent a single neuron is a typical LIF neuron, where each neuron receives both excitatory (driving towards 0 mV) and inhibitory (driving towards -70 mV) synaptic inputs from all the other neurons. There are both excitatory and inhibitory neurons in the network: excitatory neurons generate fast AMPA-mediated currents and slower NMDA-mediated currents, while inhibitory neurons generate GABA (γ-Aminobutyric acid)-mediated currents. The total synaptic input to a single neuron is the sum of these currents:

$$I_{syn} = I_{GABA} + I_{AMPA} + I_{NMDA} + I_{AMPA,ext} \text{ (Eq. 7.17)}$$

where $I_{AMPA,ext}$ is the current due to external inputs to the network, again AMPA-mediated, described in more detail below.
The GABA- and AMPA-mediated currents follow first-order kinetics, described by

$$I_{AMPA}(t) = g_{AMPA}(V(t) - V_E)\sum_{j=1}^{N_E} w_j s_j^{AMPA}(t) \text{ (Eq. 7.18)}$$
$$I_{GABA}(t) = g_{GABA}(V(t) - V_I)\sum_{i=1}^{N_I} w_i s_i^{GABA}(t) \text{ (Eq. 7.19)}$$
$$\frac{ds_j^{AMPA}}{dt} = -\frac{s_j^{AMPA}}{\tau_{AMPA}} + \sum_k \delta(t - t_k^j) \text{ (Eq. 7.20)}$$
$$\frac{ds_i^{GABA}}{dt} = -\frac{s_i^{GABA}}{\tau_{GABA}} + \sum_k \delta(t - t_k^i) \text{ (Eq. 7.21)}$$

where g_{AMPA} and g_{GABA} are the synaptic conductances, s is the fraction of open channels, V_I and V_E are the reversal potentials for GABA and AMPA currents, w_j are the synaptic weights, N_I and N_E are the numbers of inhibitory and excitatory neurons, and t_k^j is the time when the *j*-th neuron emits its *k*-th spike. In other words, GABA and AMPA-mediated spikes have negligible rise times and an exponential decay. Equations for the NMDA currents are slightly different, to account for the voltage-dependent magnesium block and the non-negligible rise time:

$$I_{NMDA}(t) = g_{NMDA}\frac{V(t) - V_E}{1 + \frac{e^{-\beta V(t)}}{\gamma}}\sum_{j=1}^{N_E} w_j s_j^{NMDA} \text{ (Eq. 7.22)}$$
$$\frac{ds_j^{NMDA}(t)}{dt} = -\frac{s_j^{NMDA}}{\tau_{NMDA,decay}} + \alpha\, x_j(t)(1 - s_j^{NMDA}(t)) \text{ (Eq. 7.23)}$$
$$\frac{dx_j(t)}{dt} = -\frac{x_j(t)}{\tau_{NMDA,rise}} + \sum_k \delta(t - t_k^j) \text{ (Eq. 7.24)}$$

where α, β and γ are numerical parameters; α regulates the steepness of the NMDA spike rise, while β and γ describe the magnesium block, which according to the voltage can limit the transmission of NMDA-mediated pulses.
Every neuron receives inputs in the form of excitatory AMPA current spikes, following a Poisson distribution, from N_{ext} independent external synaptic connections; this “background

noise" represents the result of the normal brain activity in regions not directly connected with the decision-making task. In the absence of any input, the frequency is 3 Hz for every external synapse for all the neurons in the network, which is a typical spontaneous firing rate value observed in the cerebral cortex; for a typical value of $N_{ext} = 800$, this adds up to an input spike frequency of 2.4 kHz for each neuron. The equations that describe the external current input, for each neuron, are

$$I_{AMPA,ext}(t) = g_{AMPA,ext}(V(t) - V_E)\sum_{j=1}^{N_{ext}} s_j^{AMPA,ext}(t) \text{ (Eq. 7.25)}$$

$$\frac{ds_j^{AMPA,ext}}{dt} = -\frac{s_j^{AMPA,ext}}{\tau_{AMPA}} + \sum_k \delta(t - t_k^j) \text{ (Eq. 7.26)}$$

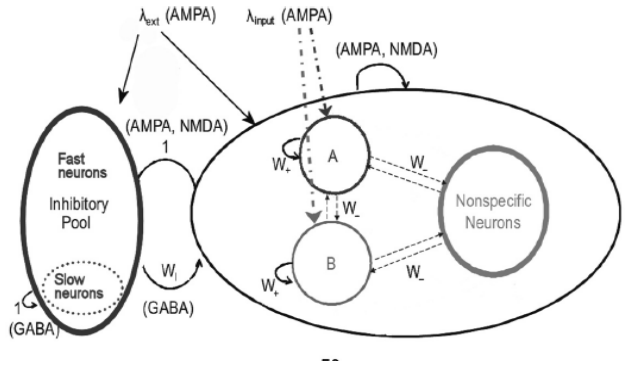

Figure 7.7: diagram of the network. A and B represent the specific excitatory pool neurons, the arrows synaptic connections, along with the synaptic weights and the neurotransmitters that mediate the connections.

The network is composed of 1000 neurons, 800 of which are excitatory and 200 are inhibitory (Figure 7.7). Two pools of 80 neurons each, taken from the 800 excitatory neurons, are taken to be the specialized A and B pools, which receive additional inputs, in the form of an augmented frequency of the Poisson input spike train in equation 7.25, supposed proportional to the intensity of each input; the remaining 640 excitatory neurons form the non-specialized pool. Neurons from the inhibition pool are physically different neurons, and are therefore modelled with a different set of parameters for the conductances and the membrane capacitances; excitatory neurons form all the pools share the same parameters, and are differentiated by the synaptic weights between them and by the kind of input that they receive.

All neurons	Excitatory neurons	Network parameters
$V_L = -70$ mV	$C_m = 0.5$ nF	$w_+ = 2.2$
$V_{th} = -50$ mV	$g_m = 25$ nS	$w_- = 0.8444$
$V_{re} = -55$ mV	$g_{AMPA,ext} = 2.08$ nS	$w_i = 1.015$
$V_E = 0$ mV	$g_{AMPA} = 0.104$ nS	$w_{medium} = 1$
$V_I = -70$ mV	$g_{NMDA} = 0.327$ nS	$N_{ext} = 800$
$\tau_{re} = 2$ ms	$g_{GABA} = 1.287$ nS	
$\tau_{AMPA} = 2$ ms	Inhibitory neurons	
$\tau_{NMDA,rise} = 2$ ms	$C_m = 0.2$ nF	
$\tau_{NMDA,decay} = 100$ ms	$g_m = 20$ nS	
$\tau_{GABA} = 10$ ms	$g_{AMPA,ext} = 1.62$ nS	
$\alpha = 0.5$ ms^{-1}	$g_{AMPA} = 0.081$ nS	
$\beta = 6.2 \cdot 10^{-5}$ V^{-1}	$g_{NMDA} = 0.0.258$ nS	
$\gamma = 3.57$	$g_{GABA} = 1.002$ nS	

Table 7.2: Parameters used for the neurons in the network model

The synaptic weights between neurons are written as if they were the result of some form of Hebbian learning: there are four different weights w_{ij} in the network, as shown in figure 7.7. The "medium" weight is the one that mediates the excitatory effect of all the excitatory neurons on the inhibitory neurons, as well as the effect of the non-specialized excitatory neurons on other non-specialized neurons. The "inhibitory" weights mediate the effect of the inhibitory neurons on all the excitatory neurons. Finally, there are the "strong" and the "weak" synaptic weight; the first mediates the effect of one neuron in a specialized pool onto another neuron in the same pool, while the second mediates the effect of an excitatory neuron in a pool on neurons in different pools. In other words, neurons in the same pool excite one another, when firing, much more than they excite the neurons in other pools.

The two specialized pools are the one that receive the information about the two inputs to be compared. This information is encoded in an increase of the frequency of the external input described by equation 7.25, that follow a Poisson distribution, for all the neurons in the pool, of the order of a few percentage points – typically, the input frequency for one specialized neuron goes from 3 Hz to 3.04 Hz. The increase is assumed to be proportional to the intensities, or anyway to the meaningful attributes, of the inputs to be compared by the circuit, f_1 and f_2 in the case described in section 7.2.1; in other word the neuronal circuit

modelled here is not responsible of encoding the external stimuli, but rather assumes that a sensory module has already encoded those informations in a spike train frequency.

Each specialized pool receives therefore inputs correlated to only one of the two inputs to be compared; the comparison happens because the increased activity in one or both pools pushes the network from a spontaneous state, in which all the excitatory neurons fire with a frequency of about 3 Hz, to one of two possible decision states, where one of the specialized pools fires with high frequency (around 40 Hz) and the other is silent. The pool that ends up in the high activity state is the winner of the competitions and represents the decision taken by the network; its high activity is self-sustained by the strong synaptic connections within the pool, and causes an increase in the excitatory currents in the inhibition neurons that in turn increase the overall inhibition level in the network, shutting off completely the losing specialized pool. As the transition is driven by the statistics in the input spike trains to the specialized pool, it is not always guaranteed that the winning pool is the one with the higher input signal, especially if the two inputs are very similar; in the limit case where the two inputs are equal, the network will choose at random, with equal probability, which one of the two pools will be the winner.

Such a transition from one state to the other is only possible because the parameters reported in table 7.2 are finely tuned in order to make it possible to have two stable decision states (and the spontaneous state to become unstable) when the additional inputs to the specialized pools are added; the next section will show the calculations needed to describe the system states.

7.2.3 A mean field analysis of the network

Many interesting features of the proposed network, like the reaction time and the effect of attention on the network [205,206], are contained in the transitions from one state to another; therefore a mean field approximation, which assumes that the network is in its steady state, will not capture them, and we need to run a numerical simulation of the network to observe the transient effects. The mean field analysis, however, is needed to tune the synaptic weights, which are the non-biological quantities in our system, in order to let the network have some stable decision state to occupy when the inputs are presented to the specific pools.

The following mean field analysis is mainly after [203], and needs several approximations in order to make the calculations viable. Let us consider first the case of the spontaneous state, where all the excitatory neuron pools have the same firing rate. The first approximation needed, called the diffusion approximation [200], assumes that at the steady state the activity of each pool can be described with a mean DC component and a fluctuation term. Considering equations 7.18, 7.19, 7.222 and 7.25, under this approximation we can write, for the average activity of each synaptic current component,

$$S_{AMPA,ext}(t) = \sum_{j=1}^{N_{ext}} s_j^{AMPA,ext}(t) = N_{ext}\tau_{AMPA}\nu_{ext} + \Delta S_{AMPA,ext}(t)$$ (Eq. 7.27)

$$S_{AMPA}(t) = \sum_{j=1}^{N_E} w_j s_j^{AMPA}(t) = N_E\tau_{AMPA}\nu_E + \Delta S_{AMPA}(t)$$ (Eq. 7.28)

$$S_{NMDA}(t) = \sum_{j=1}^{N_E} w_j s_j^{NMDA}(t) = N_E\psi(\nu_E) + \Delta S_{NMDA}(t)$$ (Eq. 7.29)

$$S_{GABA}(t) = \sum_{j=1}^{N_I} w_j s_j^{GABA}(t) = N_I\tau_{GABA}\nu_I + \Delta S_{GABA}(t)$$ (Eq. 7.30)

or, in other words, the mean synaptic activity *S(t)* for each neurotransmitter is a function of the mean firing frequency of the relative neurons ν, which is the constant component, to which we add a fluctuation term ΔS. While the terms relative to the AMPA and GABA neurotransmitters are linear in ν, the non negligible rise time and the presence of a magnesium block require a dedicated function of the firing frequency $\psi(\nu_E)$ for the NMDA component. The subscripts E, I, and ext refer to the activity of the excitatory neurons, the inhibitory neurons and the external synapses.

When looking at the time constants of the various interactions, reported in table 7.2, we can see that the decay time of AMPA mediated currents is much shorter than the one of GABA and NMDA currents; furthermore, the AMPA current itself is dominated by the input coming from the external synapses $S_{AMPA,ext}$, as there are 800 such synapses for each excitatory and inhibitory neuron. Therefore we can approximate the fluctuation terms in equations 7.28-7.30 and neglect all but the dominant one, the one in equation 7.27, which can be rewritten as a Gaussian process with zero mean and correlation $\langle \Delta S_{AMPA,ext}(t)\Delta S_{AMPA,ext}(t')\rangle = N_{ext}\nu_{ext}\tau_{AMPA}\exp\left(-\frac{|t-t'|}{\tau_{AMPA}}\right)$.

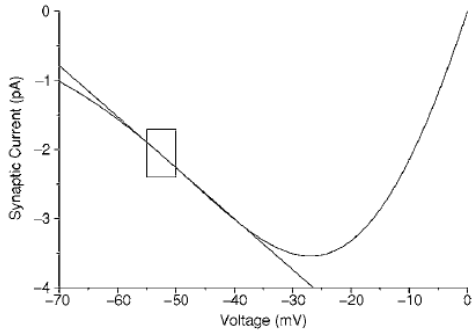

Figure 7.8: Exact and linearized current-voltage curve for the NMDA mediated synaptic currents, from [203]

Brunel and Wang [203] have also showed that it is possible to calculate the exact value for the function ψ(ν) in equation 7.29, assuming that the input spike train follow a Poisson statistic; this is true for the spontaneous state, although the approximation could be less solid for the winning pool in the decision state. Another important approximation is the linearization of the NMDA current-voltage curved, which, as figure 7.8 shows, is a good approximation when the neuron's average potential is between -50 mV and -55 mV, which is the region delimited by the firing threshold V_{th} and the reset voltage V_{re}, where the membrane potential of all the neurons should be, if they are supposed to fire with a

frequency of around 3 Hz or more. By using these approximations, one can finally write for the excitatory neurons, with an analogous reasoning for the inhibitory neurons, the mean field approximation of the evolution equation of the system

$$\tau_E \frac{dV(t)}{dt} = -(V(t) - V_L) + \mu_E + \sigma_E \sqrt{\tau_E}\eta(t) \text{ (Eq. 7.31)}$$

Which describes the evolution of the system by a constant term

$$\mu_E = \frac{\left(T_{E,ext}\nu_{ext} + T_{E,AMPA}\nu_E + \rho_1\psi(\nu_E)\right)(V_E - V_L) + \rho_2\psi(\nu_E)(\langle V\rangle - V_L) + T_{EI}\nu_I(V_I - V_L)}{S_E} \text{ (Eq. 7.32),}$$

$$S_E = 1 + T_{E,ext}\nu_{ext} + T_{(E,AMPA)\nu_E} + (\rho_1 + \rho_2)\psi(\nu_E) + T_{EI}\nu_I \text{ (Eq. 7.33)}$$

And a fluctuating term, where

$$\sigma_E^2 = \frac{g_{AMPA,ext}^2(\langle V\rangle - V_E)^2 C_{ext}\nu_{ext}\tau_{AMPA}^2\tau_E}{g_m^2\tau_m^2} \text{ (Eq. 7.34),}$$

$$\langle\eta(t)\rangle = 0 \text{ (Eq. 7.35),}$$

$$\langle\eta(t)\eta(t')\rangle = \frac{1}{\tau_{AMPA}}\exp\left(-\frac{|t-t'|}{\tau_{AMPA}}\right) \text{ (Eq. 7.36)}$$

While the details can be found in the Brunel an Wang paper [203], we remark here that the DC term $\mu_E$is basically the weighted sum of three contributions, one excitatory that depends on the potential of the excitatory neurons, one excitatory that depends on the average voltage across all neurons, and one inhibitory that depends on the voltage of the inhibitory neurons. The terms ρ_1 and ρ_2 depend on the average voltage, as the function $\psi(\nu)$, and come from the contribution of the NMDA currents; the terms T_X are constant terms that wrap up the contribution of different parameters, like the number of neurons in each pool, the conductance parameters and the relaxation times for every synaptic current.

From an equation like the 7.31, Brunel and Sergi have shown [214] that it is possible to derive the firing frequency of the excitatory neurons ν_E, and analogously for ν_I, which is given by

$$\nu_E = \phi(\mu_E, \sigma_E) \text{(Eq. 7.37)}$$

$$\phi(\mu_E, \sigma_E) = \left(\tau_{rp} + \tau_E \int_{\beta(\mu_E,\sigma_E)}^{\alpha(\mu_E,\sigma_E)} \sqrt{\pi}\exp(u^2)\,[1 + \mathrm{erf}(u)]du\right)^{-1} \text{ (Eq. 7.38)}$$

$$\alpha(\mu_E, \sigma_E) = \frac{V_{th} - V_L - \mu_E}{\sigma_E}\left(1 + \frac{0.5\,\tau_{AMPA}}{\tau_E}\right) + 1.03\sqrt{\frac{\tau_{AMPA}}{\tau_E}} - 0.5\frac{\tau_{AMPA}}{\tau_E} \text{ (Eq. 7.39)}$$

$$\beta(\mu_E, \sigma_E) = \frac{V_{re} - V_L - \mu_E}{\sigma_E} \text{ (Eq. 7.40)}$$

in the limit of $\tau_{AMPA} \ll \tau_E$, where τ_E can be tought of as the typical time constant of the system and is defined as $\tau_E = \frac{C_m}{g_m S_E}$, i.e. is a function of the membrane capacitance, the leakage conductivity and the overall synaptic activity. The average potential $\langle V\rangle$ can also be calculated [215]:

$$\langle V \rangle = \mu_E - (V_{th} - V_{re})\nu_E\tau_E \text{ (Eq. 7.41)}$$

In the case when the system reaches a decision state, we will have one equation like 7.37 for each pool in the system; every pool will have its mean activity μ and its fluctuation term σ. The firing frequencies of each pool will then be determined by a system of nonlinear equations for the inhibitory (I) pool, the two specific pools (A and B) and the nonspecific pool (N)

$$\begin{cases} \nu_I = \phi(\mu_I, \sigma_I) \\ \nu_A = \phi(\mu_A, \sigma_A) \\ \nu_B = \phi(\mu_B, \sigma_B) \\ \nu_N = \phi(\mu_N, \sigma_N) \end{cases} \text{ (Eq. 7.42)}$$

Every equation in 7.42 depends on the other three equations through the mean activities μ and the fluctuations σ of all the pools. To solve the system and find the self reproducing stationary frequencies, one can follow the pseudodynamics of the system, by integrating the equations

$$\tau_x \frac{d\nu_x}{dt} = -\nu_x + \phi(\mu_x, \sigma_x), x = I, A, B, N \text{ (Eq. 7.43)}$$

The system in 7.43 has a steady state solution that matches the one for 7.42, but the integration of 7.43 is much simpler. To find the frequencies for the spontaneous steady state, one can do the integration with low values of the firing frequencies ν_x as initial conditions, while to find the frequencies for the decision state one can start from a set of initial conditions where either ν_A or ν_B have a very high value, and let the system evolve from there.

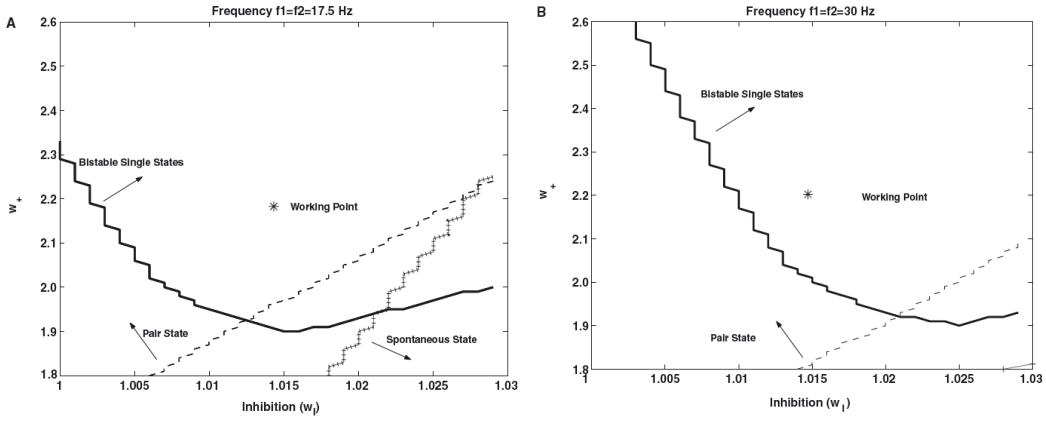

Figure 7.9: stability of the decision state as a function of the "strong" weight w_+ and the "inhibition" weight w_I, for two different values of the experimental vibrotactile frequencies f_1 and f_2 [208]

The biological parameters in the model, which in this analysis are hidden in the T_x terms of equation 7.33, are regulated so that in the spontaneous state the system satisfies certain conditions drawn from observations in the biological samples [203]; the synaptic strengths w_{ji}, which appear as well in the T_x terms, are tuned so that the final decision state is stable [208]. As it is apparent from figure 7.9, the choice for the synaptic weights is not univocal; rather, there are different regions in the space described by the synaptic strengths where

the network has stable decision (single) states, or pair states, in which both specific neuron pools fire with a high frequency. These regions change as the input frequency to the specific pools changes; the synaptic weights, which describe the working point of the system, are chosen so that the spontaneous state is stable when no additional input is present, the single states are stable for a possible range of inputs that matches the vibrotactile stimulus range (5-50 Hz) as encoded in the extra input to the specific pools, and the non-decision state where both specialized pools have a high firing rate is avoided.

7.3 A neuronal level formulation of Weber's law

Weber's law is a psychophysical law that relates the perception of a stimulus with its intensity, alone and when compared to other stimuli; it is also called Weber-Fechner's law [216]. It states that when comparing two stimuli, the Just Noticeable Difference (JND), which is the minimum difference in the stimuli intensities that an observer needs to tell them apart, is proportional to the intensities of those stimuli; or, in other words, that the ratio between the just noticeable difference in the stimuli intensities $\Delta \mathrm{I}$ and the intensity of the reference stimulus I is a constant, the Weber's constant k.

This phenomenon has been observed in a wide range of moderately intense stimuli experiments in sensory perception in terms of weights [216], vibrotactile intensity [217], light intensities [218], sizes [219], texture roughness [220], numbers [221], etc. However, Weber's law has, until now, only described the relations between stimuli and behaviour; a complete formulation of how Weber's law is enforced at the neuron network level is still missing. During my stay in Warwick, some steps in that direction were made by local scientists [6]; the network described in section 7.2 was used as a tool to confirm the theoretical findings, as it will be shown in the next chapter

The work consisted in considering, from a theoretical point of view, systems of increasing complexity, from single neurons, to independent neuron populations, to the final and more realistic case of a population of many neurons with correlated activity; for these systems, adherence to Weber's law implies some conditions on the mean rate and standard deviation of the neuron activity.

The activity of a neural system can be described by the distribution of the inter-spike intervals, ISIs: the coefficient of variation of this distribution, that is, the ratio between the variance and the mean in the ISI distribution, can be used to describe the variability of the spiking process of the system. A system that fires spikes with a Poisson distribution, for example, has a $\mathrm{CV}_{\mathrm{ISI}}$ equal to 1. From the theoretical studies performed, it turns out than when considering large number of neurons and biologically plausible values for the Weber constant k and the mean network activity μ, a network needs to have a $\mathrm{CV}_{\mathrm{ISI}}$ equal or less than one in order to follow Weber's law.

For a single neuron in which the firing rate is a linear function of the input intensities, and considering in order to distinguish two set of activities the amounts of the two firing rate

distributions that do not overlap, calculations show that the standard deviation σ and the mean μ in the spiking rates of the single neuron are linked by Weber's law with the relation

$$\sigma(\mu) = \frac{k}{C(k+2)}\mu + \mu^{-\frac{2}{k}}c_0 \text{ (Eq. 7.44)}$$

Where c_0 is a constant term, k is the Weber constant and C is a factor depending on the misclassification ϵ, given by

$$C = \sqrt{\frac{\pi}{2}\ln\left(\frac{1}{1+(\epsilon+1)^2}\right)} \text{ (Eq. 7.45)}$$

This means that if the difference between two inputs ΔI that is needed to generate activities that can be discriminated with an error rate ϵ is proportional to the reference input intensity I by the constant k, i.e., if the neuron activity satisfies Weber's law, then the neuron activity is described by equation 7.44. The factor C depends only on the misclassification rate ϵ, which is set to 0.15 in the calculations reported, for a value of C of about 1.4; the normal range for the Weber constant k is between 0.05 and 0.3. For this reason, the second term $\mu^{-\frac{2}{k}}c_0$ can be neglected (as k is much smaller than 1, and the mean discharge rate μ is fixed between 1–200 spikes/s), so the standard deviation σ and the mean μ of the discharge rate have a linear relation. We can rewrite 7.44 in terms of the CV_{ISI},

$$CV_{ISI} = \frac{\sigma^2}{\mu} = \frac{k}{C(k+2)}\sqrt{\mu} \text{ (Eq. 7.46)}$$

and, using the values of C and k provided, we can write the region of the CV_{ISI} in which we expect the output of the neuron to satisfy Weber's law

$$\frac{\sqrt{\mu}}{100} < CV_{ISI} < \frac{\sqrt{\mu}}{10} \text{ (Eq. 7.47)}$$

Where the two limits are given by the possible values of Weber's constant k.

While single neurons in the visual cortex can encode near-threshold stimuli with a fidelity that approximates the psychophysical fidelity of the entire organism [222,223], it is widely accepted that subjective intensity is based on the response of population neurons, rather than a single neuron [224]. We can modify equation 7.47 to account for the superposition of the neuronal activities of N neurons with identical distribution of firing rates; if the activities are independent, the mean discharge rate μ after superposition is still the same as single neurons, but the variance of the instantaneous spike count becomes $\frac{\sigma^2}{N}$, where N is the population size; eq.7.47 is easily modified into

$$\frac{\sqrt{\mu N}}{100} < CV_{ISI} < \frac{\sqrt{\mu N}}{10} \text{ (Eq. 7.48)}$$

which however has some limitations: for a high number of neurons, N~ 1000, the equation 7.48 requires a CV_{ISI} greater than 4 for the normal firing rates of a neuron, which is

biologically unrealistic: from the experimental observations on cortical neuronal discharge variability, the $\mathrm{CV_{ISI}}$ should be not far from the unity.

This situation is corrected if we imagine each pair of neuron in the network to have activities with the same pairwise correlation ρ; after all, cortical cells do not generate spikes independently but, rather, the spiking activity is correlated, spatially and temporally [225]. Correlation arises from shared excitatory and inhibitory inputs [226], either from other stimulus-driven neurons or from ongoing activities [227].

Including the correlation ρ in the calculations, eq 7.48 reads

$$\frac{\sqrt{\mu N \frac{1}{1+(N-1)\rho}}}{100} < CV_{ISI} < \frac{\sqrt{\mu N \frac{1}{1+(N-1)\rho}}}{10} \quad \text{(Eq. 7.48)}$$

For biological firing rates (40-100 Hz) and correlation coefficients (around 0.1), in the limit for large networks this translates in $CV_{ISI} \in [0.45, 1]$, which is the main result presented in [6] .

The activity of a network where the neurons communicate between each other follows Weber's law, therefore, only if it is as regular as, or more regular than, a Poisson process. These calculations can be made also for neurons in which the output activity is not a linear function of the input intensities, but follows a sigmoid transfer function, as it commonly happens in most biophysical and psychophysical experiments; it is still possible to calculate the conditions on the $\mathrm{CV_{ISI}}$, and in particular the upper limit $\mathrm{CV_{ISI}} \leq 1$ still holds, even if the calculations are a bit unwieldy; they are reported in the appendix of [6]. As we will see in the next chapter, these findings have been confirmed by the simulations that have been run using the model described in section 7.2

8. STUDIES IN COMPUTATIONAL NEUROSCIENCE: SIMULATION RESULTS

This chapter describes the results of several sets of computer simulations, that implemented in the MATLAB environment the model described in section 7.2; all the code used was rewritten from scratch, based on the description of the network found in [205]. After a testing stage in which we checked some basic result of our network against the properties reported in [208], we proceeded to use the model to support the theoretical findings on the Weber's law, detailed in section 7.3; we changed the statistics of the input spike trains, affecting in this way the $\mathrm{CV}_{\mathrm{ISI}}$ of the winning pool in the network, and showed that the network follows Weber's law only when the winning pool has $\mathrm{CV}_{\mathrm{ISI}} < 1$.

We then introduced some modifications in the network, inspired by biological considerations, to explore the link between the theta oscillations in a neuronal network and the reaction times of the system. In biology theta activity has been associated with an increased awareness state of the specimen examined, that leads to faster reaction times; it was also shown that the presence of fast and slow inhibition spikes can enhance theta activity. We introduced a population of slow neurons in the network, and found that the reaction times do get faster as a consequence of this modification, and the theta activity is more pronounced; however, the resulting decision states are less stable and the decision can be reverted once the input cues are taken away.

8.1 Weber's law in an attractor based model

The attractor based network described in section 7.2 is said to have reached a correct decision when the high-rate firing pool is the one with the highest input frequency, otherwise the decision is considered "wrong". The ratio of wrong to right decisions depends on the difference between the inputs, as translated into the augmented frequency of the spike inputs to each specialized pool; Deco and Rolls have shown [208] that for a certain input range the network follows Weber's law, in the sense that the difference between input frequencies required to achieve, over many trials, a certain success rate is proportional to the amplitude of one of the two input frequencies.

We recreated the model and measured the value of CV_{ISI} for each pool, while at the same time verifying that Weber's law holds for our implementation of the model. In order to do this, we considered the input to one of the specialized pools to be the reference input; for each reference input frequency I, chosen in a range that allowed the network not to be saturated by the inputs, we varied the input frequency to the other specialized pool between 30% and 100% of the reference input frequency (thus, ΔI varied between 0 and $0.7 \cdot I$); for each pair of input frequencies we ran 200 simulations and recorded the success rate achieved for each pair.

This allowed us to build, for each reference value I, a curve of the success rate versus ΔI, and by fitting the curve to find for each value of I the ΔI value needed to achieve a certain success rate, by fitting the success rate curves with a Weibull function [208]. Figure 8.1 plots, for different success rates, the relationship between the values of ΔI and I; we confirmed that the network follows Weber's law for a wide range of possible misclassification ratios, including the one (15%) used in the theoretical calculations shown in section 7.3. The value of the Weber constant *k* seems also biologically plausible, as it is comprised in a range 0.24-0.32, fully compatible with the range 0.05-0.3 found in nature [217] .

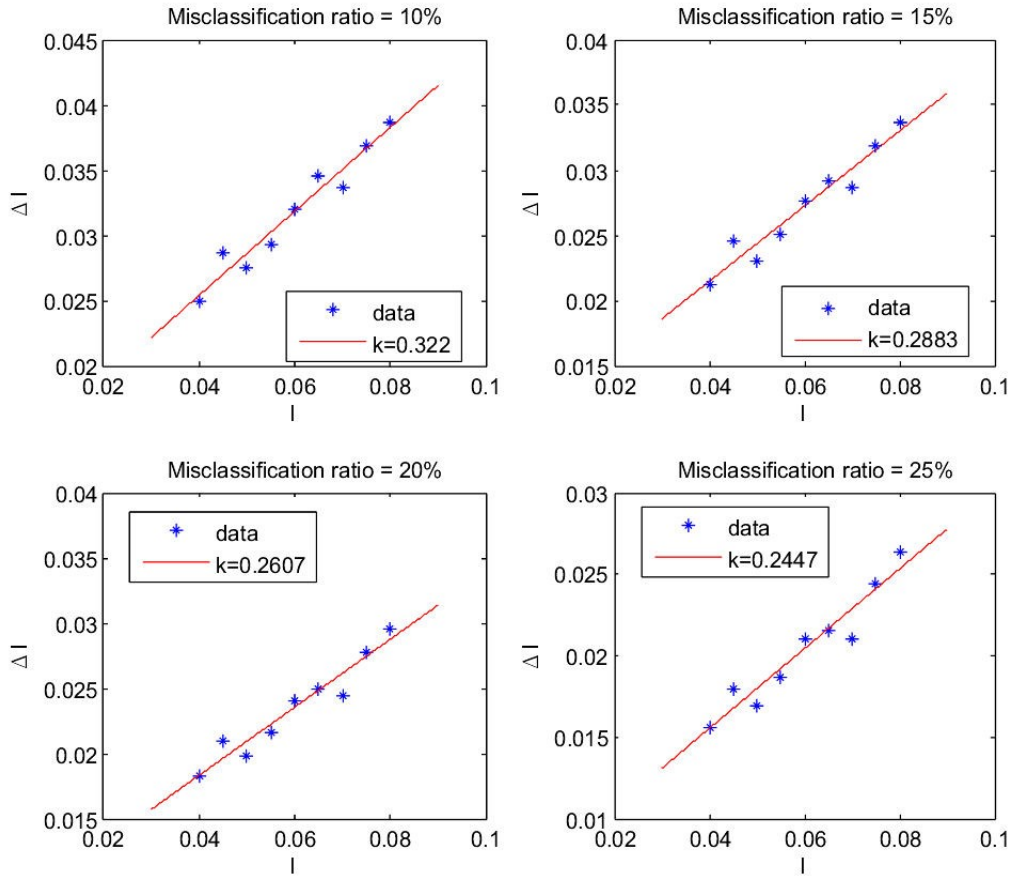

Figure 8.1: difference in the inputs ΔI needed to achieve a certain misclassification ratio, in the case of Poisson input trains to the specific pools

We then repeated the process, but this second time we altered the model by adopting a different input spike distribution, so that the distribution of the interspike input intervals was uniform between 0 and twice the average interval, which is the reciprocal of the input frequency. This modulates the total input current to the network, making it lower at the beginning of the simulation, then peaking at about time $2/F_{in}$ (which is about 660 ms since F_{in} is 3 Hz) and finally becoming nearly constant; this trend in the total input level is mirrored in the neuron spiking activity.

Figure 8.2 reports a rastergram of the network activity; a rastergram is a common way of plotting the activity of a network in neuroscience, which only keeps track of the spiking events for all the neurons. We selected one neuron out of every 10 and reported the activity of all the neurons selected in figure 8.2; neurons 1-20 come from the inhibitory pool, neurons 21-28 from the specialized pool A, neurons 29-36 from the specialized pool B, and neurons 37-100 from the nonspecific pool.

Each dot in the plots represents one spike; in the left rastergram, that shows the activity of the circuit in a typical trial with Poisson input spike distribution, it is clear how the network reaches a decision at about 0.75s from the application of the inputs, by moving from the spontaneous state, where every neuron fires with a frequency of about 3 Hz, to a state in which pool A has intense activity and pool B is almost silent.

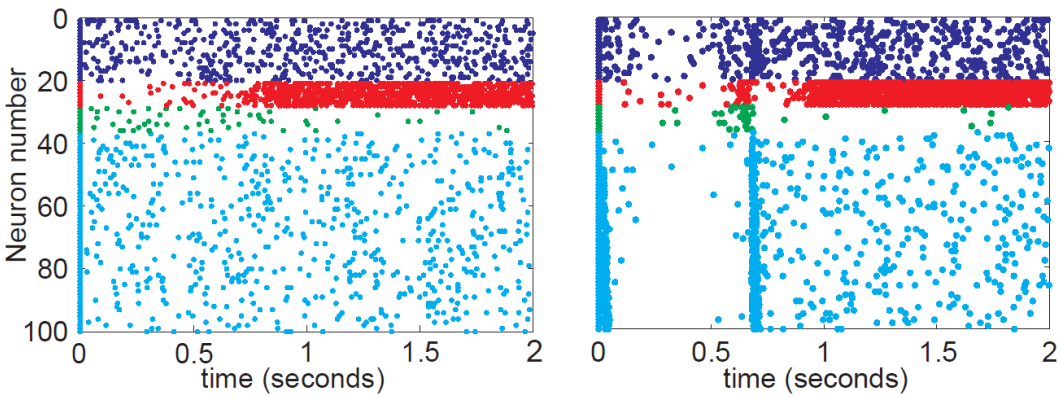

Figure 8.2: rastergrams for a standard network (left) and a network where the input spike distribution is altered (right). Each dot on the graph corresponds to the spiking of one neuron. Blue: inhibitory pool. Red: specialized pool A. Green: specialized pool B. Cyan: nonspecific excitatory neurons.

Modulating the input currents has a non-intuitive effect on the network activity, shown in the right part of figure 8.2: after a brief firing phase where most of the neurons fire once or twice, caused by the single neurons being initialized with a voltage close to the firing threshold, the network is inhibition-dominated, with very few spikes until about 660 ms. At that time, the combined effect of the peak in the input currents and the integration of the previous input spikes causes more neurons to fire again almost simultaneously, this time with a more sustained activity, and the network goes in a decision state shortly.

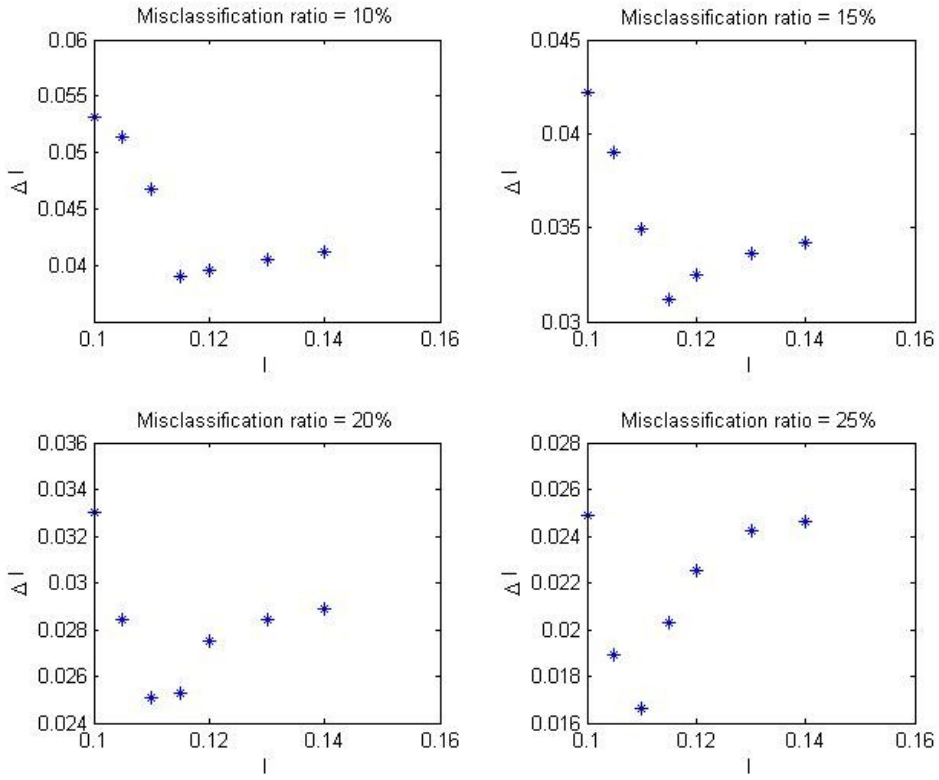

Figure 8.3: difference in the inputs ΔI needed to achieve a certain misclassification ratio, in the case where the input statistics have been modified

In Figure 8.3 we show, for the same success rates of figure 8.2, the relationship between the reference frequencies I and the values of ΔI needed to achieve the success rate, when the input currents are modulated. It is very clear that the I-ΔI curve is far from linear and is not even monotone; in this configuration the network does not follow Weber's law. It should be noted here that we did not change any of the parameters defining the network properties, which remain the ones listed in table 7.2; the same network can have the behaviour depicted in the left panel of figure 8.2 or the one depicted in the right panel, depending only on the distribution of the synaptic input spikes.

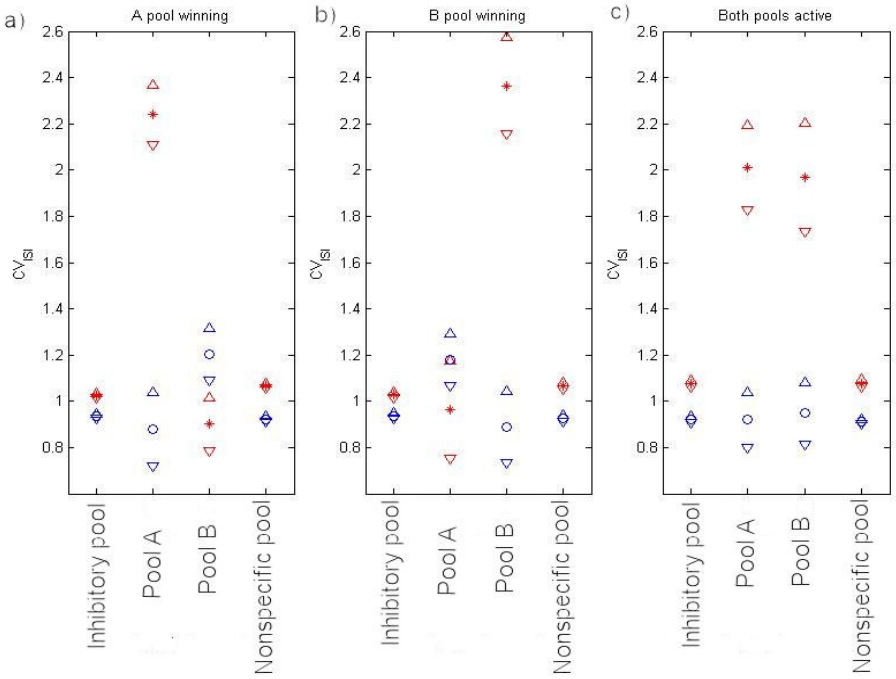

Figure 8.4: CV_{ISI} values for the original model (blue) and the one with modified input currents (red): average of 200 trials with error bars corresponding to one standard deviation. Subplot a): cases where pool A wins the competition. Subplot b): cases where pool B wins the competition. Subplot c): no pool wins the competition, they both end up in a high frequency firing state.

Figure 8.4 shows the CV_{ISI} for the different pools, measured for the three possible outcomes of a simulation (a, b, c), averaged over 200 simulations with equal inputs to pool A and pool B (ΔI=0), for the two cases where Weber's law holds (blue) and where it doesn't (red). The three possible outcomes are that either of the specialized pools win the competition, or, in rare cases, that the network goes into a "double" state, in which the two specific pools present a high firing activity. The figure shows that the inhibitory and nonspecific pools, once the decision state is reached, have values of CV_{ISI} lower than 1 for the model that follows Weber's law and greater than 1 for the model that doesn't. The specialized pool that wins the competitions has a CV_{ISI} value lower than 1 for the model that follows Weber's law and greater than 1 for the model that doesn't follow it; the converse is true for the CV_{ISI} of the pool that loses the competition. Finally, in the third possible outcome, where no decision is taken and both pools reach a high frequency firing state, all the pools have CV_{ISI} greater than 1 for the model that doesn't follow Weber's law and less than 1 for the model that follows it.

8.2 A modified version of the attractor network

The network model was also used to investigate the effect of theta oscillations on the decision making mechanisms, as this is a topic that has seen wide speculation in the literature. The term “theta oscillations” refers to a component of the Local Field Potential (LFP), which is the electric potential measured by a macroscopic electrode inserted nearby a neuronal circuit; a common way of calculating the LFP in a computational model is to average the membrane potential of each neuron in a pool of the network. Often the spectrum of the LFP is analyzed using a Fourier transform or wavelet analysis; an alternative method of research is to divide the spectrum in “regions” and then analyze one region at a time, filtering out the rest. A common, although not universal, division of the spectrum is the one that refers to the component from DC to 4 Hz as “delta”, the one from 4 to 8 Hz as “theta”, from 8 to 12 Hz as “alpha”, from 8 to 30 Hz as “beta” and from 30 Hz upwards as “gamma”.

The functions of both low- and high-frequency oscillations in the brain have been the subject of considerable investigation [228]. Low-frequency theta oscillations (4–8 Hz) have been observed to increase the phase-locked discharge of single neurons in a visual memory task [229]. In the hippocampus, the phase of the theta rhythm influences the timing of pyramidal neuron firing, long-term potentiation (theta peaks), and depotentiation (theta troughs) [230]. In this way, theta rhythm may influence synaptic plasticity and the maintenance of memory. It is speculated that recent examples of coupling between gamma amplitude and theta phase (theta-nested gamma) [231] might provide an effective combination for neuronal populations to communicate and integrate information during visual processing and learning, and might provide a process of temporal segmentation that can maintain multiple working memory items [207,229,232-236] , although the same can be accomplished more simply with several local attractor networks [207]. Oscillatory synchronization can also increase synaptic gain at postsynaptic target sites, thereby potentiating responses to learned stimuli [237,238].

There has been an interest in the relation between brain rhythms [239]and reaction time for some time. Lansing [240] reported that simple reaction time to a flash of light was shorter if the flash was delivered in the positive phase of the occipital alpha waves, and suggested that excitability was higher in this phase. Green and Arduini [241] reported that hippocampal theta usually occurs together with desynchronized EEG in the neocortex, and hypothesized that the theta is related to arousal. There is still debate as to what functional role is played by the theta rhythm. Some human EEG recording studies have reported that theta phase, rather than amplitude, is correlated with cognitive processes, the so-called phase reset model [228,242], whereas other studies on the frontal and temporal lobes have placed more importance on the theta amplitude [231].

8.2.1 Network structure and operation

To investigate the effects of the theta activity on the network model, we created a modified version of the network, in which a fraction *S* of the inhibitory neurons have a GABA spike decay time constant of $\tau_{GABA,slow} = 100\ \mathrm{ms}$ [7] . This modification was needed because,

while in the original model all the inhibitory neurons share the same parameters, in order to generate theta band activity we need to have two different populations of inhibitory neurons [243,244]. To keep constant the amount of inhibition in the network we scale the GABA conductances for all neurons by a compensating factor f, since we know that fast and slow inhibitory neurons should have the same amplitude of the conductance change when spiking [244].We kept constant the average amount of inhibition in the network by choosing f so that the average time-integrated change of conductivity caused by a GABA spike remains constant, i.e.

$$N_I w_j g_{GABA} \tau_{GABA} = S N_I w_j f g_{GABA} \tau_{GABA,slow} + (1-S) N_I w_j f g_{GABA} \tau_{GABA} \text{ (Eq. 8.1)}$$

Solving for f, this leads to

$$f = \frac{\tau_{GABA}}{S\tau_{GABA,slow} + (1-S)\tau_{GABA}} \text{ (Eq. 8.2)}$$

which can be read as f being the ratio between the original τ_{GABA} value and the new average time constant of the inhibitory neurons. The structure of the modified network can be seen in figure 8.5.

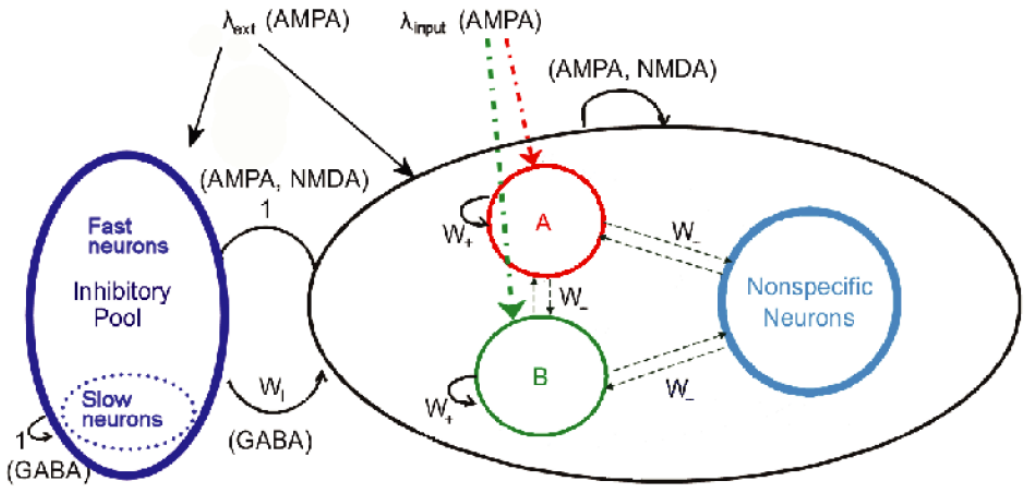

Figure 8.5: structure of the modified neural network

To check whether any difference in the network performance is due to having two different inhibitory neuronal populations, or is due to a different average τ_{GABA} value in the network, we also compared the results with ones taken from a third version of the network, with the same f value and a new value for the GABA relaxation time,

$$\overline{\tau_{GABA}} = S\tau_{GABA,slow} + (1-S)\tau_{GABA}, \text{ (Eq. 8.3)}$$

equal to the average value in the two inhibitory pool model. As we stated in section 7.3, in a mean field analysis of the network all the constant parameters are contained in the terms T_X

that describe how each pool effects the other pools. In particular, the only term that involves τ_{GABA}, following the analysis in [245], is

$$T_{EI} = \frac{g_{GABA} N_I \tau_{GABA}}{g_m} \text{ (Eq. 8.4)}$$

where g_{GABA} is the GABA conductance, N_I is the number of inhibitory neurons in the system, and g_m is the leakage conductance; T_{EI} describes the average amount of inhibition given by each spike in the inhibitory pool. The presence of a pool of slow inhibitory neurons described by equations 8.1 and 8.2 or a change of τ_{GABA} on a global scale as described by equation 8.3, with the factor f of equation 8.2 to correct for the extra amount of inhibition, leaves T_{EI} unchanged; therefore the mean field analysis for the original version of the network, reported in section 7.2.3, still holds, and all the parameters and the input levels used in the previous simulations should have the same effect with respect to the stability of the spontaneous state and the decision states.

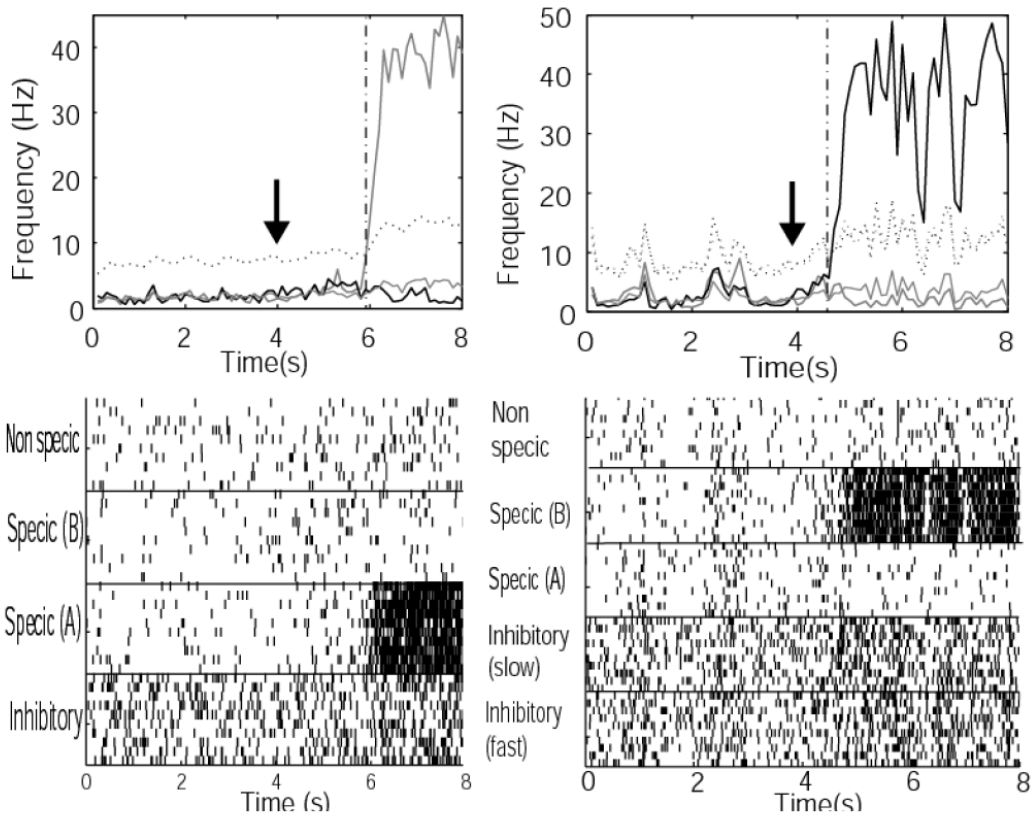

Figure 8.6: Top, left, Firing rates for all the pools for sample trials of the original model. Thick gray line, specific pool A; thick black line, specific pool B; thin gray line, nonspecific pool; dotted black line, inhibitory fast pool; dotted gray line, inhibitory slow pool. Input cues are switched on at t = 4 s (arrows). The vertical dashed line marks the moment where the decision was taken, as measured by the criterion described in the text. Bottom, left, rastergrams for the same two trials, showing the spiking activity for 10 randomly chosen neurons from each population. Middle and bottom, right, same as with middle and bottom, left, but with the two-pool model.

The model equations were evolved with an Euler algorithm with a step size of 0.05 ms, using MATLAB scripts and C language .mex files. To avoid the effect shown in figure 8.2, where all the neurons fire almost in unison at the beginning of the simulation, due to the inputs to the specific pools being already present and the neurons being initialized close to the firing threshold, we established a protocol for all the simulations. The usual protocol for a trial was to run the simulation for 4 s with no inputs to the specific pool, then add the input and run it for 4 further seconds; the addition of the input was simulated by bringing the Poisson rate to 3.04 Hz for all 800 external synapses of the neurons in both specialized (decision making) pools at t = 4s, as marked by the arrows in figure 8.6.

During a simulation run, the average membrane potential across every neuron in a pool, and the firing times for every neuron in each pool, were recorded. The average firing rates of neurons were then calculated using 100 ms bins. We defined the decision time on each trial as the time from the moment the decision-related inputs were applied until the winning pool reached a firing rate halfway between its spontaneous rate and the final firing rate when in the decision state (averaged over the last 2 s). The winning decision pool was chosen as the one that had the higher firing frequency in the last second of the simulation.

The parameters used for the model, reported in table 7.2, are such that, in the period before the decision cues are applied, the noise can occasionally trigger a transition to one of the high-firing rate attractors; any such trials were excluded from the analyses. All the experiments reported in this section were conducted as comparisons between the original version of the network, where all the inhibitory neurons have τ_{GABA} = 10 ms, which we refer to as the fast or original model; a network where a fraction S = 0.25 of the inhibitory neurons have τ_{GABA} = 100 ms and the rest have τ_{GABA} = 10 ms, referred to as the two-pool network; and a network where all the neurons have τ_{GABA} = 32.5 ms, which is the average GABA relaxation time for the two-pool network, referred to as the slow network.

8.2.2 Reaction times

Reaction times were measured for a batch of 1000 trials for each network. We note that the decision cues were of equal strength, that is, $\Delta I = 0$ (which signifies that there is no difference in the decision cues applied to each of the two decision-related populations of neurons A and B). During these trials, the inputs were turned on at a random instant between 2 and 4s to avoid any systematic contribution by possible low-frequency oscillations to the reaction times. Our data showed no correlation, however, between the input injection time and the reaction times of the network.

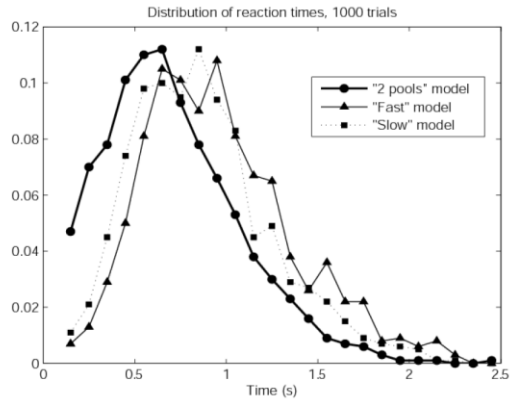

Figure 8.7: Distribution of the reaction times for the three different models. The distribution was measured using 1000 trials, and the distribution is shown with 100 ms bins. Circles, two-pool model; triangles, fast model; squares, slow model.

Binning the reaction times for each model in 100 ms bins yields the distributions plotted in Figure 8.7. As can be seen in the figure, the distribution of reaction times is skewed toward longer reaction times for all three models. The average reaction times were 0.96 s for the fast model, 0.86 s for the slow model, and 0.71 s for the two-pool model, with statistically different values according to the Wilcoxon rank sum test ($p = 0.001$, $n = 1000$ for each pair of distributions of reaction times). The median reaction times for the three models are, in the same order, 0.91, 0.82, and 0.65 s. The average reaction time for the fast model is consistent with those reported by Deco and Rolls [208]. Thus, making the inhibition longer can decrease the reaction times of this model of decision making, even when the parameters of the inhibition are selected to provide the same integrated opening of the GABA-activated ion channels, and the mean firing rate when in the attractor was similar between the three models.

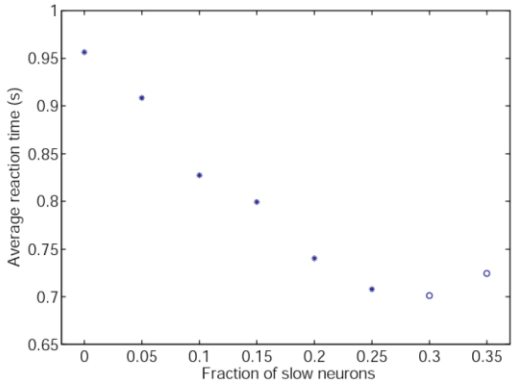

Figure 8.8: Two-pool model average reaction time as a function of the fraction of slow versus fast neurons in the inhibitory pool. Open circles mark the cases where the spontaneous state is unstable, i.e., the values for which ≈ 50% of the trials showed a transition to the decision state before the decision cues are applied.

We showed in figure 8.7 that the two-pool model has faster reaction times than the other two models. We investigated the relationship between the proportion of slow neurons in the model and reaction times by varying the fraction S of slow neurons in the two-pool

model. In figure 8.8, the point for a fraction equal to 0 corresponds to the fast or original model, and the point for a fraction equal to 0.25 corresponds to the two-pool mode.

For each ratio we ran 500 trials, with randomized decision input injection times as described above. The results shown in figure 8.8 indicate a clear decrease in the reaction time as the proportion of slow neurons increases. Thus, having a small proportion (≈ 25%) of the inhibitory neurons with a long time constant can decrease the reaction times.

When the proportion of slow neurons is increased to more than 25%, there is no further decrease in the average reaction time, and the spontaneous state becomes less stable. The spontaneous state was relatively stable when S was less than 25%, in that the network entered an attractor state in the absence of decision input cues in 2–5% of trials; and when S = 0.3 we had to reject 75% of the trials. For S = 0.35, the proportion of rejected trials with unstable spontaneous activity was approximately 90% of the total.

8.2.3 Average firing rate and membrane potential distribution

The average firing rate for the winning and the losing selective pools as a function of time is plotted in Figure 8.9. After the decision cues are applied, there is little difference in the firing rates in the three models. However, before the decision cues are applied, there is an interesting slow increase of firing rate evident for the pool that will win when all the trials are averaged from t = 1 s until t = 4 s, when the decision cues are applied. That is, the average firing rate for several seconds before the decision cues are applied is on average a predictor of which selective pool will win the competition.

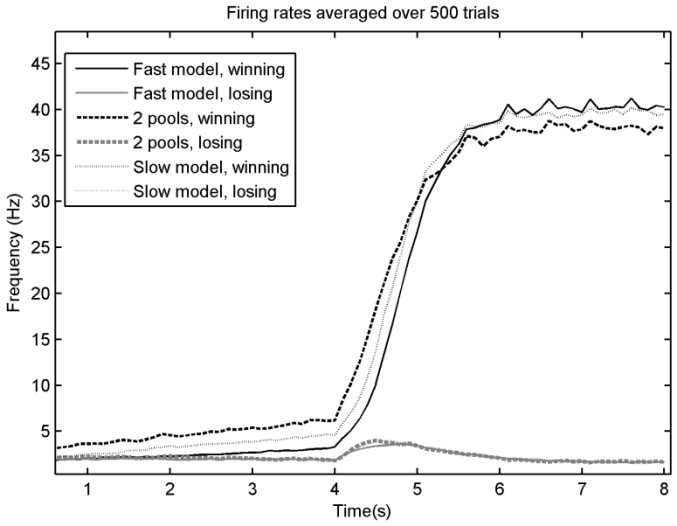

Figure 8.9:Average firing rates for the winning and losing pools over 500 trials for the three models for ΔI = 0. The decision cues were started at 4 s. (Firing rates averaged over 500 trials).

Further, the two-pool model shows in this period before the decision cues are applied a higher firing rate, on average, for the pool that will win than the slow model, and this in turn

has higher firing rates at the end of the spontaneous period when the decision cues are applied than the fast model.

Thus, the decision is anticipated or influenced by the slow change in the average firing rate for several seconds before the decision cues are applied, and the magnitude of this precue drift is greater for the models with faster reaction times. When the decision cues are applied, the pool that is already showing an upward drift (on average) will be likely to win the competition, and will have less far to go when the decision cues are applied and the strong nonlinear dynamics caused by the positive recurrent collateral feedback fully engages. In short, if the firing rate is already (on average across trials) a little up before the cues are applied, the transition to the winning attractor will be easier, and this will produce, on average, shorter reaction times.

This hypothesis was tested as follows. An unequal bias was applied to the two selective pools, and we reasoned that by chance on some trials the pool biased to win would have spontaneous activity that will facilitate the decision, but on other trials drift in the wrong direction will facilitate winning by the incorrect attractor, especially in the two-pool model. Five hundred such simulations were performed using a mean firing rate onto each synapse of 3.05 Hz to pool A, and 3.03 Hz to pool B (which corresponds to $\Delta \mathrm{I} = 16\ \mathrm{Hz}$ per neuron given that there are 800 synapses for external inputs on each neuron).

The prediction was verified with 21% ratio of error for the two-pool model, 17% for the slow model, and 12% for the fast model. Thus, the increased drift in the two-pool models can contribute to more errors when the drift is against the cues biasing the decision, in line with the hypotheses described.

We suggest therefore that the mechanism for the faster reaction times of the models with slow or two-pool inhibition is that, in the predecision period of spontaneous firing, there is a tendency for the firing rate of one of the pools to drift upward. This drift is greater for the models in the order of two-pools > slow pool> fast pool (figure 8.9), so that when the decision cues are applied, the pool that is already showing an upward drift (on average) will be more likely to win the competition, and will have less far to go when the decision cues are applied and the strong nonlinear dynamics caused by the positive recurrent collateral feedback fully engages. If the firing rate is already (on average across trials) a little up before the cues are applied, this will produce (on average) shorter reaction times.

We suggest that the drift is caused by activity in the recurrent collateral connections, which allow a form of integration of changes produced by the Poisson noise introduced into the network by the spike-firing times of each neuron. A possible mechanism for the less effective inhibition in the two-pool and slow models that leads to increased drift of the firing of the neurons in the model is that the longer the decay time for the inhibition, the greater the chance that it will be lost due to the refractory period of the excitatory neurons, as the excitatory neurons that have just fired will be insensitive to any inhibition in their refractory period.

We further note that if a network changes from asynchronous (desynchronized) to oscillatory activity, the net amount of inhibition will become smaller due to more being lost

by the refractory period effect. In more detail, the inhibition will be greatest just after the inhibitory neurons fire, as the ion channels they open in the excitatory neurons are maximally open; and, if the excitatory neurons are firing at this part of the oscillatory cycle, a large amount of inhibition will be lost as they will relatively frequently be in a refractory state. Thus, oscillations could produce a net increase in the excitatory activity in a network.

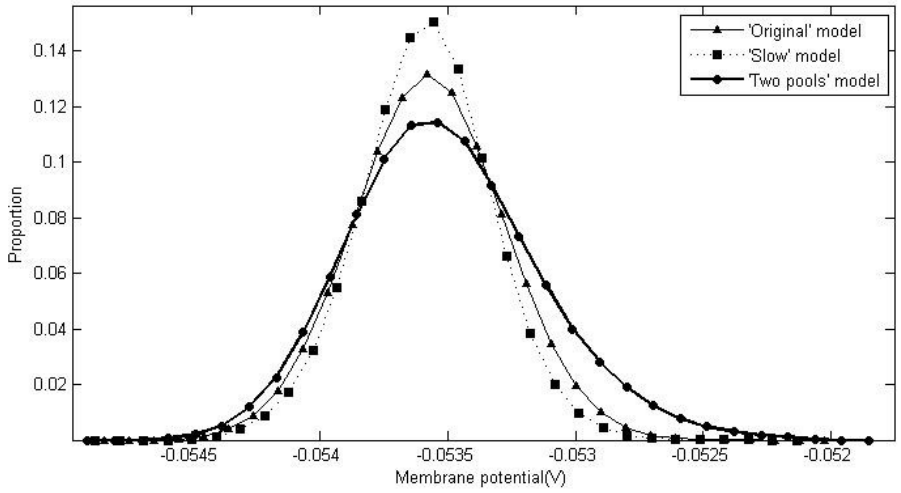

Figure 8.10: Distribution of average membrane potentials Va values in the specialized winning pool before the cue injection for the three models, using 30 bins. Triangles, fast model; squares, slow model; circles, two-pool model.

As the findings described indicate that the activity in the period before the decision cues are applied is different for the three models, and that this is related to the shorter reaction times, we investigated this further by analyzing the average membrane potential, V_a, of all neurons in the pool in the 4s precue period for each pool. Figure 8.10 shows the three distributions for the selective pools that won the competition after the decision cues were applied, although we found very similar distributions for the other pools.

As can be seen from Figure 8.10, the three models have very similar mean and peak V_a values, but the two-pool model has a distribution skewed toward increased depolarization. Two-sample Kolmogorov–Smirnov tests confirmed that all three distributions are different from each other ($p=0.001$). The skewed distribution toward greater depolarization of the two-pool model before the decision cues are applied is consistent with more activity in this model before the decision cues are applied, contributing to some faster reaction times.

8.2.4 Wavelet analysis for the local field potential

Continuous wavelet transform (CWT) of the local field potential was used to analyze the role of activity in different bands, sampling 80 points in the frequency space ranging from 1.5 to 100 Hz, using a Morlet wavelet with software in the MATLAB wavelet toolbox.

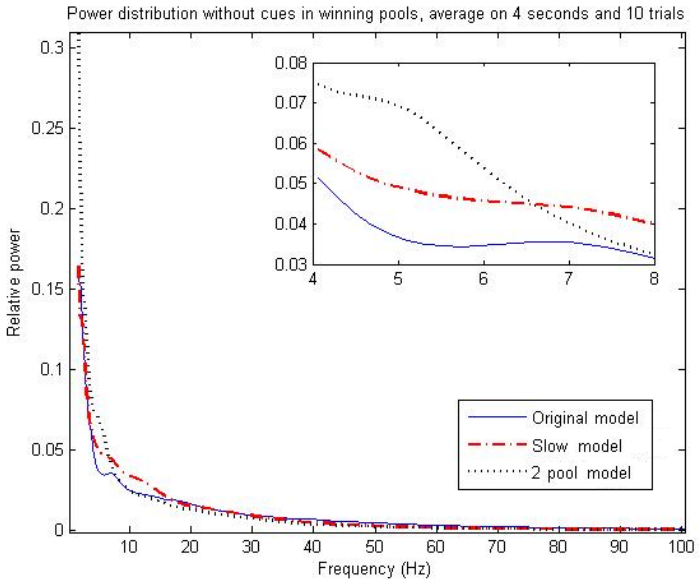

Figure 8.11: Power spectra as calculated from the continuous wavelet transform of the average membrane potential over the 1.5–100 Hz range. In the inset, detail of the spectra for the 4–8 Hz region. The blue line represents the original model, the red dashdotted line the slow model, the black dotted line the two pool model

Figure 8.11 shows the power spectra for the three different models. The spectra were obtained by averaging the square value of the CWT coefficients for the whole of the spontaneous period from a single trial, normalizing this (by setting the area under the curve to 1) to obtain a distribution of the power at different frequencies, and then averaging these power spectra across 10 trials for each model. Figure 8.11 shows the power spectra for the average membrane potential in the spontaneous period of the selective pool that eventually wins the competition for the three models (the spectra from the other pools were qualitatively similar). Figure 8.11 shows that in the theta frequency range, 4–8 Hz, the power is greatest for the two-pool model, followed by the slow and then the fast model; that is, the same order as the reaction times. We note that these effects extended to even lower frequencies, as low as 2 Hz, which is within the delta band, so that the results described in this section apply to a range of low frequencies that includes theta and delta.

To further investigate the role of theta band activity in the decision processes, we filtered the V_a values for single trials using a rectangular filter set to 1 in the range 4–8 Hz, and to 0 previously. This was implemented using a continuous wavelet transform with 40 samples in the 4–8 Hz range. Figure 8.12 shows that, for the two-pool model, such filtered V_a records for three individual trials (upper) and the average of 200 trials (lower). The results indicate that there was no phase reset phenomenon produced by the decision cues; that is, the signals did not develop, for example, peaks at the same time after the decision cues were applied. The oscillations of the single trials are 1 order of magnitude wider than the ones in the averaged trials, whereas, if phase resetting was the case, we would expect at some point oscillations that survive the averaging process.

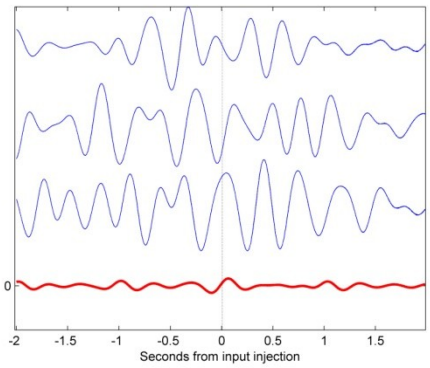

Figure 8.12: Three different trials, randomly chosen, of theta-filtered average membrane potentials V_a obtained using the slow model (top three lines), and the average of the theta-filtered V_a over 200 trials (bottom, thick line) for the same model, for 2s of simulation before and after the input injection.

In additional investigations, no significant correlation was found between the phase of theta oscillation at the moment of cue injection and the reaction time for a particular trial. As effects of the phase of slow waves at which stimuli are delivered may influence reaction times [246,247] and whether a visual stimulus close to threshold is detected [248] in some empirical studies, future investigations with the present approach might consider whether such effects can be found in the model if the degree of slow-wave modulation is larger.

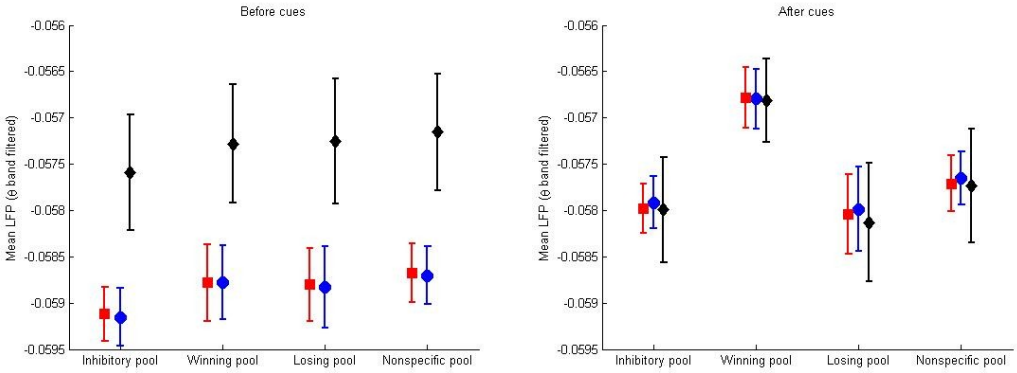

Figure 8.13: Mean values and standard deviations of the theta-filtered average membrane potentials V_a, before (left) and after (right) the cue injection, for all pools and for the three models. The values reported are the average across 200 trials for each model. Blue bars and circles: 'fast' model. Red bars and squares: 'slow' model. Black bars and rhomboids: '2 pools' model.

We also investigated whether there was a difference in the average membrane potential V_a between the different models. There was a small effect for V_a to be more depolarized in all pools in the two-pool model than in the slow or original (fast) model in the spontaneous, pre-decision cue period, but this was revealed clearly when V_a filtered as above in the range 4–8 Hz was measured, which is what is shown in Figure 8.13. In the spontaneous period, the filtered V_a indicated greater depolarization. After the decision cues were applied there were no differences in the filtered V_a for the three models or in the firing rates, in other words, while the final average value for the LFP is the same for all the three models when filtered in

the 4-8 Hz range, the initial value is different, with the value for the 2 pool model closer to the final value, and this may lead to an easier transition to a decision state.

The theta oscillations may reflect the fact that the dynamics of the system are altered toward slow state changes (increased power at low frequencies), but does not, per se and independently of the altered firing rate in the precue period, appear to play a dominant role in the faster reaction times, for there was no evidence of any relation of theta phase to the reaction time, or for phase reset of the theta at the time the decision cues were applied. However, it should be noted that if a network changes from asynchronous (desynchronized) to oscillatory activity, the net amount of inhibition will become smaller due to more being lost by the refractory period effect.

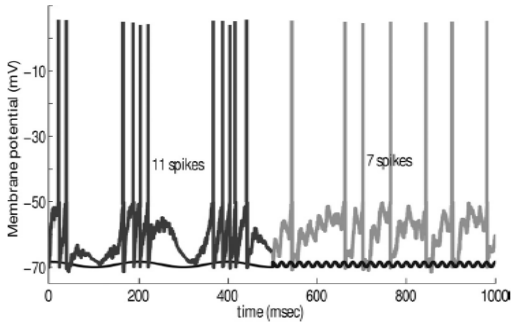

Figure 8.14 :The membrane potential of a single leaky integrate and fire neuron in response to currents applied as I_{syn} at slow (5 Hz) and at fast (50 Hz) frequencies and with identical amplitudes.

In more detail, the inhibition will be greatest just after the inhibitory neurons fire, as the ion channels they open in the excitatory neurons are maximally open; and, if the excitatory neurons are firing at this part of the oscillatory cycle, a large amount of inhibition will be lost as they will relatively frequently be in a refractory state. Thus, oscillations could produce a net increase in the excitatory activity in a network. This can be seen in figure 8.14, where the membrane potential of a single leaky integrate-and-fire neuron of the type specified in equation 7.11 in response to currents applied as $\mathrm{I}_{\mathrm{syn}}$ at slow (5 Hz) and at fast (50 Hz) frequencies and with identical amplitudes. Figure 8.14 shows that the membrane potential shows a larger modulation with the low- than with the high-frequency input. This effect is produced by the filtering effect produced by the membrane time constant, which acts as a low-pass filter, with smaller effects produced by the higher frequency of 50 Hz. Depending on the operating or average membrane potential, the larger modulation may produce more spiking events with the low than with the high frequencies, as illustrated in Figure 7. A further analysis of these dynamics is provided by Kang et al. [249].

The modified network studied, therefore, shows that there is a tight and complex relationship between the time constants of the network, its oscillatory activity and the reaction times of the network. Introducing a pool of slow neurons within the inhibitory pool affects the spectrum of the local field potential, raising the component between 2 and 8 Hz at the expense of higher frequencies, for all the pools and not just for the inhibitory neurons. The effect is specifically due to having two populations of inhibitory neurons with

different time constants, as having one pool with slower τ_{GABA} has a much less noticeable effect.

The change in the LFP spectrum does not have a direct effect on the reaction times, as there is no evidence for phase reset in the theta-filtered potential, nor any correlation between the phase of the oscillation at either the moment of input injection or at the moment of the decision making and the reaction times. Instead, shifting the network activity towards lower frequencies facilitates the integration of the excitatory inputs generated by the majority of the neurons in the network; the extra amount of excitation of the network causes the average spiking frequency of one of the two specialized pools to drift upwards, even without the extra inputs to the pool. This causes the reaction time to be faster, even if at the expense of the stability of the final state of the network and of the misclassification ratio in some trials where the cues were not symmetrical.

9. RESEARCH IN BION AND AFTER BION

The studies described in this thesis are centred on the construction, optimization and utilization of a single memristor as the key element for a network that could mimic information processing in a way that is reminiscent of what happens in neuronal circuits. They are however only a part of a larger research project, and the variety of topics touched in chapters 5 through 8 reflects the evolution of the research project itself, which required investigations on different aspects of the problem, ranging from physical investigation of the memristor properties (chapter 5) to computer simulations of memristor networks (chapter 6) to computational neuroscience (chapters 7 and 8). In this final chapter I will give a brief overview of the rest of the research undergone within the scope of BION but to which I gave only a minor contribution, as well as some reflections on the possible future research paths.

9.1 Research in the BION project

Much of the research of the BION project that has not been reported in this thesis was geared towards engineering a material capable of generating by self-assembly a three-dimensional network of memristors. To this purpose, three different materials were tried: gold nanoparticles functionalized with cavitands, PANI-PEO block copolymers, or a fibrillar support to be decorated with a PANI-Gold nanoparticles mixture. The materials were fabricated and tested in parallel, as there was no clear indication beforehand of which was the ideal choice for the network building; eventually, the chosen material comprised a mixture of PEO-Polystyrene block copolymers and functionalized gold nanoparticles. In this

section we will examine also some new techniques, both experimental and theoretical, that could allow a better understanding of what is really happening in a memristor network.

9.1.1 PANI/Gold nanoparticles hybrid

Gold nanoparticles feature prominently in the studies undergone, because it was believed that they could work as nonlinear junctions between memristors, thus taking the roles of "neurons", as opposed to the one of "synapses" taken by the memristor. In order to achieve this goal, gold nanoparticles modified at the surface by mercaptoethane sulphonic acid (MESH) have been used to fabricate an hybrid material composed by gold NP and PANI, with a procedure similar to the one used to obtain the PANI/DBSA composites described in section 5.2.1.

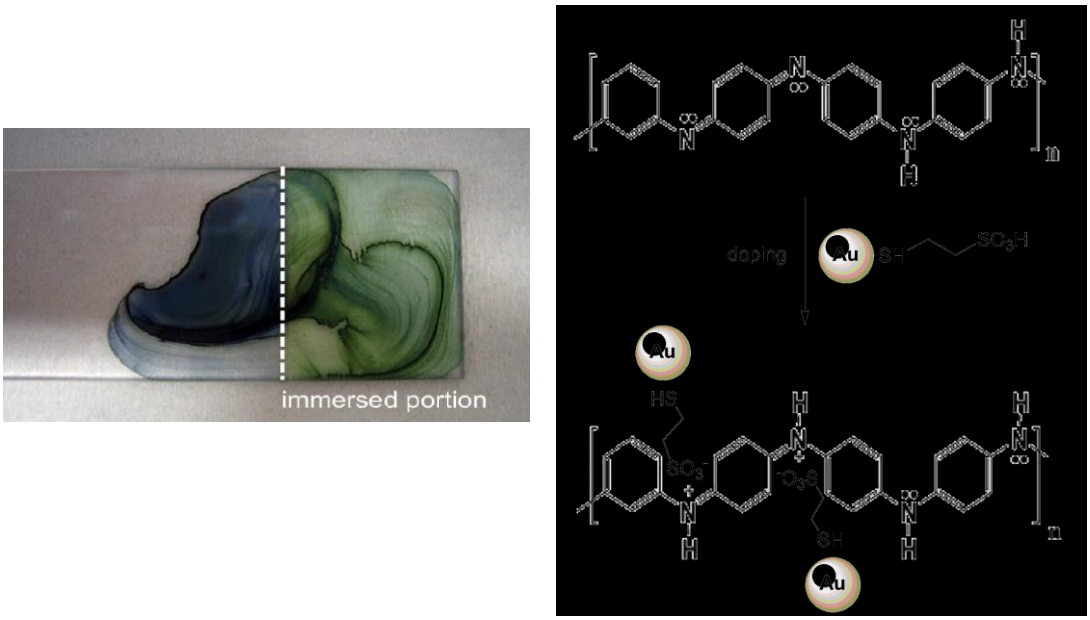

Figure 9.1: (left) An emeraldine base PANI thin film whose right half was immersed in a solution of gold nanoparticles functionalized with MESH for two hours, (right) scheme of the doping process

The PANI in the resulting material has been shown to be in the conducting state, by both FTIR and UV-VIS analysis. Moreover, the nanoparticles have proved to be a dopant for PANI films, as figure 9.1 shows: a thin film immersed in a solution of MESH functionalized gold nanoparticles change its state from the blue (insulating) emeraldine base to the doped green (conducting) emeraldine salt state.

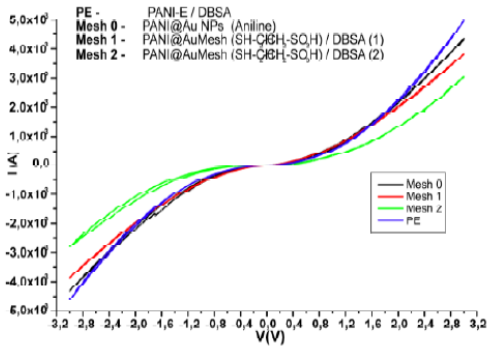

Figure 9.2: V-I characteristics for mixtures of PANI and gold nanoparticles functionalized with different composites

Figure 9.2 shows the V-I characteristics for emeraldine base PANI doped with DBSA (PE) and for three hybrid PANI-gold nanoparticles materials that differ in the composites covering the nanoparticles. Those are aniline (MESH 0), mercaptoethane sulphonic acid with 8 CH_2 repeat units (MESH 1) and mercaptoethane sulphonic acid with 12 CH_2 repeat units (MESH 2). The latter material is the one with more conductance inhibition at low voltages, caused by the Schottky junctions created in the composite materials. Moreover, memristors created using a PANI and MESH2 hybrid have practically ideal cyclic characteristics; the difference in the conductivity between conducting and insulating states is about 3 orders of magnitude, and they can be used with high voltage differences (up to 5 V) without being damaged.

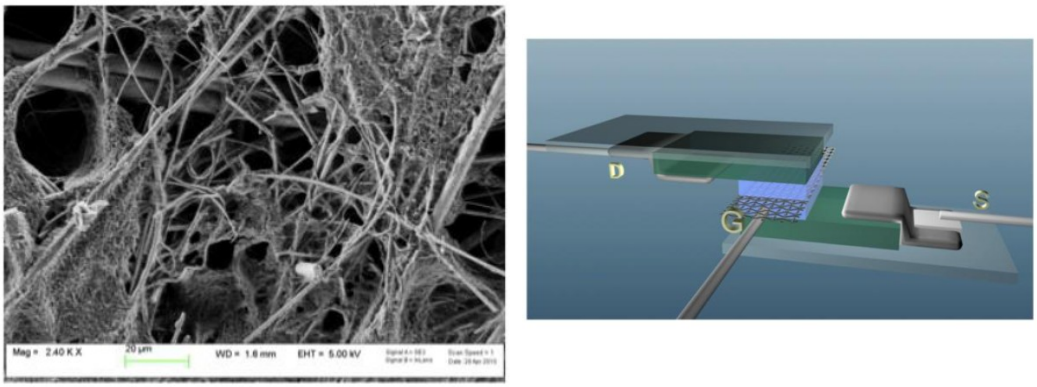

Figure 9.3: (left) SEM image of a glass fiber support covered by the MESH material; (right) scheme of the experimental setup. The blue part is the MESH coated glass fiber, the green area is the PANI, G, D and S mark the gate, drain and source electrodes respectively.

To stabilize the physical structure of the PANI/MESH hybrids, an experiment was performed where glass fiber was used as a physical support for the network. The glass fiber was covered either with the MESH1 or the MESH2 material (as shown in figure 9.3) and then placed between two PANI films on insulating substrates; a PEO covered reference electrode was then put in the middle of the glass fiber, and the device assembled in the configuration reported in figure 9.3

This structure also shows memristive behaviour, with quite slow kinetics that make the hysteresis in the I-V plot appear only when the voltage step in the I-V sweep is 3 minutes or longer. As a general conclusion, the stabilization of the fiber statistical networks based on the newly synthesized materials, with phase separation properties by using solid supports of porous or fibrillar structure, could also provide a viable alternative matrix.

9.1.2 Phase separation via molecular recognition

An alternative approach to the formation of molecular assemblies is based on the interplay between enthalpy driven molecular recognition phenomena and entropy driven microsegregation between inorganic nanoparticles (AuNPs) and polymers (methylpiridinium terminated polyethylenoxide).
The gold nanoparticles (AuNPs) were synthesized as reported in [250,251], were characterized as having an average diameter of 6 nm by means of scanning and transmission electron microscope, and were then functionalized with a tetraphosphonate cavitand, bearing a tetradisulfide moiety at the lower rim as reported in figure 9.4.

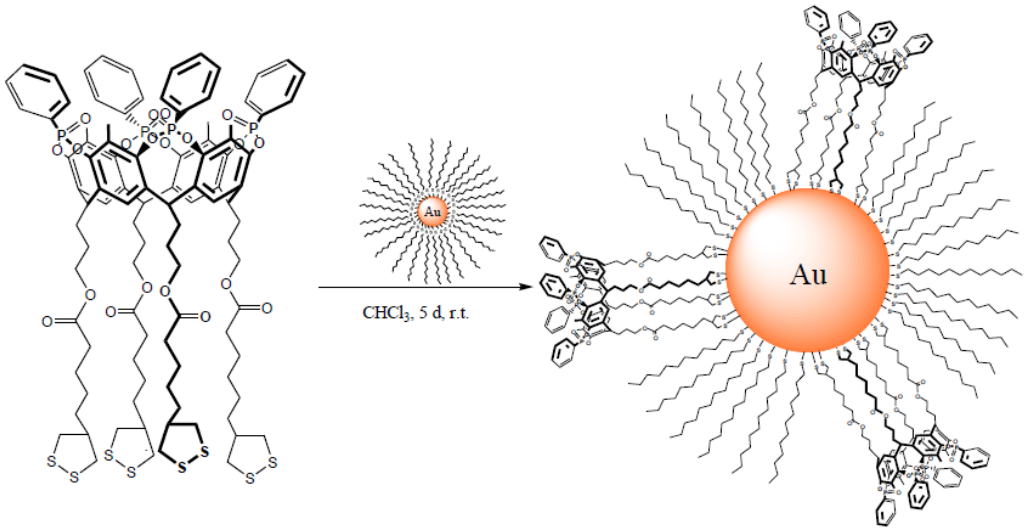

Figure 9.4: Scheme of the cavitand and preparation of the functionalized gold nanoparticles

This operation is necessary to graft a molecular receptor onto the surface of AuNPs. The tetraphosphonate cavitands are known to be a very powerful host for cationic species, in particular methylpyridinium and methylammonium salts. The synthesis of this specific receptor bearing four thioctic acid units at the lower rim for Au nanoparticle grafting and the functionalized cavity for molecular recognition at the upper rim as reported in [252]. The molecular receptor was synthesized in seven steps, in an overall yield of 15%; an innovative fluorescence characterization technique was used to estimate an average 3.3% (w/w) of

cavitand on the surface of the AuNPs, while SEM analysis showed that the grafting of the cavitands had left the diameters of the nanoparticles unchanged.

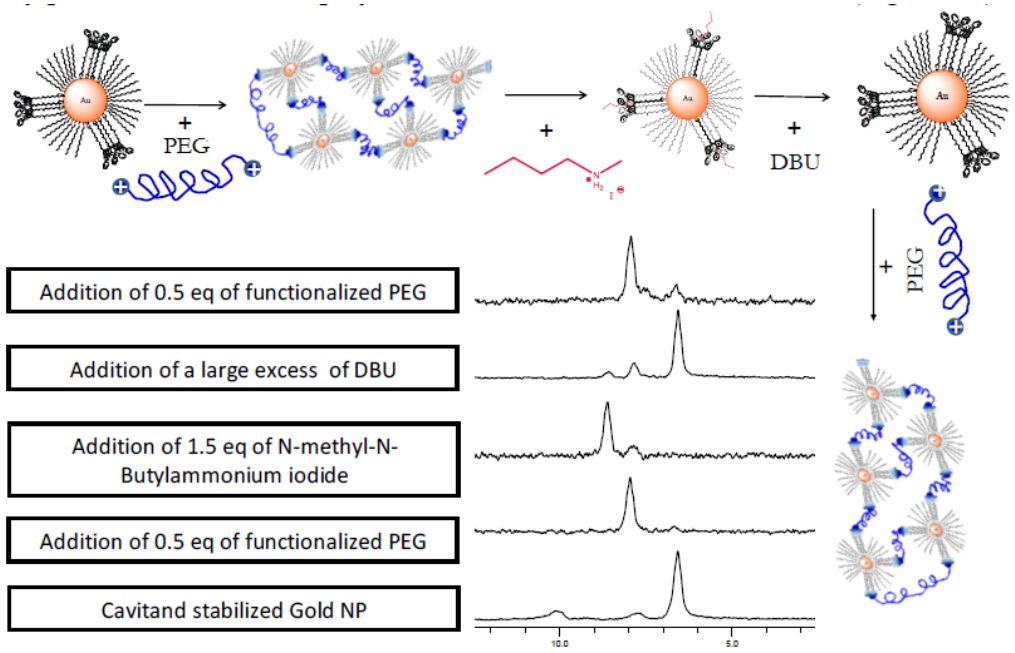

Figure 9.5: Scheme of the network disassembly and reassembly, along with NMR signals taken at the various steps of the process.

When adding to the cavitand functionalized nanoparticles a guest polymer (methylpiridinium terminated PEO) the formation of a phase segregated network can be observed both by monitoring the NMR signal of the mixture and by direct imaging with the SEM, as a consequence of the molecular recognition process which leads to a complex formation between the host and the guest. The reversibility of the network formation was demonstrated by competitive guest addition [253], using methylbutilammonium to displace the guest PEO polymer and disassemble the polymer, then removing it with an excess base (DBU) and rebuild the network by adding PEO again , as shown in figure 9.5.

9.1.3 Block copolymers

A possible strategy to develop a complex 3D memristor network is to obtain some form of phase segregation in a material containing both PANI and PEO, so that a portion of the material contains several “islands” of the two components connected between themselves, creating a high number of PANI-PEO junctions with memristive behaviour. In order to provide this kind of phase separation, a polystyrene-PEO block copolymer was prepared.

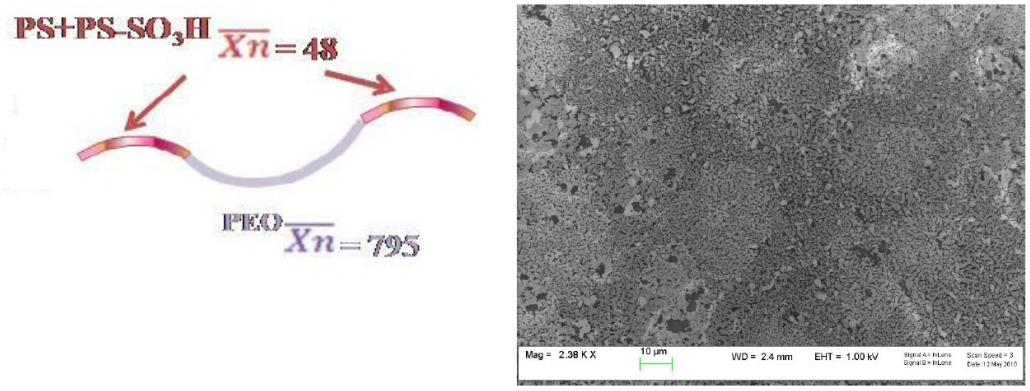

Figure 9.6: Left, scheme of the block copolymer; right, SEM image of a block copolymer/PANI mixture

In a sample of pure high molecular weight PEO-PSS block copolymer, differential scanning calorimetry analysis shows two distinct T_gs , -52.6°C for PEO block phase and +90.6°C for PSS block phase; when mixing this copolymer with a PANI solution in NMP, the PEO portions of different polymer chains stack together, forming PEO islands, while the sulphonic groups are molecularly involved in PANI polymer doping and are not segregated in a separate phase anymore. The phase segregation for a mixture of the block copolymer and PANI, with a ratio of 1:50, is shown in the right part of figure 9.6.

This structure has shown memristive behaviour, tested by placing the material in a 0.25 mm deep well in a kapton film, from which 16 electrodes emerged, disposed in a circular configuration. A metallic grid was immersed in the well, too, and kept at ground potential, taking the role of the gate electrode in a single memristor; the I-V characteristics, of which figure 9.7 reports an example, were measured by using opposite pairs of electrodes.

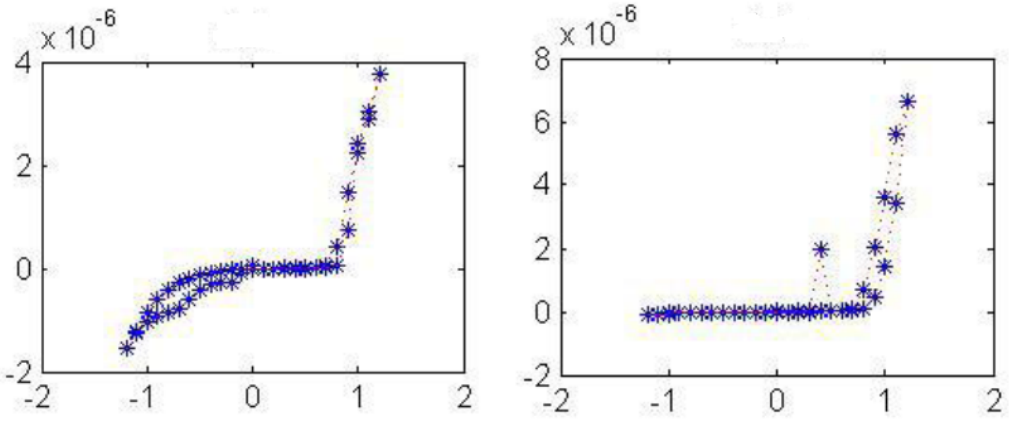

Figure 9.7: I-V characteristics for a mixture of PANI and polystyrene-PEO bloc copolymer, for two subsequent measurements

As it is clear from the figures, the phase separation has resulted in the statistical formation of the contact zones of solid electrolyte with conducting polymer, adequate for the electrochemical processes responsible for the memristor functioning. The other interesting

feature of the reported characteristics is the fact that the performance of the device was improved in the second cycle (usually, the performance is the same or even worse). This can be the indication that the phase separation was not finished when the first cycle was measured. As the active medium in this case was in the gel form, it is possible that some self-organization processes took place in the electrically biased system, resulting in a better phase separation and an improvement of the device properties.

The non linear behaviour of the matrix in the simple three electrode memristor configuration described merely reports the average conductivity of all the paths between the two chosen electrodes, but it does indicate the presence of a large quantity of memristor-like areas in the matrix. A more interesting behaviour of the matrix could be revealed only by using a multitude of microeletrodes to take the electrical measurements, which would then be sensitive to specific paths within the matrix. Overall, this method of fabricating a 3D complex network seems the most promising, as there is no need for an external structure like the fiber glass support, and the memristive characteristics of the system are quite good; the PANI/PEO mixture can furthermore be enriched with gold nanoparticles that act as nodes, and this could lead to an even more pronounced nonlinear behaviour.

9.1.4 Optical contactless method to map a memristor network

As mentioned in section 6.3, a method of knowing the state of the memristor network is an invaluable tool if we want to apply an efficient training protocol to any network that does not have a trivial structure. An electrical measurement of the resistance between different points of the network would be very slow, would require a dedicated and presumably complicated setup and would almost unavoidably perturbate the network itself; therefore, studies have been made on an optical contactless method of measuring the PANI conductivity [196].

Experiments have been made on a standard PANI/PEO device, using two homemade electrometers for the electrical characterization of the system and a reflection/backscattering fiber probe to measure the reflectivity of the film in the 400-1000 nm region. The optical probe used had a 6 around 1 design: six external optical fibers are used for illumination and connected to a tungsten halogen light source, while the central read fiber collects the reflected/back scattered light to the spectrometer. Measurements were taken both in the usual configuration where a potential sweep was applied at the drain terminal (see figure 9.8), and in a different configuration where the drain and the source electrode were kept at the same voltage, while a different voltage was applied to the gate electrode. This had the effect of avoiding all the problems of voltage redistribution described in section 4.3 and allowed to calculate directly, by integrating the gate current, the number of ions transferred from the PEO to the PANI film and back.

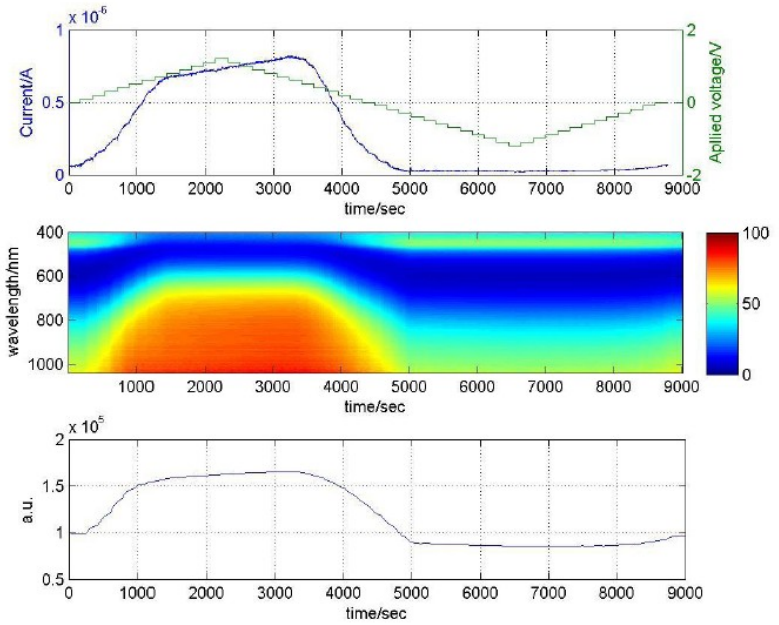

Figure 9.8 Electrical and optical behavior of organic memristor during a voltage sweep; Top panel: Electronic current flowing in the device (left axis) and Voltage applied (right axis) between device terminals. Middle panel: Reflectance spectra with pseudo-colors indicating the percentage reflectivity as a function of wavelength (vertical axis) and time (horizontal axis) Bottom panel: Near infrared reflectance obtained by integration over the range 800-1000 nm.

This latest experiment suggested the fact that there is a direct proportionality between the reflection in the near infrared (NIR) region, obtained by integrating the reflection spectra in the 900-1000 nm region, and the number of ions transferred in the PANI layer. Such direct relation between ionic charge and spectroscopic features can be accurately found using more sophisticated spectral analysis techniques, like principal components analysis. The reflection in NIR region indicates as well the conductive behaviour of film since it is due to the Drude tail, thus confirming the optical determination of conductivity, as it is evident from the comparison between the first and last panel of figure 9.8. These results provide a fast, contactless and space resolved technique for the conductance measurement of PANI which could be employed for different tasks; in our case as a tool for a parallel characterization of memristor networks producing conductivity maps with a space resolution in principle down to the nanoscale using near field optical techniques.

9.1.5 Correlated theoretical studies

In parallel with the studies in material science, the research within BION involved also the development of some theoretical tools in computational neuroscience, which, even if at present are not directly connected to the topic of stochastic memristor networks, can provide useful tools with which we could analyze said network's functioning.

One of these tools is proceeds on the basis of a theoretical framework on leaky integrate and fire (LIF) neuronal networks by including the first order moment (mean firing rate) and

the second order moment (variance and correlation): a moment neuronal network (MNN) approach [254].

The analyses performed using this approach reveal many interesting phenomena of LIF networks, focusing on rhythmic phenomena and synchronization events [249,255]. The studies show that, with a small clamped correlation, the network will finally become silent when the inhibitory input increases; but the network could enter a chaotic region when the correlation is strong and in this case the input-output firing rate is no longer a sigmoidal function.

For a feed-forward spiking network, the proposed setup allows to prove that all neuronal activities rapidly synchronize, a well-known fact in the literature observed in numerical simulations; moreover, wave propagations in the network are analyzed. Finally, we tested our MNN with the content-dependent working memory setting. Most importantly, it is expected that such results can be translated to the material matrix to be built in BION and therefore be integrated in the project. For this appropriate simulation on memristor-based networks are in progress.

In order to understand a network activity, either in a material or a neuronal network, another very useful tool is Granger causality analysis, which allows to understand, in a complex network of interacting units, which are the most important causal effects that link different units. Studies have assessed [256,257] how temporal filtering, spatial filtering, down-sampling and up-sampling of neurological data affect the estimation of Granger causality: the causal influences will remain after spatial filtering in the case that all samples are uniform enough, while down-sampling will not change directed pairwise causal relationships but will introduce false positive connections when mediated variables exist. In a refinement of the theory, Granger causality has been defined on stochastic differential equations; the results provide a solid foundation for the application of Granger causality to biological and other types of data, and also an instruction of the use of Granger causality in different situations, like the adaptive networks that are being prepared within BION.

A more neuroanatomy-oriented research activity occurring within the BION project is devoted to finalizing a model on cortical intrinsic connectivity [258] and a study on categorization [259], focusing at present on the cortical white matter. White matter is mainly composed of axons connecting the cortex with itself and thus highly relevant for understanding the network structure of the cortex; an electron microscopic study on axonal thickness is in progress. Axonal thickness is relevant for two reasons: it can provide estimates on the number of axons in the various axon bundles running through the white matter and it is strongly related to conduction time, playing therefore a crucial role in cortical dynamics. These results could be relevant to the final stages of the project since, if the proposed micro-phase separated matrix or its alternatives are successful, it would imply a downscaling of the functional structures to the micron range, with the possibility to go to the nanoscale.

9.2 Future research paths

While the BION project is scheduled to finish in April 2011 or shortly after, there are many possible research paths that it would be interesting to pursue. This is also due to the fact that the project's goals connect in a very tight and coherent way the fields of neuroscience and of material science, as well as being unique in its focus on self assembled, polymeric based memristor networks; as we have described in chapter 2 of this thesis, the vast majority of researchers that deal with memristors are considering top-down circuits based on metallic composites.

Since the memristors in our network is supposed to take the role of a synapse, an implementation of a learning mechanism similar to spike time dependent plasticity could both prove useful for the project and interesting in its own right. As of now, there are theoretical works [76,77], mentioned in chapter 2, that have relied on simulations to prove that this is possible, using a convenient memristor model and defining an arbitrary spike shape that, matching the model, is responsible for the implementation of STDP. In our case, the memristor characteristics are given by the experimental data, so all that's left is to find an adequate spike shape that can implement the STDP; the same approach used in [77]" can be followed, by having a post-spike hyperpolarization period that, matched with the high potential during the spike, brings the total potential difference above the oxidation threshold and makes the memristor more conductive.

What is still lacking in the network that is being built as of now is a reliable neuron analogue, and this is an area where research should be focused in the last stages of BION or even after it. Although so far the functionalized gold nanoparticles have been used as possible nodes of the network, and rhythmic activity as a response to a constant input voltage has been seen and described in section 4.3.2, we still lack an element with an integrate-and-fire behaviour that can be included in a self-assembled network. One intermediate step, if no such element can be found soon, could be to have a self assembled memristor network connect several spike generating circuits made by traditional elements or even simulated on a computer, thus having a circuit in which a part is assembled and adapted with a bottom-up process, and another is built in a top-down, traditional strategy. Another strategy could be to skip the spike encoding entirely, and have a circuit in which the voltage level represents the firing rate of a given neuron. A single neuron would then be represented by an element with a sigmoid I-V curve, which is definitely easier to implement that an integrate-and-fire behaviour, although the adherence to the biological model would be hurt by the impossibility to reproduce all the phenomena bound to the exact timing of the spikes, like for instance STDP.

At the whole network level, the first objective for any future research should be to link more closely the two aspects of experiments on actual devices and networks on one side, and simulations on the other. The simulations described in section 6.3 have emphasized the need for a reliable, fast technique of obtaining a conductance map of the network; the optical method described in section 9.1.4 is probably the best candidate right now to obtain

such maps. However, any method used should be fast enough to execute many (up to thousands) mappings in a single training session, because we haven't been able, up to now, to find a training protocol that allows to calculate the training inputs without constantly following the state of the network. To avoid this necessity, there could be the option of having a set of tens or hundreds of microelectrodes in contact with the network, in a configuration similar to the electrodes used for taking data on biological neuronal circuits, and then work out from the simultaneous potential reading on these electrodes either the full resistance map for the network, or at least an equivalent, simplified one that allows nevertheless to calculate the input currents needed to train the circuit.

While the simulation work presented in sections 6.3 and 6.4 undoubtedly leaves some question open, such as why some networks respond to a training strategy and some others don't, dwelling too much on a single problem can be counterproductive, as the networks described are more "toy problems" than accurate representations of the networks created. To extract more meaningful data from the simulations, a feedback from the material science side of the project is needed; investigators running the simulations should know how to physically describe the network, and have at least an approximate value for quantitative parameters like density of nodes, average connectivity of the nodes in the network, maximum and minimum memristance of the single memristors, and so on. As the project turns to completion and the network materials, as well as the building techniques, have gone through all the preliminary design phase and have settled in a final form, these data should be easily obtainable by standard investigation techniques.

Of course, the final goal of the project and of the future research remains the one of building a functional adaptive network, that mimics in its functioning the processes found in biological examples, and that can "learn" to perform a specific task on a set of data, with a learning process that is either spontaneous, caused by the encoding of the data itself in form of potential and currents, or that is directed, by adding to the network additional inputs conveniently shaped. It should be very clear that, given the fact that all the developments leading to this network are very recent, we do not expect this network to compete with the traditional computing hardware or software in term of computational power, speed or accuracy: silicon-based technology has fifty years of technological development on its side that simply cannot be covered in such a short time.

However, this research project is laying some groundwork for an entirely new computation paradigm, involving cheap, disposable organic networks that naturally operate with an analogical rather than digital logic, and whose functionality is not pre-estabilished but can be programmed, erased and reprogrammed at will. The same characteristics indicate that our network is perhaps a better candidate to physically emulate the functioning of a brain, which after all is an adaptive, self assembled system where learning continually occurs, than any silicon-based circuit, which is designed with a very specific task in mind; this could help not only neuroscientists, giving them a benchmark with which to test their theories, but also push research towards bio-inspired computational techniques.

After all, the computational power of the brain, and its performance in most of the tasks that do not involve “brute force” calculation, is still far superior than even the more modern computer cluster, while consuming less energy than the average lightbulb; if we ever want to use organic matter and memristive-like devices to build a complex, useful circuit that could one day compete with the computers, we should look for inspiration no further than our own heads.

BIBLIOGRAPHY

[1] A. Smerieri, T. Berzina, V. Erokhin, M.P. Fontana, Polymeric electrochemical element for adaptive networks: Pulse mode, Journal Of Applied Physics. 104 (2008) 114513.

[2] T. Berzina, A. Smerieri, M. Bernabò, A. Pucci, G. Ruggeri, V. Erokhin, et al., Optimization of an organic memristor as an adaptive memory element, Journal Of Applied Physics. 105 (2009) 124515.

[3] L. Cristofolini, M.P. Fontana, O. Konovalov, T. Berzina, A. Smerieri, Doping-induced conductivity transitions in molecular layers of polyaniline: detailed structural study., Langmuir : The ACS Journal Of Surfaces and Colloids. 25 (2009) 12429-34.

[4] T. Berzina, A. Smerieri, G. Ruggeri, M. Bernabò, V. Erokhin, M.P. Fontana, Role of the solid electrolyte composition on the performance of a polymeric memristor, Materials Science and Engineering: C. 30 (2010) 407-411.

[5] V. Erokhin, T. Berzina, A. Smerieri, P. Camorani, S. Erokhina, M.P. Fontana, Bio-inspired adaptive networks based on organic memristors, Nano Communication Networks. 1 (2010) 108-117.

[6] J. Kang, J. Wu, A. Smerieri, J. Feng, Weber's law implies neural discharge more regular than a Poisson process., The European Journal Of Neuroscience. 31 (2010) 1006-18.

[7] A. Smerieri, E.T. Rolls, J. Feng, Decision Time, Slow Inhibition, and Theta Rhythm, Journal Of Neuroscience. 30 (2010) 14173-14181.

[8] L. Chua, Memristor - The Missing Circuit Element, Ieee Transactions On Circuit Theory. 18 (1971) 507-519.

[9] D.B. Strukov, G.S. Snider, D.R. Stewart, R.S. Williams, The missing memristor found., Nature. 453 (2008) 80-3.

[10] R.M. Fano, L.J. Chu, R.B. Adler, Electromagnetic Fields, Energy, and Forces, American Journal Of Physics. 29 (1961) 562.

[11] L. Chua, S.M. Kang, Memristive devices and systems, Proceedings Of the IEEE. 64 (1976) 209–223.

[12] L. Chua, M. Hasler, G.S. Moschytz, J. Neirynck, Autonomous cellular neural networks: a unified paradigm for pattern formation and active wave propagation, IEEE Transactions On Circuits and Systems I: Fundamental Theory and Applications. 42 (1995) 559-577.

[13] F.A. Buot, A.K. Rajagopal, Binary information storage at zero bias in quantum-well diodes, Journal Of Applied Physics. 76 (1994) 5552.

[14] J.H. Krieger, S.V. Trubin, S.B. Vaschenko, N.F. Yudanov, Molecular analogue memory cell based on electrical switching and memory in molecular thin ® lms, Synthetic Metals. 122 (2001) 199-202.

[15] G.S. Snider, Self-organized computation with unreliable, memristive nanodevices, Nanotechnology. 18 (2007) 365202.

[16] G.S. Snider, Computing with hysteretic resistor crossbars, Applied Physics A. 80 (2005) 1165-1172.

[17] P.J. Kuekes, G.S. Snider, R.S. Williams, Crossbar Nanocomputers, Scientific American. 293 (2005) 72-80.

[18] B.L. Mouttet, Memristive Transfer Matrices for Analog Electronics, Signal Processing. (2010) 1971-1974.

[19] J.H. Krieger, N.F. Yudanov, Memory device, 2004.
[20] M.N. Kozicki, W.C. West, Programmable metallization cell structure and method of making same, US Patent 5,761,115. (1998).
[21] D.M. Morgan, Method and apparatus for reading/writing data in a memory system including programmable resistors, US Patent 5,883,827. (1999).
[22] D. Rinerson, C.J. Chevallier, S.W. Longcor, W. Kinney, E.R. Ward, S.K.R. Hsia, REWRITABLE MEMORY WITH NON-LINEAR MEMORY ELEMENT, US Patent App. 10/. (2003).
[23] D.B. Strukov, W. Robinett, G.S. Snider, J.P. Strachan, W. Wu, Q. Xia, et al., Hybrid CMOS / Memristor Circuits, New York. (2010) 1967-1970.
[24] Q. Xia, W. Robinett, M.W. Cumbie, N. Banerjee, T.J. Cardinali, J.J. Yang, et al., Memristor-CMOS hybrid integrated circuits for reconfigurable logic., Nano Letters. 9 (2009) 3640-5.
[25] W. Robinett, M. Pickett, J. Borghetti, Q. Xia, G.S. Snider, G. Medeiros-Ribeiro, et al., A memristor-based nonvolatile latch circuit., Nanotechnology. 21 (2010) 235203.
[26] J. Borghetti, Z. Li, J. Straznicky, X. Li, D.A.A. Ohlberg, W. Wu, et al., A hybrid nanomemristor/transistor logic circuit capable of self-programming., Proceedings Of the National Academy Of Sciences Of the United States Of America. 106 (2009) 1699-703.
[27] T. Prodromakis, K. Michelakis, C. Toumazou, Fabrication and Electrical Characteristics of Memristors with T iO 2 / T iO 2 + x active layers, Physical Review. 2 (2010) 1520-1522.
[28] N. Gergel-Hackett, B. Hamadani, B. Dunlap, J. Suehle, C. Richter, C. Hacker, et al., A flexible solution-processed memristor, IEEE Electron Device Letters. 30 (2009) 706–708.
[29] N.C. Cady, M. Bergkvist, N.M. Fahrenkopf, P.Z. Rice, J.V. Nostrand, Biologically self-assembled memristive circuit elements, (2010) 1959-1962.
[30] T. Driscoll, J. Quinn, S. Klein, H.-T. Kim, B.J. Kim, Y.V. Pershin, et al., Memristive adaptive filters, Applied Physics Letters. 97 (2010) 093502.
[31] T. Driscoll, H.-T. Kim, B.-G. Chae, M. Di Ventra, D.N. Basov, Phase-transition driven memristive system, Applied Physics Letters. 95 (2009) 043503.
[32] T. Driscoll, H.-T. Kim, B.-G. Chae, B.-J. Kim, Y.-W. Lee, N.M. Jokerst, et al., Memory metamaterials., Science (New York, N.Y.). 325 (2009) 1518-21.
[33] M. Di Ventra, Y.V. Pershin, L. Chua, Circuit elements with memory: memristors, memcapacitors, and meminductors, Proceedings Of the IEEE. 97 (2009) 1717–1724.
[34] S.H. Jo, K.H. Kim, T. Chang, S. Gaba, W. Lu, Si Memristive devices applied to memory and neuromorphic circuits, in: Circuits and Systems (ISCAS), Proceedings Of 2010 IEEE International Symposium On, IEEE, 2010: p. 13–16.
[35] Z.-M. Liao, C. Hou, H.-Z. Zhang, D.-S. Wang, D.-P. Yu, Evolution of resistive switching over bias duration of single Ag[sub 2]S nanowires, Applied Physics Letters. 96 (2010) 203109.
[36] N. Archontas, J. Georgiou, B. Jamaa, M. Haykel, S. Carrara, G. De Micheli, Characterization of memristive Poly-Si Nanowires via empirical physical modelling, in: Circuits and Systems (ISCAS), Proceedings Of 2010 IEEE International Symposium On, IEEE, 2010: p. 1675–1678.
[37] R. Muenstermann, T. Menke, R. Dittmann, R. Waser, Coexistence of Filamentary and Homogeneous Resistive Switching in Fe-Doped SrTiO(3) Thin-Film Memristive Devices., Advanced Materials (Deerfield Beach, Fla.). (2010) 1-4.
[38] A.A. Zakhidov, B. Jung, J.D. Slinker, H.D. Abruña, G.G. Malliaras, A light-emitting memristor, Organic Electronics. 11 (2010) 150-153.
[39] D. Sacchetto, M.H. Ben-Jamaa, S. Carrara, G. De Micheli, Y. usuf Leblebici, Memristive Devices Fabricated with Silicon Nanowire Schottky Barrier Transistors, Infoscience.epfl.ch. (2010) 9-12.
[40] N.R. McDonald, R.E. Pino, P.J. Rozwood, B.T. Wysocki, Analysis of Dynamic Linear and Non-linear Memristor Device Models for Emerging Neuromorphic Computing Hardware Design, Arxiv Preprint arXiv:1008.5117. (2010) 5.
[41] R. Riaza, Dynamical properties of electrical circuits with fully nonlinear memristors, (2010) 19.
[42] H. Yu, W. Fei, A New Modified Nodal Analysis for Nano-Scale Memristor Circuit Simulation, ReCALL. (2010) 3148-3151.
[43] E. Lehtonen, J.H. Poikonen, M. Laiho, Two memristors suffice to compute all Boolean functions, Electronics Letters. 46 (2010) 230.
[44] M. Laiho, E. Lehtonen, Cellular nanoscale network cell with memristors for local implication logic and synapses, in: Circuits and Systems (ISCAS), Proceedings Of 2010 IEEE International Symposium On, IEEE, 2010: p. 2051–2054.
[45] Z. Lin, H. Wang, Efficient Image Encryption Using a Chaos-based PWL Memristor, IETE Technical Review. 27 (2010) 318.
[46] B.L. Mouttet, Memristor Pattern Recognition Circuit Architecture for Robotics, Google Knol. (2008).
[47] D.B. Strukov, R.S. Williams, Four-dimensional address topology for circuits with stacked multilayer crossbar arrays., Proceedings Of the National Academy Of Sciences Of the United States Of America. 106 (2009) 20155-8.

[48] Y.V. Pershin, S. La Fontaine, M. Di Ventra, Memristive model of amoeba learning, Physical Review E. 80 (2009) 1-6.
[49] K. Eshraghian, K.R. Cho, O. Kavehei, S.-ku Kang, D. Abbott, S.-M.S. Kang, Memristor MOS Content Addressable Memory (MCAM): Hybrid Architecture for Future High Performance Search Engines, Integration The Vlsi Journal. X (2010) 10.
[50] E. Lehtonen, M. Laiho, CNN using memristors for neighborhood connections, in: Cellular Nanoscale Networks and Their Applications (CNNA), 2010 12th International Workshop On, IEEE, 2010: p. 1–4.
[51] J. Valsa, D. Biolek, Z. Biolek, An analogue model of the memristor, International Journal Of Numerical Modelling: Electronic Networks, Devices and Fields. (2010).
[52] O. Kavehei, A. Iqbal, Y.S. Kim, K. Eshraghian, S.F. Al-Sarawi, D. Abbott, The fourth element: characteristics, modelling and electromagnetic theory of the memristor, Proceedings Of the Royal Society A. (2010).
[53] Y.V. Pershin, M. Di Ventra, Practical approach to programmable analog circuits with memristors, Astronomy. (2009) 1-7.
[54] R.S. Williams, How We Found The Missing Memristor, IEEE Spectrum. 45 (2008) 28-35.
[55] D.L. Lewis, H.-H.S. Lee, Architectural evaluation of 3D stacked RRAM caches, IEEE, 2009.
[56] W. M. Arden, The International Technology Roadmap for Semiconductors, Current Opinion In Solid State and Materials Science. 6 (2002) 371-377.
[57] D.B. Strukov, R.S. Williams, Exponential ionic drift: fast switching and low volatility of thin-film memristors, Applied Physics A. 94 (2008) 515-519.
[58] M. Lin, A. El Gamal, Y.-C. Lu, S. Wong, Performance benefits of monolithically stacked 3D-FPGA, Proceedings Of the Internation Symposium On Field Programmable Gate arrays - FPGA'06. (2006) 113.
[59] V. Betz, J. Rose, A. Marquardt, Architecture and CAD for Deep-Submicron FPGAs, Kluwer Academic Publishers Norwell, MA, USA, 1999.
[60] W. Wang, T.T. Jing, B. Butcher, FPGA based on integration of memristors and CMOS devices, in: Circuits and Systems (ISCAS), Proceedings Of 2010 IEEE International Symposium On, IEEE, 2010: p. 1963–1966.
[61] G.S. Snider, P.J. Kuekes, R.S. Williams, CMOS-like logic in defective, nanoscale crossbars, Nanotechnology. 15 (2004) 881-891.
[62] M.R. Stan, P.D. Franzon, S.C. Goldstein, J.C. Lach, M.M. Ziegler, Molecular electronics: from devices and interconnect to circuits and architecture, Proceedings Of the IEEE. 9 (2003) 1940-1957.
[63] D.B. Strukov, K.K. Likharev, CMOL FPGA: a reconfigurable architecture for hybrid digital circuits with two-terminal nanodevices, Nanotechnology. 16 (2005) 888-900.
[64] D.O. Hebb, The organization of behavior: a neuropsychological theory, Wiley, 1949.
[65] R. Linsker, From basic network principles to neural architecture: Emergence of spatial-opponent cells, Proceedings Of the National Academy Of Sciences Of the United States Of America. 83 (1986) 7508.
[66] R. Linsker, From basic network principles to neural architecture: Emergence of orientation columns, Proceedings Of the National Academy Of Sciences Of the United States Of America. 83 (1986) 8779.
[67] R. Linsker, From basic network principles to neural architecture: Emergence of orientation columns, Proceedings Of the National Academy Of Sciences Of the United States Of America. 83 (1986) 8779.
[68] R. Linsker, A local learning rule that enables information maximization for arbitrary input distributions, Neural Computation. 9 (1997) 1661–1665.
[69] R. Linsker, Self-organization in a perceptual network, Computer. 21 (1988) 105-117.
[70] T. Roska, L. Chua, The CNN universal machine: an analogic array computer, IEEE Transactions On Circuits and Systems II: Analog and Digital Signal Processing. 40 (1993) 163-173.
[71] L. Chua, L. Yang, K.R. Krieg, Signal processing using cellular neural networks, Journal Of VLSI Signal Processing. 3 (1991) 25-51.
[72] L.A. Finelli, S. Haney, M. Bazhenov, M. Stopfer, T.J. Sejnowski, Synaptic Learning Rules and Sparse Coding in a Model Sensory System, PLoS Computational Biology. 4 (2008) e1000062.
[73] J.M. Young, W.J. Waleszczyk, C. Wang, M.B. Calford, B. Dreher, K. Obermayer, Cortical reorganization consistent with spike timing-but not correlation-dependent plasticity., Nature Neuroscience. 10 (2007) 887-95.
[74] G. Bi, M.-ming Poo, Synaptic modification by correlated activity: Hebb's postulate revisited., Annual Review Of Neuroscience. 24 (2001) 139-66.
[75] G. Bi, M.-ming Poo, Synaptic modifications in cultured hippocampal neurons: dependence on spike timing, synaptic strength, and postsynaptic cell type, Journal Of Neuroscience. 18 (1998) 10464-10472.
[76] A. Afifi, A. Ayatollahi, F. Raissi, STDP implementation using memristive nanodevice in CMOS-Nano neuromorphic networks, IEICE Electronics Express. 6 (2009) 148-153.
[77] B. Linares-Barranco, T. Serrano-Gotarredona, Memristance can explain spike-time-dependent-plasticity in neural synapses, Nature. (2009) 2-5.
[78] D. Vavoulis, Balanced plasticity and stability of the electrical properties of a molluscan modulatory interneuron after classical conditioning: a computational study, Frontiers In Behavioral Neuroscience. 4 (2010) 1-3.

[79] T. Nakagaki, R. Kobayashi, Y. Nishiura, T. Ueda, Obtaining multiple separate food sources: behavioural intelligence in the Physarum plasmodium., Proceedings. Biological Sciences / The Royal Society. 271 (2004) 2305-10.
[80] A. Adamatzky, Physarum machines, World Scientific, 2010.
[81] T. Saigusa, A. Tero, T. Nakagaki, Y. Kuramoto, Amoebae Anticipate Periodic Events, Physical Review Letters. 100 (2008).
[82] M. Jaiswal, R. Menon, Polymer electronic materials: a review of charge transport, Polymer International. 55 (2006) 1371-1384.
[83] Q. Ling, D. Liaw, C. Zhu, D. Chan, E. Kang, K. Neoh, Polymer electronic memories: Materials, devices and mechanisms, Progress In Polymer Science. 33 (2008) 917-978.
[84] A.J. Heeger, Semiconducting and metallic polymers: the fourth generation of polymeric materials, Angewandte Chemie International Edition. 40 (2001) 2591.
[85] R. Mülhaupt, Hermann Staudinger and the origin of macromolecular chemistry., Angewandte Chemie (International Ed. In English). 43 (2004) 1054-63.
[86] H. Sinn, W. Kaminsky, Ziegler-Natta catalysis, Adv. Organomet. Chem. 18 (1980) 99–149.
[87] A.J. Heeger, S. Kivelson, J.R. Schrieffer, Solitons in conducting polymers, Reviews Of Modern Physics. (1988).
[88] C. Chiang, C. Fincher, Y. Park, A.J. Heeger, H. Shirakawa, E. Louis, et al., Electrical Conductivity in Doped Polyacetylene, Physical Review Letters. 39 (1977) 1098-1101.
[89] P.J. Nigrey, A.G. MacDiarmid, A.J. Heeger, Electrochemistry of polyacetylene, (CH) x : electrochemical doping of (CH) x films to the metallic state, Journal Of the Chemical Society, Chemical Communications. (1979) 594.
[90] L. Huo, L. Cao, H. Cui, D. Wang, G. Zeng, S. Xi, Preparation and Characterization of DBSA Doped Polyaniline Thin Films, Molecular Crystals and Liquid Crystals. 337 (1999) 261-264.
[91] W.P. Su, J.R. Schrieffer, A.J. Heeger, Solitons in Polyacetylene, Physical Review Letters. 42 (1979) 1698-1701.
[92] W.P. Su, J.R. Schrieffer, A.J. Heeger, Soliton excitations in polyacetylene, Physical Review B. 22 (1980) 2099.
[93] C. Fincher, C. Chen, A.J. Heeger, A.G. MacDiarmid, J. Hastings, Structural Determination of the Symmetry-Breaking Parameter in trans-(CH)_{x}, Physical Review Letters. 48 (1982) 100-104.
[94] C. Yannoni, T. Clarke, Molecular Geometry of cis- and trans-Polyacetylene by Nutation NMR Spectroscopy, Physical Review Letters. 51 (1983) 1191-1193.
[95] D. Campbell, A. Bishop, K. Fesser, Polarons in quasi-one-dimensional systems, Physical Review B. 26 (1982) 6862–6874.
[96] S. Brazorski, N. Kirova, Excitons, polarons and bipolarons in conducting polymers, Jounal Of Experimental and Theoretical Physics Letters. (1981).
[97] K. Amanoa, H. Ishikawaa, A. Kobayashia, M. Satoha, E. Hasegawaa, Thermal stability of chemically synthesized polyaniline, Synthetic Metals. 62 (1994) 229-232.
[98] M. Pyo, J.R. Reynolds, L.F. Warren, H.O. Marcy, Long-term redox switching stability of polypyrrole, Synthetic Metals. 68 (1994) 71-77.
[99] J.C. Thieblemont, M.F. Planche, C. Petrescu, J.M. Bouvier, G. Bidan, Stability of chemically synthesized polypyrrole films, Synthetic Metals. 59 (1993) 81-96.
[100] A. Ray, G. Asturias, D. Kershner, A. Richter, A.G. MacDiarmid, A. Epstein, Polyaniline: Doping, structure and derivatives, Synthetic Metals. 29 (1989) 141–150.
[101] S. Khor, K.G. Neoh, E. Kang, Synthesis and characterization of some polyaniline–organic acceptor complexes, Journal Of Applied Polymer Science. 40 (1990) 2015–2025.
[102] Q. Pei, G. Yu, C. Zhang, Y. Yang, A.J. Heeger, Polymer light-emitting electrochemical cells., Science (New York, N.Y.). 269 (1995) 1086-8.
[103] J.H. Burroughes, D.D.C. Bradley, A.R. Brown, R.N. Marks, K. Mackay, R.H. Friend, et al., Light-emitting diodes based on conjugated polymers, Nature. 347 (1990) 539-541.
[104] J. Paloheimo, H. Stubb, P. Yli-Lahti, P. Kuivalainen, Field-effect conduction in polyalkylthiophenes, Synthetic Metals. 41 (1991) 563–566.
[105] Y.-Y. Noh, J.-J. Kim, K. Yase, S. Nagamatsu, Organic field-effect transistors by a wet-transferring method, Applied Physics Letters. 83 (2003) 1243.
[106] K. Seshadri, C.D. Frisbie, Potentiometry of an operating organic semiconductor field-effect transistor, Applied Physics Letters. 78 (2001) 993.
[107] C. Zhou, D. Newns, J. Misewich, P. Pattnaik, A field effect transistor based on the Mott transition in a molecular layer, Applied Physics Letters. 70 (1997) 598.
[108] G. Wang, Poly(3-hexylthiophene) field-effect transistors with high dielectric constant gate insulator, Journal Of Applied Physics. 95 (2004) 316.
[109] E. Genies, A. Boyle, M. Lapowski, C. Tsintavis, Polyaniline: A historical survey, Synthetic Metals. 36 (1990) 139-182.

[110] F. Lux, Properties of electronically conductive polyaniline: a comparison between well-known literature data and some recent experimental findings, Polymer. 35 (1994) 2915-2936.
[111] A.G. MacDiarmid, A. Epstein, The concept of secondary doping as applied to polyaniline, Synthetic Metals. 65 (1994) 103-116.
[112] A.G. Green, A.E. Woodhead, Aniline-black and allied compounds. Part I, Journal Of the Chemical Society, Transactions. 97 (1910) 2388.
[113] J. Ginder, A. Richter, A.G. MacDiarmid, A. Epstein, Insulator-to-metal transition in polyaniline, Solid State Communications. 63 (1987) 97-101.
[114] F. Wudl, R.O. Angus, F.L. Lu, P.M. Allemand, D. Vachon, M. Nowak, et al., Poly-p-phenyleneamineimine: synthesis and comparison to polyaniline, Journal Of the American Chemical Society. 109 (1987) 3677-3684.
[115] A.G. MacDiarmid, J. Chiang, A. Richter, A. Epstein, Polyaniline: a new concept in conducting polymers, Synthetic Metals. 18 (1987) 285-290.
[116] A. Epstein, J. Ginder, F. Zuo, H. Woo, D. Tanner, A. Richter, et al., Insulator-to-metal transition in polyaniline: Effect of protonation in emeraldine, Synthetic Metals. 21 (1987) 63-70.
[117] N. Sariciftci, M. Bartonek, H. Kuzmany, H. Neugebauer, A. Neckel, Analysis of various doping mechanisms in polyaniline by optical, FTIR and Raman spectroscopy, Synthetic Metals. 29 (1989) 193-202.
[118] E. Kang, K.G. Neoh, K. Tan, Polyaniline : a polymer with many interesting intrinsic redox states, Progress In Polymer Science. 23 (1998) 277–324.
[119] M. Ando, Optical ozone detection by use of polyaniline film, Solid State Ionics. 152-153 (2002) 819-822.
[120] S. Demarcos, N. Alcubierre, J. Galban, J. Castillo, Reagentless system for sulphite determination based on polyaniline, Analytica Chimica Acta. 502 (2004) 7-13.
[121] Z. Jin, Y. Su, Y. Duan, Development of a polyaniline-based optical ammonia sensor, Sensors and Actuators B: Chemical. 72 (2001) 75–79.
[122] S. Demarcos, O. Wolfbeis, Optical sensing of pH based on polypyrrole films, Analytica Chimica Acta. 334 (1996) 149-153.
[123] O.A. Sadik, G.G. Wallace, Pulsed amperometric detection of proteins using antibody containing conducting polymers, Analytica Chimica Acta. 279 (1993) 209-212.
[124] N.C. Foulds, C.R. Lowe, Immobilization of glucose oxidase in ferrocene-modified pyrrole polymers., Analytical Chemistry. 60 (1988) 2473-8.
[125] Y.S. Lee, B.S. Joo, N.J. Choi, J.O. Lim, J.S. Huh, D.D. Lee, Visible optical sensing of ammonia based on polyaniline film, Sensors and Actuators B: Chemical. 93 (2003) 148–152.
[126] M.A. El-Sherif, Fiber-optic chemical sensor using polyaniline as modified cladding material, IEEE Sensors Journal. 3 (2003) 5-12.
[127] M. Ram, Comparative studies on Langmuir–Schaefer films of polyanilines, Synthetic Metals. 100 (1999) 249-259.
[128] A. Riul Jr, L. Mattoso, G. Telles, P. Herrmann, L. Colnage, N. Parizotto, et al., Characterization of Langmuir-Blodgett films of parent polyaniline, Thin Solid Films. 284-285 (1996) 177-180.
[129] J. Cheung, M. Rubner, Fabrication of electrically conductive Langmuir-Blodgett multilayer films of polyaniline, Thin Solid Films. 244 (1994) 990-994.
[130] V. Troitsky, T. Berzina, Langmuir-Blodgett assemblies with patterned conductive polyaniline layers, Materials Science and Engineering:. 22 (2002) 239-244.
[131] V. Troitsky, T. Berzina, M.P. Fontana, Deposition of uniform conductive polyaniline films and approach for their patterning, Synthetic Metals. 129 (2002) 39–46.
[132] T. Porter, D. Thompson, M. Bradley, Scanning force microscope studies of Langmuir-Blodgett polyaniline thin films, Thin Solid Films. 288 (1996) 268–271.
[133] C. Constantino, A. Dhanabalan, A. Riul, O. Oliveira, Surface potentials of polyaniline lb films, Synthetic Metals. 101 (1999) 688-689.
[134] A. Ulman, An introduction to ultrathin organic films: from Langmuir-Blodgett to self-assembly, Academic Press Boston, 1991.
[135] D. Fenton, J. Parker, P. Wright, Complexes of alkali metal ions with poly(ethylene oxide), Polymer. 14 (1973) 589-589.
[136] M.B. Armand, J.M. Chabagno, M.J. Duclot, Fast ion transport in solids, 1979.
[137] B. Martin, A. Wagner, H. Kliem, A thermoelectric voltage effect in polyethylene oxide, Journal Of Physics D: Applied Physics. 36 (2003) 343-347.
[138] G. Mao, M.-L. Saboungi, D.L. Price, Y.S. Badyal, H.E. Fischer, Lithium environment in PEO-LiClO 4 polymer electrolyte, Europhysics Letters (EPL). 54 (2001) 347-353.
[139] G.S. MacGlashan, Y.G. Andreev, P.G. Bruce, Structure of the polymer electrolyte poly (ethylene oxide) 6: LiAsF6, Nature. 398 (1999) 792–794.
[140] T.J. Singh, S.V. Bhat, Morphology and conductivity studies of a new solid polymer electrolyte: (PEG)xLiClO4, Bulletin Of Materials Science. 26 (2003) 707-714.
[141] A. Wagner, H. Kliem, Dispersive ionic space charge relaxation in solid polymer electrolytes. II. Model and simulation, Journal Of Applied Physics. 91 (2002) 6638.

[142] A. Wagner, H. Kliem, Dispersive ionic space charge relaxation in solid polymer electrolytes. I. Experimental system polyethylene oxide, Journal Of Applied Physics. 91 (2002) 6630.
[143] K. Murata, An overview of the research and development of solid polymer electrolyte batteries, Electrochimica Acta. 45 (2000) 1501-1508.
[144] A. Manuel Stephan, Review on gel polymer electrolytes for lithium batteries, European Polymer Journal. 42 (2005) 21-42.
[145] J. Song, Review of gel-type polymer electrolytes for lithium-ion batteries, Journal Of Power Sources. 77 (1999) 183-197.
[146] A. Manuel Stephan, K. Nahm, Review on composite polymer electrolytes for lithium batteries, Polymer. 47 (2006) 5952-5964.
[147] C. Berthier, W. Gorecki, M. Minier, M.B. Armand, J.M. Chabagno, P. Rigaud, Microscopic investigation of ionic conductivity in alkali metal salts-poly(ethylene oxide) adducts, Solid State Ionics. 11 (1983) 91-95.
[148] W. Wieczorek, Z. Florjanczyk, J. Stevens, Composite polyether based solid electrolytes, Electrochimica Acta. 40 (1995) 2251–2258.
[149] R. Borkowska, J. Laskowski, J. Płocharski, J. Przyłuski, W. Wieczorek, Performance of acrylate-poly(ethylene oxide) polymer electrolytes in lithium batteries, Journal Of Applied Electrochemistry. 23 (1993) 991-995.
[150] R.F.T. Stepto, Polymer networks: principles of their formation, structure and properties, Blackie Academic & Professional London, 1998.
[151] L.H. Sperling, Introduction to physical polymer science, Wiley Online Library, 1986.
[152] J.R. MacCallum, C.A. Vincent, Polymer electrolyte reviews, Springer, 1989.
[153] D.W. Murphy, J. Broadhead, Materials for advanced batteries, (1980).
[154] B. Scrosati, Applications of electroactive polymers, Springer, 1993.
[155] Y. Ito, K. Kanehori, K. Miyauchi, T. Kudo, Ionic conductivity of electrolytes formed from PEO-LiCF3SO3 complex low molecular weight poly(ethylene glycol), Journal Of Materials Science. 22 (1987) 1845-1849.
[156] I.E. Kelly, J.R. Owen, B.C.H. Steele, Poly(ethylene oxide) electrolytes for operation at near room temperature, Journal Of Power Sources. 14 (1985) 13-21.
[157] G. Nagasubramanian, 12-Crown-4 Ether-Assisted Enhancement of Ionic Conductivity and Interfacial Kinetics in Polyethylene Oxide Electrolytes, Journal Of The Electrochemical Society. 137 (1990) 3830.
[158] V. Erokhin, T. Berzina, M.P. Fontana, Hybrid electronic device based on polyaniline-polyethyleneoxide junction, Journal Of Applied Physics. 97 (2005) 064501.
[159] T. Berzina, V. Erokhin, M.P. Fontana, Spectroscopic investigation of an electrochemically controlled conducting polymer-solid electrolyte junction, Journal Of Applied Physics. 101 (2007) 024501.
[160] G.G. Roberts, ed., Langmuir-Blodgett films, New York, New York, USA, Springer, 1990.
[161] A. Smerieri, V. Erokhin, M.P. Fontana, Origin of current oscillations in a polymeric electrochemically controlled element, Journal Of Applied Physics. 103 (2008) 094517.
[162] E.W. Paul, A.J. Ricco, M.S. Wrighton, Resistance of polyaniline films as a function of electrochemical potential and the fabrication of polyaniline-based microelectronic devices, The Journal Of Physical Chemistry. 89 (1985) 1441-1447.
[163] T. Abdiryim, Z. Xiao-Gang, R. Jamal, Comparative studies of solid-state synthesized polyaniline doped with inorganic acids, Materials Chemistry and Physics. 90 (2005) 367-372.
[164] A. Smerieri, T. Berzina, V. Erokhin, M.P. Fontana, A functional polymeric material based on hybrid electrochemically controlled junctions, Materials Science and Engineering: C. 28 (2008) 18-22.
[165] K. Rossberg, G. Paasch, L. Dunsch, S. Ludwig, The influence of porosity and the nature of the charge storage capacitance on the impedance behaviour of electropolymerized polyaniline films, Journal Of Electroanalytical Chemistry. 443 (1998) 49–62.
[166] Y. Saito, H. Kataoka, S. Murata, Y. Uetani, K. Kii, Y. Minamizaki, Designing of a urea-containing polymer gel electrolyte based on the concept of activation of the interaction between the carrier ion and polymer, J. Phys. Chem. B. 107 (2003) 8805–8811.
[167] A.N. Zaikin, A.M. Zhabotinsky, Concentration wave propagation in two-dimensional liquid-phase self-oscillating system., Nature. 225 (1970) 535-7.
[168] S. Stafström, J. Bredas, A. Epstein, H. Woo, D. Tanner, W. Huang, et al., Polaron lattice in highly conducting polyaniline: Theoretical and optical studies, Physical Review Letters. 59 (1987) 1464–1467.
[169] V. Erokhin, T. Berzina, M.P. Fontana, Polymeric elements for adaptive networks, Crystallography Reports. 52 (2007) 159-166.
[170] P.R. Benjamin, K. Staras, G. Kemenes, A systems approach to the cellular analysis of associative learning in the pond snail Lymnaea, Learning & Memory. 7 (2000) 124.
[171] E. Izhikevich, Which model to use for cortical spiking neurons?, IEEE Transactions On Neural Networks. 15 (2004) 1063–1070.
[172] J. Feng, Computational Neuroscience: A Comprehensive Approach, Boca raton, CRC PRESS, 2004.
[173] W. a Gazotti Jr., M.-A. De Paoli, High yield preparation of a soluble polyaniline derivative, Synthetic Metals. 80 (1996) 263-269.

[174] Y. Haba, E. Segal, M. Narkis, A. Siegmann, Polymerization of aniline in the presence of DBSA in an aqueous dispersion, Synthetic Metals. (1999).
[175] V. Erokhin, T. Berzina, P. Camorani, M.P. Fontana, On the stability of polymeric electrochemical elements for adaptive networks, Colloids and Surfaces A: Physicochemical and Engineering Aspects. 321 (2008) 218-221.
[176] A. Dhanabalan, A. Riul Jr, C. Constantino, O. Oliveira Jr, Langmuir monolayers from parent polyaniline, Synthetic Metals. 101 (1999) 690-690.
[177] N. Gospodinova, L. Terlemezyan, P. Mokreva, A. Tadjer, A new approach to the study of oxidative polymerization of aniline and transformations of polyaniline. Support by means of the Hueckel method, Polymer. 37 (1996) 4431–4433.
[178] R. Dabke, Electrochemistry of polyaniline Langmuir–Blodgett films, Thin Solid Films. 335 (1998) 203-208.
[179] J. Daillant, A. Gibaud, X-ray and neutron reflectivity: principles and applications, Springer, 1999.
[180] L. Parratt, Surface Studies of Solids by Total Reflection of X-Rays, Physical Review. 95 (1954) 359-369.
[181] L. Nevot, P. Croce, Characterization of surfaces by grazing incidence x-ray reflection. Application to the polishing study of several silicate glasses, Rev. Phys. Appl. 15 (1980) 761–779.
[182] L. Cristofolini, M.P. Fontana, P. Camorani, T. Berzina, a Nabok, Doping-induced conductivity transitions in molecular layers of polyaniline: optical studies of electronic state changes., Langmuir : The ACS Journal Of Surfaces and Colloids. 26 (2010) 5829-35.
[183] K. Lee, S. Cho, S.H. Park, A.J. Heeger, C.-W. Lee, S.-H. Lee, Metallic transport in polyaniline., Nature. 441 (2006) 65-8.
[184] M. Born, E. Wolf, Principles of Optics, Cambridge, Cambridge University Press, 1999.
[185] L. Cristofolini, S. Arisi, M. Fontana, Glass transition and relaxation following PhotoPerturbation in thin polymeric films, Physical Review Letters. 85 (2000) 4912-5.
[186] B. Jérôme, J. Commandeur, Dynamics of glasses below the glass transition, Nature. 386 (1997) 589-592.
[187] P.R. Benjamin, G. Kemenes, I. Kemenes, Non-synaptic neuronal mechanisms of learning and memory in gastropod molluscs., Frontiers In Bioscience : A Journal and Virtual Library. 13 (2008) 4051-7.
[188] W. Zhang, D.J. Linden, The other side of the engram: experience-driven changes in neuronal intrinsic excitability., Nature Reviews. Neuroscience. 4 (2003) 885-900.
[189] C.H. Bailey, M. Giustetto, Y.Y. Huang, R.D. Hawkins, E.R. Kandel, Is heterosynaptic modulation essential for stabilizing Hebbian plasticity and memory?, Nature Reviews. Neuroscience. 1 (2000) 11-20.
[190] F. Alibart, S. Pleutin, D. Guérin, C. Novembre, S. Lenfant, K. Lmimouni, et al., An Organic Nanoparticle Transistor Behaving as a Biological Spiking Synapse, Advanced Functional Materials. 20 (2010) 330-337.
[191] I. Kemenes, V.A. Straub, E.S. Nikitin, K. Staras, M. O'Shea, G. Kemenes, et al., Role of delayed nonsynaptic neuronal plasticity in long-term associative memory., Current Biology : CB. 16 (2006) 1269-79.
[192] D. Vavoulis, V.A. Straub, I. Kemenes, G. Kemenes, J. Feng, P.R. Benjamin, Dynamic control of a central pattern generator circuit: a computational model of the snail feeding network., The European Journal Of Neuroscience. 25 (2007) 2805-18.
[193] V.A. Straub, P.R. Benjamin, Extrinsic Modulation and Motor Pattern Generation in a Feeding Network : a Cellular Study, 21 (2001) 1767-1778.
[194] A. Ruehli, P. Brennan, The modified nodal approach to network analysis, IEEE Transactions On Circuits and Systems. 22 (1975) 504-509.
[195] V. Litovski, VLSI circuit simulation and optimization, (1997).
[196] L. Cristofolini, M.P. Fontana, P. Camorani, T. Berzina, A. Nabok, Doping-induced conductivity transitions in molecular layers of polyaniline: optical studies of electronic state changes., Langmuir : The ACS Journal Of Surfaces and Colloids. 26 (2010) 5829-35.
[197] a N. Burkitt, A review of the integrate-and-fire neuron model: I. Homogeneous synaptic input., Biological Cybernetics. 95 (2006) 1-19.
[198] A.L. Hodgkin, A.F. Huxley, A quantitative description of membrane current and its application to conduction and excitation in nerve., The Journal Of Physiology. 117 (1952) 500-44.
[199] G.G. de Polavieja, A. Harsch, I. Kleppe, H.P.C. Robinson, M. Juusola, Stimulus history reliably shapes action potential waveforms of cortical neurons., The Journal Of Neuroscience : The Official Journal Of the Society For Neuroscience. 25 (2005) 5657-65.
[200] H.C. Tuckwell, Introduction to theoretical neurobiology: Linear cable theory and dendritic structure, Cambridge Univ Pr, 1988.
[201] D.J. Amit, N. Brunel, Model of global spontaneous activity and local structured activity during delay periods in the cerebral cortex., Cerebral Cortex (New York, N.Y. : 1991). 7 (1997) 237-52.
[202] X.J. Wang, Probabilistic decision making by slow reverberation in cortical circuits, Neuron. 36 (2002) 955–968.
[203] N. Brunel, X.J. Wang, Effects of neuromodulation in a cortical network model of object working memory dominated by recurrent inhibition, Journal Of Computational Neuroscience. 11 (2001) 63–85.
[204] E.T. Rolls, M. Loh, G. Deco, An attractor hypothesis of obsessive-compulsive disorder., The European Journal Of Neuroscience. 28 (2008) 782-93.

[205] G. Deco, E.T. Rolls, R. Romo, Stochastic dynamics as a principle of brain function., Progress In Neurobiology. 88 (2009) 1-16.
[206] G. Deco, E.T. Rolls, Attention, short-term memory, and action selection: a unifying theory., Progress In Neurobiology. 76 (2005) 236-56.
[207] E.T. Rolls, G. Deco, The Noisy Brain : Stochastic Dynamics as a Principle of Brain Function, 2010.
[208] G. Deco, E.T. Rolls, Decision-making and Weber's law: a neurophysiological model, European Journal Of Neuroscience. 24 (2006) 901–916.
[209] R. Romo, A. Hernández, A. Zainos, Neuronal correlates of a perceptual decision in ventral premotor cortex., Neuron. 41 (2004) 165-73.
[210] V. de Lafuente, R. Romo, Neuronal correlates of subjective sensory experience., Nature Neuroscience. 8 (2005) 1698-703.
[211] R. Romo, A. Hernández, A. Zainos, L. Lemus, C.D. Brody, Neuronal correlates of decision-making in secondary somatosensory cortex., Nature Neuroscience. 5 (2002) 1217-25.
[212] C.D. Brody, Timing and Neural Encoding of Somatosensory Parametric Working Memory in Macaque Prefrontal Cortex, Cerebral Cortex. 13 (2003) 1196-1207.
[213] A. Hernández, A. Zainos, R. Romo, Temporal evolution of a decision-making process in medial premotor cortex., Neuron. 33 (2002) 959-72.
[214] N. Brunel, S. Sergi, Firing frequency of leaky intergrate-and-fire neurons with synaptic current dynamics., Journal Of theoretical Biology. 195 (1998) 87-95.
[215] N. Brunel, V. Hakim, Fast Global Oscillations in Networks of Integrate-and-Fire Neurons with Low Firing Rates, Neural Computation. 11 (1999) 1621-1671.
[216] G.T. Fechner, H.E. Adler, D.H. Howes, E.G. Boring, Elements of psychophysics, (1966).
[217] G. a Gescheider, S.J. Bolanowski, R.T. Verrillo, D.J. Arpajian, T.F. Ryan, Vibrotactile intensity discrimination measured by three methods., The Journal Of the Acoustical Society Of America. 87 (1990) 330-8.
[218] G. Wald, Human vision and the spectrum, Science (New York, N.Y.). 101 (1945) 653-8.
[219] J.B.J. Smeets, E. Brenner, Grasping Weber's law., Current Biology : CB. 18 (2008) R1089-90; author reply R1090-1.
[220] K.O. Johnson, S.S. Hsiao, T. Yoshioka, Book Review: Neural Coding and the Basic Law of Psychophysics, The Neuroscientist. 8 (2002) 111-121.
[221] S. Dehaene, The neural basis of the Weber-Fechner law: a logarithmic mental number line., Trends In Cognitive Sciences. 7 (2003) 145-147.
[222] K.H. Britten, M.N. Shadlen, W.T. Newsome, J.A. Movshon, The analysis of visual motion: a comparison of neuronal and psychophysical performance., The Journal Of Neuroscience : The Official Journal Of the Society For Neuroscience. 12 (1992) 4745-65.
[223] S. Celebrini, W.T. Newsome, Neuronal and psychophysical sensitivity to motion signals in extrastriate area MST of the macaque monkey., The Journal Of Neuroscience : The Official Journal Of the Society For Neuroscience. 14 (1994) 4109-24.
[224] F. Vega-Bermudez, K.O. Johnson, SA1 and RA receptive fields, response variability, and population responses mapped with a probe array., Journal Of Neurophysiology. 81 (1999) 2701-10.
[225] V.C. Smith, J. Pokorny, B.B. Lee, D.M. Dacey, Sequential processing in vision: The interaction of sensitivity regulation and temporal dynamics., Vision Research. 48 (2008) 2649-56.
[226] K. Morita, R. Kalra, K. Aihara, H.P.C. Robinson, Recurrent synaptic input and the timing of gamma-frequency-modulated firing of pyramidal cells during neocortical "UP" states., The Journal Of Neuroscience : The Official Journal Of the Society For Neuroscience. 28 (2008) 1871-81.
[227] J. Fiser, C. Chiu, M. Weliky, Small modulation of ongoing cortical dynamics by sensory input during natural vision., Nature. 431 (2004) 573-8.
[228] G. Buzsáki, Rhythms of the Brain, Oxford University Press, USA, 2006.
[229] H. Lee, G.V. Simpson, N.K. Logothetis, G. Rainer, Phase locking of single neuron activity to theta oscillations during working memory in monkey extrastriate visual cortex., Neuron. 45 (2005) 147-56.
[230] C. Hölscher, R. Anwyl, M.J. Rowan, Stimulation on the positive phase of hippocampal theta rhythm induces long-term potentiation that can Be depotentiated by stimulation on the negative phase in area CA1 in vivo., The Journal Of Neuroscience : The Official Journal Of the Society For Neuroscience. 17 (1997) 6470-7.
[231] R. Canolty, E. Edwards, S. Dalal, M. Soltani, S. Nagarajan, H. Kirsch, et al., High gamma power is phase-locked to theta oscillations in human neocortex, Science. 313 (2006) 1626.
[232] D.E. Broadbent, The magic number seven after fifteen years, Studies In Long-term Memory. (1975) 3–18.
[233] J.E. Lisman, M.A.P. Idiart, Storage of 7±2 short-term memories in oscillatory subcycles, Science. 267 (1995) 1512–1515.
[234] N. Cowan, The magical number 4 in short-term memory: a reconsideration of mental storage capacity., The Behavioral and Brain Sciences. 24 (2001) 87-114; discussion 114-85.
[235] O. Jensen, Maintenance of multiple working memory items by temporal segmentation, Neuroscience. 139 (2006) 237–249.

[236] J.E. Lisman, G. Buzsáki, A neural coding scheme formed by the combined function of gamma and theta oscillations, Schizophrenia Bulletin. (2008).
[237] P. Fries, J.H. Reynolds, A.E. Rorie, R. Desimone, Modulation of oscillatory neuronal synchronization by selective visual attention, Science. 291 (2001) 1560.
[238] P. Fries, A mechanism for cognitive dynamics: neuronal communication through neuronal coherence, Trends In Cognitive Sciences. 9 (2005) 474–480.
[239] D.B. Lindsley, Psychological phenomena and the electroencephalogram., Electroencephalography and Clinical Neurophysiology. 4 (1952) 443.
[240] R.W. Lansing, Relation of brain and tremor rhythms to visual reaction time☆, Relation Of Brain and Tremor Rhythms To Visual Reaction Time. 9 (1957) 497–504.
[241] J.D. Green, A.A. Arduini, Hippocampal electrical activity in arousal, Journal Of Neurophysiology. 17 (1954) 533.
[242] D.S. Rizzuto, J.R. Madsen, E.B. Bromfield, A. Schulze-Bonhage, D. Seelig, R. Aschenbrenner-Scheibe, et al., Reset of human neocortical oscillations during a working memory task., Proceedings Of the National Academy Of Sciences Of the United States Of America. 100 (2003) 7931-6.
[243] K.M. Kendrick, Y. Zhan, H. Fischer, A.U. Nicol, X. Zhang, J. Feng, Learning alters theta-nested gamma oscillations in inferotemporal cortex, (2009).
[244] J. White, M. Banks, R. Pearce, Networks of interneurons with fast and slow γ-aminobutyric acid type A (GABAA) kinetics provide substrate for mixed gamma-theta rhythm, Proceedings Of the National Academy Of Sciences Of the United States Of America. (2000).
[245] N. Brunel, X.J. Wang, Effects of neuromodulation in a cortical network model of object working memory dominated by recurrent inhibition., Journal Of Computational Neuroscience. 11 (2001) 63-85.
[246] R.E. Dustman, E.C. Beck, Phase of alpha brain waves, reaction time and visually evoked potentials, Electroencephalography and Clinical Neurophysiology. 18 (1965) 433–440.
[247] E. Callaway III, C.L. Yeager, Relationship between reaction time and electroencephalographic alpha phase, Science. 132 (1960) 1765.
[248] N.A. Busch, J. Dubois, R. VanRullen, The phase of ongoing EEG oscillations predicts visual perception, Journal Of Neuroscience. 29 (2009) 7869.
[249] J. Kang, H.P.C. Robinson, J. Feng, Diversity of intrinsic frequency encoding patterns in rat cortical neurons—mechanisms and possible functions, PloS One. 5 (2010) 5503–5515.
[250] E. Biavardi, M. Favazza, A. Motta, I.L. Fragalà, C. Massera, L. Prodi, et al., Molecular recognition on a cavitand-functionalized silicon surface., Journal Of the American Chemical Society. 131 (2009) 7447-55.
[251] F. Tancini, D. Genovese, M. Montalti, L. Cristofolini, L. Nasi, L. Prodi, et al., Hierarchical self-assembly on silicon., Journal Of the American Chemical Society. 132 (2010) 4781-9.
[252] E. Biavardi, G. Battistini, M. Montalti, R.M. Yebeutchou, L. Prodi, E. Dalcanale, Fully reversible guest exchange in tetraphosphonate cavitand complexes probed by fluorescence spectroscopy., Chemical Communications (Cambridge, England). (2008) 1638-40.
[253] F. Tancini, E. Rampazzo, E. Dalcanale, Interplay Between Cyclization and Polymerization in Ditopic Cavitand Monomers, Australian Journal Of Chemistry. 63 (2010) 646.
[254] W. Lu, J. Feng, On Gaussian Random Neuronal Field Model: Moment Neuronal Network Approach, (in Press). (2010).
[255] E. Rossoni, J. Kang, J. Feng, Controlling precise movement with stochastic signals., Biological Cybernetics. 102 (2010) 441-50.
[256] C. Zou, C. Ladroue, S. Guo, J. Feng, Identifying interactions in the time and frequency domains in local and global networks - A Granger Causality Approach., BMC Bioinformatics. 11 (2010) 337.
[257] X. Zhang, G. Leng, J. Feng, Coherent peptide-mediated activity in a neuronal network controlled by subcellular signaling pathway: experiments and modeling., Journal Of Biotechnology. 149 (2010) 215-25.
[258] N. Voges, A. Schüz, A. Aertsen, S. Rotter, A modeler's view on the spatial structure of intrinsic horizontal connectivity in the neocortex., Progress In Neurobiology. (2010).
[259] R. Sigala, J. Schultz, N.K. Logothetis, G. Rainer, "Own-species" bias in the categorical representation of a human/monkey continuum in the human and non-human primate temporal lobe, Annual Meeeting Of the Society Of Neuroscience. (2010).